INVESTIGATION OF A MULTIMODAL ELECTROSPRAY PROPULSION SYSTEM FOR SMALL SPACECRAFT

ETUDE D'UN SYSTEME DE PROPULSION DE TYPE ELECTROSPRAY MULTIMODAL POUR ENGINS SPATIAUX DE PETITE TAILLE

A Thesis Submitted to the Division of Graduate Studies
of the Royal Military College of Canada
by

Peter Lane Mallalieu, P.Eng.
Second Lieutenant

In Partial Fulfillment of the Requirements for the Degree of
Master of Applied Science in Aeronautical Engineering

October, 2022

INVESTIGATION OF A MULTIMODAL ELECTROSPRAY PROPULSION SYSTEM FOR
SMALL SPACECRAFT

ETUDE D'UN SYSTEME DE PROPULSION DE TYPE ELECTROSPRAY MULTIMODAL
POUR ENGINS SPATIAUX DE PETITE TAILLE

2Lt Peter Lane Mallalieu   Candidate, MASc in Aeronautical Engineering
Candidat, Maîtrise en génie aéronautique

Examination Committee / Comité examinateur

Prof. Fernando Fachin   Chair / Président
Royal Military College of Canada

Prof. Joshua Rovey   External / Externe
University of Illinois Urbana-Champaign

Prof. Danny Pagé   Internal-External / Interne-Externe
Royal Military College of Canada

Prof. Xiaohua Wu   Internal / Interne
Royal Military College of Canada

Prof. Manish Jugroot   Supervisor / Superviseur
Royal Military College of Canada

Acknowledgements

Abstract

Spacecraft have scaled down at a faster rate than the propulsion systems required for orbital maneuvers. As a result, the majority of small satellites launched into orbit do not have propulsion capabilities. The addition of a micro-propulsion system would allow for greater mission capability for earth-orbiting satellites. Electrospray thrusters are a promising micropropulsion technology which could be used to meet the propulsion needs of small satellites, or for fine attitude control of larger spacecraft. Electrospray thrusters operate by applying strong electric fields to electrically conductive propellants which are ejected at high speeds to produce thrust. These thrusters have many benefits over other forms of propulsion such as highly efficient propellant usage, the lack of any compressed gases required for operation, and no requirement for a neutralization process.

Combining multiple forms of spacecraft propulsion using a single common propellant is referred to as multimodal propulsion. A multimodal system would potentially provide a thruster with the capacity of selecting either high specific impulse mode or a high thrust mode. Interestingly, electrospray thrusters have the ability to operate in different modes based on the type of particle being emitted. Thus, this thesis investigates a micro-propulsion system which combines a droplet and ion mode electrospray emitter into a unified system using EMI-BF4 as the common ionic liquid propellant. Two porous wedge emitters each were manufactured using Laser milling: a high relative thrust droplet mode emitter fabricated from a commercially available P3 borosilicate glass; and a high efficiency ion mode emitter fabricated from a carbon xerogel substrate (fabricated in-house).

To characterize the multimodal thruster, a full beam and time-of-flight (ToF) experimental setup were developed at the RMC Advanced Propulsion and Plasma Exploration Laboratory (RAPPEL). The full beam experimental setup placed the thruster in close proximity of a beam collector aligned with a suppression grid designed to eliminate secondary electrons. A custom Einzel lens and Bradbury-Nielsen gate were used to focus and deflect the emitted beam, allowing for the flights times of emitted particles to be measured at the collector. These times were then used to indirectly estimate the thrust and specific impulse of thrusters operated within the low-pressure Bell-Jar chamber. The electrospray thruster was operated using a custom high voltage bi-polarity switch which alternated between positive and negative voltage of 0 to 3kV every three seconds. Both full beam and ToF measurements were successfully made for the multimodal thruster. The ion mode emitter had an onset voltage around 1400 V with an estimated thrust performance of 0.14 μN and specific impulse of 4040 s. Droplet mode had an onset voltage around 1375 V with an estimated performance of thrust at 14.5 μN and specific impulse of 140 s. The prototype thruster described in this research has demonstrated how various electrospray emitters could be combined into a multimodal system which could provide effective thrust for small spacecraft.

Résumé

Les engins spatiaux se sont réduits à un rythme plus rapide que les systèmes de propulsion nécessaires aux manœuvres orbitales. En conséquence, la majorité des petits satellites lancés en orbite n'ont pas de capacités de propulsion. L'ajout d'un système de micro-propulsion permettrait une plus grande capacité de mission pour les satellites en orbite terrestre. Les propulseurs à électropulvérisation sont une technologie de micropropulsion prometteuse qui pourrait être utilisée pour répondre aux besoins de propulsion de petits satellites, ou pour le contrôle d'attitude fin d'engins spatiaux plus grands. Les propulseurs à électropulvérisation fonctionnent en appliquant des champs électriques puissants à des propulseurs électriquement conducteurs qui sont éjectés à grande vitesse pour produire une poussée. Ces propulseurs présentent de nombreux avantages par rapport à d'autres formes de propulsion, tels qu'une utilisation très efficace du propulseur, l'absence de gaz comprimé requis pour le fonctionnement et aucune exigence de processus de neutralisation.

La combinaison de plusieurs formes de propulsion d'engins spatiaux à l'aide d'un seul propulseur commun est appelée propulsion multimodale. Un système multimodal fournirait potentiellement un propulseur avec la capacité de sélectionner soit un mode d'impulsion spécifique élevée, soit un mode de poussée élevée. Fait intéressant, les propulseurs à électropulvérisation ont la capacité de fonctionner dans différents modes en fonction du type de particules émises. Ainsi, cette thèse étudie un système de micro-propulsion qui combine un émetteur d'électronébulisation en mode gouttelette et ionique dans un système unifié utilisant EMI-BF4 comme propulseur liquide ionique commun. Deux émetteurs poreux ont chacun été fabriqués à l'aide d'un fraisage au Laser : un émetteur en mode gouttelette à poussée relative élevée fabriqué à partir d'un verre borosilicaté P3 disponible commercialement ; et un émetteur à mode ionique à haut rendement fabriqué à partir d'un substrat de xérogel de carbone (fabriqué en interne).

Pour caractériser le propulseur multimodal, une configuration expérimentale à faisceau complet et temps de vol (ToF) a été développée au RMC Advanced Propulsion and Plasma Exploration Laboratory (RAPPEL). La configuration expérimentale place le propulseur à proximité d'un collecteur de faisceau aligné avec une grille de suppression conçue pour éliminer les électrons secondaires. Une lentille Einzel et une porte Bradbury-Nielsen ont été utilisées pour focaliser et dévier le faisceau émis, permettant de mesurer les temps de vol des particules émises au niveau du collecteur. Ces temps ont ensuite été utilisés pour estimer indirectement la poussée et l'impulsion spécifique des propulseurs actionnés dans la chambre Bell-Jar à basse pression. Le propulseur à électropulvérisation était actionné à l'aide d'un commutateur bi-polarité haute tension personnalisé qui alternait entre une tension positive et négative de 0 à 3 kV toutes les trois secondes. Les mesures du faisceau complet et du ToF ont été effectuées avec succès pour le propulseur multimodal. L'émetteur en mode ionique avait une tension de démarrage de 1400 V, une performance de poussée estimée de 0,14 µN et une impulsion spécifique de 4040 s. Le mode gouttelette avait une tension de démarrage de 1375 V avec une performance estimée de poussée à 14,5 µN et une impulsion spécifique de 140 s. Le propulseur prototype décrit dans cette recherche a démontré comment divers émetteurs à électropulvérisation pourraient être combinés dans un système multimodal qui pourrait fournir une poussée efficace pour les petits engins spatiaux.

Contents

List of Tables

List of Figures

1 Introduction

Spacecraft and the systems they support have an increasingly beneficial impact to daily life on Earth. Communications, meteorology, and navigation all use Earth orbiting satellites to provide valuable information which positively impact our day to day lives [1, 2, 3]. In Canada satellites play a critical role in search and rescue operations and assisting farmers to optimize crop yields [4, 5]. Satellites are also used to track climate change by measuring arctic sea ice melt and pollution [6]. The knowledge gained by spacecraft being sent past our planet to the solar system and beyond have the potential to produce untold benefits for humanity.

Overcoming the Earth's gravity to launch objects into space has always been a costly and complex challenge. At the beginning of the space age satellites launched into orbit were small due to the limited capability of early rocket technology. From the 1960s to around 2010, there had been a general trend of satellites becoming larger and more capable. In 1958, the United States launched the Vangaurd-1 satellite, which weighed a mere 1.74 kg [7]. Just four years later in 1962, Canada's first satellite, "Alouette 1" was launched, having a mass of 145.6 kg [8]. Progressively overtime as rocket technology improved, the size and weight of spacecraft increased allowing them to perform more complex tasks in orbit. As of 2022, the International Space Station (ISS) has the combined mass of approximately 420,000 kg [9]. While impressive, larger satellites and space stations remain reserved for only the wealthiest nations on Earth who can afford them.

Recently, there has been a trend towards launching small satellites into space. Improvements to manufacturing techniques and the advent of micro-electro-mechanical-systems (MEMS) has allowed for the democratization of spacecraft missions. Smaller spacecraft, which have comparable capabilities to their larger predecessors, now comprise the majority of satellites launched into orbit. These small satellites also cost dramatically less to launch [10], which has allowed smaller countries, universities, and companies to access space. As the democratization of space continues, the hope is that innovation will accelerate [11].

While satellites have scaled down in size, it has been a challenge to develop propulsion systems which are capable of operating in a low power regime with a small form factor. This challenge has led to the vast majority of operational small satellites to omit a propulsion capability [12]. Spacecraft propulsion systems are used to launch spacecraft from Earth into space, and once in space, to control attitude and perform orbital maneuvers [13, 14]. This research investigates micro propulsion technology which can be used to enhance the capability of small satellites. The following introduction details the various types of spacecraft propulsion and their application to small satellites. Subsequent sections will detail the development and testing of a multimodal electrospray thruster produced to help drive the technology forward.

1.1 Rocket Propulsion

Spacecraft propulsion is dominated by rocket propulsion. Rockets are self-contained propulsion systems which convert potential energy from a propellant into a propulsive force. Following Newton's third law, propellant is ejected at high speeds out one side of a vehicle producing a thrust force thus pushing the vehicle in the opposite direction. In reference to spacecraft the term "rocket" is most commonly associated with orbital launch vehicles, which use large chemical boosters to lift heavy objects away from the Earth's gravitational pull into outer space. There are other types of rockets such as electric propulsion (EP) which are used on spacecraft once in outer space. Since all rockets follow the same physical principles it is useful to define relevant parameters which allow them to be characterized and compared.

1.1.1 Basics of Rocket Propulsion

The absolute thrust (T), typically measured in Newtons, can be explained by momentum. If the propellant's exhaust velocity (ν_e) is assumed to be constant and expelled axially in 1-dimension, then thrust can be seen as the change in momentum on the rocket's center of gravity. A rocket's thrust can be explained by Equation 1.1.

$$T = \dot{m}\nu_e + A_e(p_e - p_0) \approx \dot{m}\nu_e \tag{1.1}$$

Where $\dot{m}$ is the exhaust mass flow rate of propellant, A_e is the rocket exhaust cross-sectional area, and p_e is the exhaust flow pressure at the exit, and p_0 is the ambient pressure. The equation is simplified when it is assumed that nozzle exit pressure equals the ambient pressure.
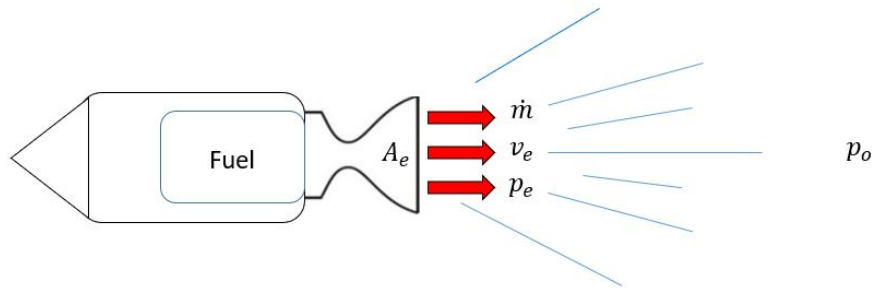
Figure 1.1: Generalized view of the parameters which impact the force or thrust a rocket produces.

A thrust force which varies with time can be explained by the total impulse (I_t) seen in Equation 1.2. This parameter equates to the total energy produced by a propulsion system for a particular period.

$$I_t = \int_0^t T dt \tag{1.2}$$

One of the most common parameters used in rocketry is the specific impulse (I_{sp}), which represents the thrust produced per unit of propellant mass flow. The I_{sp} measures how efficiently a rocket uses its propellant to create thrust. For propulsion systems with self contained propellant,

the I_{sp} is directly proportional to the exhaust velocity ν_e. The I_{sp} can be calculated using the formula in Equation 1.3.

$$I_{sp} = \frac{I_t}{m_p \, g_0} = \frac{T}{\dot{m} \, g_0} = \frac{\nu_e}{g_0} \tag{1.3}$$

Where m_p is the mass of propellant and g_0 is the standard gravitational acceleration at sea level (9.81 m/s^2). Both the total and specific impulse are described in the unit "seconds". This metric is a measure of how many seconds one pound of fuel can produce one pound of thrust.

The total change in velocity (ΔV) a rocket can produce is described using the Tsiolkovsky or ideal rocket equation shown in Equation 1.4 below. The equation takes into consideration that as thrust is produced, the mass of propellant being ejected from the rocket reduces the rocket's overall mass.

$$\Delta V = \nu_e \, ln \left(\frac{m_0}{m_f} \right) = I_{sp} \, g_0 \, ln \left(\frac{m_0}{m_f} \right) \tag{1.4}$$

Where m_o is the initial wet mass (including the propellant) and m_f is the final dry mass (without propellant) of a . The ratio of the wet mass to dry mass (m_o/m_f) is referred to as the propellant mass ratio.
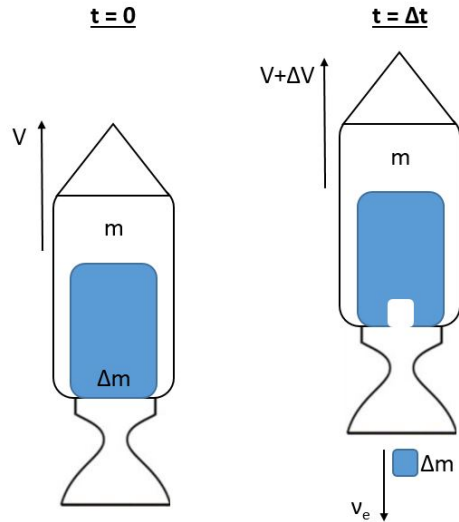
Figure 1.2: The mechanisms behind the ideal rocket equation.

The ideal rocket equation is useful for comparing the overall performance of rocket propulsion systems. It can also be used to calculate the propellant required for certain orbital maneuvers. The ΔV values of various orbital maneuvers in low Earth orbit (LEO), geosynchronous orbit (GEO) can be seen in Table 1.1.

The burn time of a propulsion system is another useful metric for planning missions and conducting orbital operations. The total burn time available to a rocket is calculated using equation 1.5.

$$t_b = \frac{m_p \, I_{sp} \, g_0}{T} \tag{1.5}$$

Table 1.1: The change in velocity "ΔV" requirements for various spacecraft maneuvers [15, 16].

Typical Propulsion Requirements	
Spacecraft Maneuver	ΔV (m/s)
Annual Attitude Control	2-6
Annual Station Keeping (GEO)	50
Annual Drag Compensation	30
Transfer from Earth to LEO	9,700
Orbit transfer from LEO to moon	5,900
LEO to Mars transfer orbit	4,300

The efficiency (η) of a particular propulsion system can be summarized in equation 1.6. Efficiency is determined by comparing the kinetic energy produced in the propulsion systems exhaust compared to the total power (P) which is available to the system. The power available is dependent on the type of propulsion. Chemical rockets obtain power from energy stored within chemical bonds, while electric propulsion (EP) obtains power from external sources, such as solar panels.

$$\eta \approx \frac{\frac{1}{2}\dot{m}\nu_e^2}{P} \tag{1.6}$$

1.1.2 Chemical Propulsion

Chemical rockets utilize a rapid series of reactions to extract energy stored within the chemical bonds of a propellant. These chemical propellants produce tremendous amounts of thermal energy which is expanded through a converging-diverging nozzle to produce acceleration [17]. Many historical spacecraft used chemical rockets as the primary form of propulsion. Examples include the Atlas V rocket which launched the first humans to the moon and the Space Shuttle's rocket boosters. A summary of the different types of chemical propulsion is shown in Table 1.2.

Table 1.2: Typical performance parameters for the various type of chemical propulsion.

Chemical Rocket Parameters					
Propulsion Type	Thrust (N)	Specific Impulse (s)	Power Range (W)	Common Propellant	Ref
Solid Rocket	10^7	250	10^{11}	Al, Mg, Zn	[15]
Monopropellant Rocket	1-500	200	10^5	N_2H_4	[15]
Bipropellant Rocket	10^6	300-400	10^{10}	LOX + H_2	[15]
Cold Gas Thruster	0.1-100	50	50	N_2, NH_3	[15]

Chemical rockets can be broken down into three general types based on the type of propellant used: solid, mono-propellant, and bi-propellant [17]. As its name would suggest, solid rockets utilize solid chemical propellants. The propellant is often made up of many small grains or pellets of highly combustible material. Solid propellants have many advantages such as their ease of storage and their high launch reliability. Solid-rockets are often used in military applications such as ballistic missiles, and as boosters to liquid rockets [18]. One drawback of solid propellants is they lack the ability to be throttled, so once ignition has begun all of the propellant is burned. Unlike solid propellants, liquid propellants can be fired in a series of impulses making them more useful for a wide array of maneuvers. Mono-propellant rockets use a singular liquid propellant such as hydrazine (N_2H_4) to produce thrust. The propellant is decomposed once it passes through a

catalytic bed and the resulting hot gas is then expanded through a nozzle [19]. Mono-propellants are typically used for attitude and orbital control for spacecraft where reliability outweighs the need of high efficiency [17]. Bi-propellant rockets store two separate chemicals in different storage tanks: a liquid oxidizer and a liquid fuel. When the rocket is fired, the two propellants are pressured into a thrust chamber, where they react. An example of a bi-propellant system would be the liquid oxygen (LOX) and kerosene used on the primary booster of the Saturn V rocket [20]. Bi-propellants have the highest overall performance of chemical thrusters in terms of having both high thrust and specific impulse. This performance requires complicated components, such as cryogenic cooling, and turbo-machinery, to pressurize and pump propellant.

Cold gas thrusters are the simplest, and one of the most trusted forms of spacecraft propulsion [13]. These thrusters operate in a similar fashion to a SCUBA tank, where a pressurized gas propellant is connected to a release valve. Released gases accelerate through a nozzle thereby producing thrust. While no chemical reactions occur during this process, cold gas thrusters are often categorized as chemical rockets. These simple systems are limited by the size of the tanks holding the propellant. The specific impulse of cold gas systems is typically low. The ability to produce many small impulses and the relative simplicity of cold gas systems make them a useful choice for certain applications [21]. Schematics of a few types of chemical propulsion can be seen in Figure 1.3.
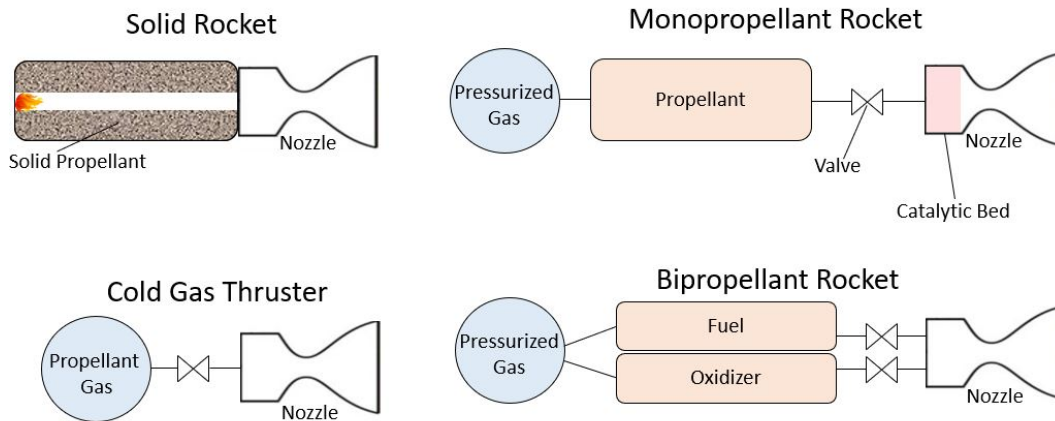
Figure 1.3: Overview of the various types of chemical rockets.

1.1.3 Electric Propulsion (EP)

The concept of using electricity to propel spacecraft reaches back to the advent of modern rocketry at the turn of the 20th century [14]. EP (also known as electric rockets) utilizes an electrical power source to accelerate propellant. Early on many EP concepts were developed, but it was not until after the Second World War that the technology gained serious attention. Over time technological advances such as solar panels, small electric power sources, and microelectronics have made EP a viable option for spacecraft today [22, 23]. More recently, EP has been used for orbital transfers between the Earth and the moon [24] and deep-space exploration [25]. Spacecraft can use a variety of methods to obtain electric power such as nuclear reactors, batteries, fuel cells, or solar panels [26]. The electric source varies based on the size and requirements of the satellite. As discussed in equation 1.4 the ΔV produced by a rocket is directly proportional to the exhaust velocity

of the propellant ν_e. Both the theoretical, and attainable exhaust velocities of EP systems are several magnitudes greater than chemical rockets allowing for the more efficient use of propellant. EP is generally broken into three categories, based on how the electrical power is used to create thrust. Electric power can accelerate propellant gases through heating (electrothermal propulsion), through the manipulation of electrically powered magnetic fields (electromagnetic propulsion), or by directly applying a electrical force (electrostatic propulsion) [27]. Table 1.3 describes some of the most established forms of EP and some in the developmental stage which are seen as promising for small spacecraft applications.

Table 1.3: Typical performance parameters for various type of Electric Propulsion.

Electric Propulsion Parameters					
Propulsion Type	Thrust (N)	Specific Impulse (s)	Power Range (W)	Common Propellant	Ref
Electrothermal					
Resistojet	0.2	100 - 300	10 - 100	N_2, H_2O	[15, 28]
Arcjet	0.1	500	1k	N_2H_4, NH_3	[15]
Electromagnetic					
MPD Thruster	0.5 - 50	1000 - 10k	10^4 - 10^6	Ar, Li	[15]
PPT	1μ - 1m	500-1500	10	PTFE	[15]
Electrostatic					
Ion Thruster (GIE)	1m - 0.1	3000	100-5k	Xe, I	[15, 28]
Hall Thruster	0.01 - 1	1500	200-20k	Xe, Kr	[15, 28]
Electrospray, FEEP	1μ - 10m	225 - 5000	4 - 100	Various	[28]

1.1.3.1 Electrothermal Propulsion

Electrothermal propulsion uses electric energy to produce thermal energy or heat. The thermal energy is absorbed by a gaseous propellant which is then converted into kinetic energy as it is accelerated through a nozzle [27].

Resistojets are a type of electrothermal propulsion which heat a gas propellant using an electric heater. Propellant is excited while travelling through a chamber with an electric heating coil, which is then accelerated through a nozzle. A schematic of a resistojet thruster can be seen on the left hand side (LHS) of Figure 1.4. The system is a straight forward form of EP and has low power requirements. The overall performance of a resistojet is constrained by the maximum temperature of the electric heater, and the surrounding structural materials. The heat transfer from the heating element to the structure leads to thermal efficiency losses not seen in other forms of EP. Many propellants have been used by resistojets with the most common being hydrazine and ammonia [28].

Arcjet thrusters heat the gaseous propellant using an electrical arc discharge. A typical thruster will produce an arc between a central cathode rod and an interior chamber wall anode. Arc heating allows the propellant to be directly heated at higher temperatures, with limited impact to the surrounding structure. Limitations of arcjets come in the form of arc instability, electrode material erosion, and higher electrical power requirements compared to a resistojet [29]. A sample arcjet can be seen on the right hand side (RHS) of Figure 1.4.
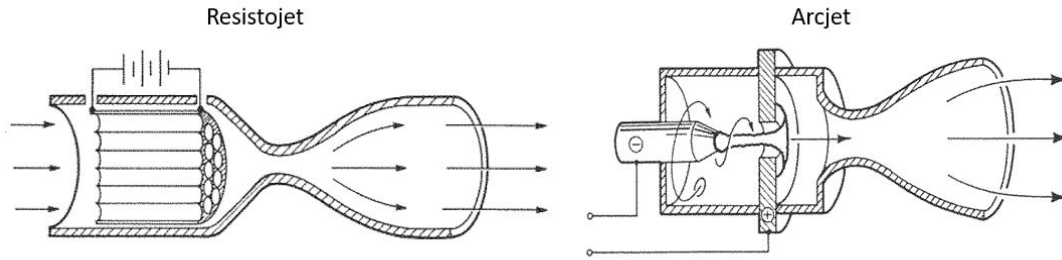
Figure 1.4: Schematics of a resistojet and arcjet thruster from [27].

1.1.3.2 Electromagnetic Propulsion

Electromagnetic propulsion (EMP) accelerate plasma by utilizing the interactions between currents within an ionized gas and magnetic fields [27]. The first step in both electromagnetic and electrostatic thrusters is to take a stored propellant and convert it into an ionized gas. Often referred to as plasma, an ionized gas contains large numbers of charged particles, such as ions and electrons. These charged particles makes a plasma conductive, allowing it to be controlled by electric and magnetic fields. Electromagnetic propulsion systems and some electrostatic thrusters are sometimes referred to as "plasma thrusters" due to their use of ionized gases. EMP accelerates charged particles using a magnetic field. When an ionized gas of a certain directional velocity ($\overrightarrow{v}$) is exposed to an electric ($\overrightarrow{E}$), magnetic field ($\overrightarrow{B}$), and a charge density (ρ), a current density ($\overrightarrow{j}$) will form parallel to the electric field. The magnetic field will interact with the current to create a force ($\overrightarrow{f_B}$) in the same direction as the flow. This force is referred to as the electromagnetic force or the Lorentz force described in Equation 1.7 and visualized in Figure 1.5.

$$\overrightarrow{f} = \rho\overrightarrow{E} + \overrightarrow{j} \times \overrightarrow{B} \qquad \overrightarrow{f_B} = \overrightarrow{j} \times \overrightarrow{B} \tag{1.7}$$
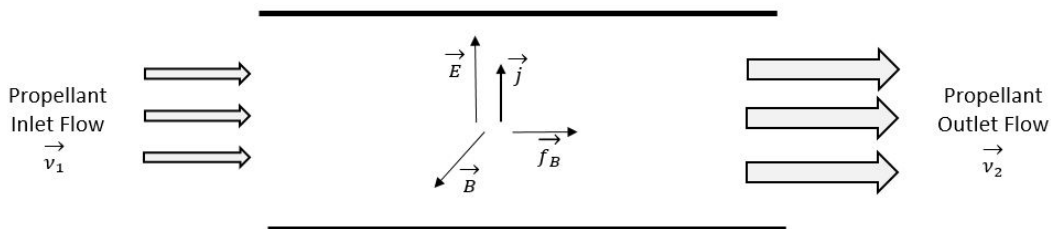
Figure 1.5: Overview of the principles behind electromagnetic propulsion.

Magento-plasma-dynamic (MPD) thrusters are seen to be potentially the most powerful form of EP in terms of theoretical thrust[30]. In order to produce high thrust, MPD's require a large supply of electric power [31], for example the electricity produced by a nuclear reactor [32]. MPD thrusters could be a useful tool for long range space travel on spacecraft. A typical MPD thruster

uses a rod-shaped anode electrode surrounded by a cylindrical anode as seen on the RHS of Figure 1.6. Similar to the arcjet thruster, a high current electric arc discharge is created between the anode and cathode. Electrons emitted from the cathode collide with heavier particles, forming an ionized gas. A self-induced magnetic field forms when the current returns from the cathode to the power source. This magnetic field produces the Lorentz force which accelerates the ionized gas out of the engine creating thrust. Some types of MPDs use externally induced magnetic fields formed by magnets to further accelerate the ionized gas [33].

Pulsed plasma thrusters (PPTs) were one of the first space tested electric propulsion systems having flown on the Soviet Zond II spacecraft in 1964 [27]. An example of a typical PPT, seen on the LHS of Figure 1.6, operates using two plate electrodes placed close to a solid propellant. When the electrodes are activated, an arc discharge ablates and then ionizes the solid material into a plasma. This cloud of plasma creates an electrical connection between the two electrodes, allowing current to pass between the two. The resulting Lorentz force accelerates the plasma creating thrust. Between each burst of the electric arc, charges need to be replenished at the electrodes. This leads to the thruster operating in a series of pulses instead of continuously. As the solid propellant is ablated a spring pushes the remaining propellant between the electrodes so firing may continue. PPTs are robust due to their simplicity and solid propellant.
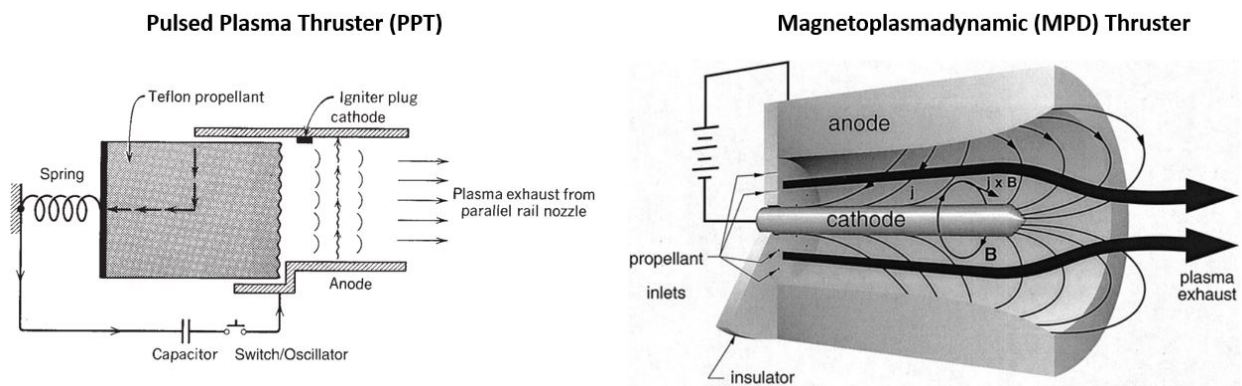
Figure 1.6: Operational overview of a PPT from [17], and a MPD Thruster from [34].

1.1.3.3 Electrostatic Propulsion

Electrostatic thrusters produce thrust by applying an electrostatic force to accelerate ions or highly conductive liquids to high speeds.

Ion thrusters, also known as gridded ion engines (GIEs), produce and accelerate positively charged ions. GIE's operate in three physical steps: ionization of a gas into plasma, acceleration of ions, and neutralization of the ion beam. Propellant gas is injected to an ionization chamber where a process such as electron bombardment or radio-frequency radiation is used to create plasma. The produced ions are then accelerated by a series of grids which form a steep electric potential gradient. The first grid (screen grid) is biased to a high potential which allows electrons to be "screened" from the accelerating ions. The second grid (acceleration grid) has a low potential applied, so a strong electric field between the two grids can accelerate the ions to high speeds. In some thrusters, a third grid (deceleration grid) can be used to create more space between ion extraction and acceleration,

and help to reduce grid erosion of the acceleration grid. As the thruster releases a beam of positively charged ions, the spacecraft can develop a negative charge. This charge can cause some ions to back stream towards the spacecraft, causing erosion and reducing beam strength. The final step performed by an ion thruster is neutralization, where a stream of electrons is fired into the exhaust plume to neutralise the positively charged ions. A schematic giving an overview of an ion thruster's operation may be seen in Figure 1.7. Noble gases such as xenon or krypton are common propellants, since they are easily ionized into plasma and their heavy atomic mass increases thrust.

Between the ion thruster's acceleration grids there is a region of positive charge. The ion current which can be obtained from these grids is limited by the space charge. The closer the grids are, the less voltage is needed to produce a desired electric field. Space charge is described by Child's law for a 1-D assumption shown in Equation 1.8.

$$j_i = \frac{4\epsilon_0}{9} \sqrt{\frac{2q_i}{m_i}} \frac{V^{3/2}}{d^2} \tag{1.8}$$

where ϵ_0 is the permittivity of free space, V is the discharge voltage, d is the distance between the two grids, q is the charge, and m is the mass of a particular ion.
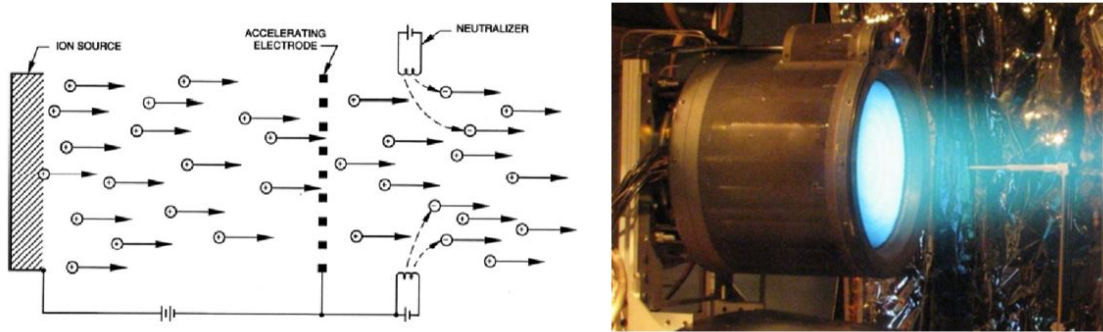
Figure 1.7: LHS - Schematic of the mechanisms behind an ion engine from [27]. RHS - The ESA's T6 Ion thruster being fired during testing from [35].

Hall Thrusters or Hall Effect Thrusters (HETs), like ion thrusters, use a strong electrostatic field to accelerate ions. HETs utilize magnetic fields for propellant ionization, and electric fields to accelerate ions, creating thrust. A radial magnetic field is formed using permanent magnets, or magnetic coils on both the inner and outer sections of the thruster. This field is used to contain electrons within the thruster, so that they can be used for ionization. Once a propellant is introduced, it becomes ionized through collisions with these electrons. The produced ions have a large enough mass that they cannot be contained by the magnetic field and are accelerated by an axial electric field produced by a set of electrodes. Figure 1.8 shows a schematic of the HETs principles of operation and an example thruster being tested. HET's acceleration region have both ions and electrons present which allows these thrusters to avoid the space charge limitation that impact ion thrusters. Like ion thrusters, HETs typically use heavy noble gases such as krypton or xenon as propellant. Hall thrusters come in two major variants: the stationary plasma thruster (SPT), primarily developed in Russia, or thruster with anode layers (TAL), developed in the USA [36].

Electrospray thrusters are an emerging form of EP, with the ability to produce precision attitude control on larger satellites [38], and perform orbital maneuvers on small satellites [39]. They operate
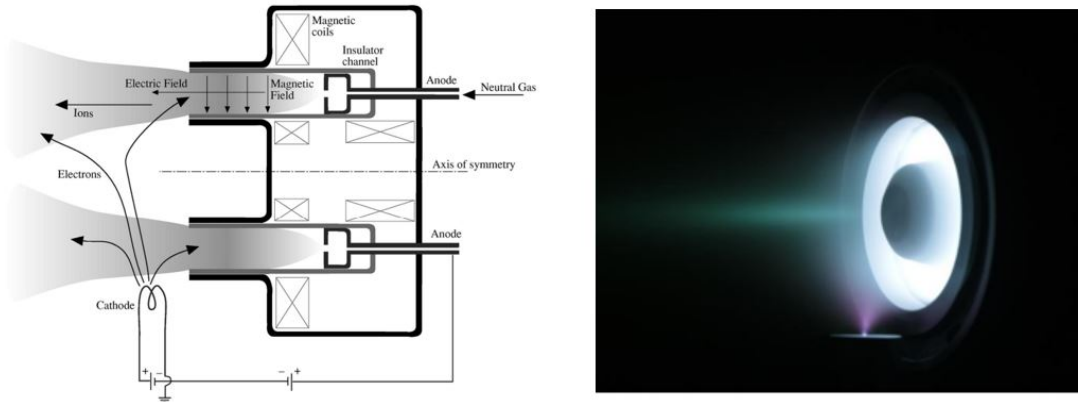
Figure 1.8: LHS - Schematic of the mechanisms behind an Hall Thruster from [36]. RHS - The HT100 Hall thruster produced by SITAEL from [37].

in a similar manner to ion engines. The primary difference is that electrosprays use electrically conductive liquid propellants, instead of inert gases. These propellants can be thought of as a soup of positive and negative ions. Since ions already exist in the liquid propellant there is no need for electrosprays to perform an ionization process. A strong electric field is formed by applying a large voltage difference between an emitter and an extraction grid. The conductive propellant reacts to the field and deforms into a liquid meniscus, extending outward towards the extractor grid in a cone shape called a Taylor cone [40]. At the apex of the meniscus the electrostatic forces overpower the liquid's surface tension forces and produces a stream of liquid droplets, ions, or a combination of both. The particles are then accelerated to high speeds producing thrust. Figure 1.9 gives a schematic of how an electrospray thruster operates. The type of particles emitted from the thruster depends on several factors, which are discussed in Chapter 2.

Electrospray thrusters have several different modes of operation. When purely emitting liquid droplets, the thruster is operating in droplet mode. The droplet mode of operation has traditionally been called a colloid thruster. Ionic liquid (IL) propellants are the focus of most research due to their excellent vacuum properties and ability to emit pure ions [41]. When an electrospray thruster emits only ions, it is said to be operating in an ion mode or in the purely ionic regime (PIR). Ion mode electrosprays have also been called ionic liquid ion sources (ILIS) in order to distinguish them from Field Emission Electric Propulsion (FEEP). The thrust and specific impulses are dependent upon the mode of operation. Droplet mode produces a higher relative thrust, while ion mode produces a higher specific impulse in the range of several thousand seconds.

Electrosprays have several benefits compared to other forms of EP. First, as mentioned earlier, there is no requirement for an ionization process. Second, the propellant can be fed from a reservoir to the emitters by capillary action caused by the electrostatic forces. This process eliminates the need for pressurized components or pumps to transport propellant. In spacecraft, it is optimal to have fewer moving parts and if possible remove pressurized gases, as these can cause failures during launch or in orbit. Third, since propellants contain both anions and cations, electrospray thrusters have the ability to produce a quasi-neutral beam. This can be achieved by emitting both positive and negative ions in close proximity, or by conducting bi-polar operation, where a positive beam is fired for a period followed by a negative beam. When emitting a quasi-neutral beam, there is no need for a neutralization process. The main drawback of electrosprays is that they are only capable of producing low amounts of thrust in the range of μN to mN. A single emission site

from these thrusters produces low thrust in the range of tens of nN to μN [42]. In order to obtain useful thrust levels, electrosprays use large arrays of hundreds or thousands of emitters being fired simultaneously.
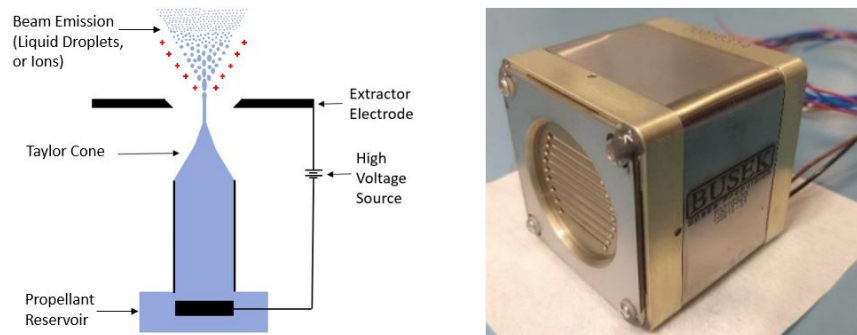
Figure 1.9: LHS - Schematic of the mechanisms of Electrospray and FEEP. RHS - Busek's BET-300-P Electrospray thruster designed for high precision control of small satellites from [43].

FEEP thrusters come from the same family as electrosprays. These thrusters also use an electric field to accelerate charged particles from highly conductive liquid propellant. The main difference is that a FEEP thruster extracts ions directly from a liquid metal ion source (LMIS). Common metals used are Indium, Cesium, and Gallium [28]. These metals can be launched as a solid, and then melted into a liquid propellant while in orbit. While an additional heating device is required, most metals used have low melting points, such as Gallium which melts at 29.76 °C. FEEP thrusters cannot produce a quasi-neutral beam, so a neutralizer is required to operate this thruster.

1.1.4 Other Spacecraft Propulsion Systems

1.1.4.1 Propellantless Propulsion

There are a variety of propulsion concepts, which are currently being researched and experimented on, that harness naturally occurring celestial energy in space to create propulsion. Some examples include solar sails and electrodynamic tethers.

The sun constantly emits photons, which radiate throughout the solar system. These photon particles collide with satellites, imparting their momentum in the process. Some of these particles are absorbed by satellites, but the majority are reflected. This solar radiation pressure (SRP) can cause a perturbation to a satellite's orbit, which over time can have a noticeable impact in its trajectory [44]. Similar to how sailboats harness the wind for movement, a solar sail or light sail utilizes SRP to create propulsion in space. The Japanese Aerospace Exploration Agency (JAXA) demonstrated the first use of a propulsive solar sail in their 2010 IKAROS mission to Venus [45]. The CubeSail mission has shown that there is an interest in deploying solar sails on small satellites [46]. The concept is seen to have a large future potential in many applications, such as long term interplanetary travel [47]. A photograph of a solar sail deployed in space can be seen in Figure 1.10.

Naturally occurring magnetic fields in space could also be used to provide a source of propellantless propulsion. Electrodynamic tethers (EDTs) are long conductive wires which can be deployed from satellites to produce a propulsive force [49]. These can only be used when orbiting celestial bodies which have a strong magnetic fields such as planets. Using Earth as an example, tethers from satellites in LEO could extend many kilometers into the ionosphere, and collect an electric
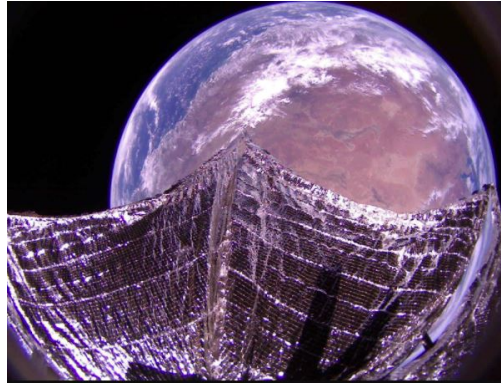
Figure 1.10: Deployed solar sail from the LightSail2 mission from [48].

charge as it interacts with charged particles. The electric current formed in the wire interacts with the Earth's magnetic field, which produces a Lorentz force capable of accelerating or decelerating a satellite. EDT's have been demonstrated on several space shuttle missions [50] and the concept has been proposed as a cheap method of de-orbiting satellites [51]. Another concept known as a magnetic sail uses a magnetic field to either accelerate or decelerate the charged particles in solar wind [52].

1.1.4.2 Nuclear Propulsion

Utilizing the energy released by nuclear reactions has been a proposed method of spacecraft propulsion since the start of the space era. Nuclear fission and fusion are seen as the most promising current technology to allow for future long term space travel [26]. Overall, nuclear propulsion has experienced a slow development due to budgetary, safety and political reasons [14].

Thermal Nuclear propulsion uses the heat released by nuclear reactions to pressurize and eject a propellant at high speeds. This method of propulsion is similar to a chemical rocket, except the energy comes from nuclear rather than chemical bonds. Twenty rocket reactors were tested on Earth during the 1950-1970s for NASA's Rover and Nuclear Engine for Rocket Vehicle Applications (NERVA) programs [53]. Recently, NASA has started to partner with the commercial sector to develop concepts for new thermal nuclear rockets [54].

Scientists have also investigated using a series of mini nuclear explosions to propel spacecraft referred to as pulsed nuclear propulsion [55]. NASA's project Orion in the 1950s and 1960s attempted to develop a pulsed nuclear propulsion vehicle, though it was unsuccessful [56].

Instead of using nuclear reactions to directly propel a spacecraft, on-board nuclear reactors could be used to produce large amounts of electricity. This electricity could be used to supply the energy required for a variety of spacecraft subsystems including EP. The use of Nuclear electric power sources could open the door for spacecraft to utilize high power EP systems such as MPDs [57] and the Variable Specific Impulse Magentoplasma Rocket (VASIMR) [58].

1.2 Small Satellites

The advent of small capable satellites has led to a revolution in space. Over the last decade, there has been a trend in the space industry to deploy small, low cost satellites. As the barrier to space is lowered, it is anticipated that the rate of innovation and progress within the industry will increase. While small satellites will not completely eliminate the need for larger satellites, the numerous benefits they provide show great promise for the future.

As can be seen in Figure 1.11, the number of small satellites being launched into space has been growing rapidly in the last decade. This upward trend is expected to continue, as small satellites start to be used by large commercial enterprises. Another important factor seen in this figure is the number of nanosats launched with propulsion capability. As shown in Figure 1.11 less than 7% of the total number of nanosats (1-10 Kg) launched have any kind propulsion capability [59].
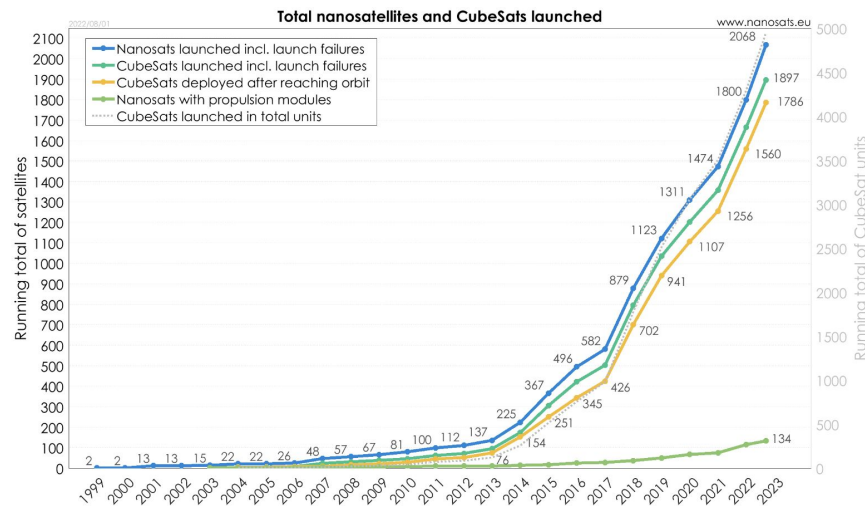
Figure 1.11: The number of nanosatellites which have been launched over the last few decades. Data shows that the majority of nanosatellites launched are CubeSats, and how few of these satellites have a propulsion capability [59].

It is common to categorize satellites by their total mass. A satellite is considered to be small if it has a mass less than 500 kg [60]. Small satellites are further broken down into several categories [61], which can be seen in Figure 1.12.

A common and established type of small satellite are CubeSats [64]. The CubeSat concept was introduced to create a common standard form for small satellites with the goal of being compact, light weight, and using standard commercial off the shelf (COTS) components. A 1U or single unit CubeSat has the dimensions of 10 cm x 10 cm x 10 cm and weighs approximately 1 kg. Larger CubeSats such as 2U, 3U, 6U, etc., are also commonly used configurations. This puts most CubeSats within the size category of Nanosats. CubeSats have seen a huge adoption and more than 1,600 of them have been launched into orbit as of 2022 [59].

Femto-satellites are currently the smallest category of satellites. These include satellites with a total mass of less than 100 grams. Many of the satellites in this category are referred to as Chipsats, due to there resemblance to small computer microchips. In 2019 the KickSat-2 mission successfully deployed over one-hundred Chipsats called sprites using a single 3U CubeSat[63]. This mission clearly demonstrated the growing trend of smaller and cheaper satellites.

Instead of developing one powerful satellite, which comes in and out of range as it orbits, a

Category	Mass
Large	>1000kg
Medium	500 – 1000kg
Mini	100 – 500kg
Micro	10 – 100kg
Nano	1 – 10kg
Pico	0.1 – 1kg
Femto	<0.1kg
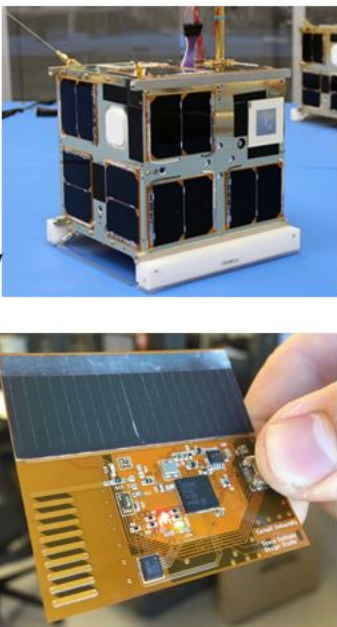
Figure 1.12: The classification of satellites based on mass. The image on the upper RHS is a nanosatellite from the University of Toronto's CanX-4,5 mission from [62]. The bottom RHS shows Cornell University's "Monarc" Chipsat which is a femto satellite from [63].

constellation containing a large number of small satellites can be launched in many different orbits to obtain continuous coverage of Earth. Satellite constellations have been deployed in orbit for many decades. The global positioning system (GPS) first launched in the late 1970s, triangulates a position on the surface of the Earth by using four satellites which are in direct view of the position [65]. Using small satellites, the concept of constellations has been amplified to the point where hundreds or thousands of satellites could be used to form mega-constellations. It has been proposed that these large groupings of small satellites would be cheaper, more robust, and offer more complete coverage compared to traditional constellations [66]. The SpaceX company's Starlink program has gained approval for an initial constellation of 1,584 small satellites, and has applied to expand the mega-constellation to 12,000 satellites long term [67]. Figure 1.13 shows the results of a simulation which presents the satellite coverage of the complete (12,000 satellites) StarLink constellation. Many other companies such as Boeing, OneWeb, and several Chinese firms have plans to launch mega-constellations with thousands of small satellites [67].

As tens of thousands of satellites are put into orbit, the total amount of objects surrounding the planet is continuously increasing. At a certain point, the orbits around Earth could become saturated by a swarm of orbital debris [68]. Similar to an electron avalanche, a series of collisions between orbital objects could experience exponential growth, leading to a layer of tiny projectile-like objects surrounding the Earth. In 2011, the Canadian Armed Forces (CAF) launched the "Sapphire" satellite designed to observe and track objects in space [69]. Sapphire tracking data is used to predict potential collisions with space debris.
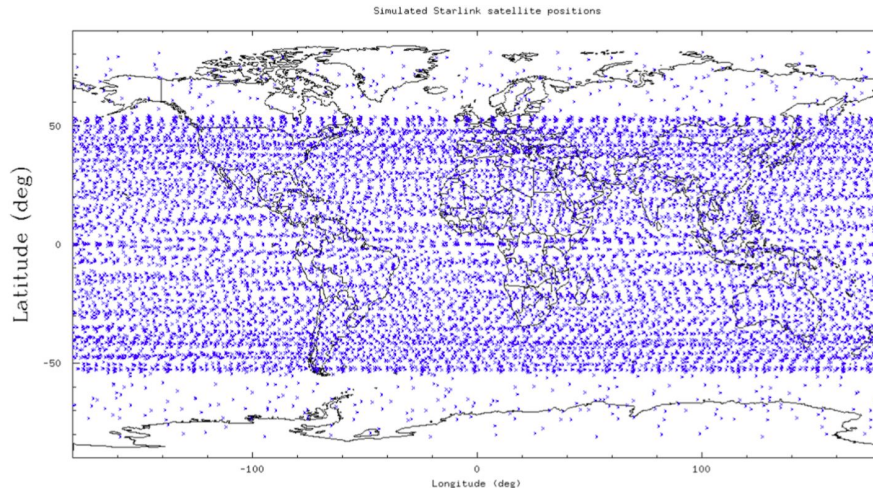
Figure 1.13: A simulation of the StarLink constellation's satellite coverage of Earth assuming the purposed 12,000 small satellites are launched from [67].

1.2.1 Propulsion Miniaturization

The many types of spacecraft propulsion have not been scaled down at the same rate as other spacecraft components. The scaling of a thruster's physical size does not lead to a linear change in performance. Many electrical components of spacecraft are designed to use the same MEMS technology previously developed for use in computers and cell phones [70]. Small spacecraft propulsion systems do not have other industries from which to obtain and adapt technology. There is currently a plethora of research underway to investigate propulsion geared toward small satellites [60, 71].
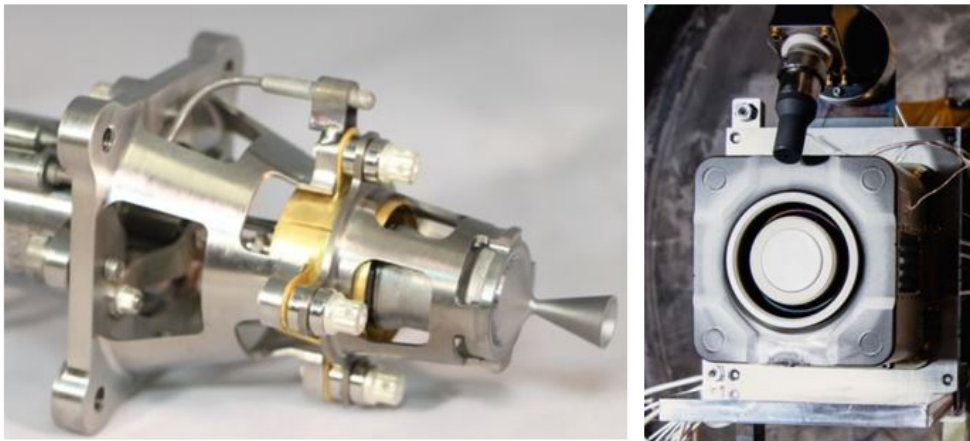
Figure 1.14: LHS - Aerojet's prototype "GR-1" green monopropellant chemical thruster, capable of thrust in the 1 N range and I_{sp} 231 s from [72]. RHS - Busek's "BHT-600" Hall thruster which can achieve approximately 39 mN of thrust and 1500 s specific impulse from [73].

While being able to produce large amounts of thrust, chemical thrusters are limited by relatively low I_{sp}. As chemical thrusters are scaled down the theoretical I_{sp} will not increase, but several factors could cause it to decrease. Some of these factors include:

- Many hydrocarbon-based propellants used in chemical rockets have difficulty producing adequate atomization in small combustion chambers. This leads to losses from incomplete combustion of the propellant [74].
- Miniaturized chemical thrusters have much higher losses from viscous forces. The smaller geometry leads to additional viscous losses, since boundary layers next to walls will be proportionally larger [75].
- The transfer of thermal energy from the hot gas exhaust to the rocket's structure increases when scaled down. The thermal transfer can be compensated for by reducing the exhaust temperature from the combustion chamber, but this will cause a reduction to the I_{sp}. A cooling system could be added, but would be complicated in a small scale [75].
- Several propulsion system components such as valves, regulators, and propellant tanks are difficult to miniaturize.

Even with the limitations which come with scaled-down chemical rockets, they can still be fit to a small satellite [76]. Electrothermal thrusters share most of the same challenges of chemical thrusters due to the mechanisms of expanding a hot gas through a nozzle.

EP systems which generate and utilize plasma, such as MPDs, GIEs, and HETs, all must confront the challenge of ionization when they are scaled down. The ionization process relies upon collisions between electrons and larger neutral particles. Only a certain portion of gaseous propellant fed into an ionization chamber will become plasma. The non-ionized neutral gas particles do not contribute to propulsion, so it is important that these thrusters maximize propellant ionization. The propellant utilization efficiency (α_u) [15], can be calculated using Equation 1.9

$$\alpha_u = \frac{\dot{m}_i}{\dot{m}_p} = \frac{I_b}{e}\frac{M}{\dot{m}_p} \tag{1.9}$$

where the mass flow rate of ions ($\dot{m}_i$) is compared to the total propellant mass flow rate ($\dot{m}_p$). The equation assumes that the exhaust particle beam is only comprised of singly charged ions. In the elaborated equation I_b represents the ion beam current, e is the element charge of an electron, and M is the atomic mass of the chosen propellant. In order to obtain a high ionization efficiency the distance an electron travels between each collision needs to be minimized. This distance, referred to as the mean free path (λ_m), can be explained with Equation 1.10.

$$\lambda_m = \frac{1}{n_e Q} \tag{1.10}$$

Q is the collision cross-section area (m^2), and n_e is the number density of electrons. In order to maintain a certain probability of ionization, the mean free path will vary based on the size of the ionization chamber. In small ionization chambers, the n_e is increased to obtain the desired mean free path. The resulting plasma density is higher in small chambers. This increased plasma density leads to efficiency losses caused by:

- Increased heat flux which leads to thrusters becoming too hot, to the point of melting. Increased heat requires an additional cooling system to be designed, or for reduced performance to be accepted.
- A higher number of particles will collide with the thruster's walls causing erosion and geometric changes. In many cases, such as with the an ion engine or Hall thruster, erosion is the primary life-limiting factor, meaning the thruster erodes away before it can use all the available propellant [77, 78].

The magnetic fields used to trap particles within a thruster's ionization chamber are also impacted when thrusters are scaled down. In order to keep electrons within an ionization chamber, they must

be within a magnetic field's Larmor radius (r_L). The r_L needs to be scaled based on the size of the thruster as noted in Equation 1.11. As an ionization chamber decreases in size, more powerful magnets are required to contain electrons. In order to accommodate more powerful magnets, small HETs often require higher power electromagnetic coils or larger permanent magnets.

$$r_L = \frac{m_e v_e}{eB} \tag{1.11}$$

Here m_e is the mass of an electron, v_e is the thermal velocity of the electron, and B is the magnetic field strength. Due to the reasons above, plasma based propulsion systems generally have higher efficiencies at higher power.

Propulsion systems which use highly conductive liquid propellants, such as Electrospray and FEEP, do not need to perform a gas ionization process. The emission sites of these thrusters are typically on the scale of microns. For these thruster types the challenge is not with scaling down, rather it is with scaling up. Single emission sites do not produce adequate thrust for most spacecraft applications. To achieve higher thrust levels, electrosprays use large arrays of emissions sites. The ion electrospray propulsion system (iEPS) thruster developed by the Massachusetts Institute of Technology (MIT) contains 480 emission sites within a 1cm^2 area [79]. Figure 1.15 shows examples of current state-of-the-art electrospray and FEEP thrusters [28].

Figure 1.15: LHS - Accion System's TILE 3 electrospray thruster [80], RHS - Enplusion NANO FEEP Thruster [81]

Figure 1.16 (A) shows the various types of propulsion compared by their thrust and specific impulse. Looking at this in isolation, it may be concluded that chemical rockets are capable of high thrust missions, while hall thrusters and ion thrusters are best suited to missions where higher specific impulse is required. This conclusion does not take into account the limited power available to EP propulsion systems on small satellites. The majority of small satellites use a combination of solar panels and batteries to produce power. A 3U CubeSat will typically produce approximately 20-30 watts of power [12]. This is the total power allocated to the entire satellite, of which propulsion is considered a secondary payload. Figure 1.16 (B), shows that only PPTs and electorspray/FEEP are capable of operating in this low power regime.
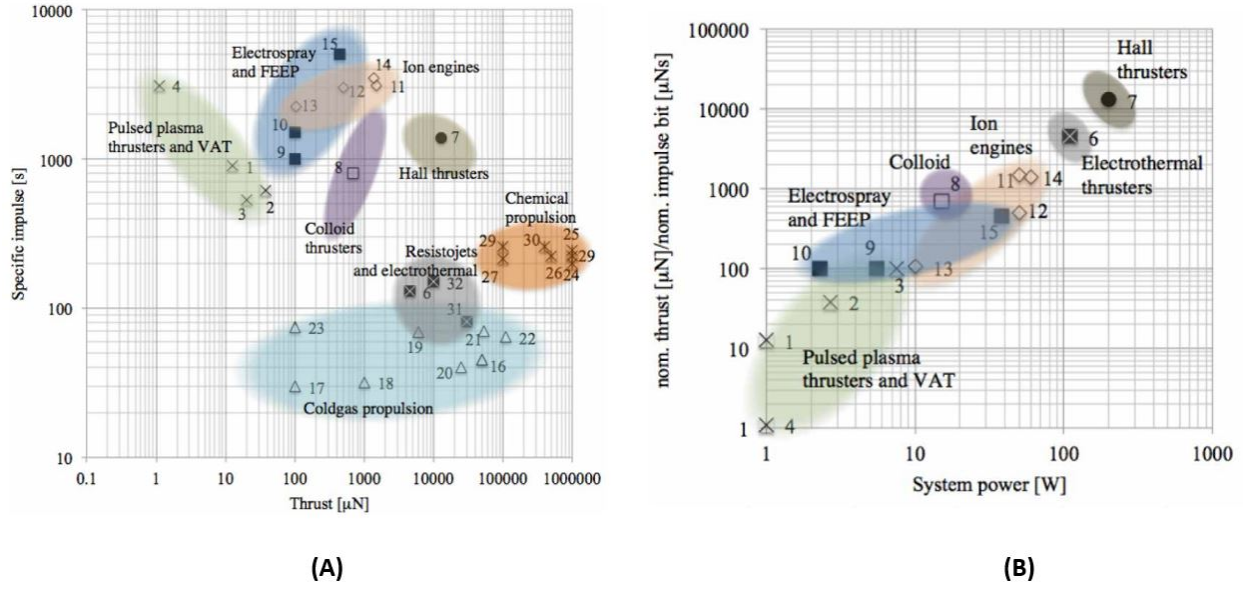
Figure 1.16: Graphs showing a comparison of propulsion systems for small satellites from [60]. LHS - Compares thrust (μN) to specific impulse (s). RHS - Compares the required system power (W) to the nominal thrust (μN).

1.3 Mission Capability of Micro Propulsion Systems

Satellites in space can benefit from the enhanced capability and flexibility which a propulsion system provides. This section describes a variety of orbital maneuvers beneficial to small satellites.

1.3.1 Orbital Altitude and Inclination

To change orbits, a propulsion system produces a change in velocity, either in the direction of motion (prograde burn), or against the direction of motion (retrograde burn). In this case the goal of a burn is to change the altitude and or inclination of satellite.

To better describe changes in orbit, an example small satellite in LEO that is required to overfly several locations around the globe will be used. For simplicity, the satellite has a circular Keplerian orbit. The satellite's velocity can be described by Equation 1.12:

$$\nu = \frac{\mu}{r} \tag{1.12}$$

where μ is the Earth's gravitational parameter (398,000 km^3/s^2) and r is the radius (km) of the satellite from the Earth's center. A method to change the altitude (r) of a satellite from one circular orbit to another is called a Hohmann transfer. This maneuver requires one burn to move a spacecraft into a transfer orbit, and a second burn to move off the transfer into the final orbit. The change in velocity required by these burns can be calculated using Equation 1.13 and 1.14.

$$\Delta V_1 = \sqrt{\frac{\mu}{r_1}} \left(\sqrt{\frac{2r_2}{r_1 + r_2}} - 1 \right) \tag{1.13}$$

$$\Delta V_2 = \sqrt{\frac{\mu}{r_2}} \left(1 - \sqrt{\frac{2r_1}{r_1 + r_2}} \right) \tag{1.14}$$

Here r_1 is the radius of the original orbit and r_2 is the radius of the final orbit. To change the inclination of the satellite between two circular orbits where the radius does not change, an engine burn needs to be performed along an orbit where the two orbits intersect. The change in velocity required to change the direction can be described by Equation 1.15.

$$\Delta V_i = 2\nu sin \frac{\Delta i}{2} \tag{1.15}$$

The maneuvers described above have assumed that a rocket burn produces an instantaneous change to velocity. In actuality, these impulsive maneuvers are often performed using high thrust propulsion, where the required change in velocity is achieved with a short burn period. Since most EP systems have low thrust, a significant amount of time is required to obtain adequate velocity change for orbit changes. These long duration burns are referred to as non-impulsive or continuous burns. To change the altitude of a 500 kg satellite from an orbiting radius of 800km to 20,000 km using EP, it is estimated to take anywhere from 113 to 400 days. For changes to inclination the transfer times could be even longer [82]. When a continuous burn is conducted it sends a satellite into a spiral trajectory. A visual representation of the spiral trajectory, caused by a continuous burn, can be seen in Figure 1.17. The change in velocity required to move from one circular orbit to another using a continuous burn could be estimated using Equation 1.16.

$$\Delta \nu_{con} = \left(\frac{\mu}{r_1} \right) - \left(\frac{\mu}{r_2} \right) \tag{1.16}$$
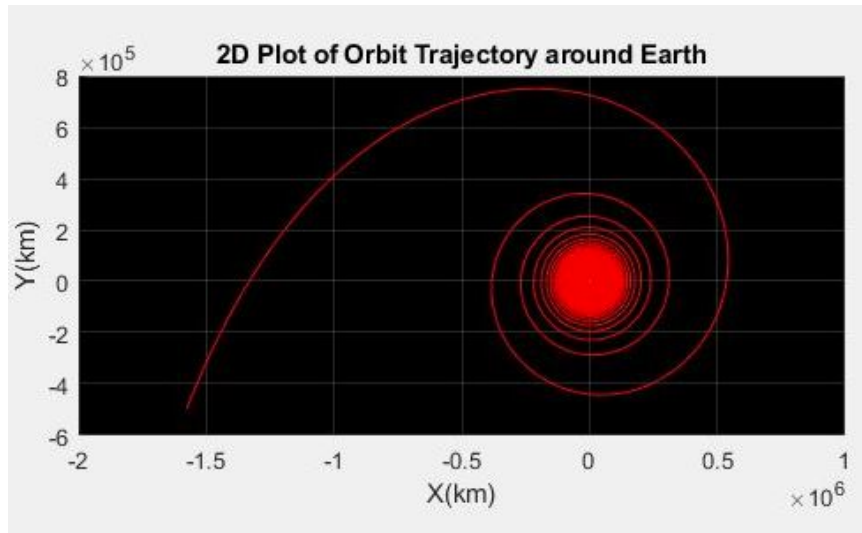
Figure 1.17: Matlab simulation of a spiral orbit formed when continuous thrust is applied to a small satellite. In the simulation a 3U Cubesat with a mass of 4 kg starts at a circular equatorial orbit with an altitude of 1000 km. If the satellite's propulsion system provides a continuous 0.45 mN of thrust, it would take approximately 2 years and hundreds of orbits to escape Earth's gravity.

1.3.2 Orbital Station Keeping

Satellites which are orbiting the Earth do not experience an ideal Keplerian orbit. Several astronomical effects are constantly working to set a satellite off its desired course. These phenomena are commonly referred to as perturbations.

To alleviate congestion, space law recommends that at the end of an Earth orbiting satellite's lifetime, it must be de-orbited within a 25 year period [83]. Most CubeSats (due to the lack of propulsion) are placed into low orbits, so that they will naturally decay into the atmosphere. At these low altitudes, the decay is mostly caused by aerodynamic drag, due to the rarefied air particles of Earth's outer atmosphere. The force caused by atmospheric drag can be described by Equation 1.17.

$$F_D = -\frac{1}{2}\rho C_D A \nu_{rel}^2 \tag{1.17}$$

Where ρ is the atmospheric density at a given altitude, C_D is the coefficient of drag, A is the area of the satellite depending on its attitude, and ν_{rel} is the relative velocity of the satellite with respect to the atmosphere. The density of the atmosphere decreases roughly exponentially with increasing altitude, which means that as a satellite drops in altitude the drag force becomes more pronounced.

At an altitude of around 800 km and above the SRP begins to have a greater perturbing force than atmospheric drag. The amount of force exerted on a satellite by solar radiation depends on many factors, such as the solar cycle, solar flares, and if a third body such as the Earth is blocking the sun. In orbits around the Earth, this energy can be generally represented by the solar radiation constant $G_{sc} = 1350^{W}/m^2$. The radiation will impart a momentum ($P = G_{sc}/c = 4.57 \times 10^{-6} \ N/m^2$) on orbiting spacecraft where c is the speed of light. The force this momentum causes can be described by Equation 1.18.

$$F_{SRP} = PC_{ref}A \tag{1.18}$$

Where C_{ref} is the reflection coefficient representing how well a satellite reflects solar radiation.

The shape of the Earth also causes perturbations. The Earth is not perfectly round and has an oblate shape having approximately a 22 km larger radius at the equator when compared to the poles. This variation in shape impacts an orbit's trajectory, which over time can change various orbital parameters, such as inclination. In astrodynamics, these impacts are referred to as the J2 perturbation.

While atmospheric drag, solar radiation pressure, and J2 are the primary perturbations within LEO, there are many other perturbation forces in space. The gravitational force of large celestial bodies such as the moon, the sun, and even Jupiter have an impact on a satellite's trajectory. To counteract all of these perturbations, occasional impulses from a propulsion system can be used. This type of propulsion is especially important for satellites which are expected to have a long lifetime, or need to maintain a precise orbit.

1.3.3 De-orbiting

As mentioned in section 1.2, debris orbiting Earth, especially in LEO, could soon become a widespread problem. To prevent a future where orbital collisions become a serious problem, it is important satellites or debris, which are no longer serving a function, be removed from orbit. At the end of a satellite's service life, propulsion systems can be used to decelerate satellites toward the Earth, where they will be destroyed in the atmosphere.

Disposal orbits are close to the Earth's surface where satellites would naturally decay due to atmospheric drag and be destroyed. Putting a satellite into a disposal orbit instead of completely

de-orbiting, lowers the required ΔV a propulsion system would need, while obtaining the desired effect. Graveyard orbits are designated areas where satellites can be put at the end of their life. These orbits are selected to be far away from any densely populated parts of space around the Earth. Graveyard orbits are often used when a satellite does not have the required ΔV to de-orbit back into the Earth's atmosphere. While graveyard orbits solve a short term problem, it is not the ideal solution in the longer term. Having the propulsion capability to de-orbit would allow small satellites to have higher operational orbits.

1.3.4 Attitude Control

Attitude Determination and Control Systems (ADCS) is typically a standard feature on most spacecraft. After a satellite is launched into orbit, a process called de-tumbling occurs, where any unwanted rotation is eliminated. Once a satellite is settled, attitude determination can be used to position a satellite in any required direction, for example orienting solar panels toward the sun. The colloid micro-newton thruster (CMNT), developed by Busek, was used for high precision attitude control on the Laser Interferometer Space Antenna (LISA) mission [84].

1.3.5 Formation flying

A grouping of satellites following the same orbital trajectory gives expanded reach not possible with a single satellite. The satellites in a constellation act like a large extended antenna. Several spacecraft missions could use formation flying as a way to reduce costs and increase mission flexibility [85]. Small satellites are suited to formation flying since they are individually less complex compared to larger satellites and cheaper to deploy on a large scale [86]. In order for a constellation to complete a mission, the relative spacing between satellites needs to be maintained. This spacing is usually achieved using a propulsion system. The University of Toronto has launched several CubeSat missions to demonstrate formation flying. The CANX-2 mission, which launched in 2008, contained several technologies needed for formation flying, such as propulsion systems and precise position sensors [87]. The CANX-4 and 5 mission flown in 2014 demonstrated the relative position control between two CubeSats to a control accuracy of one meter [88].

1.3.6 Interplanetary Travel

Having seen great success in LEO, small satellites are now becoming mature enough to be launched into interplanetary space [89]. The first interplanetary CubeSat mission, NASA's Mars Cube One (MarCO), was launched in 2018 [90]. Building off that success there are 13 interplanetary small satellites planned for launch on NASA's Artemis 1 mission to the moon [91]. Future missions involving interplanetary travel will require adequately miniaturized propulsion systems [92].

1.4 Multimodal Propulsion

The various modes of propulsion available to spacecraft discussed in section 1.1 each have their strengths and weaknesses. Chemical rockets exhibit high thrust and have low fuel efficiency or I_{sp}, while EP thrusters exhibit low thrust, but high I_{sp}. There is a growing interest in developing ways to combine the strengths of high thrust and high I_{sp} modes of propulsion on a single spacecraft. This ability to operate in different modes is referred to as hybrid propulsion. On large spacecraft, multiple propulsion systems with their own subsystems can be implemented at the expense of space.

Hybrid propulsion can provide more efficient propellant usage, expanded mission capability, and satellite mission flexibility.

The joint European Space Agency's (ESA) and JAXA's BepiColombo mission, to orbit and study the planet Mercury, demonstrates how multiple propulsion modes can be integrated. The satellite used in the mission is comprised of three primary units, the JAXA's Mercury Magnetosphere Orbiter (MMO), ESA's Mercury Planetary Orbiter (MPO), and the Mercury Transfer Module (MTM), which are used to deliver the two orbiters from Earth to Mercury [93]. Figure 1.18 shows the configuration of the three modules at launch. For the 7 year voyage, the MTM is equipped with a hybrid propulsion system comprised of a high thrust bi-propellant chemical thruster, and a high I_{sp} xenon ion engine propulsion system [94]. The MPO utilizes a separate hybrid propulsion system where a set of bipropellant chemical thrusters capable of 22 N of thrust are used for orbital insertion and ΔV correction, while a second set of monopropellant chemical thrusters producing 5 N of thrust are used for attitude control [95]. Finally, after being placed into orbit by the MPO's propulsion system, the MMO uses its own cold gas thruster for attitude control [96].
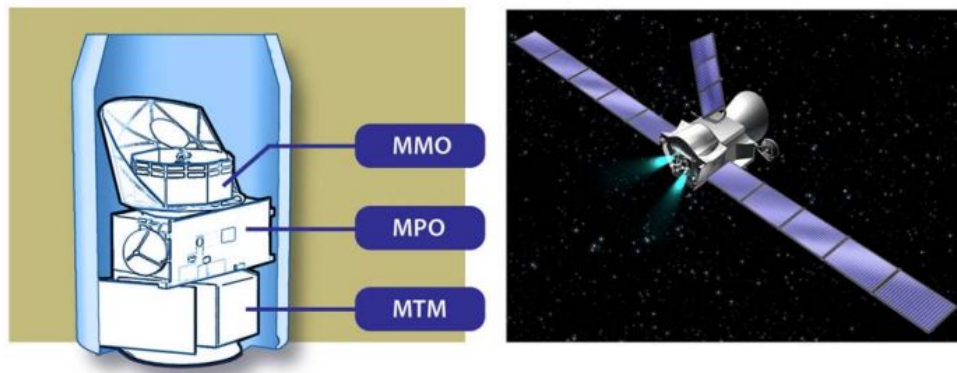
Figure 1.18: The BepiColombo mission satellite. LHS - The satellite components during orbital launch, RHS - satellite in a cruise flight configuration from [97].

Taking hybrid propulsion a step further, multimodal propulsion is the integration of two or more propulsion modes into a system which utilizes a common propellant source [98]. A multimodal propulsion system integrating two different modes is sometimes referred to as bi-modal or dual mode propulsion. Multimodal systems share all the same benefits of hybrid mode propulsion with the added benefit of increased mass savings and mission flexibility. On smaller spacecraft, where physical space comes at a much higher premium, it is ideal to combine many propulsion modes into a single unified system. Having multiple modes of operation can greatly expand the possible missions a satellite can undertake. This means additional adaptability in orbit, and also lowers research and development costs, since a single multimodal system can be used in many mission types. Two identical satellites could be launched into orbit and perform different missions depending on how propellant is used.

Many multimodal concepts are in varying levels of development. Multimodal propulsion has been demonstrated in space by the University of Tokyo's PROCYON mission. The small satellite (50 Kg) used in the mission was equipped with the "ion thruster and cOld-gas thruster unified propulsion system" (I-COUPS). Both the ion thruster and cold gas thruster use a common xenon gas propellant [99]. PROCYON successfully demonstrated how the I-COUPS propulsion system could propel a micro-spacecraft in deep-space missions [100].

The combination of monopropellant chemical thruster, and an ion mode electrospray have been investigated. Finding a propellant which is conductive enough to be used in electropraying, and will still react as a chemical propellant is challenging. This type of propellant is referred to in literature as Energetic Ionic Liquids (EIL) [28]. The Electric Propulsion Laboratory at the University of Illinois has tested a purposely designed chemical/electrospray propellant called FAM-110A in both modes of operation [101, 102]. This work has shown the capability of the concept and has generated interest for future research.

Hybrid Propulsion

	Monopropellant Chemical Rocket	Electrospray
Thrust	250-25,000mN	$0.01 - 1mN$
I_{sp}	$200 - 285s$	$225 - 5000s$

Multimodal Propulsion

	Monopropellant Chemical Rocket	Electrospray
Thrust	1000mN	0.5mN
I_{sp}	226s	780s
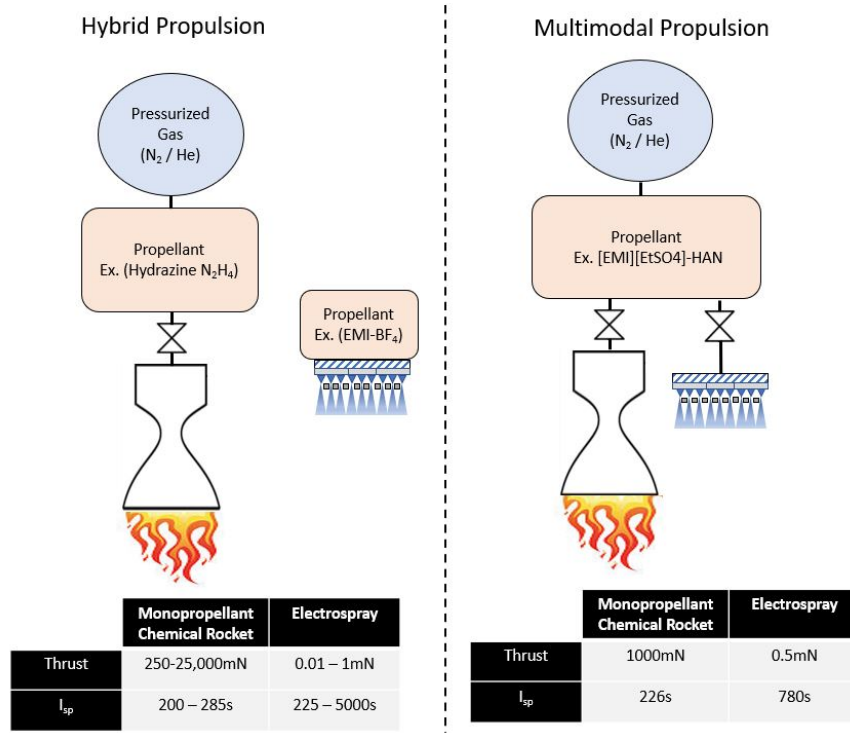
Figure 1.19: Comparison between a theoretical hybrid, and multimodal propulsion system integrating a monopropellant chemical thruster, with an electrospray [103, 98].

Current concepts for multimodal propulsion do have some drawbacks. When many modes of propulsion are combined into a system, the performance of each mode is generally not as high as any state-of-the-art stand alone thruster. This comparison is illustrated in Figure 1.19 and tables. One of the main hurdles in combining two modes together is finding an optimal propellant which can operate in both modes of operation.

1.5 Concluding Remarks

An overview of the various types of spacecraft propulsion (section 1.1), small satellites (1.2), orbital maneuvers performed by satellites (1.3), and the concept of multimodal propulsion (1.4) have been introduced. Electrospray thrusters, described in section 1.1.3.3, can be operated in either a relatively high thrust droplet mode or a high specific impulse ion mode. In this research, the development of a multimodal system, where a droplet and ion mode electrospray are unified using a single propellant is investigated. Since both modes of operation utilize the principles of electrospray thrusters, the concept is suited to providing a more flexible, light-weight propulsion system to the small satellites of today and in the future. Chapter 2 contains an overview of the mechanisms, and design considerations, and testing methods of electrospray thrusters.

2 Electrospray Theory Overview

This chapter will review the fundamental theories and operational modes of electrospray propulsion. The different forms of electrospray emission are important to highlight since understanding these different modes is critical to forming a multimodal system. The different types of electrospray emitters, propellants, manufacturing techniques, and performance testing methods will be covered.

2.1 Electrospray Phenomena and Applications to Propulsion

The concept of electrospraying is over a century old. As early as 1882, Lord Rayleigh predicted that a liquid with a particular charge could become unstable and eject small droplets into fine jets [104]. In a series of experiments from 1914-1917, Zeleny demonstrated that when a sufficiently strong potential is applied to conductive liquids, they deform into a cone shape and form a liquid jet [105, 106, 107]. In 1964, Taylor developed an analytical model for describing the cone shape formed during electrospraying [40]. Taylor proposed that the cone shape is a result of a balance between the surface tension force of a liquid and the pressure force caused by the electric field. This characteristic cone shape is referred to as a Taylor cone [40].

Around the same time as Taylor's work, droplet emission electrosprays, called colloid thrusters, were being proposed as a form of spacecraft propulsion [108]. Thruster designs and methods of measurement were developed in the early 1960s [109, 110]. Krohn distinguished between the different modes of electrospray operation, including a liquid jet of droplets, a liquid jet accompanied by ions, and ion emission [110]. Various designs also investigated bipolar operation to create a quasi-neutral droplet stream and the use of linear slit geometries to increase thrust density [111]. More advanced colloid thrusters designed in the early 1970s were able to produce 111 μN thrust per emitter [112] and operate by using large emitter arrays with I_{sp} values above 1,000 seconds [113, 114]. Despite good performance records, research in these colloid thrusters dwindled after the 1970s, due to the high voltages (10-20 kV) required for operation and rudimentary micro-fabrication techniques at the time [108].

While propulsion was on the backburner, research into electrosprays continued. Mass spectrometry (MS) is a method used to measure the mass-to-charge ratio of ions. Ions produced by electrospray were first used in MS by Dole [115]. Further developments in Electrospray Ionization (ESI) on large biomolecules by Fenn resulted in him being awarded a Nobel Prize [116]. Investigations into the various modes of electrospray emission were investigated by Cloupeau and Prunet-Foch [117]. This research coined the term "cone-jet" for a Taylor cone which emits a continuous jet of droplets. Electrospraying has been used in many applications such as a method of drug delivery [118], nano-particle material deposition [119], and air purification [120].

Around the turn of the millennium, there was a renewed interest for electrospray as a method of spacecraft propulsion. It was found that Electrospray propulsion was a useful method to perform precision attitude control on larger spacecraft. In 2008, the Busek company developed the colloid

micro-newton thruster (CMNT) to perform fine attitude control on the ESA's Laser Interferometer Space Antenna (LISA) Pathfinder mission [121]. The CMNT became the first electrospray propulsion unit operated in space after the launch of the LISA Pathfinder mission in 2015 [122]. Advances in micro-manufacturing techniques led to the small satellite revolution discussed in Chapter 1. Consequently, there has been an increased focus on the development of micro-propulsion systems as the primary form of propulsion for small satellites. The opportunity has led companies, such as Busek [43], as well as newer start-ups, including Enpulsion [123] and Accion systems [124], to develop electrospray technology for micro-spacecraft propulsion. Research within Universities is still very active.

2.1.1 Principles of Electrospray Emission

To produce thrust, electrospray propulsion accelerates charged particles using an electric field. The field is formed between an electrospray emitter and an extractor electrode. In the presence of a strong electric field, highly conductive liquids will deform into a cone-shape. The applied field draws free ions from propellant to the surface of the liquid. This layer of high charge density causes a physical bulge in the liquid toward the extractor intensifying the electric field. This process continues until the electrical forces on the surface of the liquid exceed the surface tension forces causing particles to be ejected. Taylor developed an ideal mathematical model of the electrospray cone formation, assuming that the liquid being used is a perfect conductor and that the electric field is in the normal direction from the surface of the liquid [40]. Based on these assumptions the cone structure forms due to the balance between the surface tension force of the liquid (P_γ), the electrostatic pressure (P_E) caused by the electric field, and the pressure difference between the conductive liquid and its surroundings (Δp). The counteracting forces which cause the formation of a Taylor cone can be seen in Figure 2.1.
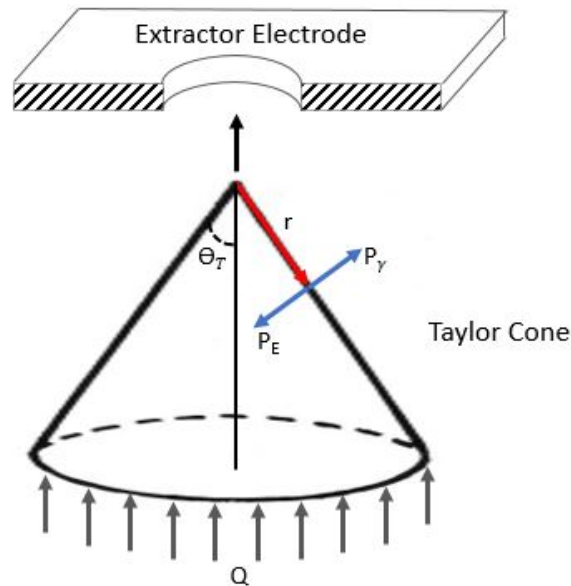
Figure 2.1: Schematic of a Taylor cone and the forces which influence its formation. The liquid flow rate (Q) is drawn towards the emission site. The cone shape is formed by the equilibrium between the liquid surface tension force (P_γ) and the electrostatic pressure force (Δp).

The pressure force caused by the surface tension of a liquid is described in Equation 2.1.

$$P_\gamma = \gamma \kappa_c \tag{2.1}$$

In this equation γ is the surface tension coefficient of the liquid and κ_c is the surface curvature of the liquid. The electric pressure on the liquid caused by the electric field can be described using the normal of the Maxwell stress tensor seen in Equation 2.2.

$$P_E = \frac{1}{2}\epsilon_0 E_n^2 \tag{2.2}$$

In this equation ϵ_0 is the electrical permittivity of free space and E_n is the electric field in the normal direction of the liquid cone's surface. The electric field E_n is described in equation 2.3

$$E_n = \sqrt{\frac{2\gamma cot(\theta_T)}{\epsilon_0 r}} \tag{2.3}$$

where θ_T is the Taylor cone half angle, as seen in figure 2.1, and r is the distance from the cone's apex to a position on the surface of the liquid. The equilibrium at any point along a Taylor cone is a result of the force balance seen in Equation 2.4.

$$P_E + \Delta p - P_\gamma = 0 \tag{2.4}$$

In a situation where propellant is passively fed to the emitter and there is no external pressurization, the applied liquid pressure (Δp) can be considered to be negligible. Under this assumption the equilibrium of forces is described by equation 2.5.

$$P_E = P_\gamma \tag{2.5}$$

At the apex of the Taylor cone where the electric field is strongest, a stream of charged particles is ejected. This occurs when the surface tension forces of the liquid have been overcome by the electrostatic forces. These charged particles come in the form of liquid droplets, ions, or some combination of both. The type of emission is based on several factors including the geometry of the emitter, the electric field strength, the liquid propellant flow rate, and the properties of a chosen propellant. The assumption of equilibrium at the surface of a Taylor cone is true, up to the region of emission. The distance where equilibrium can no longer be assumed has been analytically defined using Equation 2.6 [125],

$$r^* = \left(\frac{\epsilon\epsilon_0 Q}{K}\right)^{\frac{1}{3}} \tag{2.6}$$

where ϵ, Q, and K are the electric permittivity, flow rate and electric conductivity of the liquid being used.

2.1.2 Droplet Emission

Electrosprays emitting purely droplets can take many forms including a pulsating jet, conejet and multi-jets as shown in Figure 2.3 [117]. The conejet mode of emission is best able to maintain a consistent controllable emission of droplets. (Note: In this thesis, unless otherwise stated, the droplet mode electrospray will be synonymous with a conejet emission.)

In order to produce an electrospray emission, a certain applied voltage threshold must be surpassed. The voltage at which an electrospray beam is produced is known as the onset voltage
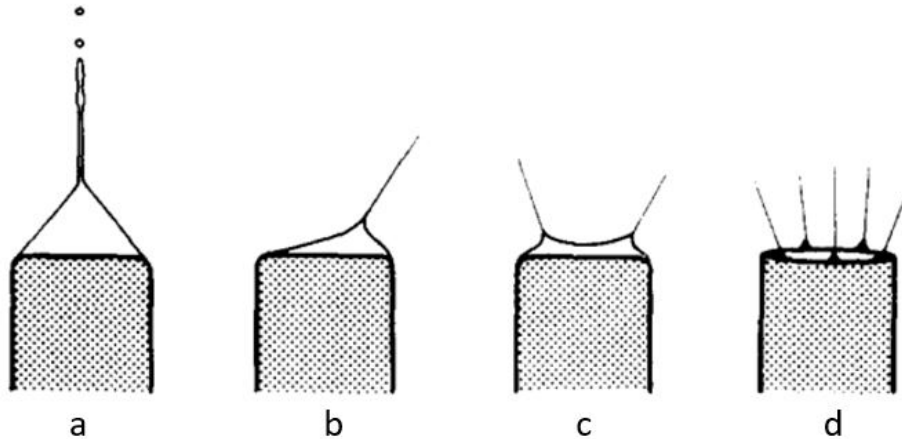
Figure 2.2: Several modes of droplet electrospray emission. Conejet emission can be seen in a and b. Multi-jet emission can be seen in part c and d from [117].

(V_{onset}). Many factors such as the tip radius of an emitter (r) and distance between the tip radius and the extractor electrode (d) have a large influence on an onset voltage. If it is assumed that an electrospray emission site has a hyperboloid shape and the extractor electrode is a flat plate, then V_{onset} can be determined analytically using Equation 2.7 [126].

$$V_{onset} = \sqrt{\frac{\gamma r}{\epsilon}} ln \left(\frac{4d}{r} \right) \tag{2.7}$$

The beam an electrospray produces is comprised of charged particles which carry a current (I) that can be measured. The emission current of a droplet mode electrospray is characterized by Equation 2.8 [125].

$$I \propto \sqrt{\frac{\gamma K Q}{\epsilon}} \tag{2.8}$$

The flow rate can have a large impact on the resulting electrospray emission. Once an emission site begins emitting droplets, a portion of the liquid is ejected away from the Taylor cone. When this happens, a minimum flow rate (Q_{min}) is required to maintain a consistent conejet emission. (Q_{min}) is characterized by Equation 2.9 [125].

$$Q_{min} \approx \frac{\gamma \epsilon_0 \epsilon_r}{\rho K} \tag{2.9}$$

In this equation, ρ represents a propellant's density and ϵ_r is the relative dielectric constant of a propellant. At low flow, near and below (Q_{min}), electrosprays have been shown to emit ions in addition to droplets.

2.1.3 Mixed Ion-Droplet Emission

Electrospray emitters being operated at low Q using propellants which have high conductivity can emit ions in addition to droplets [127]. The process by which ions are emitted from a conductive liquid is called field evaporation. Common models outlining the field evaporation process are

outlined in the following section 2.1.4. Operation in the mixed Ion-Droplet mode is generally unwanted for the purposes of propulsion, since the combination of both emission modes leads to inefficient emission.

The charge to mass ratio (q/m) of a particle is an important factor to determining its velocity. Charged droplets have a much smaller q/m compared to ions. This equates to ions being accelerated to higher velocities than droplets. If both droplets and ions are being emitted simultaneously, most of the thrust is produced by the larger droplets. When this occurs, the energy used to accelerate ions is much greater than any additional thrust they produce. The losses caused by this wasted energy are referred to as the polydispersive inefficiency [128, 129]. Whenever an electrospray thruster releases particles, which have varying mass and charge, it will cause inefficiencies. For this reason, it is ideal to produce a uniform particle beam.
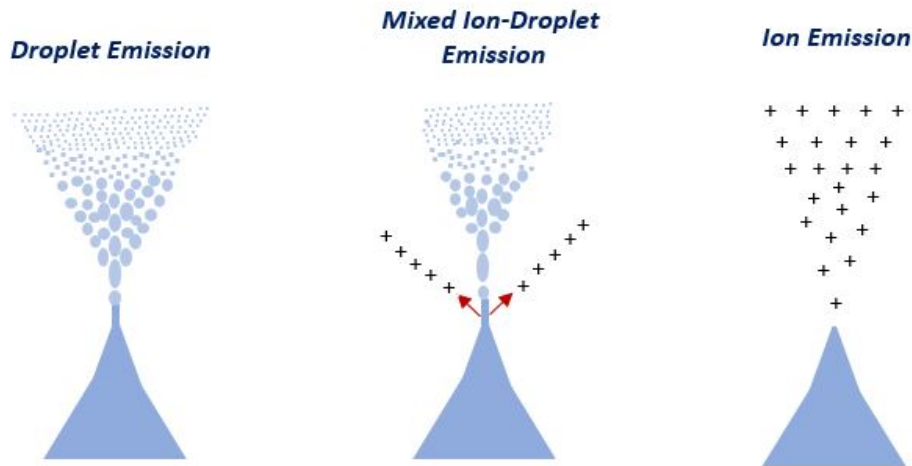
Figure 2.3: The various modes of electrospray emission from a Taylor cone.

2.1.4 Ion Emission

In 2003, an electrospray using an ionic liquid (IL) propellant, demonstrated operation in a pure ion mode [130]. Propulsion in ion mode is desirable because of the high specific impulses which can be achieved. Ions are emitted from an electrospray through the process of field evaporation. The rate at which ions evaporate from the surface of the liquid can be estimated using equation 2.10 [131, 132],

$$j_e = \frac{kT}{h}\sigma\,exp\left(-\frac{\mathcal{E}}{kT}\right) \tag{2.10}$$

where k is the Boltzmann constant, T is the liquid's temperature, h is Planck's constant, σ is the free charge density at the liquid surface, and $\mathcal{E}$ is the required activation energy for evaporation. Many methods of approximating $\mathcal{E}$ have been developed. A method commonly used in electrospray research can be seen in Equation 2.11 [133],

$$\mathcal{E} = \Delta G - \sqrt{\frac{q^3 E_n}{4\pi\epsilon_0}} \tag{2.11}$$

where ΔG is the solvation energy for a particular ion. From Equation 2.11, if temperature remains constant as the electric field strength increases, the activation energy for ion evaporation decreases. The electric field strength needed for ion emission can be estimated using Equation 2.12.

$$E_n \approx \frac{4\pi\epsilon_0}{q^3}\Delta G^2 \tag{2.12}$$

Ion solvation energies are typically in the range of 1-2 eV, which would equate to an electric field strength around $1 - 2 \cdot 10^{-9} V/m$ for ion emission.

2.2 Types of Electrospray Emitters

There are three common types of electrospray emitters: capillary, externally-wetted, and porous. Each emitter type uses a different process to transport propellant from the reservoir to the Taylor cone emission site. A schematic of these three emitter types can be seen in Figure 2.4. Emitter selection plays an important role in design, since certain emitters are better suited to the various modes of electrospray operation. In this section, we will review the three types of emitters and review the theory behind their use.

Capillary emitters have been used since the inception of electrospray science. These emitters use small syringe-like channels through which a liquid propellant flows toward the tip. Capillary emitters will typically be a pressurized system, so propellant is externally forced toward the emission site. Previous studies at RAPPEL have used capillary emitters controlled using pressurized nitrogen gas [134]. Capillary emitters are often used when aiming to achieve droplet mode emission. They have also been able to achieve ion mode emission using highly conductive ILs [130]. For ion mode operation, the small emitter geometry needed to achieve low flow rates often leads to failure due to clogging and overflow of propellant [135].
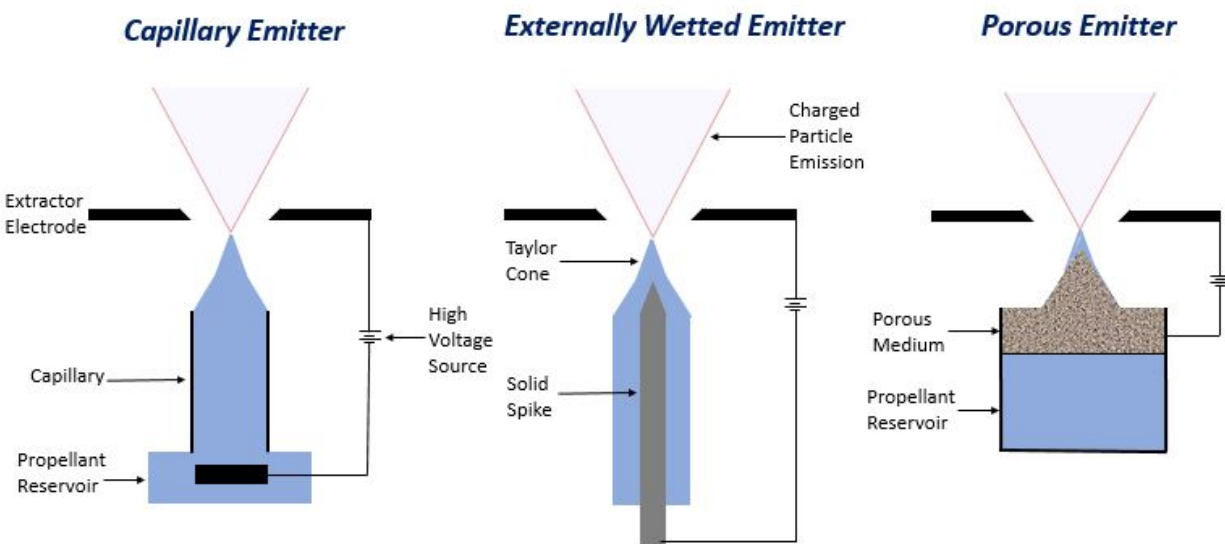
Figure 2.4: The three common types of electrospray emitters used for propulsion.

Externally-wetted emitters are coated in a layer of propellant, which migrates to the emitter apex once a sufficient electric field is applied. Inspired by tungsten tip emitters used by liquid metal

ion sources (LMIS), externally-wetted emitters were first used with IL propellants in 2004 [136]. The solid structure emitters are often cone-shaped to assist with the formation of Taylor cones. This emitter type has shown that numerous IL propellants with lower conductivity were capable of achieving operation in ion mode, even if they had poor performance when used with capillary emitters [137]. Only a limited selection of propellants can be used with externally-wetted emitters, since liquid directly exposed to a vacuum environment will evaporate. Externally-wetted emitters also often have multiple emission sites and off-axis emission which reduces efficiency [138].

With the knowledge that low propellant flow rates were needed to obtain ion mode emission, research began on using porous substrates as electrospray emitters. Porous structures transport liquid from a reservoir to the emitter tip through capillary action. Since the liquid travels between the pores of the material, it is not directly exposed to its surroundings. This allows porous emitters to incorporate the high efficiency ion mode found in externally-wetted emitters with the internal structure of a capillary emitter. A material's porosity and mean pore size influence the attainable propellant flow rate. Porous emitters were chosen as the focus of this research due to the advantages stated above and their use in several state-of-the-art designs [139, 124]. Several different types of porous emitters can be seen in Figure 2.5.

The development of porous emitters started relatively recently and has quickly become a major area of research. Krpoun produced and tested small capillary electrospray emitters which were filled with small ceramic beads in 2008 [140]. The beads were used to increase hydraulic impedance of ILs with the goal of obtaining ion mode emission. Around the same time Legge was the first to develop a porous electrospray emitter which operated in ion mode [141, 42]. These porous tungsten emitters showed that the current produced by a single porous tungsten emitter was greater than a comparable externally-wetted emitter. Following on from this work, Courtney developed an array containing 480 electrospray emitters made from porous nickel [142]. The emitters experienced a high rate of failure, due to electrochemical effects, which led to the formation of solid deposits clogging the pores. Coffman developed an electrospray thruster using a porous borosilicate glass filter [143]. This material has the advantage of being easily commercially available. Borosilicate glass is not a conductive material. In order to apply the required potential needed for operation, a separate conductive electrode in contact with the borosilicate is required. One of the main drawbacks of borosilicate glass emitters is that they lack pore uniformity. To mitigate the lack of uniformity other materials have been explored. Carbon xerogel is a material used to produce porous electrospray emitters which has greater pore uniformity and small pore sizes [144, 145, 146]. The pore uniformity increases the overall efficiency, while smaller pore size increases impedance, promoting ion emission.

Initially many of the porous materials being tested as electrospray substrates had shorter than expected lifespans. The reduced lifetime was caused by chemical reactions, produced between the propellant and electrode when high voltage was applied. This electrochemistry resulted in solid particle deposits, which clogged porous emitters. Work by Brinker demonstrated that by applying the voltage to an upstream distal electrode separated from the emitter by propellant would greatly reduce the electrochemical effects at the emitter tips [147, 148]. The insights from this work have led to distal electrodes being a common component of several thruster designs.

Aside from the substrate material, several additional factors need to be considered when working with porous emitters. Porous emitters have been developed in several different geometries including a square based pyramid [149], cone [150], and triangular prism (also known as porous wedge or edge emitter) [151]. As discussed in section 1.1.3.3, to increase thrust density, electrospray emitters are arranged into densely packed arrays. Courtney showed that porous wedge emitters produced numerous emission sites from a single emitter [152]. Using porous wedge emitters can produce comparable results to conical emitter arrays, while reducing complexity and manufacturing time
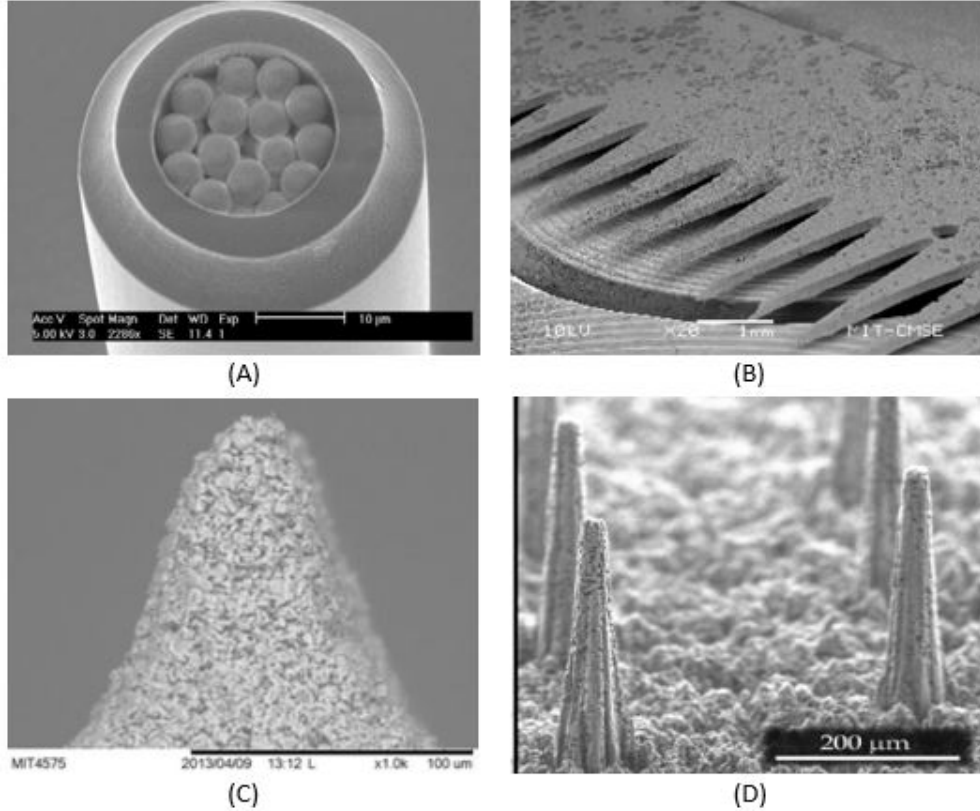
Figure 2.5: Examples of porous substrates developed for electrospray propulsion. (A) A capillary emitter filled with 5μm ceramic beads from [140]. (B) Linear array of porous tungsten emitters from [141]. (C) Single porous borosilicate glass emitter from [143]. (D) Array of porous carbon xerogel emitters from [146].

[151].

2.2.1 Flow through a Porous Medium

When using porous emitters, liquid propellant is most often transported from the reservoir to the emission site passively through capillary action. The volume of liquid per unit area (Q_s) through a porous medium can be described using Darcy's Law seen in Equation 2.13,

$$Q_s = -\frac{\kappa}{\mu}\nabla P \tag{2.13}$$

where κ is the porous materials permeability, μ is the viscosity of the propellant, and ∇P is the pressure gradient. The pressure drop between the emission site and the porous bulk for a conical emitter can be described by equation 2.14 [142] and for a wedge emitter in equation 2.15 [153]. Figure 2.6 can be used as a reference to these equations by visually showing the various parameters involved with flow in a porous medium.

$$\Delta P_{conical} = \frac{\mu}{2\pi\kappa}\frac{Q}{1-cos(\theta_T)}\left[\frac{tan(\theta_T)}{r_t} - \frac{cos(\theta_T)}{H}\right] \tag{2.14}$$

$$\Delta P_{wedge} = \frac{\mu Q_{site}}{\kappa \theta_{wedge}} \left(\frac{1}{\lambda} ln \left(\frac{R_2}{R_1} \right) - \frac{1}{2\pi R_2} \frac{K_0(\frac{2\pi R_2}{\lambda})}{K_1(\frac{2\pi R_2}{\lambda})} \right) \qquad (2.15)$$

In these equations, r_t is the radius at which the conical structure becomes spherical, Q_{site} is the flow rate at an emission site, θ_{wedge} is the specified angle of a porous wedge, based on the upstream radius (R_1) and the downstream radius (R_2), λ is the distance between each emission site along the apex of a porous wedge, and K_0 and K_1 represent the Bessel function of the second order.
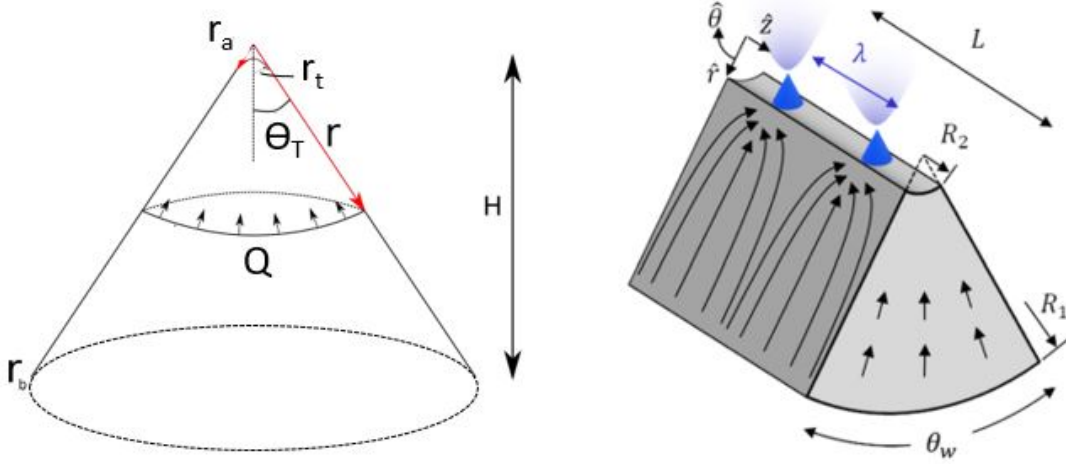
Figure 2.6: Flow through porous geometry used in electrospray propulsion. LHS - Flow through a porous cone emitter adapted from the work done by Courtney [142]. RHS - Flow through a porous wedge emitter adapted from the work done by Wright from [153].

Permeability is the degree to which a material allows a fluid to pass through it. The permeability of a porous substrate can be estimated using the Kozeny-Carman equation [154]. The equation considers a material's effective particle diameter (D_{eff}) and porosity (ϕ_p) as seen in Equation 2.16. Porosity is the measurement of the void space within a material from a scale of 0-1.

$$\kappa = \frac{D_{eff}^2}{180} \frac{\phi_p^3}{(1 - \phi_p)^2} \qquad (2.16)$$

The propellant reservoir has an impact on the emission produced by porous emitters. Typically, a porous emitter is accompanied by a porous reservoir with larger pores. The porosity of the reservoir has been shown to have a direct impact on the propellant flow rate. A study by Courtney showed the results of a P5 grade (D_{pore} 1 - 1.6μm) borosilicate glass emitter paired with P4 grade and P0 grade borosilicate glass reservoirs [152]. The results showed that the emitter attached with the P4 reservoir resulted in mostly ion emission, while the emitter attached to the P0 reservoir had mostly droplet emission. The effect of reservoir porosity on flow rate can be explained by the interfacial pressure jump (P_{int}) seen in Equation 2.17

$$P_{int} = -\frac{4\gamma}{D_{pore}} - Q\kappa \qquad (2.17)$$

2.3 Propellants

In the early days of electrospray propulsion, propellants were based on organic liquids. Propellants such as doped glycerol [110, 114, 134] and Octoil [109] were common during the development of colloid thrusters in the 1960s and 1970s. Due to the relatively low conductivity of these early propellants, the extraction voltages required to produce electrospray emission were extremely high. In the early 2000s, room temperature IL propellants were tested with Colloid thrusters [155]. ILs had been developed throughout the 20th Century and for the majority of that period were used as solvents [156]. These liquids, commonly referred to as molten salts, are entirely comprised of cations and anions. ILs were found to have three distinct advantages for use as an electrospray propellant. First, their high conductivity made electrospray propulsion more practical as emissions could be achieved at lower applied voltages. Second, ILs have negligible vapour pressure, which means they are extremely resistant to evaporation. Finally, the presence of cations and anions means that both positive and negative emissions can be produced. This bipolar operation can eliminate the need for a separate neutralizer component, common in other forms of electric propulsion (EP). A summary of IL properties which are commonly used for propulsion is shown in Table 2.1.

Table 2.1: The properties of ILs which are commonly used in electrospray propulsion.

Ionic Liquid Properties							
Ionic Liquid	M^+ (amu)	M^- (amu)	Conductivity "K" (S/m)	Density "ρ" (g/cm^3)	Surface Tension "γ" (dyn/cm)	Viscosity "μ" (Pa · s)	Reference
EMI-BF$_4$	111.2	86.8	1.36	1.24	45.2	0.038	[157, 158, 159]
EMI-Im	111.2	280.2	0.88	1.52	35.8	0.028	[157, 160]
EMI-Beti	111.2	380.2	0.34	1.6	28.7	0.061	[157, 160]
EMI-GaCl$_4$	111.2	211.5	2.2	1.53	48.6	0.013	[157, 161]
BMI-I	139.2	445	0.069	1.44	54.7	1.11	[157, 162, 163]
EMI-FAP	139.2	126.9	0.57	1.71	35.3	0.0745	[164, 165]

In 2003, 1-ethyl-3-methylimidazolium tetrafluoroborate (EMI-BF$_4$) was the first IL propellant to obtain a pure ion mode emission at room temperature [130]. Since this discovery, there has been a great deal of research into the use of many IL propellants for electrospray propulsion. ILs have become so common that an entire sub-category of electrsprays called ionic liquid ion sources (ILIS) has been created. EMI-BF$_4$ has been the most widely tested IL for electrospray propulsion. A handful of other ILs, such as EMI-GaCl$_3$, which have demonstrated ion mode emission at room temperature [166]. The IL EMI-Im is capable of operating in both a pure droplet mode and an almost purely ion regime at room temperature [167]. Temperature plays a role in IL performance, as many ILs are able to emit purely ions when subjected to elevated temperatures [168]. The chemical structure of the common IL EMI-BF$_4$ can be seen in Figure 2.7.

In addition to individual ions called monomers, ILs can also emit clusters of ions which have heavier atomic masses. For example, an ion which is attached to a neutral particle is called a dimer. Using the example of EMI-BF$_4$, a single ion of BF$_4^-$ would be considered a negative monomer, and that same ion attached to a neutral particle (EMI-BF$_4$)BF$_4^-$ would be negatively charged dimer. The various ILs all emit different compositions of monomers and larger clusters. The composition is based on the liquid's properties and several other factors such as emitter geometry. EMI-BF$_4$ will typically emit a beam comprised of half monomers and half dimers [136].

Larger clusters of ions have a tendency to break apart into neutral particles or ions with lower
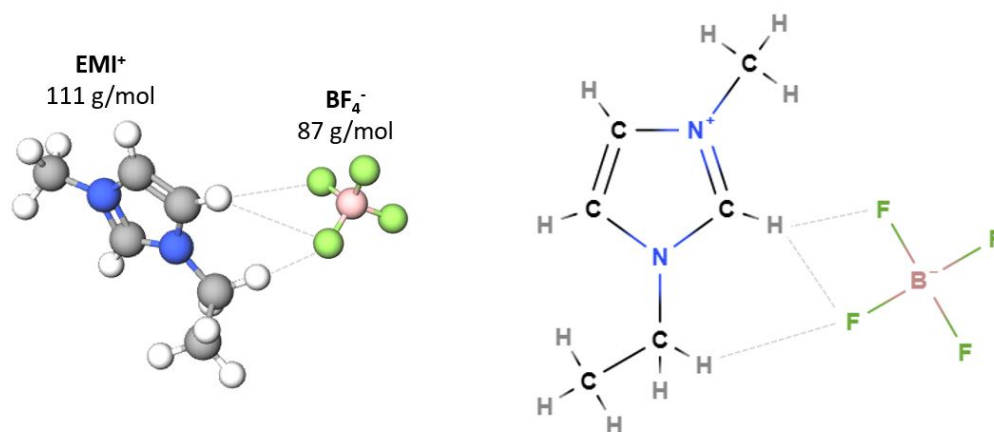
Figure 2.7: Chemical diagram of the ionic liquid EMI-BF$_4$. The dashed grey lines represent the weak bonds between the anion and cation.

mass. This process, called fragmentation, can have a detrimental effect on the performance of an electrospray thruster. The resulting neutral particles caused by fragmentation will reduce thrust. A visualization of fragmentation can be seen in Figure 2.8.
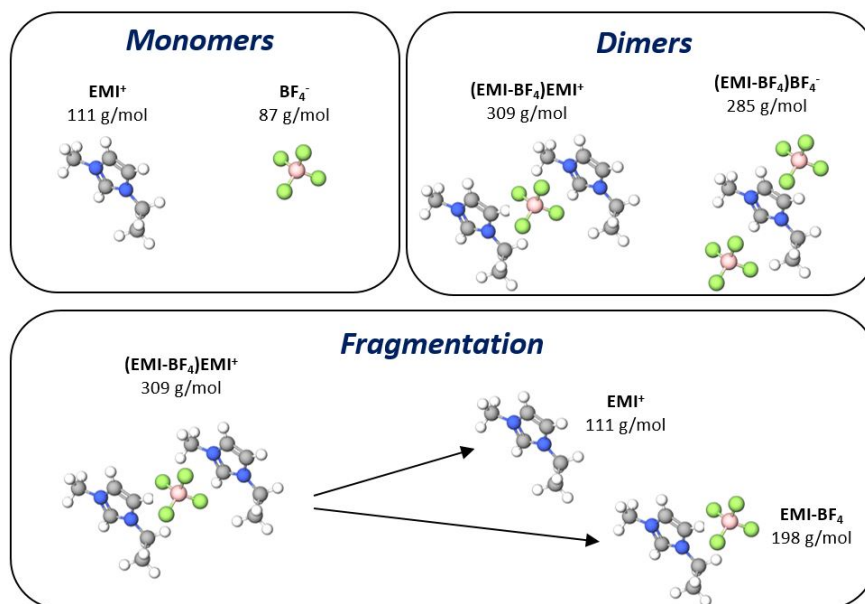
Figure 2.8: Example of an EMI-BF$_4$ monomer ion, dimer ion and fragmentation.

2.4 Emitter Fabrication Techniques

Fabricating an electrospray emitters is a complex challenge. There are several conventional and MEMS manufacturing techniques which have been used to fabricate emitters. Capillary and externally-wetted emitters have been fabricated using methods such as reactive ion etching (RIE), additive manufacturing techniques such as 3D printing and traditional computer numerically controlled (CNC) machining [140, 169]. To manufacture porous emitters a technique must be able to consistently produce emitters with the same height and shape, while preventing pores from collapsing or becoming clogged with debris. The most common and successful methods of fabricating porous emitters are described below.

2.4.1 Electrochemical Etching

In electrochemical etching, a metal sample is fully immersed into an electrolyte solution connected to an anode and cathode electrode. When a source current is applied to the electrolyte, the metal at the anode is dissolved, while metal particles are deposited at the cathode. To produce a desired shape, an etching mask is patterned onto the surface of the substrate and then cured. When etching occurs, it dissolves the material not covered by the mask. After the desired amount of material is removed, the mask is also removed to reveal the final structure.

Figure 2.9 (A) shows an example of electrochemically etched emitters. The linear array of porous tungsten emitters, developed by Legge, used electrochemical etching [42]. In that work, the tungsten substrate was filled with a photo-resist material, so the porous structure would not be impacted by etching. The outside of the substrate was then covered in a polyimide mask which was covered with an additional photo-resist layer. The substrate was then exposed to UV radiation transferring the geometry from the mask. The polyimide was cured and then the entire substrate was immersed into a sodium hydroxide electrolyte solution for etching. Notable challenges include removing all the photo-resist material from the porous structure, and difficulty producing uniform structures.

Courtney also used electrochemical etching to produce an array of porous nickel electrospray emitters [142]. A porous nickel substrate was patterned with FX515 resist mask and then etched in two steps: first in a Hydrochloric Acid Solution, then in a combined mixture of Hydrochloric Acid Solution and nickel chloride. The resulting emitters and electrochemical masks can be seen in Figure 2.9 (A).

2.4.2 Laser Ablation

Laser ablation is a process by which a high-power laser is used to essentially melt and evaporate solid material. Laser ablation is used in many micro-manufacturing applications [171]. Since the energy of the laser is concentrated to a small area, usually microns in size, it can remove layers of material without impacting the porous structure below.

Coffman used laser ablation to produce electrospray emitters from porous borosilicate glass [143]. A Lambda Physik LPX-200 laser was used to create an array of 480 porous emitters approximately 200 microns in height. The results of laser ablation on this substrate can be seen in Figure 2.9 (B). This work with laser ablation was integrated into the fabrication of MIT's iEPS thruster which contains 480 porous emitters within a 1 cm^2 area [128]. Porous emitters made of carbon xerogel have also been created using laser ablation [146].

An integrated hybrid thruster, developed at RAPPEL by Little, also used laser ablation to fabricate an electrospray emitter [172]. Here, a P5 porous borosilicate glass filter was fabricated
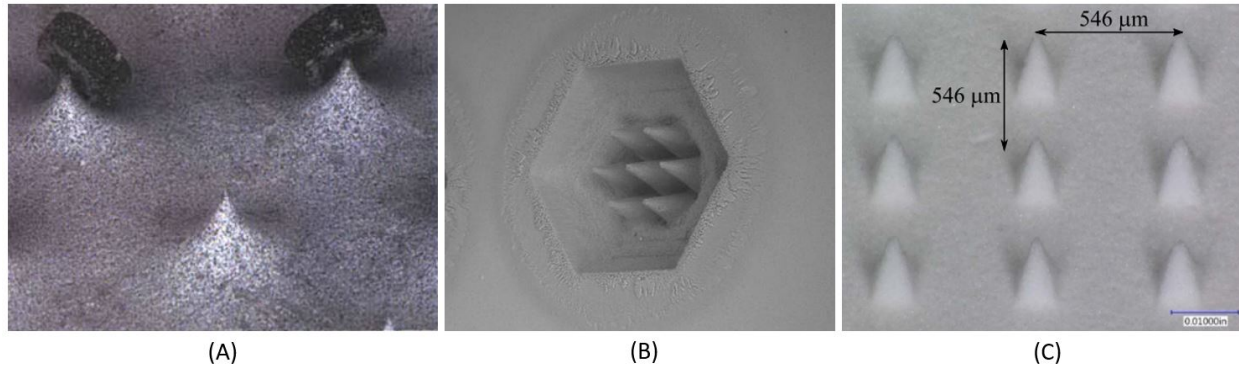
Figure 2.9: Porous electrospray emitters fabricated using three different processes. (A) Conical porous nickel emitters fabricated using electrochemical etching. Two leftover masks used in the process can be seen from [142]. (B) An array of laser ablated conical borosilicate glass emitters fabricated using a Lambda Physik LPX-200 laser from [143]. (C) Array of porous pyramid emitters produced using a a Tormach PCNC 1100 CNC machine from [170].

using an Oxford Series A picosecond laser. With the laser set to low power, a series of 20 passes of the laser was used to remove material producing a 3-dimensional porous wedge emitter. In this work laser ablation was the method chosen to fabricate porous emitters for the multimodal thruster detailed in Chapter 4.

2.4.3 Micro CNC Machining

While excellent for prototyping, both electrochemical etching and laser ablation are time consuming and expensive, making them difficult methods for producing emitters on a large scale. Several recent thruster prototypes have used porous emitters fabricated using conventional micro-CNC machining.

Research by Courtney from 2016 used a table-top Step-Four basic 540 CNC mill to fabricate an array of porous wedge emitters [151]. A series of five steps used Titanium aluminum nitride mill bits to fabricate the wedge emitters from P5 borosilicate glass frits. The prisms were 300 microns in height, and 7mm in length with an apex curvature of approximately 10-30 microns.

In 2020, the United States Air Force Research laboratory developed an electrospray thruster using entirely conventional CNC machining [170]. In this work, a Tormach PCNC 1000 CNC machine was used to fabricate 576 pyramid emitters over a 1.7 cm^2 area from a P5 borosilicate glass frit. The mill used aluminum titanium nitride coated carbide tools and used a Nakanishi HES510 high-speed electric spindle to achieve speeds of 50,000 RPM. The emitters were approximately 300 microns in height with an apex radius of curvature around 10-20 microns. The emitters produced in this work can be see in Figure 2.9 (C).

2.5 Multimodal Electrospray Systems

Multimodal propulsion, which combines more than one mode of propulsion using a common propellant, was previously introduced in Section 1.4. A variety of multimodal concepts involving electrospray thrusters have been investigated. A large amount of research has focused on combining an electrospray thruster and a monopropellant chemical rocket into a unified system. There have

also been some investigations into designing and combining cold-gas propulsion with electrospray thrusters, and several concepts which are capable of operating in different modes of operation.

Multimodal monopropellant-electrospray (ME) is a method of combining the high thrust of a monopropellant catalytic decomposition thruster with the high specific impulse of an ion mode electrospray. Research into propellants capable of operating in both chemical and electrospray modes has been an important aspect to developing ME systems. Specifically, there have been investigations into developing green energetic ionic liquids, which can operate in both modes. Multiple studies have tested the performance of various energetic ionic liquids [173, 174]. Berg and Rovey investigated combining ionic liquids with hydroxylammonium nitrate (HAN) [175]. The ionic liquid component would allow for operation in an ion mode electrospray, while the HAN acts as an oxidizer which allows for the catalytic decomposition required for a chemical mode operation. Combinations of IL with HAN, such as [Emim][EtSO$_4$]-HAN, have been shown to have positive characteristics for operating in a multimodal system [176, 177]. A multimodal ME thruster designed at the University of Illinois, Urbana-Champaign, using the propellant FAM-110 (59% wt. HAN, 41% wt. [Emim][EtSO4], <1% H$_2$O), demonstrated stable operation in both chemical and electrospray modes [102, 178]. The commercially available propellants "ASCENT", developed by the United States Air Force research Laboratory, and the green electric monopropellant (GEM) by DSSP Inc, have also been characterized for use in a multimodal ME propulsion system [179, 180].

A multimodal system combining a cold-gas thruster and an electrospray thruster has also been investigated [181]. A common propellant tank of IL feed into both systems. Propellant is passively fed into the electrospray emitters when the electrospray electrodes are biased to high potential. Propellant from the reservoir can also be fed through a valve connecting to a chamber where the IL is electrically decomposed into a gas, which is subsequently accelerated through a converging diverging nozzle. The work indicated that combining a cold-gas with an electrospray would increase propulsion capability with a high thrust mode.

Combining the various modes of electrospray thrusters into a single propulsion unit has also been explored. Wright developed a dual-mode electrospray emitter [182]. The concept has an externally-wetted needle emitter protruding through a capillary emitter. At high flow rates, a droplet mode emission is produced with the capillary emitter, while at low flow rates a mixed or ion mode emission is emitted from the externally-wetted emitter. The emitter was shown to produce two stable emission areas at high and low flow rates. The addition of an acceleration grid to an electrospray thruster, used to modulate emission, has also been investigated [183, 184]. An acceleration grid is an additional electrode, which is placed above the extractor electrode. The addition of this electrode allows a thruster to be operated in both high thrust and high specific impulse modes.

2.6   Electrospray Propulsion Experimental Testing Methods

The low absolute thrust produced by electrospray thrusters has led to challenges using direct thrust measurement (DTM) testing methods. Measuring low thrust devices directly is typically performed using a spring-mass-damper system with highly sensitive displacement sensors [185, 186, 187]. These systems can be susceptible to outside influence, such as vibrations produced by vacuum chamber pumps and background noise. The sensitivity of these methods also leads to involved calibration processes [188]. Indirect thrust measurement (ITM), using the time-of-flight (ToF) method, is commonly used as an alternative to DTM of electrospray thrusters [127, 189, 151]. Developed by Cameron and Egger in 1948 [190], ToF mass spectrometers are able to measure the charge to mass ratio (q/m) of emitted particles in real time. ToF apparatus includes an electrostatic gate, which

interrupts the beam of charged particles, and a collector which measures the particle beam current. The collector is placed a known distance from the gate. When the gate is turned off, the beam is free to travel directly to the collector. When the gate is turned on, the beam is deflected so that it is unable to reach the collector. The time taken for the beam to travel from the gate to the collector can be used to calculate the velocity of the charged particles and subsequently their charge-to-mass ratio. The composition of various species of particles within a beam can be determined based on the varying flight times. A schematic showing the ToF components divided into four regions can be seen in Figure 2.10.
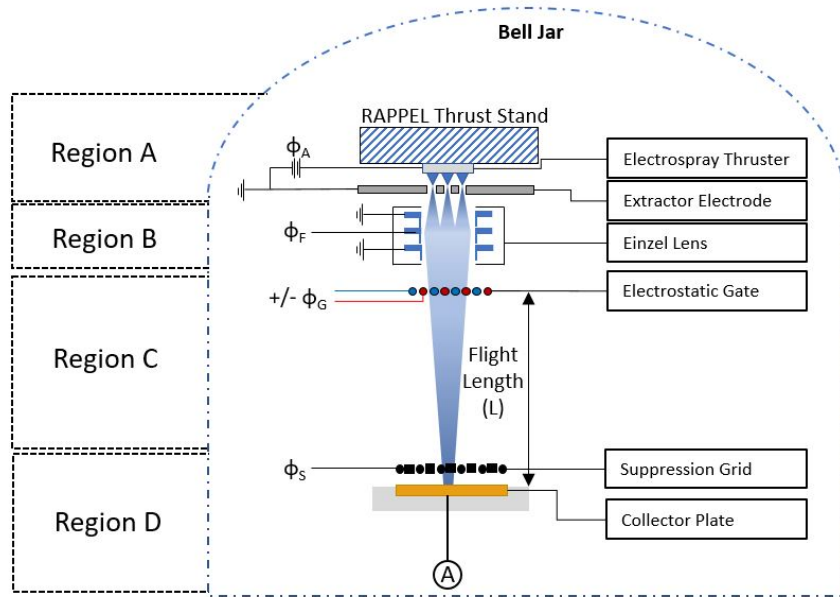
Figure 2.10: Time-of-Flight Diagnostic System. Region A: The electrospray thruster; Region B: Focusing of the charged particle electrospray beam; Region C: ToF gate and flight length; Region D: Collector and suppression grids.

2.6.1 Time-of-Flight Measurement

The ToF method measures the exit velocity (v_e) of charged particles by measuring the time (t) taken to traverse and known flight length distance (L) seen in Equation 2.18. Once the velocity of the beam has been determined, the q/m or the charge per unit mass can be found using equation 2.19.

$$v_e = \frac{L}{t} \tag{2.18}$$

$$\frac{q}{m} = \frac{v_e^2}{2\phi_B} \tag{2.19}$$

In order to complete this calculation, the beam potential (ϕ_B) must be known. In most applications, it is likely that only the voltage applied to the thruster emitters (ϕ_A) will be known. The ϕ_B and the ϕ_A are closely related, but not identical. This is due to electrospray loss mechanisms which reduce the overall energy of the particle beam.

Equations 2.18 and 2.19 can be rearranged to determine the theoretical flight time of a known ion or droplet with a known mass / charge. This can be seen in Equation 2.20.

$$t_{theo} = \sqrt{\frac{L^2}{2\phi_B} \frac{m}{q}} \tag{2.20}$$

If we assume the beam potential is known, then the mass flow rate, thrust and specific impulse can be indirectly calculated using Equations 2.21, 2.22, 2.23.

$$\dot{m}_i = I_B f_i \frac{m_i}{q_i} \tag{2.21}$$

Here I_B is the beam current measured at the collector, f_i is the current fraction produced by an individual species of ions or droplets. The total mass flow rate is the sum of the flow rates of each particle species emitted in the beam.

$$T = \Sigma(\dot{m}_0 v_{e0} + \dot{m}_1 v_{e1} + ...) \tag{2.22}$$

$$I_{sp} = \frac{T}{\dot{m}_T g_0} \tag{2.23}$$

Here $\dot{m}_T$ is the total mass flow rate. The velocity of a particular charged particle is based on its mass-to-charge ratio. If charge remains constant, heavier particles will take longer to travel a set distance. The use of a ToF system allows for the accurate measurement of the thrust and specific impulse of electrospray emitters.

Electrospray Thruster (Region A)

The electrospray thruster region is where the charged particle source is placed. In this research the source will be an electrospray thruster.

Particle Beam Focusing (Region B)

Electrospray beams are prone to spreading outward from their source, making accurate measurement of a beam over long flight distances difficult. Spherical and chromatic aberration are two factors which cause a reduced percentage of beam emission detection at the collector. In ToF, a longer flight length leads to superior current measurement resolution. To counteract the beam spreading phenomena, researchers have used large area emission detectors [191, 192, 193], or axially aligned electrostatic lens, such as an Einzel lens, as alternatives to focus charged particles towards a detector [194, 195].

An Einzel lens is a focusing device which contains a series of three electrodes where the first and third electrodes share a potential (often ground) and the second is biased to a required focusing potential (ϕ_F). The degree to which particles are focused is dependent on the dimensions and shape of the electrodes, the magnitude of ϕ_F, and the energy of the charged particles. Figure 2.11 shows how a Einzel lens will change charged particle beam's trajectory. An Einzel lens will have a focusing effect regardless of voltage polarity.

If charged particles get too close to the Einzel lens electrodes, the electric field formed between the electrodes can distort the particle beam instead of focusing it. For this reason, it is important to design the lens with a diameter twice as large as the expected beam diameter [194]. A larger

diameter means the magnitude of potential required to focus the beam also increases. Placing the Einzel lens close to the electrospray source helps to reduce the need for high potentials.

A typical Einzel lens contains only a single focusing stage of three electrodes. The single stage lens set to a particular focusing potential will focus beam particles of a particular energy. This may deflect beam particles of differing energies away from the detector. In order to collect a larger percentage of beam current at the collector, researchers have developed several designs for an ion guide [196, 197, 198, 199]. Ion guides use a series of Einzel lens electrodes from the source of charged particles all the way to the collector.
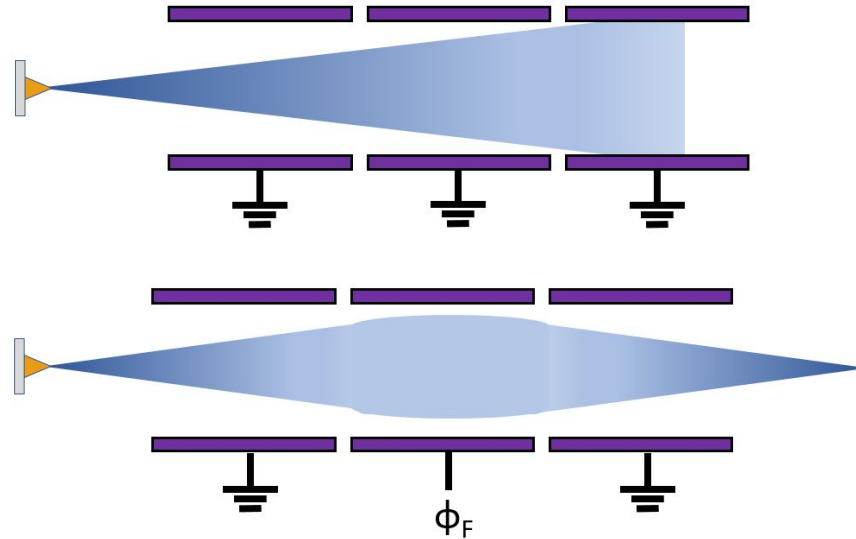
Figure 2.11: Beam of charged particles being focused by an Einzel Lens.

ToF Electrostatic Gate (Region C)

Within a ToF system, the electrostatic gate is used to prevent the beam of charged particles from being measured by the collector. When the gate is activated, a particle beam is prevented from reaching the collector, and when deactivated, the beam can travel uninhibited to the collector. There are three general types of electrostatic gates: a stopping gate, deflection gate, and interleaved comb gate. A stopping gate completely blocks the passage of charged particles, while deflection and interleaved comb gates deflect the beam's trajectory away from the collector.
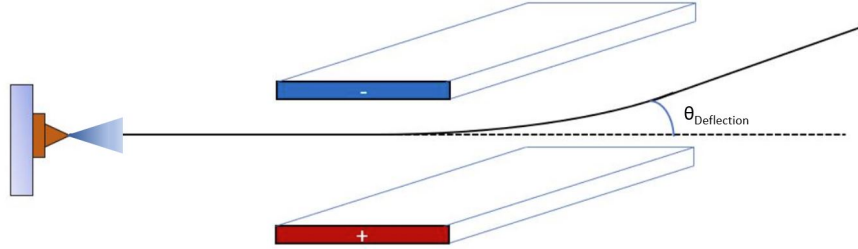
Figure 2.12: A deflection gate comprised of two parallel plates.

Stopping gates are comprised of several closely spaced metallic grids. When the central grid is biased to a higher voltage than the thrusters ϕ_A, the charged particles are prevented from moving through the gate. Stopping gates may cause erosion to the electrospray extractor electrode when particles are reflected back toward the source optics by the gate.

A deflection gate uses two parallel plates are biased to opposite polarities, creating an electric field which deflects charged particles away from the collector. A schematic of a deflection gate can be seen in Figure 2.12. This type of gate is simple to implement and has reliable performance. However, this gate is energetically costly to produce the high voltage required to obtain meaningful deflection. The angle required to deflect charged particles away from the collector is described in equation 2.24

$$\theta_{required} = tan^{-1}\left(\frac{d_C}{2L}\right) \tag{2.24}$$

where d_C is the diameter of the collector surface. The angle of deflection actually produced by a deflection gate can be described using equation 2.25

$$\theta_{deflection} = tan^{-1}\left(\frac{w}{4d_G}\frac{\phi_G}{\phi_A}\right) \tag{2.25}$$

where w is the thickness of the deflection plates, d_G is the diameter of aperture, and ϕ_G is the potential difference between the electrode plates.

A common type of Interleaved comb gate is the Bradbury-Nielsen Gates (BNGs). In 1936 Bradbury and Nielsen developed the BNG to measure the ion mobility of gases [200]. Weinkauf first used a BNG for ToF experiments in 1989 [201] where the gate only allowed ions of a certain mass-to-charge ratio to pass through. BNGs have since been commonly used for ToF measurement of electrospray thrusters [42, 151, 189, 202, 203]. A typical BNG consists of electrically isolated sets of interleaved wires which are held together by a frame. The wires are equally spaced on the same plane and alternate in potential. When both sets of wires have equal potential, charged particles can pass through freely. When the two sets of wires are biased to the same potential magnitude and

opposite polarity, the resulting electric fields will deflect any charged particles travelling through the gate. A schematic showing the operation of a BNG can be seen in Figure 2.13.
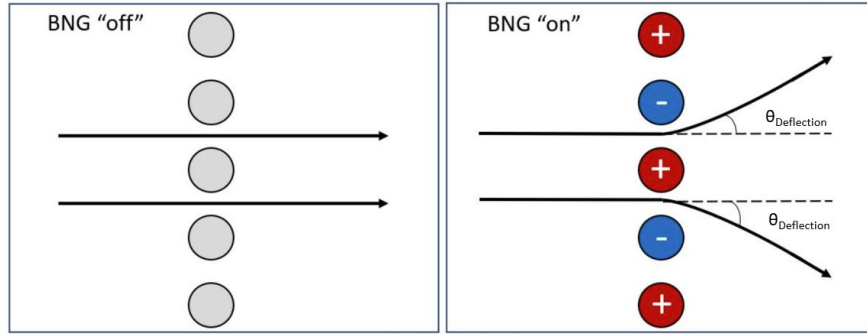
Figure 2.13: The particle beam deflection caused by a BNG.

Wire spacing is an important factor in the BNG design. Minimal spacing between the wires leads to improved mass resolution. Many early BNGs were laborious to produce, often taking several days. Wiring is achieved by placing controlled grooves in a synthetic polymer, such as polyether ether ketone (PEEK), and then feeding wires through the grooves. The maximum deflection angle produced by a BNG gate is described by equation 2.26 [204]

$$\theta_{max} = tan^{-1}\left(k\frac{\phi_G}{\phi_A}\right) \tag{2.26}$$

k being the deflection constant described by equation 2.27.

$$k = \frac{\pi}{2ln[cot(\pi R/2d)]} \tag{2.27}$$

Here R is the radius of the wire and d is the distance between each wire.

The finely spaced wires may not by ideal for thrusters operating in droplet mode, since liquid could accumulate on the wires, potentially causing a short circuit [194]. If large liquid droplets are expected, a parallel plate deflection gate could be used.

Collector and Suppression Grids (Section D)

The collector is placed a known flight length from the electrostatic gate and is used to measure the current of charged particles which impact its surface. The fastest charged particles to reach the collector will be indicated as a step increase in current, followed by the larger slower particles until the full beam current is being collected. The composition of the species within a beam can be identified by the time needed to register a current change at the collector. Broadly speaking there are two types of ToF collectors, full-beam and partial-beam. Full-beam measurement collects the entire emitted beam from the electrospray source. Since electrospray beams spread out spherically as they travel outward, the size of the collector needs to increase with the distance the collector is placed from the source. Partial-beam collectors receive only a portion of the electrospray emission. This makes them easier to implement, but with less utility. Using a partial-beam collector allows the collector to be placed further away from the source, which increases the resolution of the results due to the increased flight time.

A device known as an electron multiplier can be used as a collector when sensitive low current density measurement is required. These devices are partial beam collectors sampling a small portion

of the electrospray emission with low noise and high resolution. An electron multiplier amplifies the current collected by utilizing the mechanism of secondary electron emission. The interior of an electron multiplier is covered with a material that has a high secondary electron emission coefficient. As charged particles collide with the walls of the electron multiplier, secondary electrons are produced, which leads to an electron cascade amplifying current [205]. With this method, the output of current can be amplified by a factor of one million. The two common types of electron multipliers are Single Channel Electron multipliers (CEMs) and Microchannel plates (MCPs).

Single or multiple suppression grids can be placed just before the collector to offset the impact of secondary electron emission. When measuring the current of an electrospray beam at the collector, higher than theoretically expected values can occur. This current offset is usually caused by secondary electron emission. As high energy particles from the electrospray beam collide with the collector, the metallic surface can potentially release electrons. As these electrons are released, the collector will draw additional electrons from its connection source. The process will have the effect of creating a positive current offset.

When a suppression grid is set to a negative voltage the secondary electrons released from the collector are suppressed back to the collector surface. In other research using suppression grids, a voltage between -30 to -50 volts has been applied [151, 42, 189]. Often a second suppression grid connected to ground is placed directly ahead of the first suppression grid in order to reduce any change acceleration caused by the potential difference between the extractor and suppression grid.

2.7 Concluding Remarks

This chapter reviewed the principles of electrospraying conductive liquids and their application to spacecraft propulsion. The different types of electrospray emitters, modes of emission, and propellants all play an important role in thruster design. Common methods of how electrospray emitters are manufactured were reviewed. Finally, an overview of a time-of-flight measurement system, commonly used to measure the thrust produced by electrospray thrusters, was elaborated upon. This research focus is the development of a multimodal electrospray thruster. The design combines a droplet and ion mode electrospray emitter into a single unified system. Both modes of emission use a porous wedge design, which allows form multiple points of emission and lower manufacturing time compared to conical emitter arrays. The ionic liquid EMI-BF$_4$ was selected as the common propellant used by both emitters. Laser Ablation was used to manufacture both porous emitters. In order to characterize the electrospray thruster a ToF measurement system has been designed and implemented (Chapter 5). Chapter 3 will detail a numerical simulation produced to enhance knowledge of electrospray for propulsion. The simulation was used to aid in the design of the multimodal thruster detailed in Chapter 4.

3 Numerical Modelling of Electrospray Thruster

3.1 Introduction

Numerical methods provide a technique of predicting the behaviour of electrospray thrusters. While there have been numerous experimental demonstrations, numerical methods modelling electrospray propulsion are still growing in maturity. In this work, both droplet and ion electrospray emissions are used to create a multimodal system. It is a challenge to model the behaviour of droplets and ions using the same simulation methodology. The mechanisms of droplet or ion formation occur at different scale lengths. The behaviour of liquid droplets is commonly solved using computational fluid dynamics (CFD). CFD modelling takes a more macroscopic view of a system, breaking down a continuous fluid flow into a set of discretized units. Each of these units has a set of equations solving for their behaviour. Modelling ions takes a microscopic approach by determining the position and other parameters such as velocity, of each individual particle. Solving for the behaviour of ion emission can be achieved using methods such as molecular dynamics (MD).
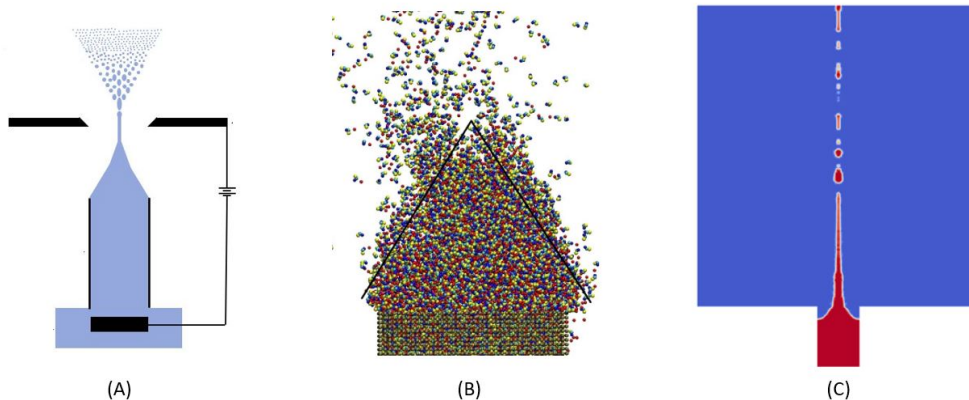
Figure 3.1: (A) Schematic of droplet electrospray emission. (B) Sample droplet electrospray simulation using molecular dynamics from [206]. (C) Sample droplet electrospray simulation using computational fluid dynamics.

Droplet mode electrosprays have been modelled for the purpose of propulsion [207, 208, 209, 210] and for use in medical applications [211, 212]. The majority of droplet mode electrosprays are modelled using electro-hydrodynamics (EHD) based on the leaky dielectric model [213]. EHDs explain how liquids deform when in the presence of an electric field. The leaky dielectric model attempts to explain how droplets form when an electric field is applied to a liquid [214]. The

motion of a conductive liquid is often solved using the Navier-Stokes equations. Additional source terms are used for calculating the electric field, electric charge migration and droplet break up. In the case of ion mode electrosprays, the mechanisms behind their operation are not completely understood, posing a challenge to producing accurate simulations. A simulation developed by Petro used a combination of three simulation methodologies to give a representation of pure ion emission [215]. First, an EHD model was used to calculate the emission current and current density of an electrospray meniscus [216]. Second, the trajectory of emitted ions was individually tracked [217]. Finally, the fragmentation of ion particles was determined using a MD simulation based on the Large-scale Atomic Molecular Massively Parallel Simulator (LAMMPS) program [218].

In this Chapter a simulation of a droplet electrospray emission using CFD numerical methods is presented. The simulation models the onset of a cone-jet electrospray and development of liquid droplets. An electrospray emitter with a porous substrate was incorporated to investigate its impact on droplet formation. Performing these simulations allowed for greater understanding of the mechanisms behind electrospray propulsion and enhanced current electrospray simulation capabilities. This work will be expanded upon in future droplet and ion electrospray simulations.

3.1.1 CFD Approach

As expected, there are currently no out-of-the-box CFD simulation packages which have the built-in capability to solve the EHD equations used to simulate electrospray emission. Several researchers have built custom EHD solvers into publicly/commercially available CFD programs. Lastow created an electrospray simulation using a liquid heptane propellant by incorporating an EHD model into the CFD solver ANSYS-CFX 4.4 [207]. The simulation was capable of producing a cone-jet structure by calculating the electric body forces caused by an electric field. The model did not contain droplet break up or calculate current. Forbes developed a simulation which could describe both cone-jet formation and droplet break up using the volume-of-fluid (VOF) method within the CFD program ANSYS Fluent [208]. The VOF method is used to describe the interaction between a fluid and its surroundings [219]. For example, the VOF method may be used to describe how liquid droplets might interact with air under atmospheric conditions. Lopez-Herrera and Herrada used the VOF method to simulate a cone-jet emission using the open-source program Gerris/Basilisk[220, 209]. EHD solvers which model cone-jet formation and droplet break up, using the open source program OpenFOAM, have been developed by Roghair [221] and Huh[210, 222].

In this work, the ANSYS Fluent multi-phase flow solver was used to simulate an electrospray cone-jet and droplet formation [223]. Fluent has a built-in framework to model complex flows such as free surface flows and fluid interface evolution. User defined functions (UDFs) and user defined scalars (UDSs) within Fluent allow for custom source terms and equations to be built into the program. UDSs were implemented to solve for the electric potential and charge transport. UDFs of the charge stress and electric (Maxwell) stress were also implemented in order to solve for the EHD equations. The EHD model and UDS/UDF code developed by Forbes [224, 208] was used as the basis for this work.

The electrospray propulsion engineering toolkit (ESPET) was also used to estimate various performance parameters of the simulated geometry [225]. ESPET was designed for quick iteration of electrospray thruster designs using an engineering model approach. The program allows the user to apply various conditions to common electrospray emitter types, emitter substrates, reservoirs and propellants. The results from ESPET were used to accompany the droplet mode simulation.

3.2 Simulation Methodology

This section outlines the fluid flow, EHD model and porous media equations implemented in the simulation. The VOF method using Fluent's multiphase flow solver was used as the basis. The simulations were comprised of two phases, a conductive liquid propellant and air under atmospheric conditions. The pressure-implicit with splitting of operators (PISO) algorithm was used for the calculations. Gravity was not considered in the model, since its impact would be much smaller than the surface tension and electrostatic body forces. The liquid propellants were always assumed to be at a room temperature ($300\ K$) throughout. The simulations were performed under atmospheric pressure conditions. Simulating the pressure vacuum of space within ANSYS Fluent is challenging, since the fluid continuum and Navier-Stokes equation assumptions are invalid at low pressures. Conducting the simulation under atmospheric conditions was still useful for understanding the characteristics of electrospray emission, but were not capable of exactly replicating high vacuum conditions.

3.2.1 Fluid Equations

When using incompressible fluids the mass conservation equation in ANSYS Fluent is simplified to Equation 3.1 where $\overrightarrow{u}$ is the velocity vector of the liquid.

$$\triangledown \cdot \overrightarrow{u} = 0 \tag{3.1}$$

Fluid flow of the two-phase liquid/gas simulation is governed by the Navier-Stokes equation described in Equation 3.2

$$\frac{\delta}{\delta t}(\rho \overrightarrow{u}) + \triangledown(\rho \overrightarrow{u}\, \overrightarrow{u}) = -\triangledown p + \rho[\nu(\triangledown \overrightarrow{u} + \triangledown \overrightarrow{u}^T)] + \rho \overrightarrow{g} + \overrightarrow{F} \tag{3.2}$$

where $\overrightarrow{u}$ is the velocity, ρ is density of liquid, v is the kinematic viscosity of the liquid, p is pressure, and $\overrightarrow{F}$ is the net body force.

3.2.2 Electrical Field and Charge

The EHD model incorporates electric field forces, Maxwell stresses, and surface tension into the liquid domains body force term from equation 3.2. The Poisson equation seen in equation 3.3 was used to create the electric potential resulting from charges within the domain.

$$\triangledown^2 \phi = -\frac{q}{\varepsilon_0 \varepsilon_r} \tag{3.3}$$

Where ϕ is the electric potential, q is the net charge density, ε_0 is the permittivity of free space, and ε_r is the relative permittivity of material. A fluids behaviour under the influence of an electric field is described by the charge advection $q\overrightarrow{u}$ and charge migration $\mu_e q\overrightarrow{E}$ where $\overrightarrow{E}$ is the electric field vector, and μ_e is the electrical mobility. This leads to the charge transport equation (equation 3.4).

$$\frac{\delta q}{\delta t} + \triangledown \cdot (\mu_e q\overrightarrow{E} + q\overrightarrow{u}) = 0 \tag{3.4}$$

The Coulombic force ($q\overrightarrow{E}$) and the dielectric force ($-\frac{1}{2}E^2\triangledown \varepsilon$) are incorporated into the hydrodynamic momentum equation as source terms. The momentum balance equation implemented for

CFD simulation incorporates the EHD body forces into Equation 3.2. This can be seen in Equation 3.5.

$$\rho(\frac{\delta \overrightarrow{u}}{\delta t} + \overrightarrow{u} \cdot \triangledown \overrightarrow{u}) = -\triangledown p + \triangledown^2 \overrightarrow{u} + q\overrightarrow{E} - \frac{1}{2}E^2\triangledown\varepsilon \qquad (3.5)$$

3.2.3 Porous Medium

ANSYS Fluent also has a built-in porous media model which was used to simulate porous electrospray emitters. A region defined as porous in the simulation will have an additional momentum resistance. The momentum sink includes two components, a viscous loss term (Darcy's Law) and an inertial loss term seen in equation 3.6,

$$\triangledown p = -(\frac{\mu}{\kappa}\overrightarrow{u} + C_2\frac{1}{2}\rho\overrightarrow{u}\,|u|) \qquad (3.6)$$

where κ is the permeability of porous material and C_2 is the inertial resistance factor. For laminar flows the C_2 term can be considered zero, reducing the equation to just Darcy's law.

The porosity (λ) assigned to the porous section of a simulation will also impact the scalar transport equations and the continuity equation. The impact porosity has on the various scalar quantities (represented in this work by Φ) within the simulation is described by Equation 3.7.

$$\frac{\delta}{\delta t}(\lambda\rho\Phi) \qquad (3.7)$$

3.2.4 Simulation Set-up

There were two simulations conducted using the EHD model. The first was a validation test case using a capillary emitter with a liquid heptane propellant. The simulation domain dimensions and propellant properties were based on similar simulations by Lastow [207], and Ganan-Calvo [226]. The simulation domain contains a rectangular capillary at the base and an extractor electrode at the top as seen on the LHS of Figure 3.2. The domain mesh was comprised of 12,510 elements focused along the domain symmetry axis. The time-steps used for each iteration ranged from $1 \cdot 10^{-9}$ s to $5 \cdot 10^{-8}$ s. The capillary component of the domain was set to 4,000 volts, while the extractor electrode at the top of the simulation domain was grounded to 0 volts. An inlet flow rate of heptane at the base of the capillary was set to 0.033 $\mu l/s$. Under these input conditions the expected result was a continuous flow cone-jet with noticeable droplet breakup before the flow reached the extractor.

After completing the validation test case, a porous emitter was simulated using the EHD model. This second simulation domain had a capillary channel with a conical porous emitter at the top, as seen on the RHS of Figure 3.2. The dimensions of the simulated emitter were based on experimental work by Courtney using porous wedge emitters [151]. EMI-BF$_4$ was selected as the propellant in this simulation due to its prevalence in electrospray experiments. The mesh was comprised of approximately 23,000 elements equally distributed across the domain. The time-steps used ranged from $1 \cdot 10^{-9}$ s to $2.5 \cdot 10^{-8}$ s. The porous emitter domain was set to the properties of a porous P0 grade borosilicate glass. The porous emitter and capillary zone were biased to 1,500 V and the extractor electrode was grounded to 0V. The properties of the porous domain were set to a porosity of 0.35 and a permeability of $4.6 \cdot 10^{-10}$ m^2 based on the standard pore sizes from ISO 4793. The propellant flow rate was set to 1 $\mu l/s$ to ensure that droplet mode was achieved. In addition to the CFD simulation, the second electrospray simulation was supplemented by ESPET estimates of thrust, specific impulse, extractor velocity, and droplet/ion emission current. ESPET's domain modeler was used to produce these results.
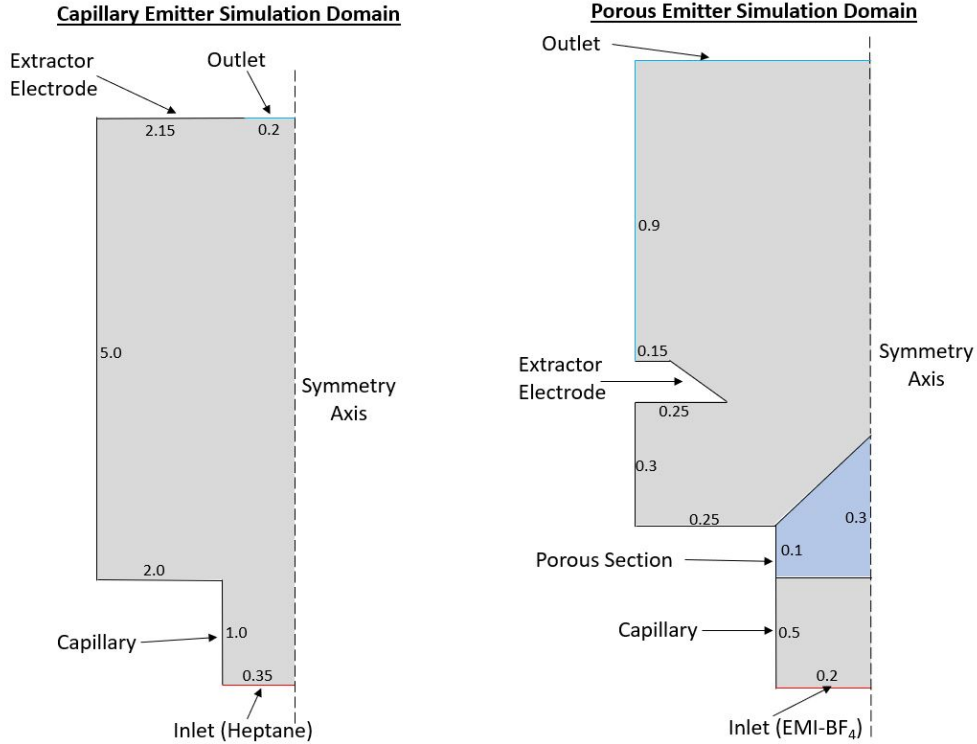
Figure 3.2: Emitter geometry used in the ANSYS Fluent CFD simulation. The simulations are asymmetric with all units in millimeters.

The simulated propellants, liquid heptane and EMI-BF$_4$, have their properties detailed in Table 3.1.

Liquid heptane				EMI-BF4		
Density (ρ)	684 (Kg/m^3)	[207]		Density (ρ)	1240 (Kg/m^3)	[227]
Conductivity (K)	$3 \cdot 10^{-12}$ (S/m)			Conductivity (K)	1.36 (S/m)	[227]
Surface Tension (γ)	19.8 (dyn/cm)	[207]		Surface Tension (γ)	45.2 (dyn/cm)	[227]
Dielectric Constant (ϵ)	1.90	[207]		Dielectric Constant (ϵ)	12.9	

Table 3.1: Propellant properties of liquid heptane and EMI-BF$_4$

3.3 Simulated Emitter Results

The capillary-heptane simulation resulted in the formation of a cone-jet emission as seen in figure 3.3. Following the initial onset of emission by 0.3 ms, a clearly identifiable Taylor cone structure and droplet formation can be identified. In the initial phase of the simulation (0 ms to 0.1 ms), clumps of liquid were emitted outward toward the extractor electrode in larger quantities than expected. Throughout the simulation the cone-jet structure retracted into the capillary, which was identified in previous simulations using the model [208]. The quantitative results of the simulation were validated by comparing the simulation by Lastow [207] and the experimental work by Ganan-

49

Calvo [226]. The model displayed visually similar results with slight discrepancies from variation geometry and boundary conditions such as in inlet flow rate and applied emitter voltage.
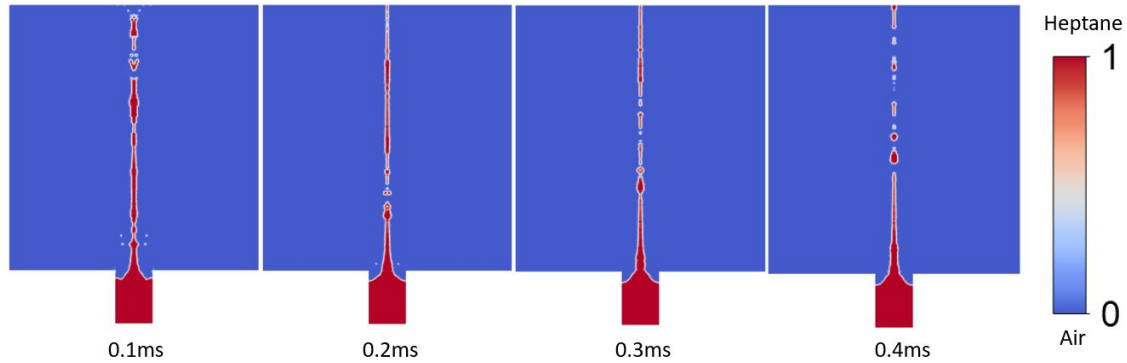
Figure 3.3: The volume fraction of liquid heptane from 0.1 ms to 0.4 ms with an applied voltage of 4000 V, and inlet flow rate of 0.033 μl/s

The droplets formed at 0.4 ms were measured as approximately 15 μm to 150 μm in diameter. Similar experimental work by Ganan-Calvo[155] found a mean droplet size of 36 μm. The droplets in the simulation are on average larger than the compared experimental results. The measurable droplets beyond the extractor electrode (not simulated here) could potentially be more aligned to the experimentally measured droplets. It is also possible that once a more steady-state emission is reached the droplet sizes would decrease. The simulation demonstrates the expected cone-jet and droplet behaviour.

Figure 3.4 shows three contour plots of the capillary emitter simulation at 0.4 ms. The electric potential and electric field contours clearly show how the initial boundary conditions impact on Taylor cone formation and droplet emission. The fluid velocity contour shows that a maximum velocity of 15 m/s is reached at the extractor electrode.
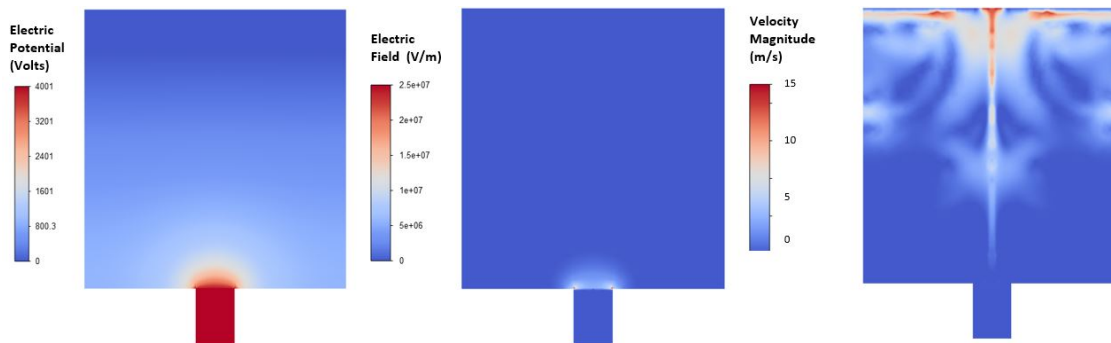
Figure 3.4: Contours of the electric potential, electric field strength and the velocity profile of the capillary heptane simulation at 0.4 ms.

Two plots showing the varying electric field and velocity magnitudes at 0.4 ms are shown in figure 3.5. These plots correspond directly to the information shown in figure 3.4. The data is plotted along the axis of symmetry through the entire simulation domain. The portion of the simulation within the capillary is highlighted in red and the remainder in black. The red data points clearly show the sharp potential gradient at the end of the capillary. The velocity magnitude shows

an oscillatory type behaviour. The variation seems to be the result of the liquid droplets being accelerated to a different velocity compared to the air surrounding them.
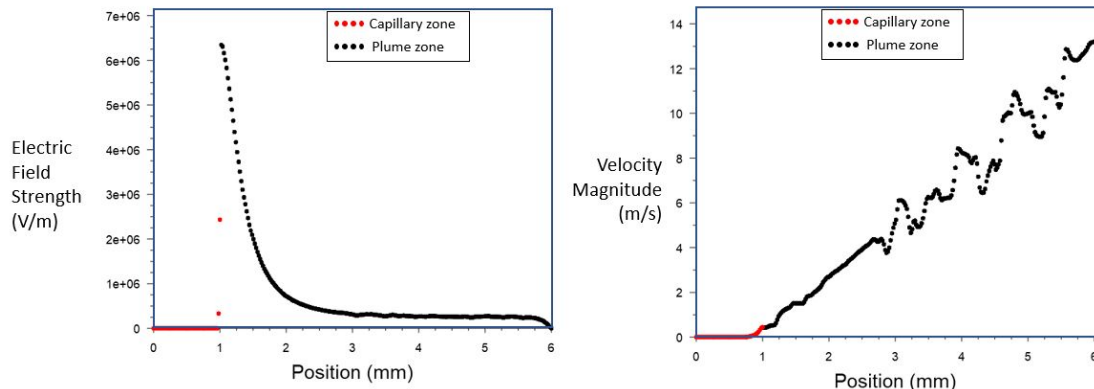
Figure 3.5: Plots of the electric field strength and fluid velocity through the simulation domains axis of symmetry. Values are shown for the heptane capillary simulation at 0.4 ms.

After the capillary heptane simulation demonstrated the correct EHD behaviour and general agreement with previous work, the model was then applied to a porous emitter using the properties of EMI-BF$_4$ propellant. The results seen in figure 3.6 show a cone-jet structure extending from the apex of the porous emitter to beyond the extractor electrode.
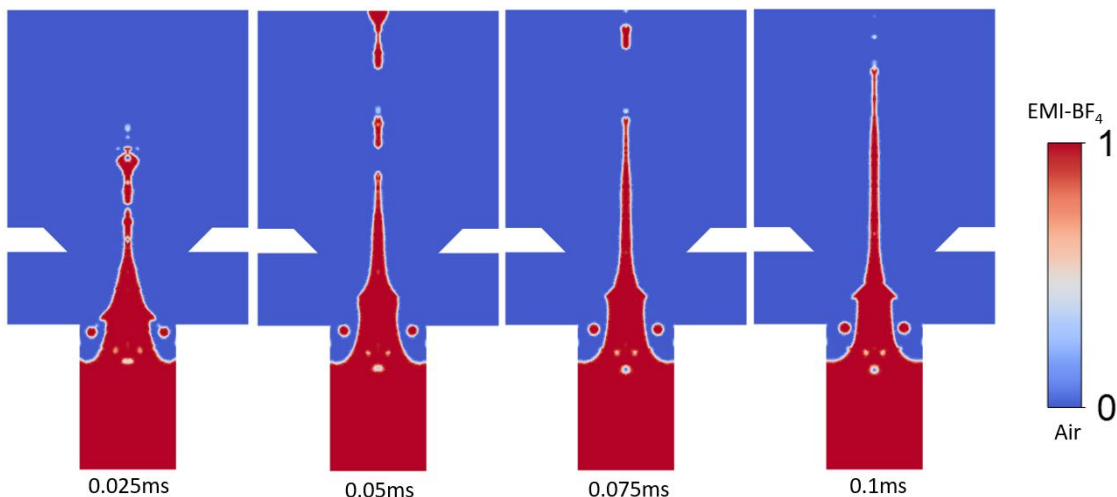
Figure 3.6: The volume fraction of EMI-BF$_4$ from 0.025 ms to 0.1 ms with an applied voltage of 1500 V, and inlet flow rate of 1 μl/min.

The porous emitter geometry protrudes closer to the extractor electrode when compared to a capillary, creating a stronger electric field at the apex of the emitter tip. This can be seen in figure 3.7, where the electric field is magnified at a point above the emitter apex. In this simulation, the expected behavior would be cone-jet and droplet formation occurring prior to reaching the extractor followed a spreading spray. Instead, the cone-jet formation reaches a large distance beyond the extractor electrode with few droplets being formed.
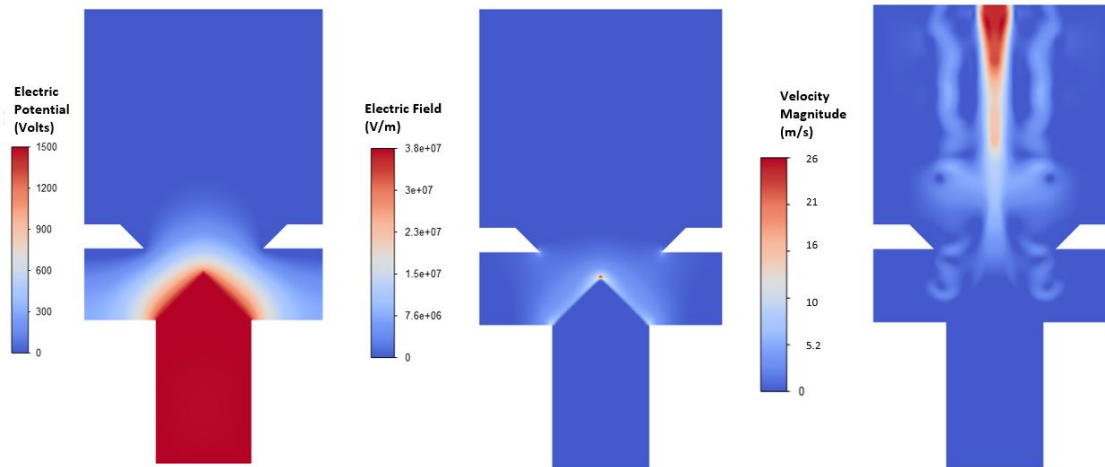
Figure 3.7: Contours of the electric potential, electric field strength and the velocity profile of the porous EMI-BF$_4$ simulation at 0.05 ms.

The plots in figure 3.8 show the electric field and velocity magnitude through the capillary (red), porous emitter (green), and remainder (black). It is clear that the momentum sink of the porous emitter slows the flow rate of propellant.
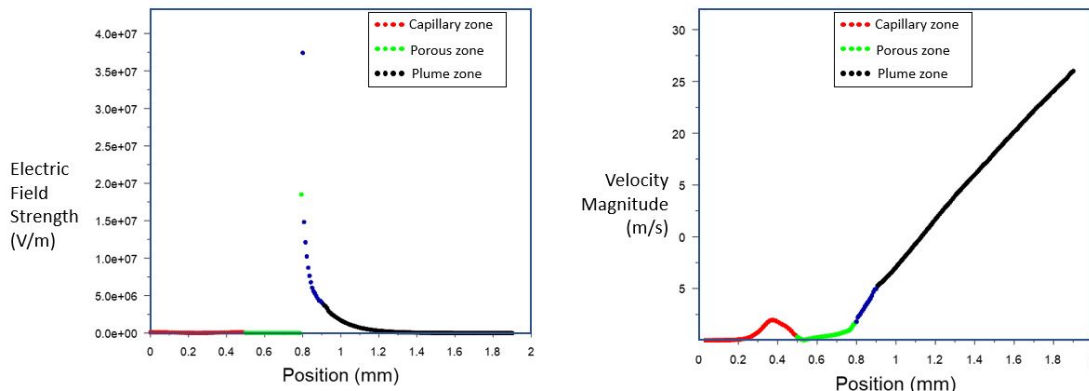
Figure 3.8: Plots of the electric field strength and fluid velocity through the simulation domains axis of symmetry. Values are shown for the EMI-BF4 porous emitter simulation at 0.05 ms.

Some circular anomalies appeared in the simulation within the porous emitter zone. These were likely caused by fluid re-circulation. Figure 3.9 shows two areas within the simulation, which clearly show flow re-circulation behaviour. This mechanism is seen as an unsteady behaviour leading to instabilities in the electrospray emission. This can potentially lead to a reduction in thruster lifetime [228].

The porous properties used in the CFD simulation were entered into the ESPET domain modeler to compare global parameters. The results shown in table 3.2 that the configuration would operate in droplet mode with a high relative thrust of approximately 0.4 mN. This high thrust value was paired with low specific impulse making this emitter extremely inefficient. A direct comparison can be made between ESPET estimated extractor velocity of 77 m/s and the CFD simulation maximum velocity of 26 m/s.
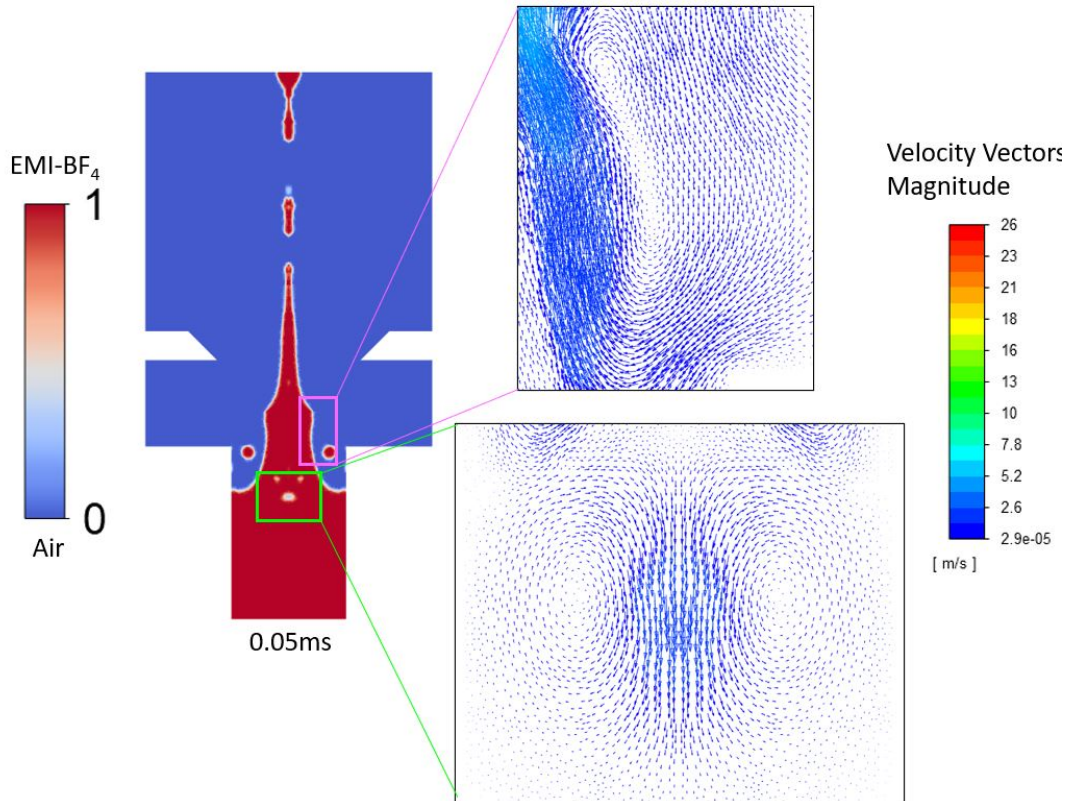
Figure 3.9: Expanded view of velocity vectors from the porous emitter simulation at 0.05 ms. Vectors indicate fluid flow re-circulation below the porous domain, and along the side of the cone-jet.

Thrust	394 (μN)
Specific Impulse	7.85 ($V/(m/s^2)$)
Extractor Velocity	77 (m/s)
Droplet Current	5.7 $\cdot 10^{-5} Amp$
Ion Current	1.2 $\cdot 10^{-20} Amp$

Table 3.2: Estimated performance - Simulated porous emitter

3.4 Concluding Remarks

A CFD simulation was developed to evaluate the behaviour of electrospray thrusters operating in droplet mode. The simulation output was verified by comparing a simple heptane capillary electrospray emitter to previous simulations and experimental results. The results show that the CFD program can be used to model electrospray cone-jet emission and droplet formation. The simulation model was then applied to a porous electrospray emitter. The results of this simulation varied from the expected behaviour and will require additional analysis to develop a more accurate simulation tool. Results from the model were able to replicate the general behaviour of a droplet mode electrospray. Building upon these analytical models allows for greater understanding and

eventually accurate simulation of both droplet and ion electorspray behaviour. To this end future iterations of this simulation will improve the underlying model and incorporate ion mode emission. The simulation described in Chapter 3 was also used as a preliminary design tool for the multimodal thruster described in Chapter 4.

4 Multimodal Electrospray Propulsion System

Chapter 4 describes the design of a novel multimodal electrospray thruster to be used as a propulsion module on a small satellite. The designed thruster incorporates an ion mode electrospray thruster with a droplet mode electrospray thruster using the common IL propellant EMI-BF$_4$. The two modes of propulsion use porous electrospray emitters, where the properties of the porous material determine the mode of operation. As described in section 1.4, the multimodal system benefits from using only one type of propulsion to create both a relatively high thrust droplet mode and high efficiency ion mode. The combination of these two modes allows for greater operational capability and mission flexibility to small satellites operating in LEO. A 1U CubeSat was used as a point of reference for determining the constraints on the thruster, such as available power and mass of the satellite.
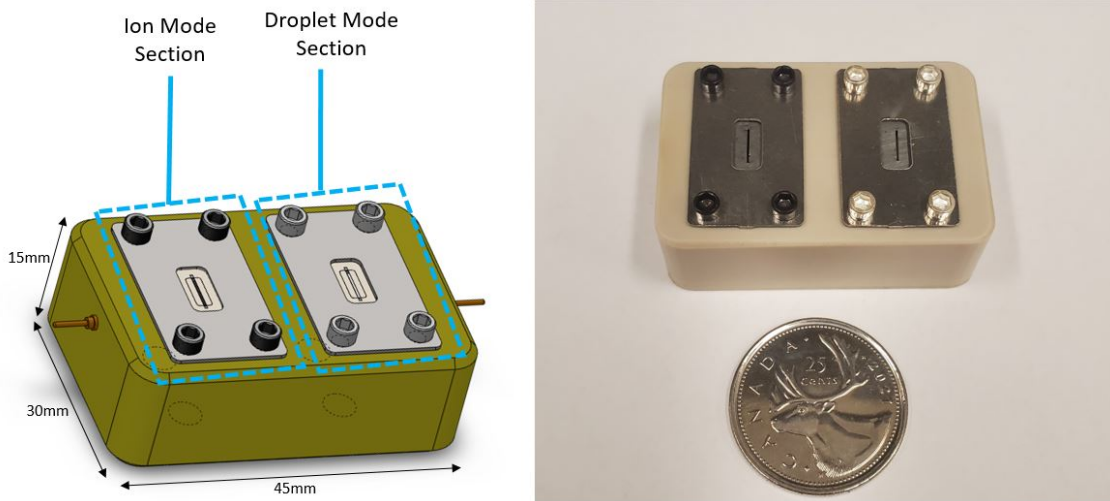
Figure 4.1: The exterior components of the assembled multimodal electrospray prototype thruster. The LHS shows the CAD model of the thruster and RHS shows the final thruster assembly next to a Canadian quarter (diameter of 23.88mm) for size comparison.

The research on thruster design builds off previous studies conducted at RAPPEL [172]. It was decided based on previous work and literature review that one mode of propulsion would be an ion mode electrospray. Ion electrospray thrusters are capable of producing useful thrust in a small, fuel-efficient module. This part of the thruster would act as the high efficiency mode and has several benefits including passive propellant transportation, a stable liquid propellant, the lack of any pressurized systems, and small scale. For the high thrust mode of operation several modes

of propulsion were considered. RAPPEL has investigated the integration of a cold gas thruster with an ion mode electrospray [172]. Recently, there has been growing interest in combining a monopropellant chemical/ion mode electrospray (ME) [173, 176, 177, 179]. It was decided using two completely different modes of operation, such as a ME thruster, led to complexity from each mode requiring specialized components. By selecting a porous droplet mode electrospray as the high thrust part of the multimodal thruster, all the benefits of an ion mode electrospray would be maintained. Commonality between the components used in both modes of operated allowed for additional mass reduction and saving on development time. The thrust produced by a droplet mode electrospray is notably less than a monopropellant chemical thruster but is still useful for certain mission types.

The following subsections detail the design of the thruster prototype, materials selection, manufacturing processes, assembly, and estimated performance for the multimodal thruster.

4.1 Multimodal Prototype Design

The design was inspired by several recent electrospray prototypes [152, 193, 229, 172, 151]. The core components of the multimodal thruster are two porous wedge emitters of varying pore size. The variance in pore properties impacts the propellant flow rate and thus the characteristics of electrospray emission. Using only porous electrospray emitters in the design allowed for consistency in both modes of operation. The final thruster design can be seen in figure 4.1. As a proof-of-concept design, the multimodal thruster was a demonstration of how emission from the two different modes could be integrated.

The outer dimensions of the thruster were 30 mm x 45 mm x 15 mm. A polyether ether ketone (PEEK) plastic block was used as housing for all thruster components. PEEK plastic was used as an insulator material throughout the design due to its excellent high vacuum properties [230]. The housing was spilt into two sections as seen in Figure 4.1. One section produced an ion mode emission, while the other section a droplet mode emission. The various internal components which make of the thruster can be seen in Figure 4.2.

The two electrospray emitters are a porous wedge geometry. Porous wedge emitters allow for multiple emission sites using a single emitter structure, which helped to reduce the machining time. Each porous wedge emitter had a height of 0.3 mm and a length of 4 mm. The emitters were designed to have an apex curvature of 10 microns. The emitters were positioned on top of a rectangular alignment platform 0.3mm high, both of which were milled into the emitter substrates. The ion mode emitter was fabricated from a porous carbon xerogel substrate, and the droplet mode emitter from a P3 porous borosilicate glass filter. The P3 grade borosilicate glass filter had a mean pore size of 40 microns, while the carbon xerogel was determined to have a mean pore size of 1.2 microns. The larger pore sizes of the borosilicate glass emitter created an increase to the propellant flow rate allowing for droplet emission. The small pores of the carbon xerogel substrate inhibited propellant flow allowing for ion emission. Laser ablation was used to fabricate both porous wedge emitters and alignment platforms.

Extractor electrodes made from 0.05mm thick molybdenum foil were separated from the electrospray emitter by a PEEK spacer. The molybdenum extractor and PEEK spacers were attached using double sided kapton tape. By pressure fitting the PEEK spacer to the emitter alignment platform it allowed for automatic alignment of the emitter apex and the extractor electrode during assembly. The distance from the apex of the electrospray emitters to the extractor electrodes was designed to be 0.3 mm.
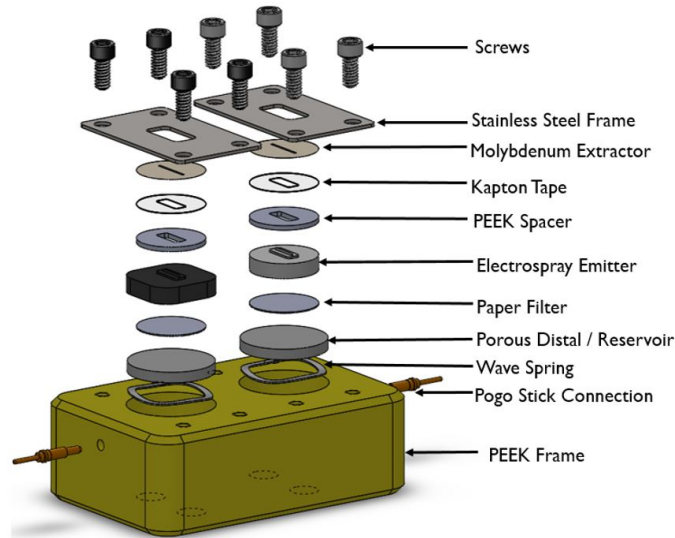
Figure 4.2: Exploded view of internal multimodal thruster components.

Stainless steel porous discs were used as both distal electrodes and propellant reservoirs for the electrospray emitters. The ion mode emitter was coupled with a stainless steel disc that had a porosity of 28 - 32% and pore rating of 5 microns. A pore rating measures the diameter of a particle the porous material would not allow to pass through. The droplet mode distal electrode was a disc with a porosity of 55 - 65% and pore rating of 40 microns. An enhanced view of the two distal electrodes can be seen in Figure 4.3. As discussed in section 2.2.1, the porous properties of the distal electrode have an impact on electrospray emission. A single piece of filter paper was placed between the distal electrodes and the electrospray emitters to ensure that the components were hydraulically coupled during operation. Two small holes were drilled into the sides of the PEEK housing and were aligned to the edge of the distal electrodes. After the internal components were assembled, a pogo pin electrical connection was pressure fit into the holes, permitting for the high voltage power supplies to be in contact with the distal electrodes.
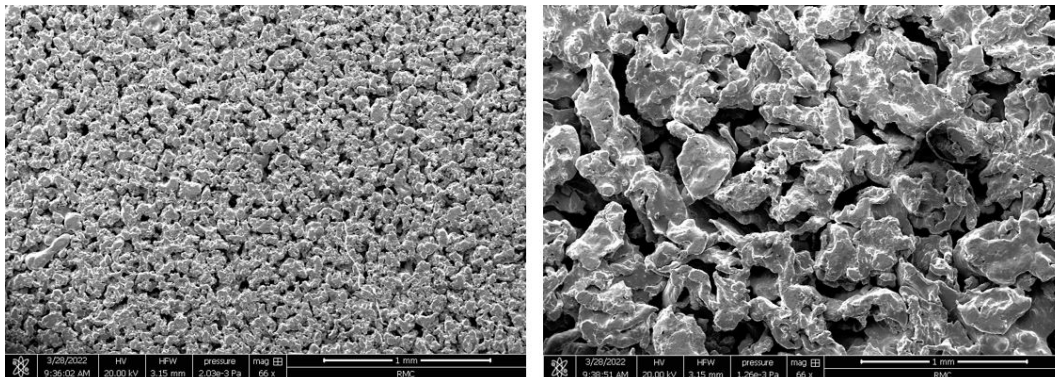
Figure 4.3: SEM Imagery of the porous stainless steel distal electrodes. LHS 5M disc used with carbon xerogel emitter, RHS 40M disc used with borosilicate glass emitter (x66 magnification of both samples).

The emitter, extractor, and distal electrode were sandwiched between a wave spring and stainless steel frame. The compression from the spring ensured that all components maintained good contact throughout operation. The wave spring was placed on the bottom of a circular hole drilled into the thruster's PEEK housing. A set of four screws fastened each stainless steel frame to the molybdenum extractors. To distinguish between the ion and droplet mode emitters seen in Figure 4.2, different coloured screws were used. The ion mode emitter had black oxide coated stainless steel screws, and the droplet mode side used silver-plated, stainless steel screws. A ring connector attached to each stainless steel frame was used to ground both the frame and the extractor.

The majority of parts in the thruster assembly were available as commercial-off-the-shelf (COTS) products. Several of the COTS components were further machined into parts at the RMC machine shop. A supply of PEEK was machined into the thruster's frame and extractor spacers. Stainless steel shim shock was cut into the stainless steel frame. An exploded view of the multimodal thruster's components can be seen in Figure 4.2.

The electrospray emitters are a challenging component to fabricate. The droplet mode emitter was made from a ROBU Porous borosilicate glass filter disc (P3) (referred to as "frits") purchased from Adams and Chittenden Scientific Glass Coop. The 10 mm discs had a measured thickness of approximately 2.8 mm. The carbon xerogel material used in the ion mode emitter was not easily available commercially. It was decided to synthesize resorcinol-formaldehyde (RF) carbon xerogel in-house at the RMC's chemistry department. RF Xerogel was selected due to the material's porous properties and recent heritage with ion mode electrospray emitters [146]. The material had been shown to have uniform pore sizes, mold-ability, and high porosity [231].

4.2 Carbon Xerogel Synthesis

Carbon aerogels and xerogels are a type of porous foam material. They are often fabricated using a process called sol-gel seen in Figure 4.4. The sol is a collection of microscopic particles which are suspended in a solution. These particles will slowly turn into a gel over time, as the particles collide becoming larger particles and eventually forming structures. The gelation process is often slow, so a catalyst is often added to accelerate the reaction. Once a gel has formed, a drying process removes any remaining liquid solvent, revealing a solid porous structure. Different drying methods would lead to the formation of either an aerogel or a xerogel. When directly evaporating a solvent from its liquid phase the porous network shrinks creating a xerogel. Supercritical drying evaporates the solvent without shrinking the porous structure resulting in an aerogel.

There have been several researchers who synthesized carbon xerogels following a relatively similar process. RF aerogels were first developed by Pekala as a method to produce an organic gel with similar properties to silica gels [232]. Work by Brant introduced acetic acid as a useful catalyst in the gelling process of RF xerogels [233]. Arestie was the first to use carbon xerogels as distal electrodes of electrospray thrusters [145]. Their process used to fabricate the xerogel was adapted from the aerogel process developed by Baumann [144]. A similar process was then used to create electrospray emitter tips directly from the carbon xerogel material [234]. The process used to synthesize carbon by the above researchers could take up to two weeks to complete. Work by Rojas-Herrera streamlined the process down to four days [231]. In this work three carbon xerogel synthesis recipes developed by Arestie [145], Perez-Martinez [234], and Rojas-Herrera [231] were tested. The process outlined by Arestie was slightly adapted to produce the carbon xerogel substrate used in the multimodal thruster.

The dimensions in which an RF xerogel substrates is formed play a large role in the final pore size and skin thickness of the material. In this work, two separate molds were developed to create
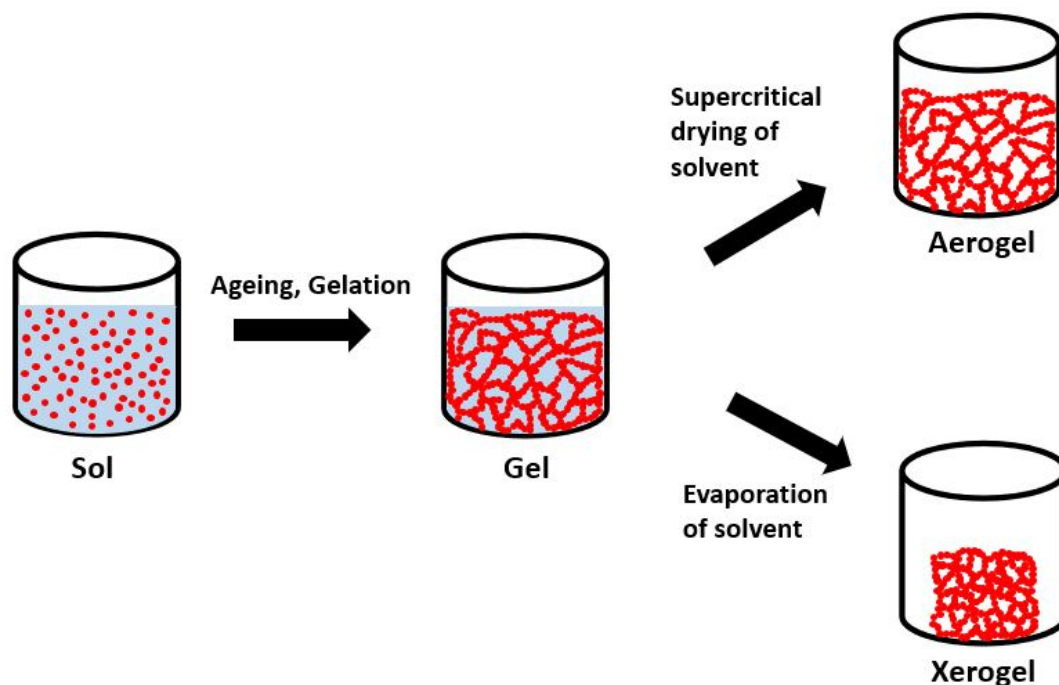
Figure 4.4: The Sol-Gel process.

the xerogel. The first, or "base", mold was sized to produce square samples with side lengths of 15 mm with a thickness of 4.350 mm (side to depth ratio of 1 : 3.45). These dimensions factored in the estimated 10% shrinkage during the curing process, 20% shrinkage during pyrolysis, and outer skin removal. Similar dimensions in previous studies [231] have shown resulting pore radii in the desired range from 450 - 574 nm.

The second mold contained the same dimensions as the first with the addition of a rectangular protrusion (length 12 mm, width 0.6 mm, thickness 0.55 mm) in the center of each mold square. The purpose of adding this extra feature was to produce an electrospray emitter during synthesis and thus reduce emitter machining after synthesis.

4.2.1 Molds

The two molds were made using a hydrophilic Polydimethylsiloxane (PDMS) [235]. PDMS is a low cost, easily fabricated silicon elastomer widely used in MEMS applications. The addition of Poly(dimethylsiloxane-b-ethylene oxide) (PDMS-b-PEO) gives hydrophilic properties to the mold. Here the PDMS was made using a Sylgard 184 Silicone Elastomer kit purchased from Krayden Canada Inc., a distributor of DOW products in Canada. The PDMS-b-PEO was purchased from Polysciences Inc.

1. The PDMS polymer base, curing agent, and PDMS-b-PEO are added to a 1,000 ml beaker in a 100:10:1 ratio, then mixed. The mass of each component was 266.3 g, 26.6 g, 2.7 g.
2. The mixture then degassed in RAPPEL's main vacuum chamber using an Edwards dry scroll pump (100 mTorr) for 45 minutes to remove bubbles.
3. The degassed silicon mixture was then poured into aluminum molds manufactured in house at the RMC machine shop.
4. The silicon mixture was then cured in a low temperature oven at 80°C for 90 minutes.

Figure 4.5: LHS The PDMS-b-PEO mold cooling in the aluminum mold. RHS - The stand alone PDMS mold.

4.2.2 RF Solution

The RF xerogel solution used in this research was produced in-house in the RMC Organic Chemistry lab. Details of the lab equipment used during carbon xerogel synthesis can be found in Appendix A. To create the RF solution the process followed was:

1. Add solid resorcinol powder (4.92 g, 0.224 mol) to a small round-bottomed flask and completely dissolve in de-ionized water (6.00 g, 6 ml)
2. Mix 37% formaldehyde (8.60 g, 0.108 mol, 7.88 ml) into the solution for 5 minutes, while covered by a rubber stopper, to avoid evaporation.
3. Add and mix acetic acid (0.176 g, 3 mmol, 0.168 ml) into the solution.
4. Transfer final solution to the PDMS molds.

The process is altered in the following subsections.

4.2.3 Gelation and Drying

The molds filled with the RF solution were sealed into an airtight plastic container. The samples were then aged giving the material time to gel. The gelation process follows:

1. Gelation at room temperature for 48 hours. Effort was taken to make sure the samples were undisturbed.
2. Baked samples consecutively at 40°C for 24 hours, 60°C for 24 hours, and then 80°C for 72 hours

After the samples had undergone gelation, an acetone exchange was performed as an optional step. The goal of the acetone bath was to replace chemically stable compounds with acetone, which easily evaporates. In this research an acetone exchange was performed by:

1. Open airtight container and saturate samples with acetone.
2. Reseal container and soak samples for 12 hours.
3. Remove acetone and replace with fresh acetone. Soak samples for an additional 12 hours.

4. Removed used acetone.

Following the acetone exchange the samples were dried. To obtain a xerogel, the solvent material was removed through natural evaporation. Throughout the drying process, the initially white gel slowly became yellow, orange, and finally a red colour, as the resorcinol oxidized. The steps for the drying process include:

1. Remove samples from airtight container and place under a fume hood at room temperature for 24 hours.
2. Bake samples at 60°C for 24 hours.
3. followed by 80°C for 48 hours.

After drying was completed, the samples became solid porous structures, but were not a conductive material. In order to change the polymer into a conductive carbon material, they underwent a pyrolysis process.

4.2.4 Pyrolysis

The samples were inserted into a high temperature tube furnace to be carbonized. The samples were slowly heated to 900°C, left at this temperature for three hours, then slowly cooled down to room temperature. The slow heating and cooling of samples prevents the samples from deforming or fracturing. An inert atmosphere is required to avoid combustion. To achieve this argon gas is injected into the furnace at one end and vented out the fume hood at the other end. Argon gas (99.99 %) was input at a flow rate of approximately 450 standard cubic centimeters per minute (SCCM).
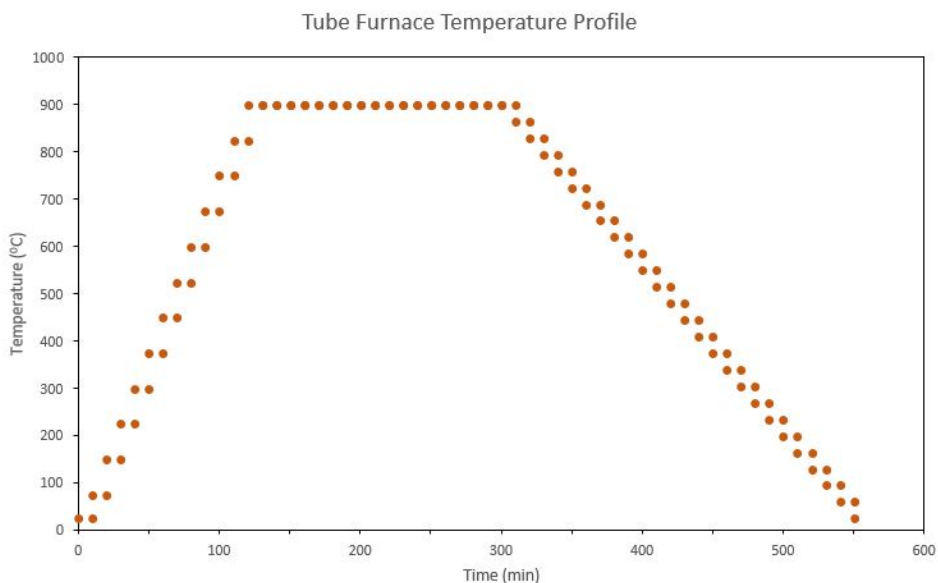
Figure 4.6: Tube furnace temperature profile used for carbon xerogel pyrolysis. Temperature variation increments were made every 10 minutes.

Initially pyrolysis was attempted using a Thermo Scientific Series 1269 high temperature furnace. After several failed attempts it was discovered that a crack in the ceramic tube had allowed air to enter causing the samples to combust. After this discovery, the smaller LECO TF-1 tube

furnace was successfully used. The downside of using this older tube furnace was that the temperature could not be pre-programmed into the furnace, which was possible with the series 1269. This limitation made pyrolysis a very involved process. During the 2 hour ramp up and the 4 hour ramp down, the temperature was manually changed every 10 minutes. This heating and cooling procedure can be seen in 4.6.

4.2.5 Shaping and Cleaning

During the fabrication process, a shiny non-porous skin formed on the exterior of the xerogel. The skin was most pronounced on the surface exposed to air during drying. The sample's surface skin was careful removed using 200 grit sandpaper under a fume hood. Further shaping of the samples was performed using fine grit micro-finishing discs (500 - 2,000 grit).
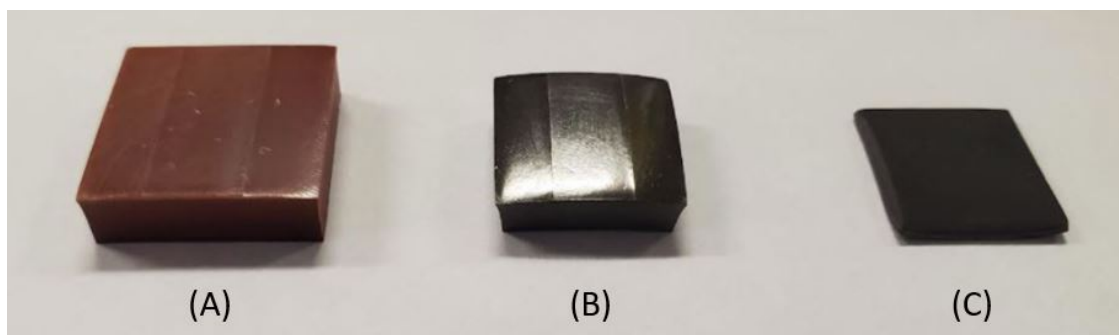
Figure 4.7: The progression of carbon xerogel production. (A) is the dried RF xerogel prior to pyrolosis, (B) is the sample after pyrolosis, and (3) is the pyrolized sample after shaping and cleaning.

After the samples were properly shaped, a cleaning procedure was performed to remove any carbon particulate which may have been blocking the pores [145]. This cleaning process was conducted by:

1. Submerge samples in acetone and put into an ultrasonic bath for 1 hour.
2. Submerge samples into isopropyl alcohol and once again put into an ultrasonic bath for 1 hour.
3. Dry samples in a low temperature oven at 100°C for 30 minutes.

4.2.6 Pore Measurement

The carbon xerogel samples were analyzed in order to determine their mean pore size and porosity. As discussed in Chapter 2, these two parameters play a large role in the propellant flow rate through a porous electrospray emitter. A scanning electron microscope (SEM) was used to take micron scale images of the samples. Ten images from the top and bottom of five carbon xerogel samples were analyzed to determine their average pore diameter. An example SEM image of the carbon xerogel can be seen in Figure 4.8 (A). The top of the carbon xerogel samples tended to dry faster than the bottom, due to their direct exposure to air. This led to smaller pores on the top of the samples. To ensure the best estimate of the mean pore size, SEM images were examined from both the top and bottom of each sample.

The SEM images were analyzed using image processing software ImageJ [236]. The program used an algorithm to differentiate the carbon xerogel structure from the background pores. The

SEM images were converted into a binary black and white image, then the pore edges were then smoothed using a filter. Once the image was processed, the average Feret's diameter of the all the pores was calculated. Of the SEM images sampled, the carbon xerogel had an average pore size of 1.204 microns. The steps taken during image analysis can be seen in Figure 4.8 (A - D).
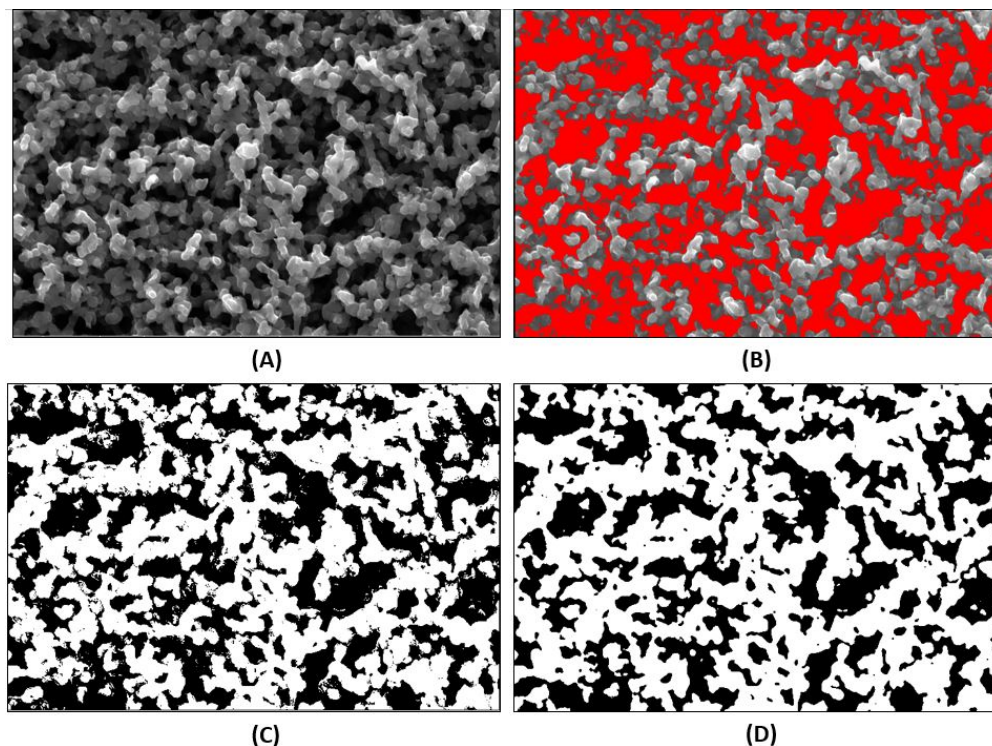
Figure 4.8: SEM imagery of carbon xerogel samples analyzed using the program ImageJ. (A) sample SEM image, (B) separation algorithm used to distinguish pores, (C) binary view of the SEM image, (D) smoothing filter applied to the binary image.

The porosity and internal surface area of the samples was estimated by measuring the difference between dry mass and wet mass of a dry sample and one fully saturated with water. In the future, porosity of materials at RAPPEL could be more accurately determined by using a porosimeter.

4.3 Component Fabrication

As discussed in section 4.1, several of the thruster components were purchased COTS. The PEEK frame, stainless steel frame, and PEEK spacer were all machined in-house at the RMC machine shop using a CNC machine. Laser ablation was used to etch wedge emitters and alignment platforms out of the carbon xerogel and borosilicate glass filter. Laser milling was also used to cut the extractor electrodes. Laser manufacturing was performed at Nanofabrication Kingston (NFK) using an Oxford Lasers Series A picosecond laser.

4.3.1 Electrospray Emitters

Carbon xerogel and borosilicate glass are niche materials, which required specific laser calibration prior to milling. Several 400 micron length squares were laser milled on test substrates in order to determine the mill depth at various laser power settings. The depth of the milled squares was measured using a Bruker DektakXT Stylus Profilometer. At the 100% laser power setting, a single pass of the laser with a milling speed of 1mm/s removed on average 215.0 microns on the carbon xerogel, and 123.4 microns from the P3 borosilicate glass. The various calibration tests were used to determine the tool parameters used to produce the emitter and alignment platform with the desired dimensions.

The laser fabrication process first milled the alignment platform to a depth of 600 microns. Next the emitter was milled by a series of 25 laser passes at low power. Using lower laser power was less efficient, but decreased the potential for a sample's pores being fused together [237]. Each of the 25 laser passes were rectangular with a length of 400 microns, and width varying from 10 to 250 microns. The 25 passes created a series of steps which closely resembled a 3D wedge emitter shape.
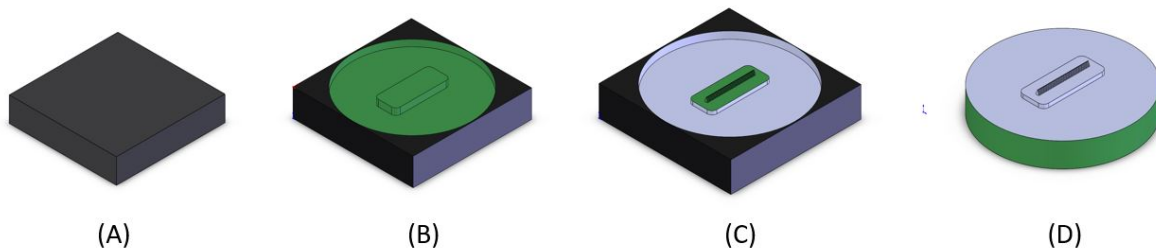
Figure 4.9: The steps taken to fabricate the carbon xerogel electrospray emitter. (A) Carbon xerogel sample, (B) Alignment platform laser milled, (C) Emitter laser milled through a series of 25 laser passes, (D) Excess material is sanded away to leave circular shape.

4.3.1.1 Droplet Mode Emitter

The droplet mode electrospray emitters were fabricated from a P3 borosilicate glass substrate using laser ablation. The alignment platform was milled using a series of 4 passes at a 100% power setting and mill rate of 0.5 mm/s. The laser beam width at this power setting was 65 microns. Before each laser pass, the sample was auto-focused so that the laser was focused to the correct depth. Next,

the emitter was milled in a series of 25 laser passes at a power setting of 13% and mill speed of 1 mm/s. In total, there were three borosilicate glass emitters produced. An example emitter can be seen in Figure 4.10. Part (A) of this figure shows some warping along the edges due caused by the minimum magnification settings used by the SEM.
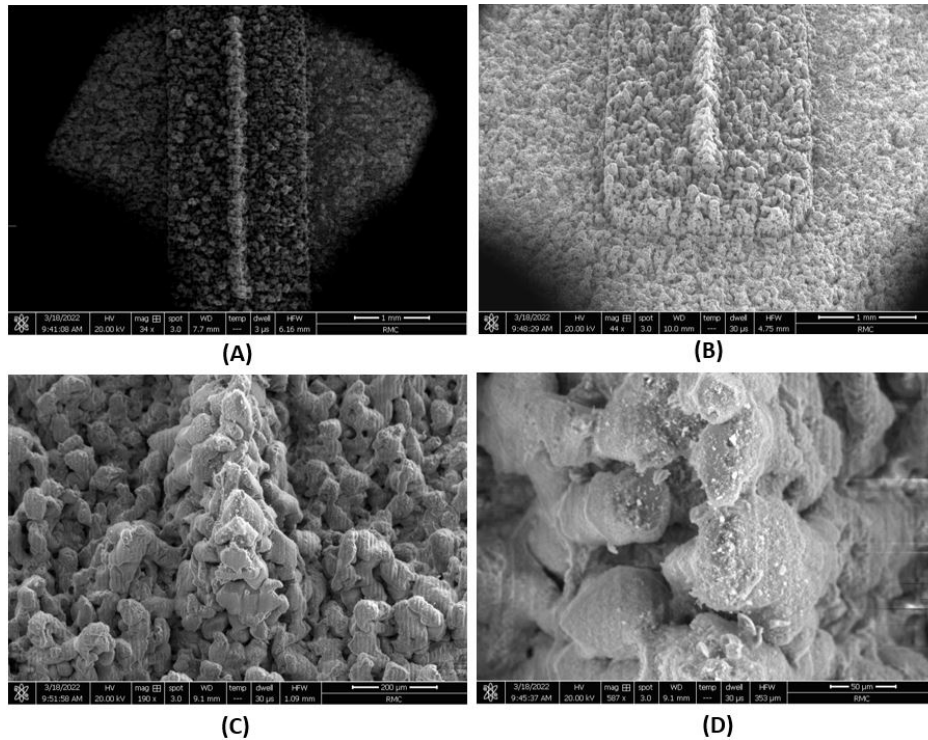
Figure 4.10: SEM imagery of fabricated P3 borosilicate glass wedge emitter. (A) Top view of emitter and platform (magnification x34), (B) Enhanced view of emitter and platform (magnification x44), (C) One side edge view of the wedge emitter (magnification x190), (D) View of wedge emitter apex (magnification x587).

4.3.1.2 Ion Mode Emitter

The ion mode electrospray emitters were fabricated using a similar process to the droplet mode emitters but used a carbon xerogel substrate and different Laser settings. The alignment platform was milled in a series of 2 Laser passes at a power setting of 100% and mill rate of 0.65 mm/s. Before each Laser pass, the samples were auto-focused so that the Laser was focused to the correct depth. Next, the emitter was milled in a series of 25 Laser passes at a power setting of 3% and mill speed of 1 mm/s. After the emitter was formed, the outside edges were sanded by hand, to give the sample the same circular shape as the borosilicate glass. Magnified views of a sample carbon xerogel emitter can be seen in Figure 4.11. Part (A) of this figure shows some warping along the edges due caused by the minimum magnification settings used by the SEM.
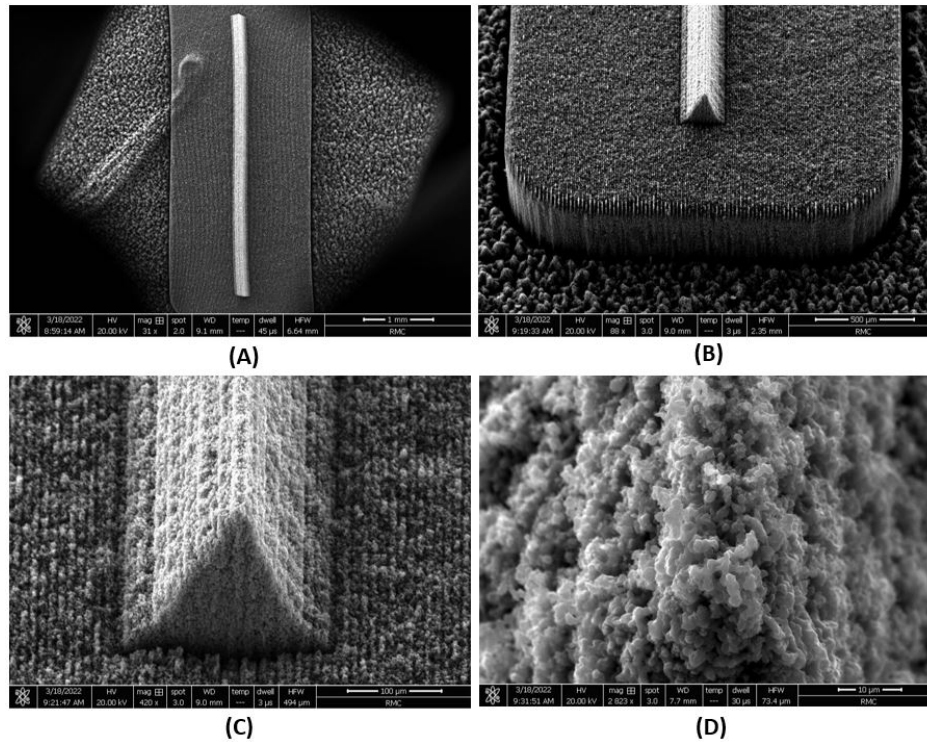
Figure 4.11: SEM imagery of fabricated Carbon Xerogel wedge emitter. (A) Top view of emitter and platform (magnification x31), (B) Enhanced view of emitter and platform (magnification x88), (C) One side's edge view of the wedge emitter (magnification x420), (D) Emitter apex view (magnification x2823).

4.3.2 Extractor Electrode Fabrication

To fabricate the extractor electrodes, 10 mm circles were Laser cut from a sheet of molybdenum foil using 10 passes of the Laser at a power setting of 100% and milling speed of 0.5 mm/s. Each of the circles were then adhered to a PEEK spacer using double sided kapton tape. The extractor assembly was then put back into the Laser machine to have the extractor slit cut out. The slit was a rectangular hole 5 mm in length and 0.35 mm in width. The Laser was aligned to the center of the molybdenum foil, and the slit was cut using the same laser parameters as the molybdenum

circle cuts. An example of the extractor electrode being aligned the ion mode emitter can be seen on the left-hand side of Figure 4.12.
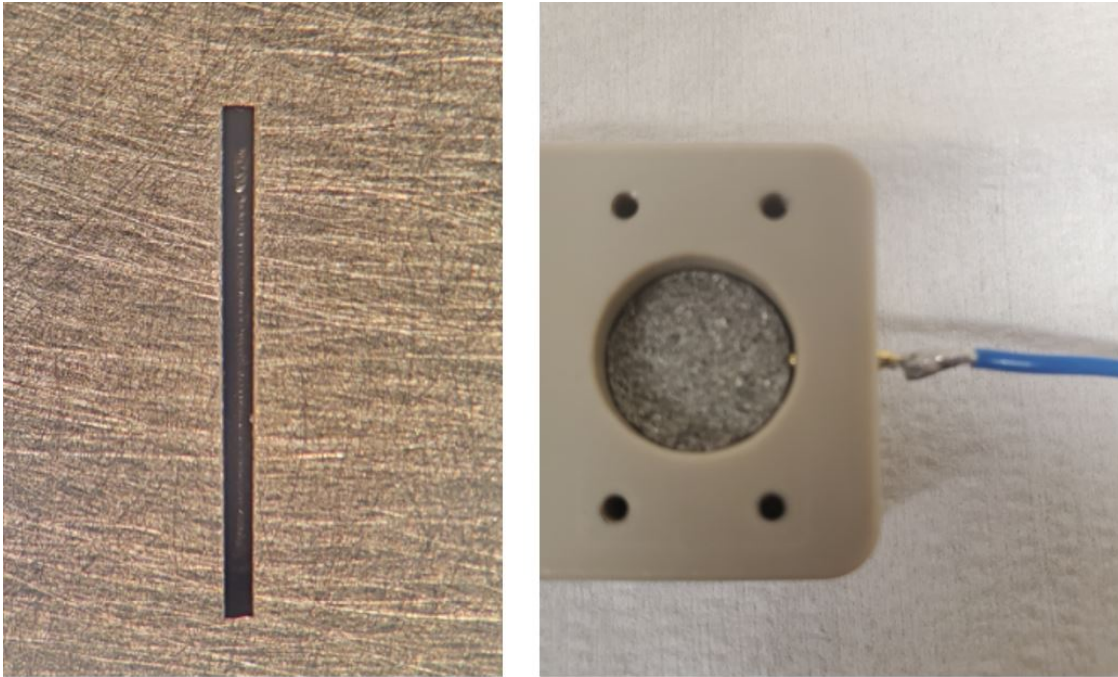
Figure 4.12: Elements of the multimodal thruster assembly. LHS - The carbon xerogel emitter being aligned to the molybdenum extractor electrode. RHS - Pogo pin connecting to a porous distal electrode.

4.4 Estimated Performance

Prior to experimental testing, the performance parameters of several multimodal thruster designs were estimated. The electrospray propulsion engineering toolkit (ESPET) [225] was used to estimate the performance of electrospray emitter designs. The program considers factors such as emitter and reservoir material, emitter geometry, emitter properties, as well as the propellant used. Known parameters of the multimodal thruster were input to ESPET's quick solver tool. ESPET input parameters such as pooling radius and P-scale were estimated using the provided examples from the ESPET manual. Electrospray thrusters, like many forms of EP have the ability to throttle their output. Throttling the applied voltage can have a large impact on the performance parameters such as thrust, specific impulse, and current. The ESPET provided the estimated outputs over a range of applied voltages. To maintain consistency for estimates, all output parameters were calculated at a common applied voltage of 1,750 V. The expected results for the multimodal thruster design described in this chapter can be seen in Table 4.1. Performance estimates of the designed multimodal thruster from ESPET were used as a baseline for the experimental results.

Table 4.1: The estimated performance parameters of the multimodal electrospray thruster, determined using the ESPET at an applied voltage of 1750 volts.

Multimodal Electrospray Thruster Estimated Performance				
Performance Parameter	Thrust (μN)	Specific Impulse (s)	Current (μA)	Mass Flow Rate (μg/s)
Ion Mode	0.33	1865	3.68	0.0178
Droplet Mode	543	123	275	448

4.5 Concluding Remarks

The design, fabrication, and expected results of a multimodal electrospray thruster are detailed in this Chapter. The thruster combined an ion mode electrospray emitter made from carbon xerogel, with a droplet mode electrospray made from a P3 borosilicate glass. The combination of these two modes is predicted to allow for greater mission capability and flexibility in orbit. Using only porous electrospray emitters in the design grants the benefits of passive propellant transportation, a stable liquid propellant, the lack of any pressurized systems, and small form factor. The majority of thruster components were COTS. Carbon xerogel samples used to make the ion mode electrospray emitter were fabricated in-house at RMC. Both ion and droplet mode electrospray emitters were fabricated using laser ablation. Chapter 5 details the experimental apparatus used for testing, and the multimodal thruster results are presented and discussed in Chapter 6.

5 Experimental Methods

5.1 Introduction

The experimental methods used for testing are described in the current Chapter. All testing performed for this thesis was conducted at the Royal Military College's Advanced Propulsion and Plasma Exploration Laboratory (RAPPEL). Equipment used for testing purposes include: a vacuum test chamber, electrospray operation electronics, and diagnostic equipment.

Tested electrospray propulsion prototypes were characterized using two experimental configurations (to be elaborated later in the chapter): 1) Full beam setup, and 2) Time-of-Flight (ToF) setup. The full beam setup was used to collect the entire charged particle beam from an electrospray source. The ToF setup collected only a portion of the source beam and was used to determine the indirect thrust, specific impulse and particle species of emission.

A bimodal thrust stand has been previously developed at RAPPEL [238]. The stand is capable of direct thrust measurement (DTM) in the millinewton (mN) range, using torsional balance, and indirect thrust measurement (ITM) to collect current from charged particle beams using a metallic collector plate. This work builds upon the ITM system to allow for ToF measurements of electrospray thrusters. The pre-existing thrust stand was used as a base on to which components were added to create the diagnostic ToF system.

5.2 Vacuum Chamber

To replicate as much as possible the conditions of outer space, high vacuum pressure chambers are used to remove as much ambient air as possible. To achieve high vacuum at RAPPEL, a custom bell jar chamber built by the Kurt J. Lesker company, seen in Figure 5.1, was used. The chamber was brought to high vacuum using a two-stage vacuum pump system. Using an ULVAC Technologies Inc. GLD-136A and Edwards Vacuum XDS10 dry scroll roughing pumps the system pressure was brought from atmospheric pressure to low pressure. A Leybold TURBOVAC 90i turbo-molecular pump, capable of removing 90 litres of nitrogen per second was connected in series with the GLD-136A. Once the foreline valve, positioned between the GLD-136A and 90i turbo pump, had a pressure below 37 mTorr, the 90i was activated using an on-off switch. The combination of pumps allowed the chamber to reach a high-vacuum state [239]. The lowest absolute pressure observed was 5×10^{-6} Torr after 10 hours of continuous operation. During testing, a pressure between 8×10^{-6} to 1.5×10^{-5} Torr was used. This range of pressures was achieved after on average 2.5 hours of vacuum operation.

Pressure within the vacuum chamber was measured using a Superbee CVM201 pressure gauge and a Kurt J. Lesker company 354 Series hot cathode ionization gauge. An additional Kurt J. Lesker company 275i Pirani gauge was positioned between the GLD-136A and the 90i turbopump, to measure the pressure within the foreline valve. Both the CVM201 and 275i were convection
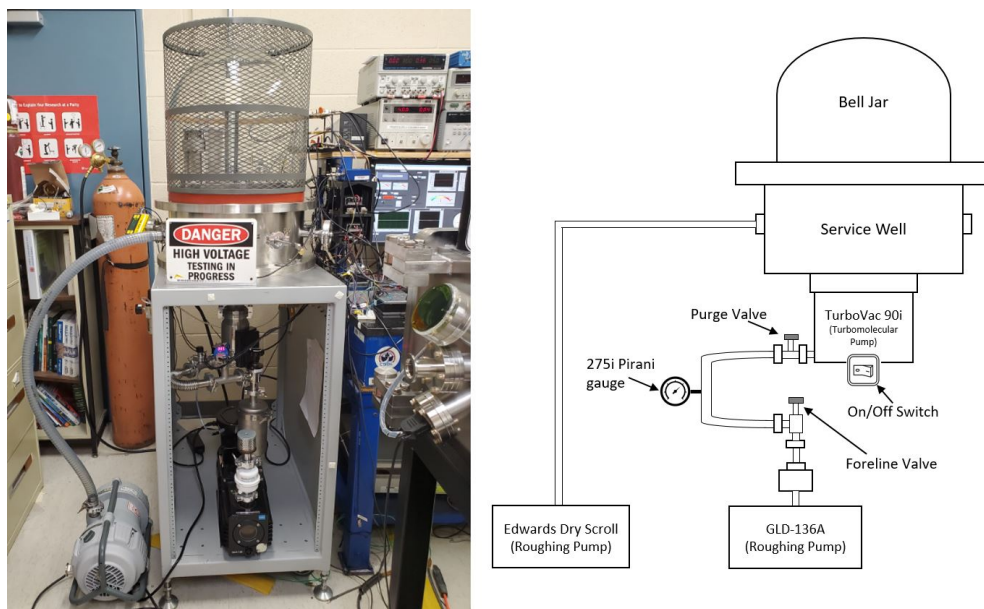
Figure 5.1: Bell Jar Vacuum Chamber used for experimental testing. Two roughing and one turbo-molecular pump are used to bring the chamber to a maximum measured pressure of $5\mathrm{x}10^{-6}$ Torr.

pressure gauges. Convection gauges contain a heated wire whose temperature changes based on the density of particles colliding with it. More particles in contact with the hot wire leads to more heat loss. These changes in heat were used to measure the pressure. The CVM201 can be used to measure pressure from one atmosphere down to 20 mTorr, beyond which it no longer is effective. Below 20 mTorr, the 354 series ion gauge is used to measure pressures down to 10^{-8} torr. The ion gauge measures the pressure by producing plasma, used to determine the density of particles within the chamber. Since the ion gauge can be damaged if exposed to higher pressures, it is tied to the CVM201 output signal which automatically turns the ion gauge off at higher pressures.

The 90i turbopump and the GLD-136A roughing pumps were connected to the primary vacuum port at the base of the bell-jar chamber. The chamber also had eight input/output connection ports around its outside surface. These ports were used to connect pressure gauges, the Edwards dry scroll roughing pump, and various voltage/current signals. The various inputs and outputs used in this work are visualized in Figure 5.2.

5.3 Electrospray Source

Two electrospray sources were used in this thesis, namely a single tungsten needle externally-wetted emitter, and the multimodal electrospray thruster, detailed in Chapter 4.

The main purpose of the experimental setup was to characterize the multimodal thruster. The externally-wetted emitter, seen in Figure 5.3, was used to test all of the ToF components to ensure they functioned correctly. This emitter was a modified prototype previously characterized at RAPPEL [238]. The design had a tungsten needle protruding through a Teflon base and was aligned to a 1 mm hole within the stainless steel shim extractor plate. Polyether ether ketone (PEEK) plastic washers were placed between the Teflon and extractor plate, creating a space of approximately 1 mm. The tip of the Tungsten needle was placed approximately 150 microns away
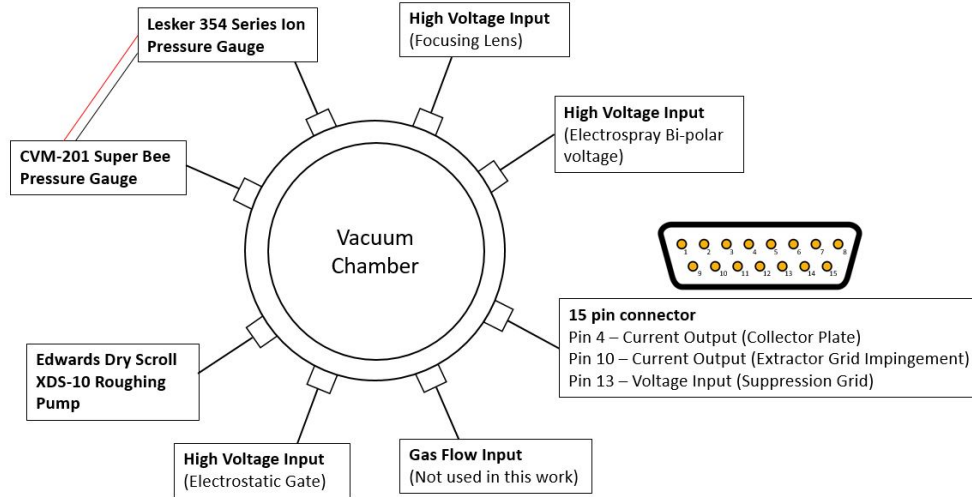
Figure 5.2: Schematic detailing the various inputs and outputs to the bell jar vacuum chamber.

from the extractor plate.
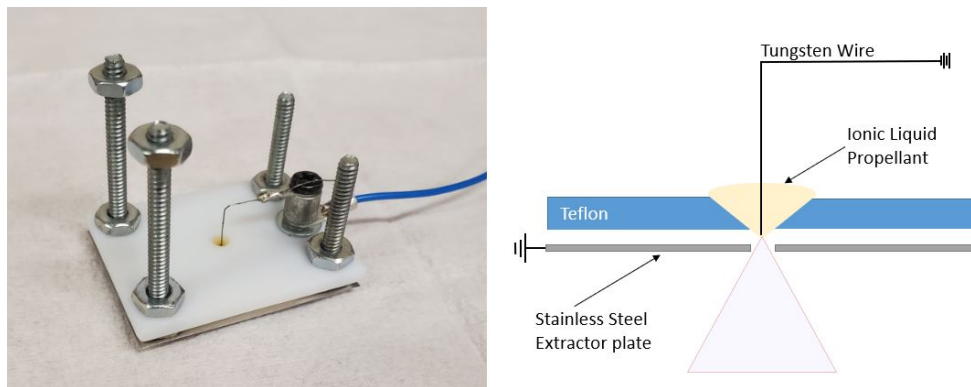
Figure 5.3: LHS shows the assembled externally-wetted emitter, RHS give a schematic overview.

The tested electrospray sources were supplied high voltage by two EMCO H60 (0-6kV) power sources. The H60 units supplied both positive and negative potentials to the electrospray. A Keysight 6038A power supply was used to supply 40 VDC to two RSD-60L-24 DC-DC converters which powered the EMCO H60 power supplies with a consistent 24V. The DC-DC converters provided an extra layer of voltage protection to the power supplies and connected circuit boards. Data acquisition input and output modules, used to create signals and collect data for this work, are detailed in Appendix B. The EMCO H60 power supplies were controlled via a 0-to-5-volt signal supplied from a National Instruments (NI) 9265 current output module. The voltage output from each power supply was measured using each unit's monitor channel, which gives a 0-5V reading (corresponding to 0-6 kV) output.

Bipolar voltage operation is an important aspect of testing electrospray thrusters using ionic liquids (ILs). High voltage was alternated to either positive or negative polarity using two high voltage power supplies connected to the circuit. A square wave signal from a LabVIEW control

program was used to produce the voltage switching input. A switching frequency of 0.333 Hz was used to ensure there was enough time to make ToF readings, while negating electrochemical effects of single polarity operation. The output of the bipolar switching circuit was connected to a data acquisition circuit board, which measured the voltage and current applied to the electrospray source being tested. While the EMCO H60 power supplies are rated to 6 kV, they were only operated from 0 to 3 kV, in order to prevent damaging the custom-built PCB circuit boards. Details of the bipolar switching and data acquisition circuit board can be found in Appendix B.

5.4 Full Beam Measurement

The purpose of full beam measurements was to collect the entire emitted charged particle beam of the selected electrospray source. The charged particles produced by an electrospray carry a current characterizing a thruster's output. In this configuration, an electrospray source was placed near a metallic collector plate. As charged particles collided with the collector, the strength of the emitted current was measured. A schematic giving an overview of the full beam measurement setup can be seen in Figure 5.4.
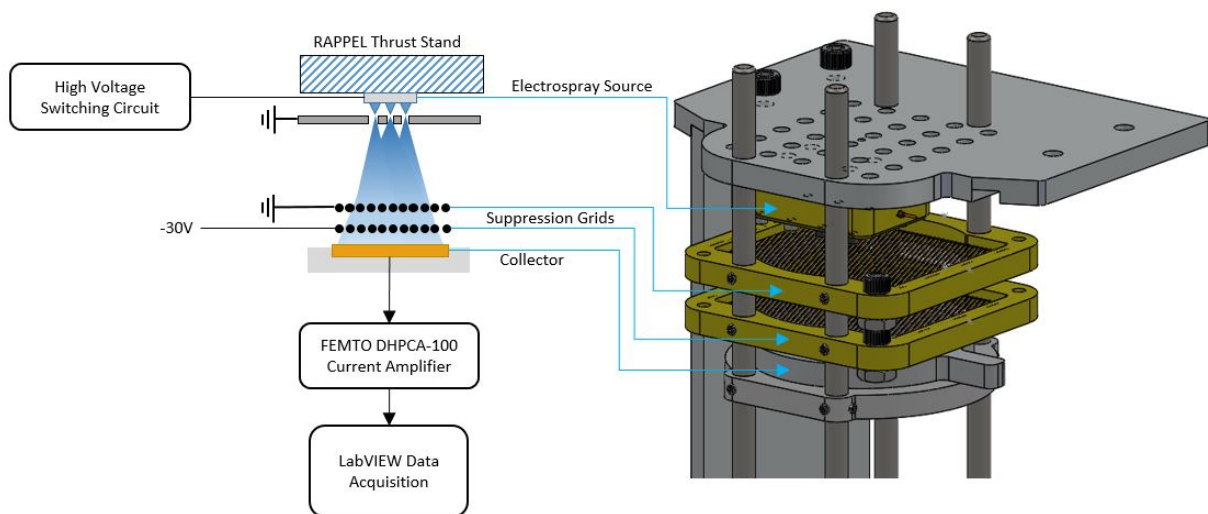
Figure 5.4: Experimental setup used to collect full beam current measurements from electrospray source.

5.4.1 Collector

The collector used in this work was a circular flat metallic plate. The plate with a diameter of 29 mm made of stainless steel, was screwed into the outer Teflon base to ensure current at the plate remained isolated. Holes in the side of the Teflon base were used to attach the collector to the RAPPEL thrust stand. The collector assembly was manufactured in-house during previous work at RAPPEL [238]. To obtain full beam measurement, the collector was placed near the electrospray source.

The collector plate was connected to a FEMTO DHPCA-100 series variable-gain high-speed current amplifier. The amplifier provided a range of gain settings from 10^2 to 10^8 volts per ampere of current. The DHPCA-100 amplifier outputs a voltage from -1V to 1V which was connected to the data acquisition setup. To collect the appropriate current measurements, a gain setting of 10^6 was used while testing the externally-wetted emitter, and 10^5 while testing the multimodal electrospray. The amplifier is capable of operating at a collection frequency of 10 MHz, allowing for measurements on the scale of micro-seconds (needed for ToF).

Figure 5.5: Electrospray beam collector. A flat metallic plate surrounded by a Teflon frame.

5.4.2 Suppression Grids

As detailed in section 2.6.1, as particles collided with the collector, secondary electrons can be released. In order to compensate for the secondary electrons, two suppression grids were placed directly upstream of the collector. The grids were manufactured in-house at RMC's machine shop. The design used a PEEK frame with forty-nine 0.025 mm diameter fine tungsten wires strung across an open area. The PEEK frame was tapped with four screw holes in the corners, so that the wires could be connected to common points. The wires were weaved through the PEEK frame by hand using a microscope. Only 2.45% of the frontal area was blocked by the wires, allowing the majority of electrospray emission to pass through uninhibited. One of the completed grids can be seen in Figure 5.6. The wires of the first suppression grid were positioned 5mm from the top of the collector plate. During testing, ring connectors connected to a GwINSTEK GPS-4303 power supply were attached to screws, allowing the wires to be biased to -30 volts. The second grid was positioned directly above the first grid and was connected to ground.

5.5 Time-of-Flight Measurement

ToF is an indirect measurement method used to determine the thrust and specific impulse of electrospray thrusters. The utility and components of ToF systems were previously detailed in section 2.6. The ToF setup used in this work used all the components from the Full beam tests and added an Einzel lens and a Bradbury Nielsen Gate. A schematic of the ToF experimental setup is shown in Figure 5.7 [240].
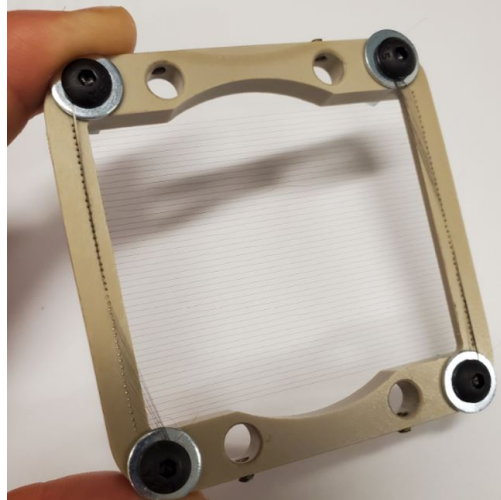
Figure 5.6: Suppression grid composed of a PEEK frame with interwoven tungsten wires.
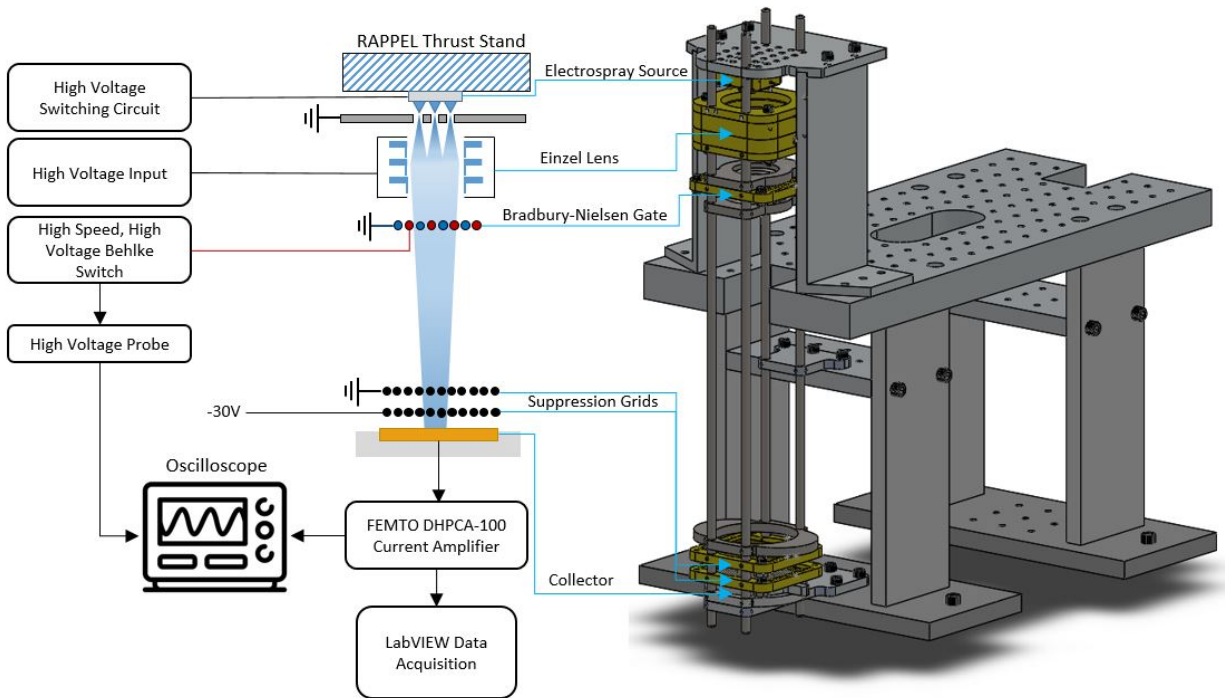
Figure 5.7: Experimental setup used to collect time-of-flight data from electrospray source.

5.5.1 Time-of-Flight Stand

The pre-existing RAPPEL thrust stand could be configured to have a long flight path of approximately 30cm, from the electrospray source to the collector [238]. A longer flight distance leads to increased flight times, allowing for increased resolution for the current readings at the collector. To increase the flight distance and allow additional room for the relatively large Einzel Len, a ToF

stand was manufactured at the RMC machine shop. The stainless steel stand was fastened on top of the pre-existing thrust stand base, extending the flight length from the electrospray source to the collector to approximately 50cm.

5.5.2 Einzel Lens

A single stage Einzel lens was designed to be easily integrated into the RAPPEL thrust stand. While not critical to operate a ToF system, the lens was a useful supplementary tool for focusing electrospray emission over a large distance. Design of the lens was inspired by previous work on ToF systems [194]. The asymmetric lens was comprised of three cylindrical stainless steel electrodes spaced apart using a PEEK frame. Electrode 1 was an aperture and electrodes 2 and 3 were cylindrical. This setup allowed for minimal axial distance before the beam reached the high potential electrode 2, which in turn reduced beam spreading. The component was fabricated at RMC's machine shop. The final assembly and design of the Einzel lens can be seen in Figure 5.8. The second electrode in the Einzel lens was supplied with a voltage from a EMCO USB20N high voltage power supply, capable of providing a negative voltage from 0 to -2 kV. The first and third electrodes were biased to a common ground.
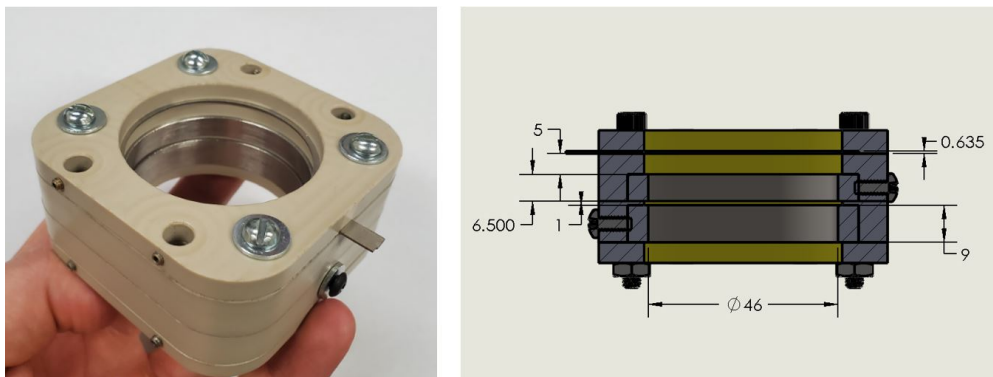
Figure 5.8: Asymmetric Einzel lens used to focus the electrospray beam towards the collector plate.

Several Einzel Lens designs were simulated and optimized using SIMION 8.0, an ion optics simulation tool. SIMION had previously been used at RAPPEL to investigate the beam propagation of colloid thrusters [241]. The simulation ejected monomer EMI^+ and BF^- particles at 50,000 m/s from an initial emission point, through the Einzel lens, and down a 50 cm flight path to a collector plate. The dimensions of the Einzel lens, flight path, and collector were made as close as possible to the RAPPEL ToF configuration. In initial simulations, seen in Figure 5.9, the particles were ejected in a straight line toward the collector. The half angle of the Taylor cone emission was 49.3°s. To account for the fact that particles will spread after being ejected, a second simulation was conducted with a cone shaped beam spread with a half-angle of 49°. This simulation can be seen in Figure 5.10.

From the first simulation, it was inferred that particles emitted straight toward the collector were focused to a central point with a focusing potential of -325 V. In the second simulation, where beam particles spread at an angle of 49°s, the BF_4 particles were focused on the collector at -1,710V, and the EMI^+ particles focused at -2,120 V. The expectation from these simulations was that the optimal focusing potential for a wide range of beam trajectories would lay somewhere between -325 V and -2,120 V. It should be expected that both the negative and positive beam emissions have different focusing potentials, due to differences in particle mass.
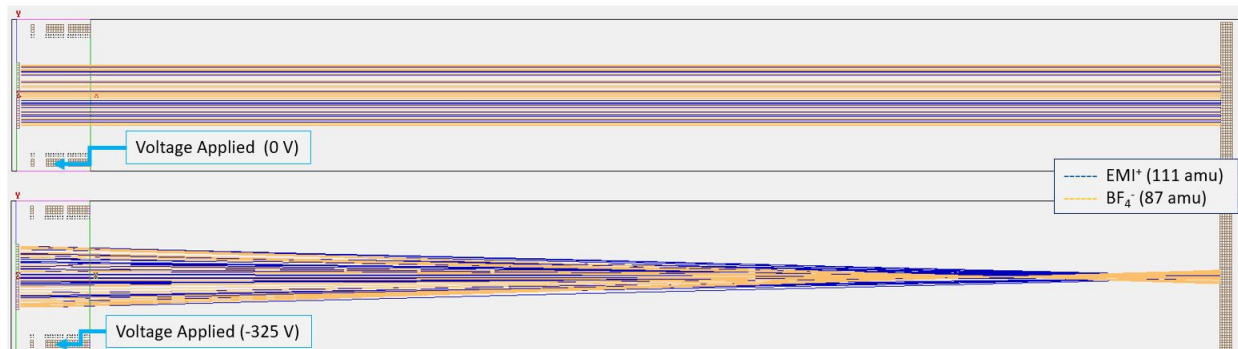
Figure 5.9: SIMION Einzel lens simulation particles ejected in a straight trajectory.
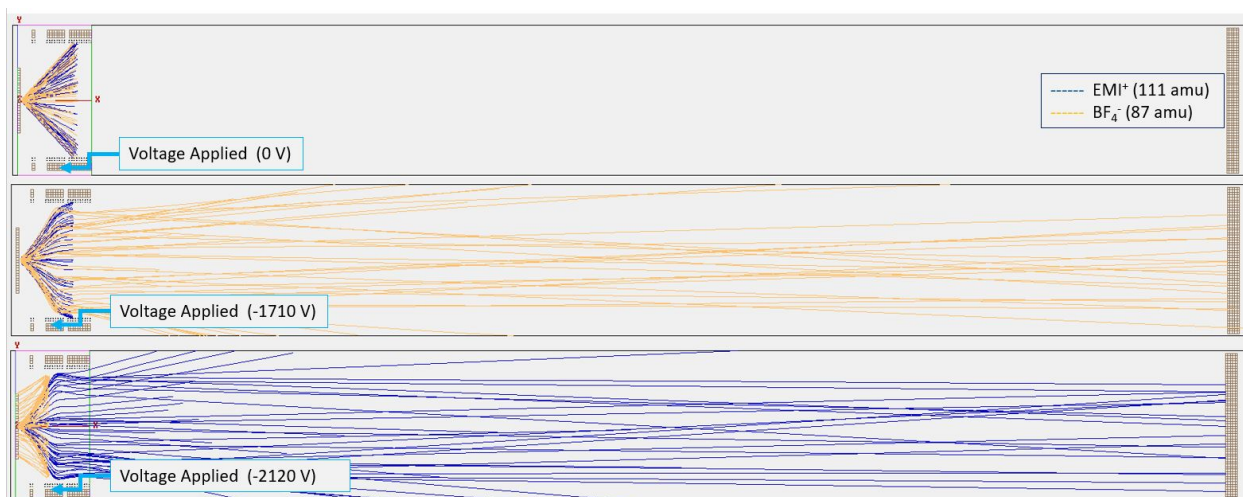
Figure 5.10: SIMION Einzel Lens simulation particles ejected at a 49°half angle trajectory.

It should be noted that the simulations are not exhaustive as they did not take into account dimer particles and the variation in particle velocity based on emission criteria. It is also a challenge to simulate emitter alignment and the impacts of the extractor electrode on beam emission. The simulations were however useful in giving a good estimate to how the Einzel lens would perform experimentally and some baseline values for testing.

5.5.3   Bradbury Nielsen Gate

A Bradbury Nielsen gate (BNG) was selected to deflect the particle beam in the ToF setup. The BNG was converted from a pre-existing suppression grid used in previous work at RAPPEL [238]. Ninety-eight (98) strands of 0.025 mm diameter tungsten wire were strung through a PEEK frame. Small holes drilled into the PEEK frame were spaced by 0.4 mm to create wire separation.

Adjacent wires were isolated so that alternating wires could be biased to different voltages. A 75% complete BNG and a visualization of the alternating wires can be seen in Figure 5.11. The tungsten wire blocked 5% of the frontal area, allowing the majority of the particle beam to pass

through undisturbed. The final design looked similar to the suppression grids described previously, with a higher density of tungsten wire. Due to wear and tear on the pre-existing structure grid, the entire BNG was restrung, so that all wire was tightly bound. It is interesting to note that if wires were loose, they could be attracted to one another during high voltage operation. If the adjacent wires touched, a short circuit would disable the entire gate.

BNGs deflect charged particle beams by creating electrical fields between each adjacent wire. To create these fields, one set of wires was connected to ground and the other was supplied high voltage of 0 to 2 kV from an EMCO USB20P power supply. High speed particles emitted from the electrospray source traveled at speeds of tens of km/s. At these speeds, the particles reached the collector on the timescale of microseconds. To capture the minute changes in current, high voltage applied to the BNG was raised at high speed. To accomplish this application, a high speed HTS 31-03-HB-C Behlke switch capable of nano-second rise times was used. The Belhke switch was controlled using a custom PCB circuit board described in Appendix B. The high voltage power supply was connected to the Behlke switch, which was controlled through the LabVIEW control program.

Figure 5.11: Bradbury Nielsen gate which is 75% of the tungsten wire threaded. RHS shows how the adjacent wires are isolated to different potentials (blue wires ground, red wires high voltage).

The output of the Behlke switch also connected to a Tetronix TBS 1052B-EDU digital oscilloscope after passing through a Tektronix P6015A high voltage probe. The actual flight time of charged particle beam species was calculated as the change in time from when the electrical signal from the Behlke switch reached the oscilloscope to when the current output from the collector reached the oscilloscope. The electrical signal from the Behlke switch traveled several magnitudes faster than the electrospray particle beam, so the error from signal delay would be negligible.

5.5.4 Collector and Suppression Grid

The ToF setup used the same collector and suppression grids described in Section 5.4. Instead of being placed close to the electrospray source, the collector and suppression grids were placed a fur-

ther distance from the electrospray source, at the bottom of the vacuum chamber, to accommodate ToF readings. The Flight length from the BNG to the collector was measured to be 33 cm.

The Collector was once again connected to a FEMTO DHCPA-100 current amplifier. A T-bar connection at the amplifier's output leads the collector signal to both the Data acquisition setup and the same oscilloscope to which the BNG was connected.

5.6 Experimental Preparation Methods

The IL EMI-BF$_4$ was the propellant used in all experimental testing. The chemical was sourced from Sigma-Aldrich at a concentration of $\geq 99\%$ purity. When exposed to air, EMI-BF$_4$ has a tendency to absorb surrounding particles leading to impurities. Most notably, concentrations of water inside the EMI-BF$_4$ can cause poor performance and bubbles which can potentially cause short circuits. When exposed to a low vacuum environment, water within the IL evaporates. This process is often referred to as de-gassing the propellant. Before experiments the EMI-BF$_4$ was poured into a 500ml beaker and put into the vacuum chamber to be de-gassed for 2 hours. The liquid was then kept under vacuum, whenever possible, and was subsequently de-gassed whenever it was exposed to air for an extended period.

De-gassed propellant was added to the externally-wetted emitter using a micro-liter syringe. The porous emitters and reservoirs of the multimodal thruster could not be wet with propellant using this technique. In order to ensure all the pores within these substrates were saturated with IL propellant, the samples were fully immersed in a beaker filled with EMI-BF$_4$ and put under vacuum for 1 hour. As air was removed from the pores, bubbles were observed in the beaker. Once saturated, the samples were removed from the liquid and excess propellant was wiped off the surface of the substrates, using filter paper. The porous materials were then assembled into the multimodal thruster.

During assembly of the multimodal thruster, a microscope was used to align the wedge emitters directly in the center of each extractor electrode. After fully assembled, a final connection check was performed. A multi-meter was used to check if there was any resistance reading between the pogo stick high voltage input and the extractor electrode of the multimodal thruster. During assembly it was not uncommon for some residual IL to inadvertently adhere to the internal walls within the thruster. Even a very small amount of IL could connect the high voltage source to the grounded extractor causing a short circuit. If there was a resistance reading found during the ohmmeter check, the thruster was dis-assembled, fully cleaned, and then reassembled.

The assembled externally-wetted or multimodal thruster was then fastened to the ToF stand and the vacuum chamber was brought down to pressure. The voltage applied to the thruster was increased from 0 to a maximum of 3,000 V in 25 V increments a few seconds at a time. The voltage was raised until the first sign of emission, where it was held constant for longer periods of time to allow for emission to reach equilibrium. Data was then collected, based on the particular test which was being performed. Initial tests with the externally-wetted emitter used just the emitter placed 5cm from the collector, in order to get some baseline data. The emitter was then used to test the suppression grids, Einzel lens, and BNG individually, culminating in a ToF measurement. The multimodal thruster was then tested first in the full beam configuration, and then ToF configuration for both droplet and ion mode several times.

5.7 Concluding Remarks

This chapter gave an overview of the testing apparatus and experimental methods used for testing. A full beam and time-of-flight setup were used to characterize a single tungsten needle externally-wetted emitter and the multimodal thruster described in Chapter 4. The setup utilized a custom-built Bradbury Nielsen gate, Einzel lens, suppression grids, collector, and apparatus stand. Chapter 6 will detail the collected experimental results and analysis for this work.

6 Electrospray Operation: Results and Discussion

Chapter 6 presents the results of the designed multimodal electrospray thruster outlined in Chapter 4 using the experimental setup outlined in Chapter 5. Initial trial run testing confirmed the functionality of the suppression grid, Einzel lens, Bradbury-Nielsen Gate (BNG), and ToF measurement equipment using the externally-wetted emitter described in Section 5.3. Testing the apparatus with the externally-wetted emitter gave a baseline control group for comparison and allowed the multimodal thruster results to be less impacted by emitter degradation during testing. After confirming the functionality of the testing apparatus, both ion and droplet mode of the multimodal thruster were independently tested. The results and discussion of the externally-wetted emitter tests are presented first in Section 6.1 and 6.2, followed by the results and discussion of the multimodal thruster in Section 6.3 and 6.4.
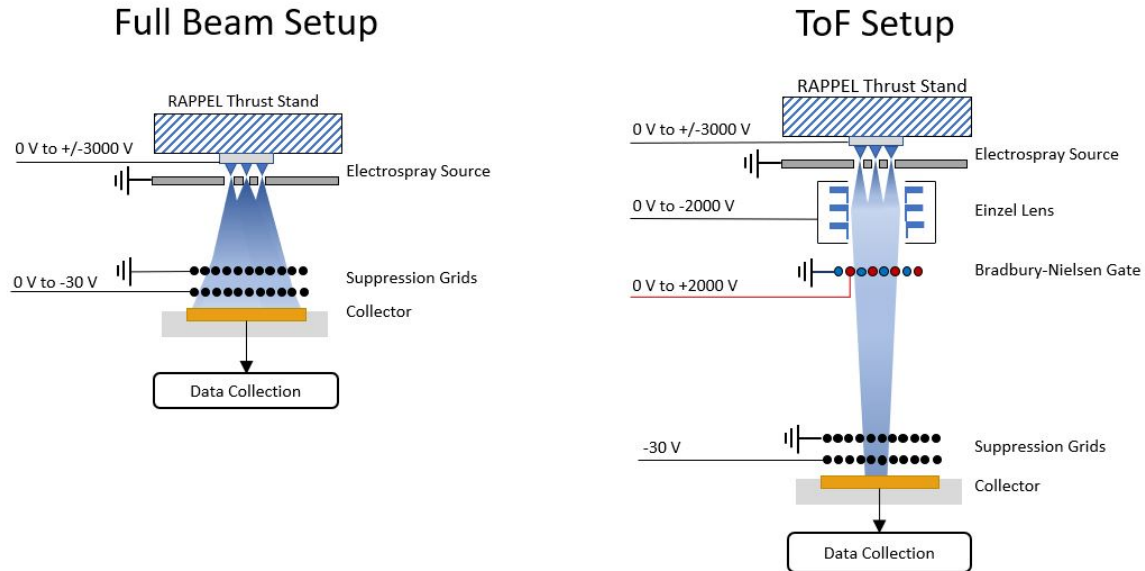
Figure 6.1: Overview of the two experimental setups used during testing.

6.1   Externally-Wetted Emitter Results

6.1.1   Full Beam

Initial trials with the externally-wetted emitter used the full beam experimental setup described in Section 5.4 to test the emitter's functionality. On average, onset of emission occurred around 2100 V. After onset, it took between 2 to 10 minutes for the emitter to reach a steady-state emission. A sample of steady emission showing the applied voltage and measured beam current can be seen in Figure 6.2. The measured current ranged from around [-120 / +200 nA]. The positive emitted beam current was higher than the negative polarity due to the impact of secondary electron emission described in Section 2.6.1.
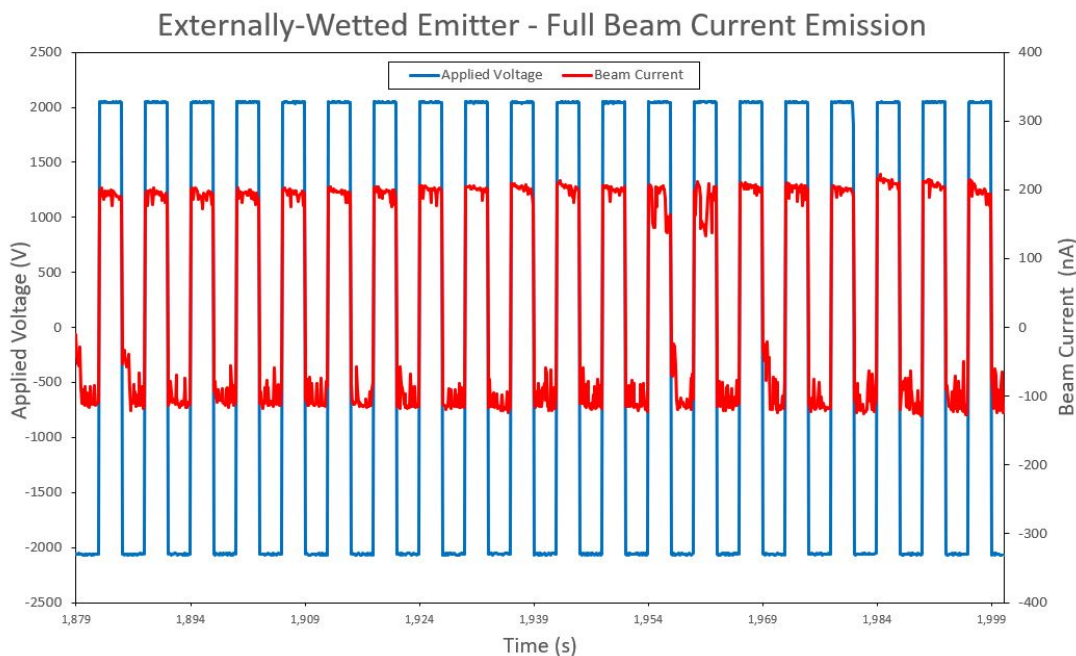
Figure 6.2: Current measurement of externally-wetted emitter using the full beam setup.

6.1.2   Suppression Grid

Following the full beam test, the externally-wetted emitter was configured into the ToF set up described in Section 5.5.   Once the externally-wetted emitter obtained a steady emission, the suppression grid was tested to confirm its ability to remove extra positive beam current caused by the emission of secondary electrons. Suppression grid testing using voltages of -10 V, -20 V and -30 V were conducted. A summary of these tests can be seen in Table 6.1. A sample suppression grid test at -30 V can be seen in Figure 6.3. In this test, the initial current measurement showed a range around [-60 / +100 nA]. After a potential of -30 V was applied to the suppression grid, the current range was measured to be [-60 / +55 nA]. The impact of activating the suppression grid was immediate. The maximum output of the power supply used, -30 V, was best at removing positive current caused by secondary electron emission. All subsequent tests utilized the activated suppression grid biased to -30 V.

Table 6.1: Summary of the changes to measured beam current based on different tested suppression voltages.

Suppression Grid Results	
Suppression Voltage (V)	**Beam Current (nA)**
0	[-61 ±5 / +100 ±10]
−10	[-60 ±10 / +62 ±15]
−20	[-60 ±8 / +55 ±9]
−30	[-60 ±8 / +55 ±7]
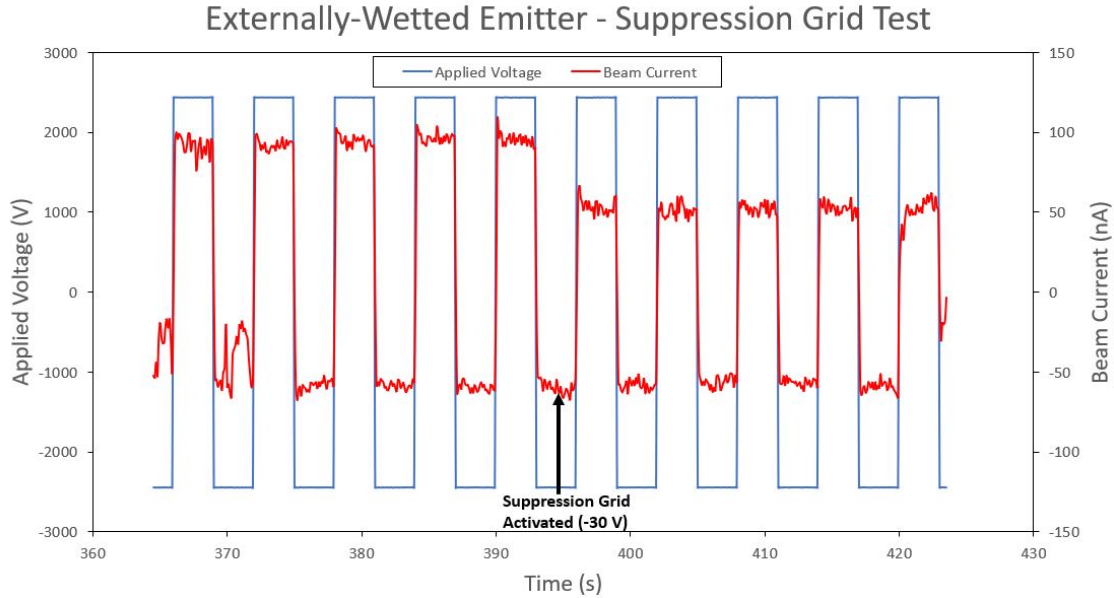
Figure 6.3: Suppression grid test results using the externally-wetted emitter using the ToF setup.

6.1.3 Einzel Lens

The Einzel lens was tested by applying a series of increasing negative voltage from 0 to -2000 V. A summary of Einzel lens testing can be seen in Table 6.2. Initial steady-state current emission from the externally-wetted emitter was measured to be around [-40 / +35 nA]. Focusing potentials from 0 to -1500 V, as seen in Figure 6.4, had a minimal impact to the beam current measured at the collector. In these tests, the negative current increased from approximately -47 nA to -58 nA as the focusing voltage increased, while the positive beam showed small fluctuations in current providing no clear focusing effect.

Tests using higher focusing potentials of -1750 V and -2000 V can be seen in Figure 6.5. A focusing potential of -1750 V showed around a 72.5% increase in the measured negative beam current from approximately -40 nA to -69 nA. A focusing potential of -2000 V demonstrated greater than a 100% increase in beam current from approximately -40 nA to -90 nA. From full beam testing, the expected total beam current of the externally-wetted emitter was in the range of 100 nA.

Table 6.2: Summary of the changes to measured beam current based on different tested focusing voltages applied to the Einzel lens.

Einzel Lens Results	
Focusing Voltage (V)	**Beam Current (nA)**
0	[-40 ±10 / +35 ±10]
−250	[-40 ±11 / +35 ±12]
−500	[-45 ±5 / +35 ±10]
−750	[-48 ±7 / +30 ±12]
−1000	[-55 ±3 / +35 ±6]
−1250	[-53 ±4 / +30 ±5]
−1500	[-58 ±5 / +28 ±10]
−1750	[-69 ±7 / +27 ±15]
−2000	[-90 ±12 / +20 ±10]
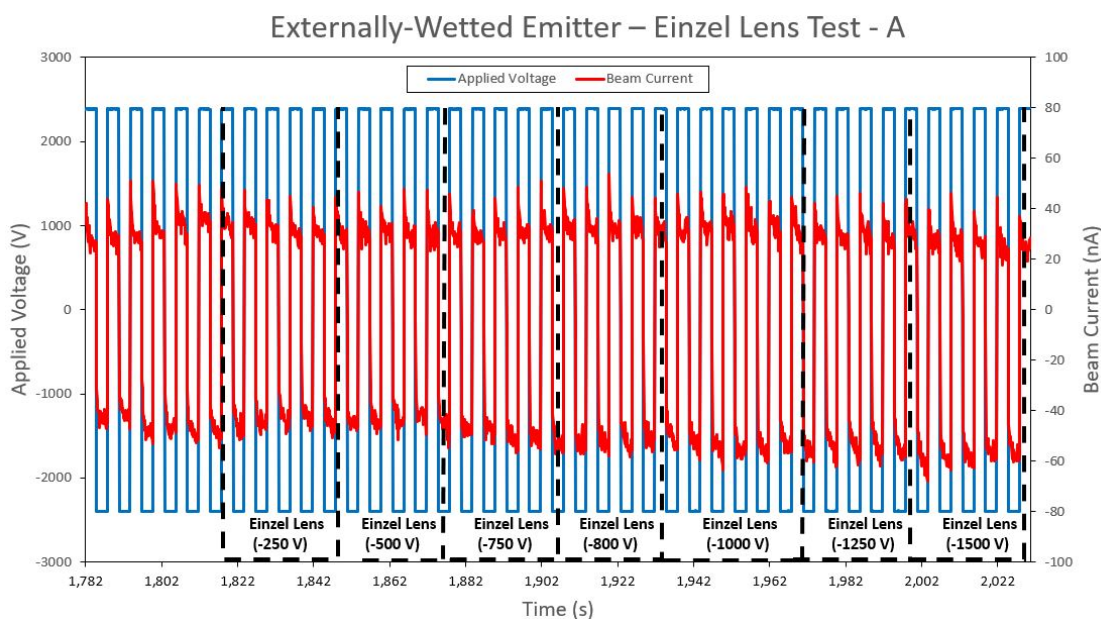
Figure 6.4: Einzel Lens test results using the externally-wetted emitter. The voltage applied to the lens is varied between 0 V and -1500 V.

6.1.4 Bradbury-Nielsen Gate

The BNG was tested to characterize its ability to deflect charged particles away from the collector. Applied gate voltages between 0 and +2000 V were tested, the results of which are summarized in Table 6.3. In all BNG tests, there was a larger deflection on the positive beam current, compared to the negative beam current. For example, at an applied gate voltage of +1000 V, 70% of the positive current beam was deflected, while only 20% of the negative beam. A BNG test with an applied gate voltage of +1000 V can be seen in Figure 6.7. Beyond an applied gate voltage of +1000 V, the BNG had a tendency to fail, due to short circuits between the gate wires. Testing with a gate voltage at +1750 V and above saw near total gate failure. To allow for consistency, an applied gate voltage of +1000 V was used for all ToF testing of the externally-wetted and multimodal thruster.
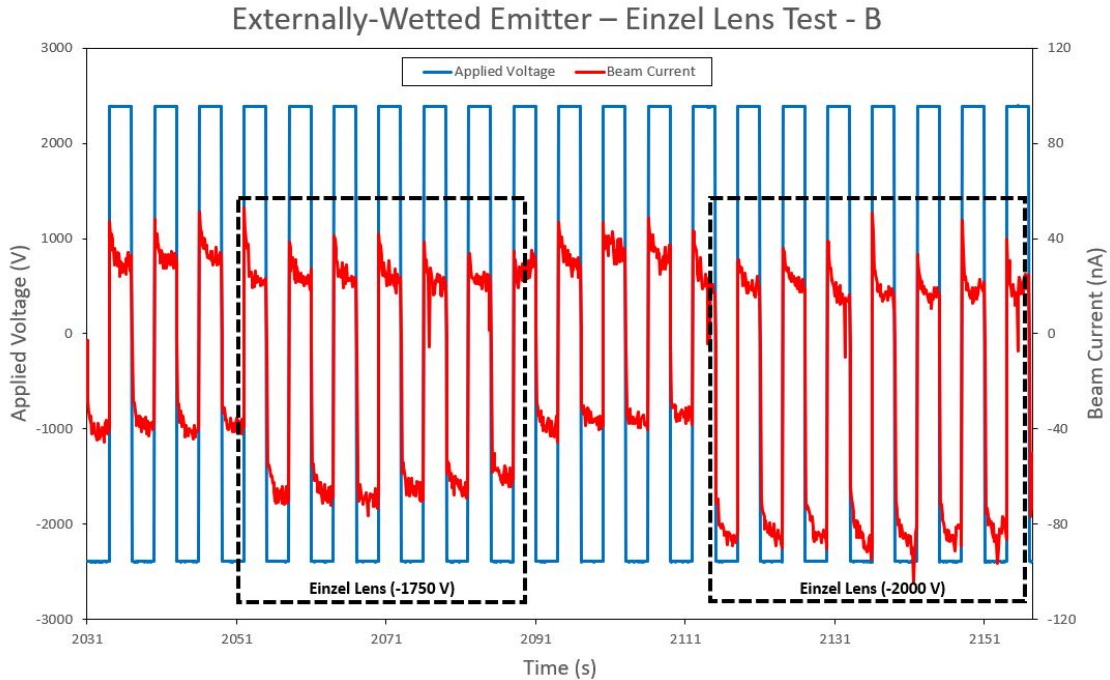
Figure 6.5: Einzel Lens test results using the externally-wetted emitter. The voltage applied to the lens is varied between 0 V and -2000 V. Focusing effect becomes more pronounced closer to the maximum applied voltage.
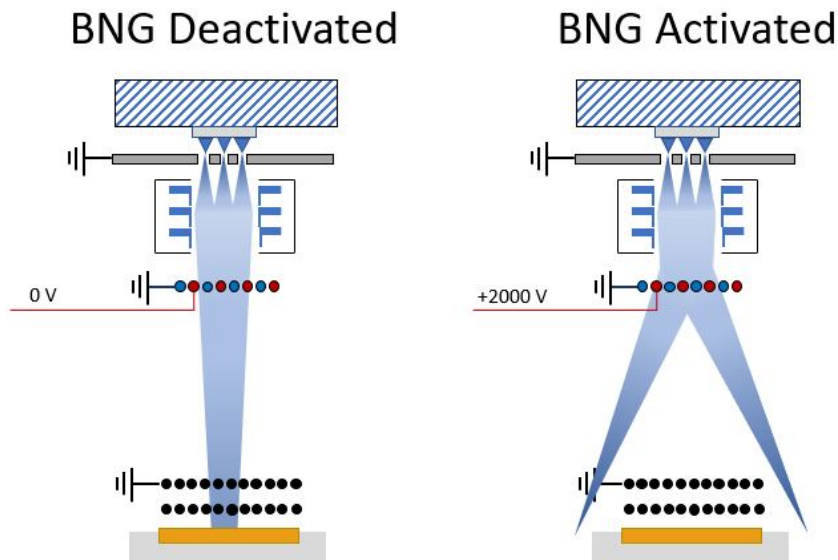
Figure 6.6: Overview of the BNG functionality. When adequate voltage is applied a beam of charged particles is deflected away from the collector.

Table 6.3: The percentage of electrospray beam current deflected away from the collector by the BNG at various gate voltages.

BNG Results			
Gate Voltage (V)	Beam Current (nA)	% (-) Beam Deflection	% (+) Beam Deflection
0	[-63 ±2 / +65 ±8]	0	0
+500	[-54 ±2 / +42 ±5]	15 ±3	35 ±7
+1000	[-50 ±3 / +20 ±4]	20 ±6	70 ±6
+1250	[-44 ±4 / +18 ±6]	30 ±7	73 ±10
+1500	[-44 ±5 / +16 ±3]	30 ±3	76 ±6
+1750	[N/A / +0]	N/A	100
+2000	[N/A / N/A]	N/A	N/A
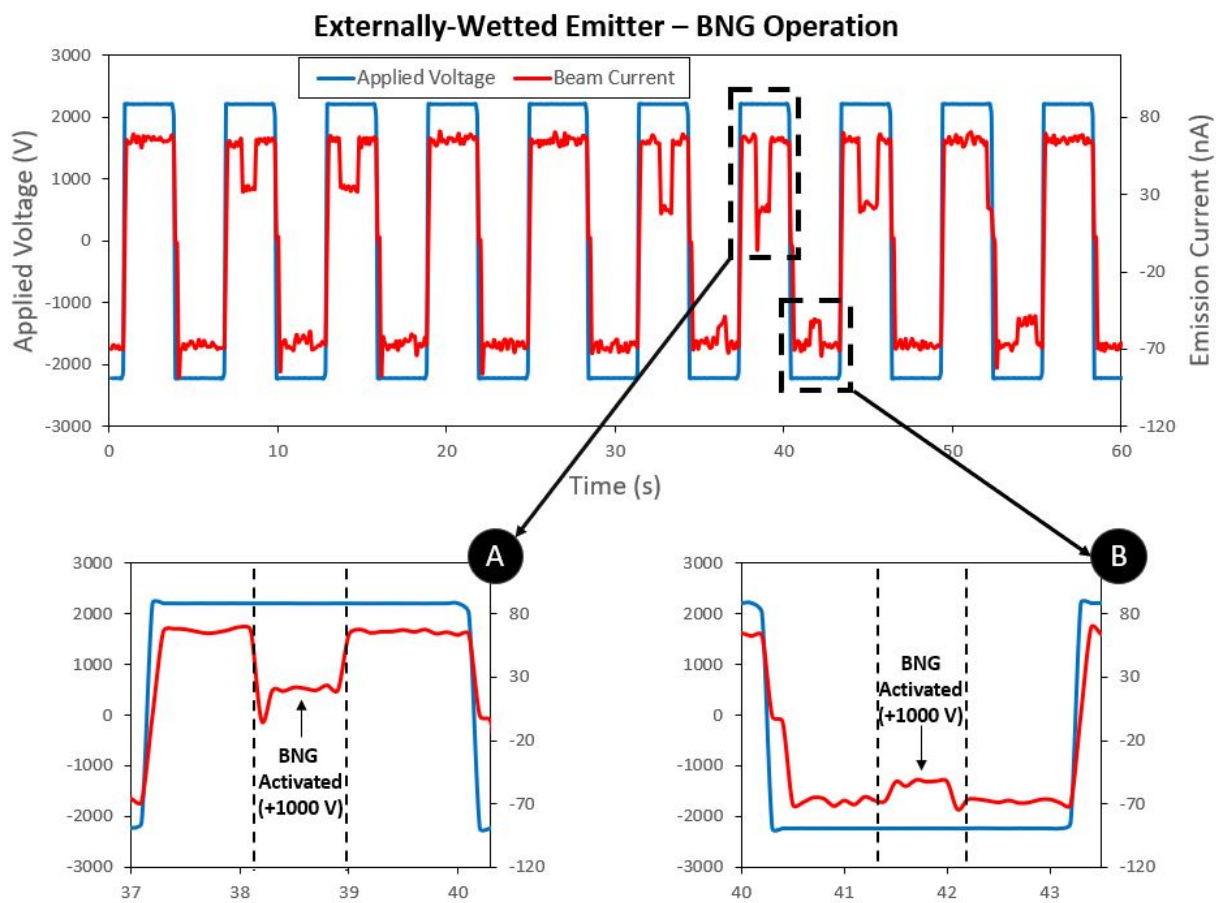
Figure 6.7: BNG test results using the externally-wetted emitter. Results show that the gate is more effective deflecting positive electrospray beam.

6.1.5 Time-of-Flight Measurement

After the functionality of the other components were tested, ToF readings were measured using the equipment outlined in Appendix B. ToF data was collected from an oscilloscope which measured

the gate voltage applied to the BNG, and the emission current signal received at the collector. Figure 6.8 shows both the raw and filtered data from a sample ToF test of the externally-wetted emitter. The open-source program GNU radio was used to filter the raw ToF signal. Three finite impulse response (FIR) filters were applied to the ToF data:

1. A low pass filter used to remove high frequency components.
2. A band reject filter used to remove noise from the current amplifier reading between 2.7 MHz and 4.0 MHz.
3. A band reject filter used to remove noise from the current amplifier reading between 300 kHz and 1.5 MHz.

The ToF results of the externally-wetted emitter used data from the positive polarity current emission. During testing, when the BNG was deactivated, the voltage signal rapidly decreased to zero in the span of nano-seconds. When this occurred, a large negative current spike was followed by the expected step positive increase in current. Figure 6.8 shows the first 100 μs of the same ToF test from Figure 6.9. This second figure is on a shorter timescale and better shows the negative current spike which occurred immediately after the BNG was deactivated.
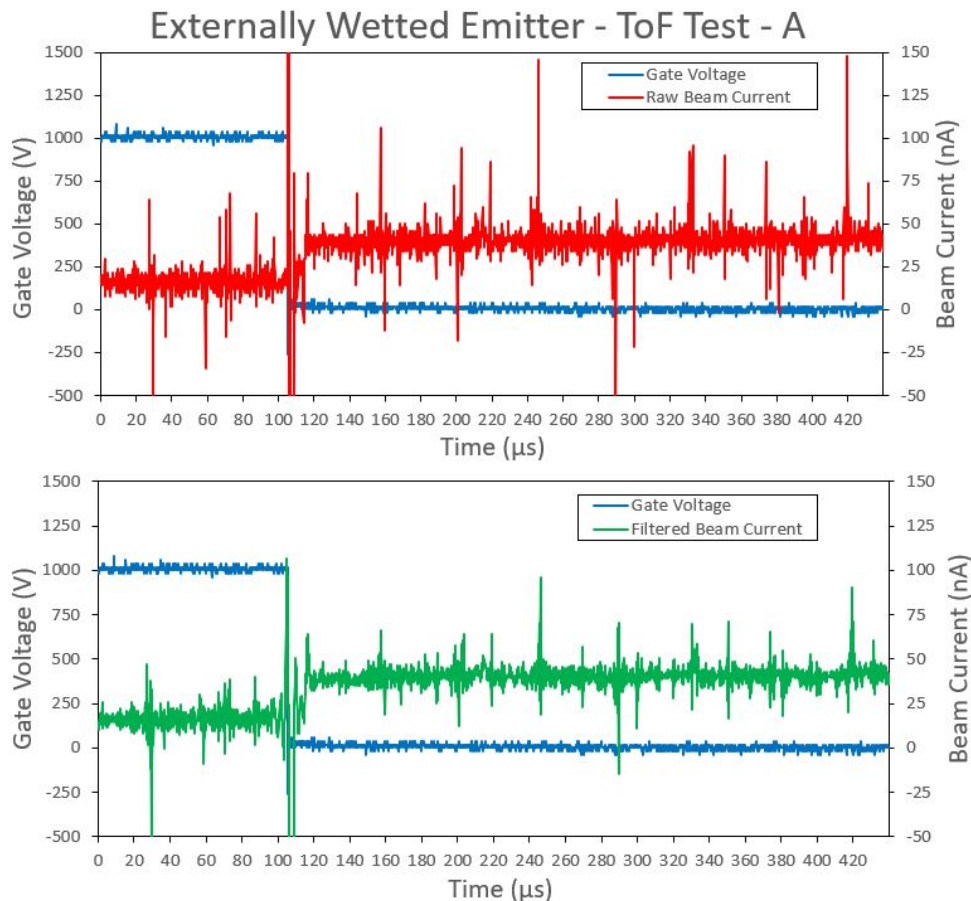
Figure 6.8: Externally-wetted emitter ToF results from 0 to 450 μs. The top graph shows the raw data collected from the oscilloscope, the bottom graph shows the collected data filtered.
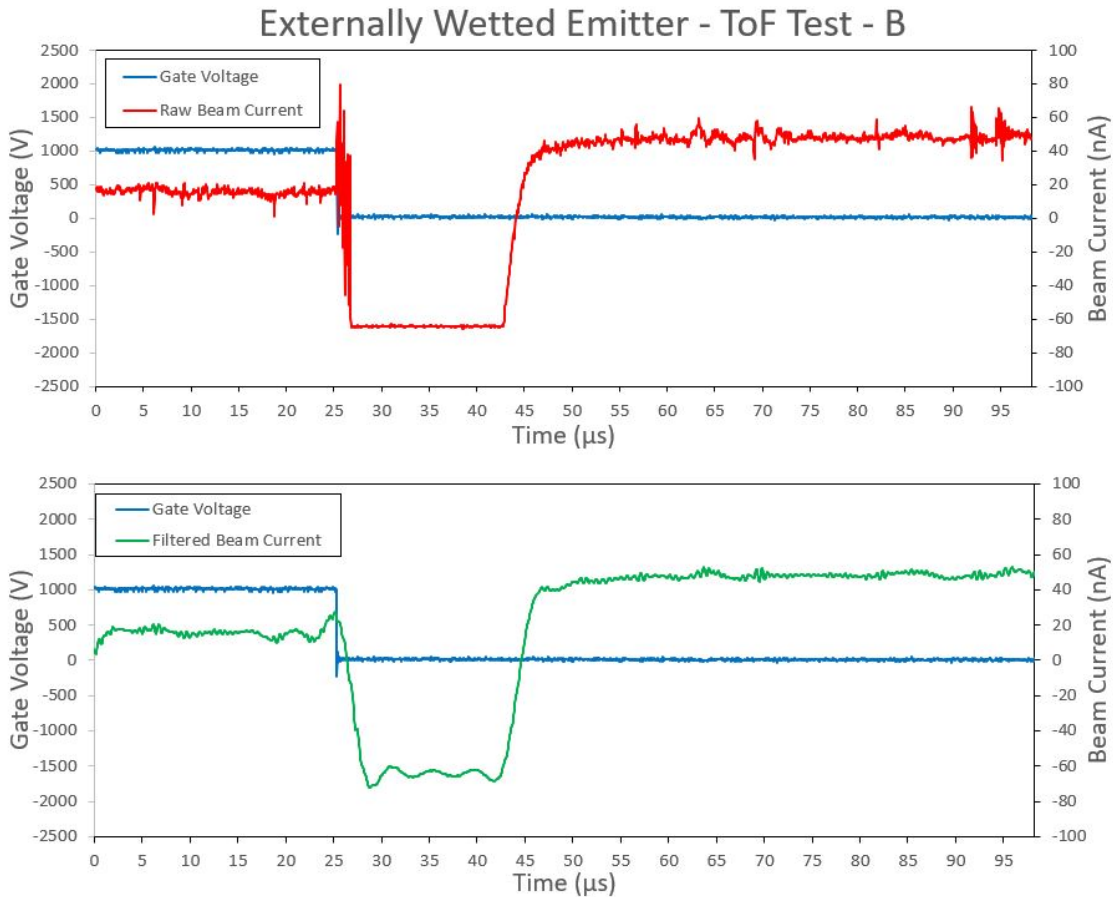
Figure 6.9: Externally-wetted emitter ToF results from 0 to 100 μs. The top graph shows the raw data collected from the oscilloscope, the bottom graph shows the collected data filetered.

6.2   Externally-Wetted Emitter Testing Discussion

It can be concluded that the externally-wetted emitter functioned well as a test emitter to validate the experimental apparatus. The overall results have been summarized in Table 6.4. Uncertainty measurements in the results were derived from the variation in values over multiple tests. Several modifications were made to the emitter to increase the likelihood of emission including new tungsten wire, and PEEK spacers. During emission, local arcing between the tungsten wire and extractor electrode was common and led to some tests ending due to a short circuit. It is recommended that future work develop a new, more reliable test emitter to replace the externally-wetted emitter.

The suppression grids were reliable throughout testing. The total measured beam current during ToF testing was lower than in the full beam tests due to the longer flight path. As expected, results showed that higher suppression voltages led to greater removal of effects caused by secondary electron emission. The results showed that a suppression voltage of -20 V provided the same effect as -30 V. Previous research has shown that at high applied emitter voltages, higher suppression voltages are needed in order to suppress all secondary electrons [229]. A suppression voltage of -30 V was used in all subsequent testing to ensure that secondary electrons were suppressed as much as possible, regardless of the emitter voltage.

The Einzel Lens successfully focused negative beam current. The lens focusing simulation from

Section 5.5.2 estimated that the negative beam current would be optimally focused below -1710 V. The experimental results showed that a focusing voltage of -2000 V more than doubled the beam current from approximately -40 nA to -90 nA. Since the maximum expected current from full beam testing was -100 nA, the negative beam was close to optimally focused. The trends seen in both the focusing simulation and experimental results indicate that applying a voltage greater than -2000 V would likely lead to the optimal beam focusing voltage for the negative current emission.

The Einzel lens results did not have a large effect on focusing the positive beam current. These experimental results indicate that a focusing potential beyond -2000 V would likely be required to optimally focus the positive emission beam. The positive ions have a higher atomic mass, and therefore require a higher voltage to focus them to the desired point. The simulation in section 5.5.2 predicted an optimally focused positive beam below -2120 V. While this could not be experimentally verified, based on the negative beam results the optimal positive beam potential is likely higher than expected.

The Einzel lens results do indicate the expected trends, but were not able to conclusively demonstrate its full functionality. The power supply used for Einzel lens testing was an EMCO USB20N, which has a maximum voltage output of -2000 V. It is possible that using a more powerful voltage source could be used to further characterize the effectiveness of the lens. Since only the negative beam current could be focused using the current set up it was decided that the Einzel lens would not be used during the testing of the multimodal thruster.

The BNG demonstrated the capability of adequately deflecting the beam of charged particles away from the collector. Results showed a trend that as applied gate voltage increased, a larger percentage of beam current was deflected. There was a dichotomy operating the BNG. On one hand, at higher gate voltages (+1750 V), the gate was able to deflect either 100% or near 100% of the emitted beam. However, applying a voltage above +1000 V to the BNG often led to a gate malfunction to occur. The cause of the malfunctions was determined to be a short circuit formed when a high voltage wire came in contact with a grounded wire. Any minor misalignment of the tungsten wires in the gate can cause an imbalance of charge allowing a high voltage wire to be attracted to a grounded wire. When two wires touch, a short circuit is formed, disabling the entire gate. After several gate tests it was determined that using a gate voltage of +1000 V (deflection 70% of positive beam and 20% of negative beam) was a useful compromise between functionality and reliability. After this determination, a gate voltage of +1000 V was used on all subsequent ToF tests for both the externally-wetted emitter and multimodal thruster.

Based on the percentage of beam current deflected from Table 6.3, the BNG was less effective when activated during negative electrospray emission. This could be due to the combination of high positive voltage, +1000 V, and ground applied to the BNG. Biasing the gate's wires using alternating positive and negative polarities, such as +500 V, and -500 V would likely increase performance. Adding a second polarity using the existing set up would require an additional high speed, high voltage switch and negative high voltage power supply.

The externally-wetted emitter ToF tests gave a positive indication that it was capable of differentiating between ion and droplet emission, but not between individual species of ions. In testing after the BNG was deactivated, a negative current spike lasting anywhere from 10 to 20 μs would occur. The various types of ion species are expected to reach the collector within the first 10 μs after the BNG is deactivated. In order to differentiate between ion species these gate transition effects would need to be reduced or eliminated. These transition effects are potentially being caused by a pulse of electromagnetic radiation caused by the sudden high voltage transition at the BNG. One method to negate these effects would be improving the shielding of both the BNG and collector similar to other ToF set ups [229]. Electromagnetic absorbent paint could also be applied to the surfaces around the collector reducing the amount of radiation affecting the collector.

During testing it was determined that the gain setting selected on the FEMTO DHPCA-100 current amplifier had an impact on the transition effects duration. Figure 6.10 shows two experiments where the BNG was operated at two different current amplifier settings. When the amplifier gain setting was set to the maximum 10^7, the gate transition effects lasted for 14 μs. When the amplifier gain setting was set to 10^6 the saturation period was only 5 μs. In tests using amplifier gain setting from 10^2 to 10^5 the transition effects were negligible. Since the externally-wetted emitter only produced 65 nA of beam current, the maximum gain settings of 10^7 was used throughout testing of the externally-wetted emitter. By increasing the beam current reaching the collector, a higher amplifier gain setting could be used to help eliminate the gate transition effects, improving ToF data resolution. This higher current could be achieved by using the Einzel lens or using an electrospray source with a higher current output.
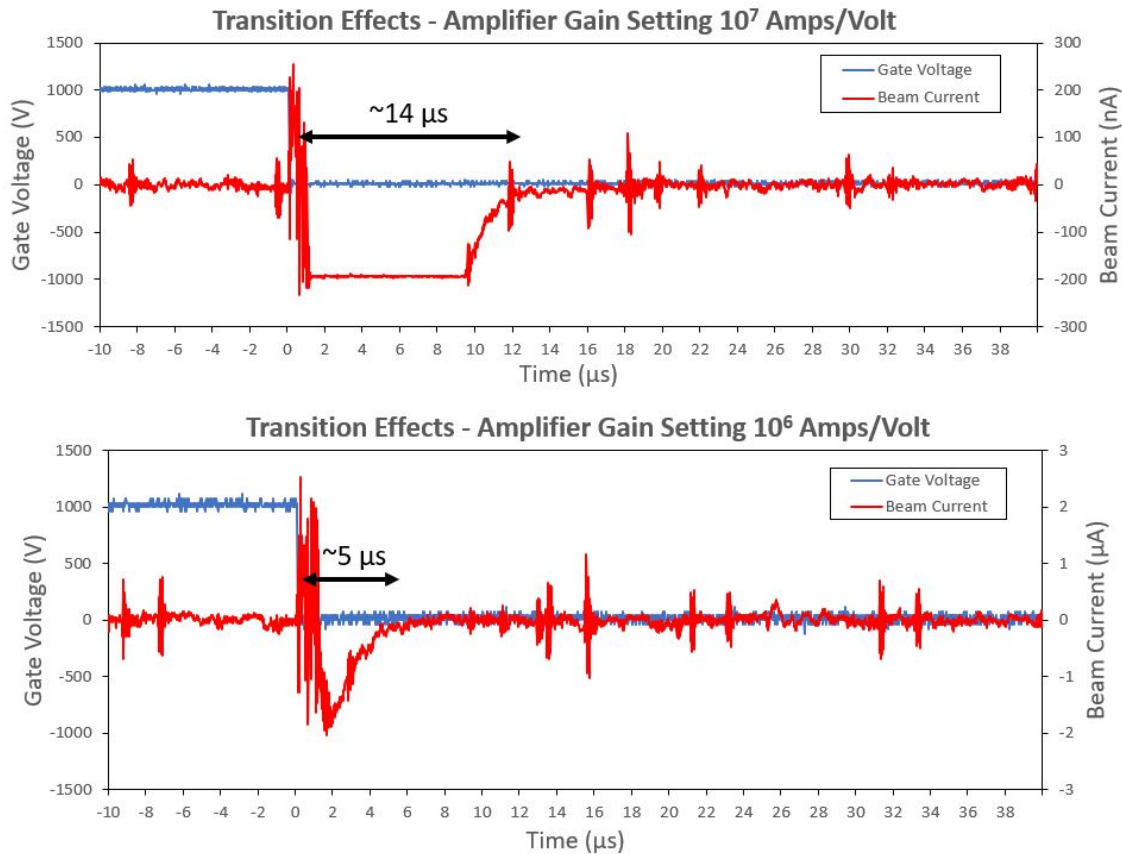
Figure 6.10: Variation in the measurement delay caused by the BNG transition on the FEMTO current amplifier. Higher gain settings show a reduced delay.

Table 6.4: Summary of the various externally-wetted emitter tests. The experimentally measured emission current is compared to the ideal expected current. Trend indicates either an increase or decrease in the measured current caused be the testing conditions.

Externally-Wetted Emitter Summary			
Electrospray Condition	**Measured Emission Current (nA)**	**Trend**	**Ideal Current (nA)**
Full Beam	+200 ±15	→	+120
	-120 ±10	→	-120
ToF Beam	+100 ±10	↘	+60
	-60 ±5	↘	-60
Suppression Grid (-30 V)	+55 ±7	↘	+60
	-60 ±8	→	-60
Einzel Lens (-2000 V)	+20 ±10	↘	+120
	-90 ±12	↗	-120
BNG (+1000 V)	+20 ±4	↘	0
	-50 ±3	↘	0

6.3 Multimodal Thruster Results

The ion and droplet emitters which comprise the multimodal thruster were each tested independently. Data was collected using both the full beam and ToF setups described in Section 5.4, and 5.5. Initial testing led to changes in the thruster's design which will be elaborated upon in the discussion section. Results using this final configuration are presented in this section. Full beam testing of both emitters demonstrated a measured current range in line with expected results. ToF measurements allowed for the distinction of various ion species from the ion mode emitter, and between ions and droplets in the droplet mode emitter. Using data collected from ToF testing, indirect values for the mass flow rate, thrust, and specific impulse were calculated for each of the modes.
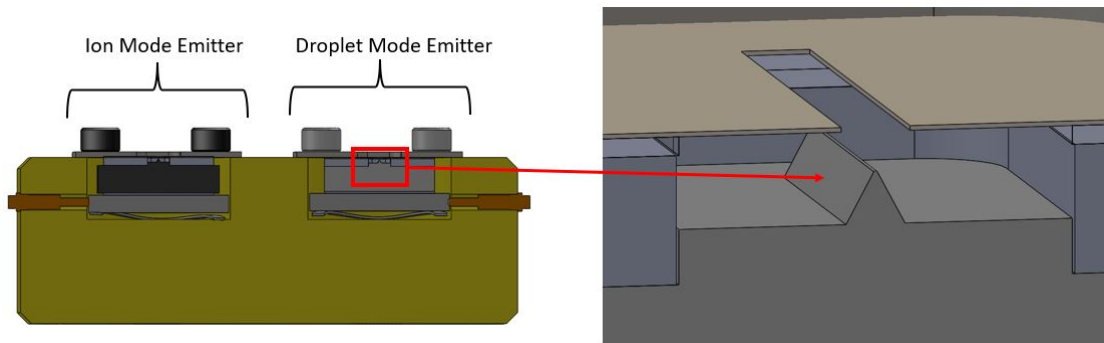
Figure 6.11: Cross-sectional schematic of the designed multimodal thruster.

6.3.1 Ion Mode Emitter Results

6.3.1.1 Full Beam

The ion mode emitter had an average emission onset voltage of 1400 V. A sample unipolar test shown in Figure 6.12 had an onset voltage of 1375 V. In this test, the measured current was around +2.3 μA and -1.85 μA at $\pm$1750 V. As the emitter voltage was increased in increments of 25 V, there was a clear correlation in the measured beam current. This relationship between the current and voltage can be seen in I-V curve from Figure 6.13.
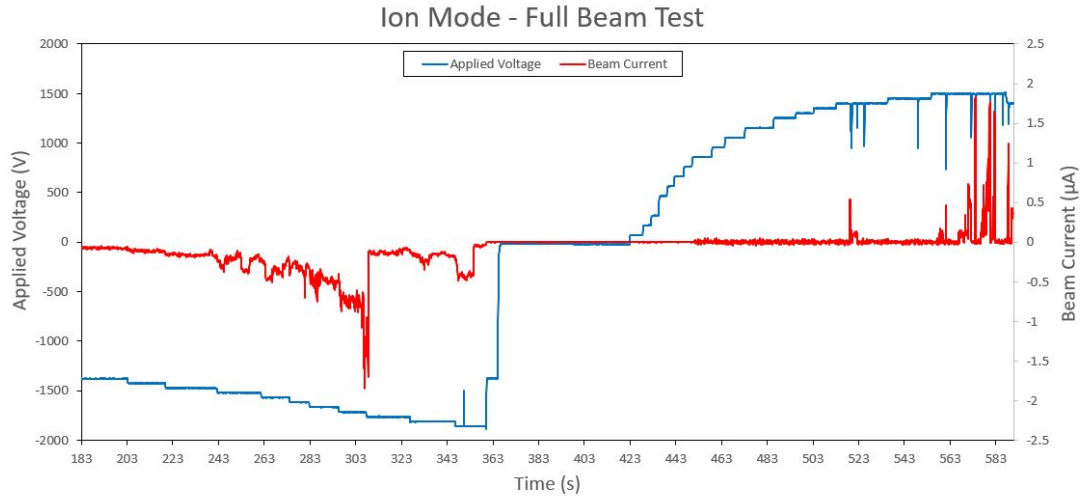
Figure 6.12: Full beam measurement test results for the Ion mode emitter. Presented test results show unipolar application of voltage where positive voltage is first applied then the negative voltage.

6.3.1.2 Time-of-Flight Measurements

Using the ToF experimental setup from Section 5.5, ToF measurements for both positive and negative ion mode emission were collected. Collected oscilloscope data was filtered with GNU radio using the method described in section 6.1.5. The ToF data revealed that the ion mode emitter operated in either the purely-ionic-regime (PIR) or near PIR. Figure 6.14 shows a sample ToF test demonstrating the changes in beam current after the BNG is deactivated. Similar to the externally-wetted emitter there is a negative current spike followed by multiple step increases in current.

From Figure 6.14, two current step increases within the first 10 μs indicate the presence of multiple species of ions. The lack of any noticeable current increases beyond the first 10 μs indicates that there were no heavier charged particles, such as droplets, within the emitted beam. In order to better identify the species of ions present within the first 10 μs, Figure 6.15 focused on a shorter timescale. Based on the flight times of the two current spikes, they were identified as the monomer ion (EMI$^+$), and the dimer ion ((EMI-BF$_4$)EMI$^+$).

The current data from Figure 6.15 was further filtered and normalized in order to determine the percentage of each ion species present in the beam. Normalization converted the total measured beam current value to be equivalent to 1.0 which allowed the beam composition to be more easily identified. To make the data more readable, major current spikes caused by the current amplifier were removed from the data set. Next, a 20 point running average of data points was calculated to
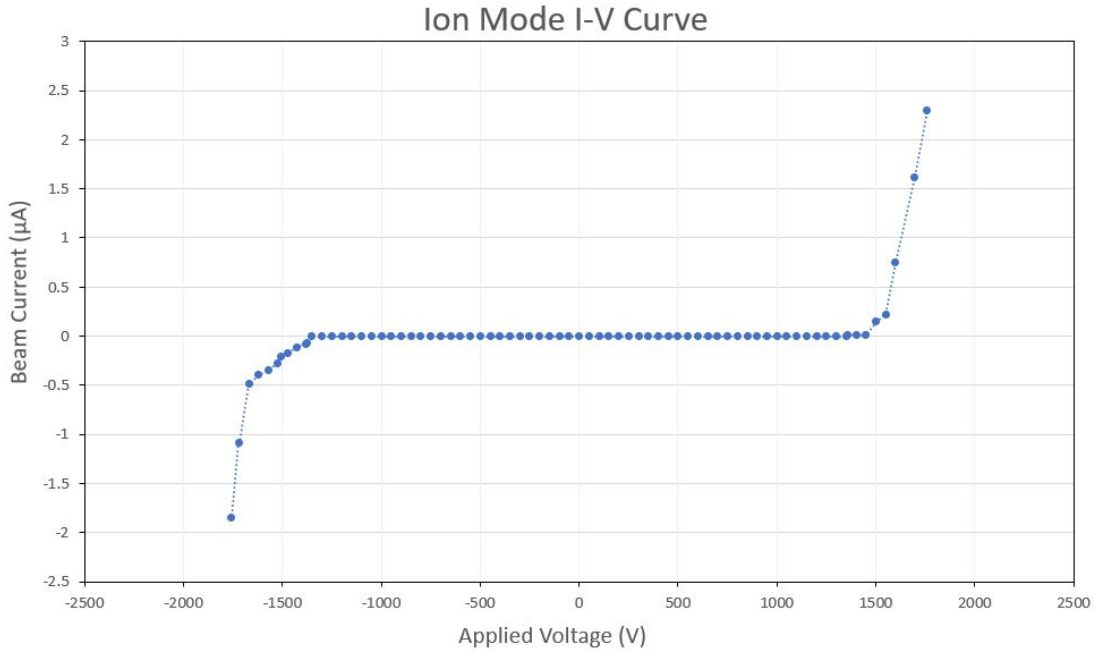
Figure 6.13: Ion mode emitters current to voltage relationship (I-V Curve).

Figure 6.14: Filtered Ion mode ToF results from 0 to 420 μs. The top graph shows the positive polarity results and the bottom graph shows the negative polarity.

Figure 6.15: Filtered Ion mode ToF results from 0 to 80 μs. The top graph shows the positive polarity results and the bottom graph shows the negative polarity.

smooth the results. Finally, the current data was normalized from the point when the BNG was deactivated (t=0). This normalized data is shown in Figure 6.16.

The normalized data determined that around 42% of the beam consisted of monomer ions and 58% were dimers. No larger ions such as trimers or liquid droplets were identified. For the negative beam current ToF, an estimate was made at what ion species were present, but the data was not conclusive.

The flight time and beam composition were used to indirectly determine the mass flow rate, thrust and specific impulse. In order to complete these calculations, several other parameters need to be known. The flight distance was known from the experimental setup. The applied beam voltage and collector current were taken from LabView. As described in Section 2.6, the emitted beam voltage is not the same as the applied voltage. The experimental setup was not capable of measuring beam voltage. The beam voltage was assumed to be equivalent to the applied thruster voltage.

With the known values and assumptions, the mass flow rate, thrust, and specific impulse were indirectly calculated using Equations 2.21, 2.22, and 2.23. For comparison, the theoretical flight times of the ion species were also calculated using Equation 2.20. The thrust of ion mode was determined to be in the range of 0.14 μN, and the specific impulse 4040 s. A summary of the ion mode emitters parameters are shown in Table 6.5.

Figure 6.16: Normalized ToF data. The start of the plot (time = 0) is when the BNG is deactivated. Positive polarity on the top graph shows two distinct currents steps indicating the presence of both monomer and dimer species.

Table 6.5: Summary of calculated performance parameters of ion mode emitter. Values were calculated using data from ToF testing.

Ion Mode Performance Results							
Performance Parameter	Atomic Mass (amu)	Expected Flight Time (μs)	Measured Flight Time (μs)	Beam Compo- sition (%)	Mass Flow Rate ($\mu g/s$)	Thrust (μN)	Specific Impulse (s)
EMI^+	111	5.22	6.1 ±0.1	42 ±10	$7.62 \cdot 10^{-4}$		
$(EMI\text{-}BF_4)EMI^+$	309	8.71	9.2 ±0.5	58 ±10	$2.79 \cdot 10^{-3}$	0.14	4040
$(EMI\text{-}BF_4)_2\ EMI^+$	507	11.16	N/A	0	N/A		
Droplets	N/A	N/A	N/A	0	N/A		
BF_4^-	87	4.62	N/A	0	N/A		
$(EMI\text{-}BF_4)BF_4^-$	285	8.37	8.8 ±0.5	100	$3.52 \cdot 10^{-3}$	N/A	N/A
$(EMI\text{-}BF_4)_2 BF_4^-$	483	10.89	N/A	0	N/A		
Droplets	N/A	N/A	N/A	0	N/A		

6.3.2 Droplet Mode Emitter Results

6.3.2.1 Full Beam

Droplet mode had an onset voltage around ±1375 V. The emitter fired consistently from onset up to 1650 V. After 1650 V, the current output spiked to as high as 80 μA. In the sample droplet mode test seen in Figure 6.17 the emitter had a consistent output of around 0.5 - 1 μA and then jumped to between +20.5 μA and -18.7 μA with current spikes up to -55 μA. Following the spike

in current output, emission would only remain stable from anywhere from 5 to 60 seconds before a short circuit ended the tests. Short circuits during emission were more common in the droplet mode emitter. The trend of applied emitter voltage to output current can be seen in Figure 6.18.
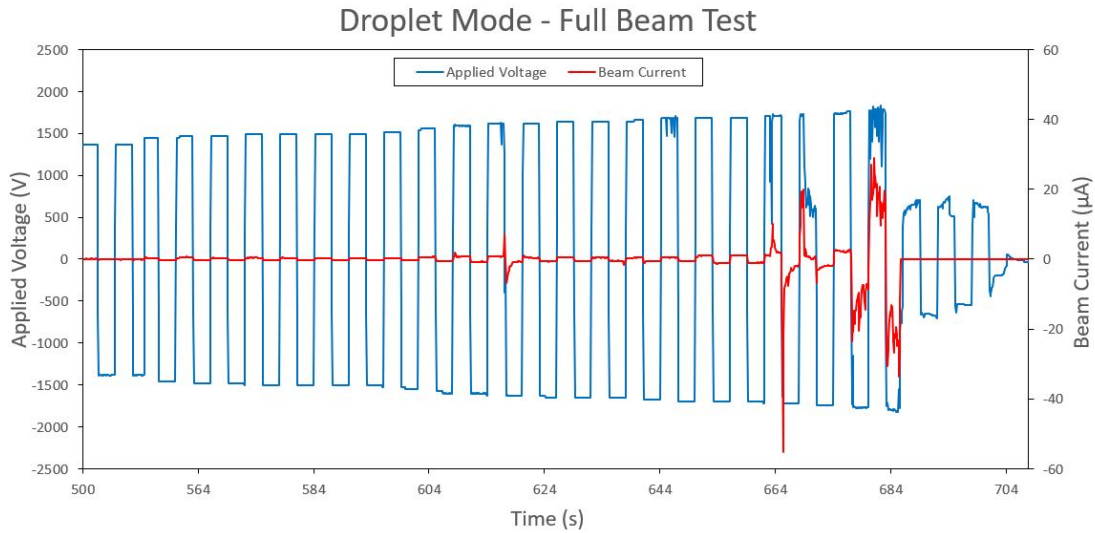
Figure 6.17: Full beam measurement test results for the Droplet mode emitter. Test used bi-polar operation with voltage polarity alternating every 3 seconds.
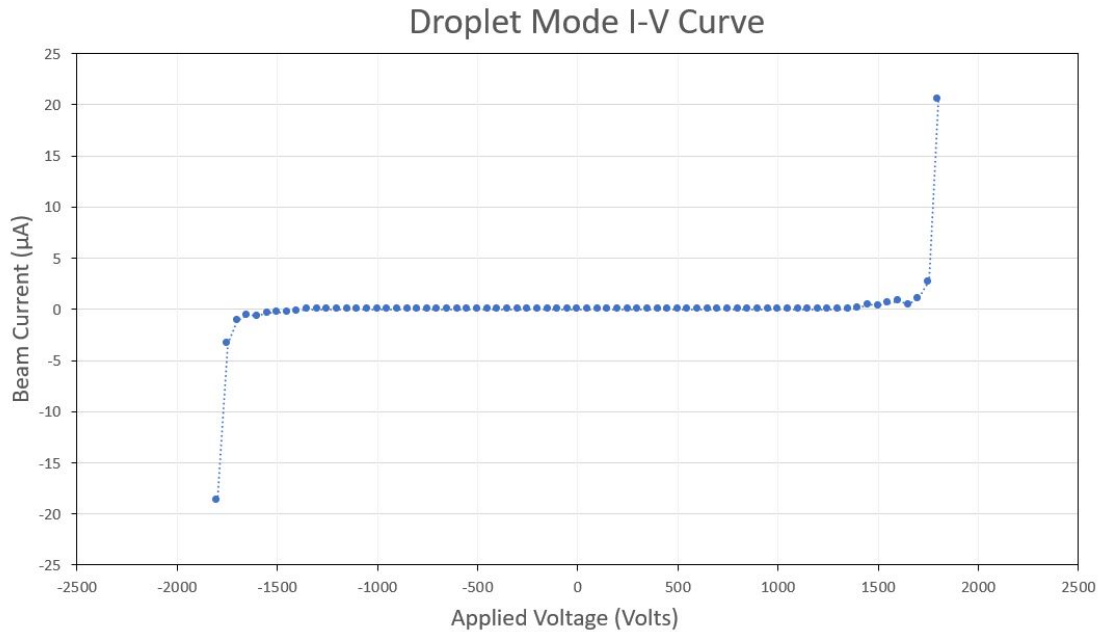
Figure 6.18: Droplet mode emitter's current to voltage relationship (I-V curve).

95

6.3.2.2   Time-of-Flight Measurements

Droplet mode ToF measurements and filtering were performed in the same process described in Section 6.3.1.2. The droplet mode emitter operated in the mixed ion-droplet regime meaning that both ions and liquid droplets were emitted. As with the ion mode emitter, the positive current ToF measurements were more representative of the emitter beam and the negative current results were less conclusive.

The top graph in Figure 6.19 identifies multiple species of ions in the first 10 μs. This is followed by a step current increase at 275 μs indicating the presence of larger charged droplets. In the negative polarity results seen at the bottom of Figure 6.19 it is difficult to identify species of charged particles.
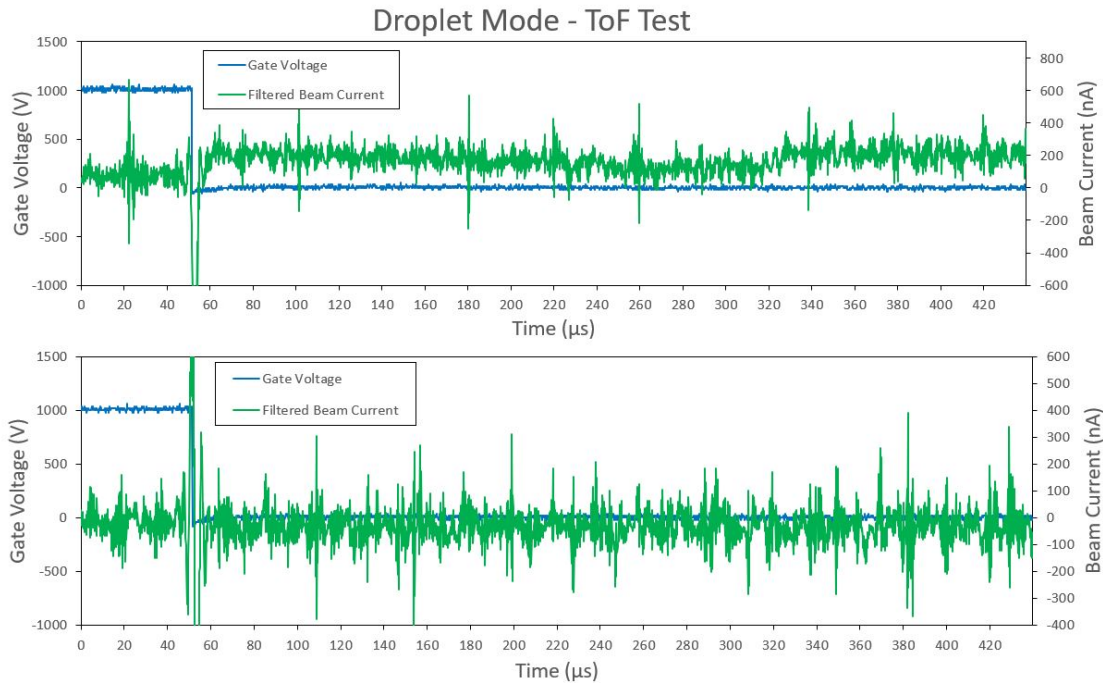
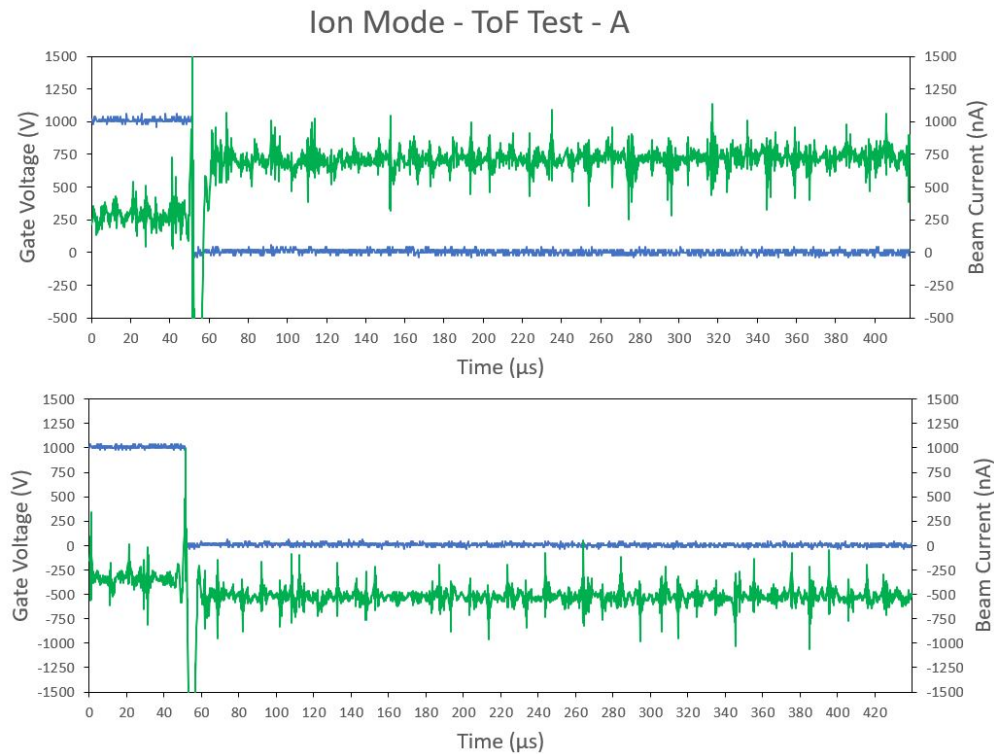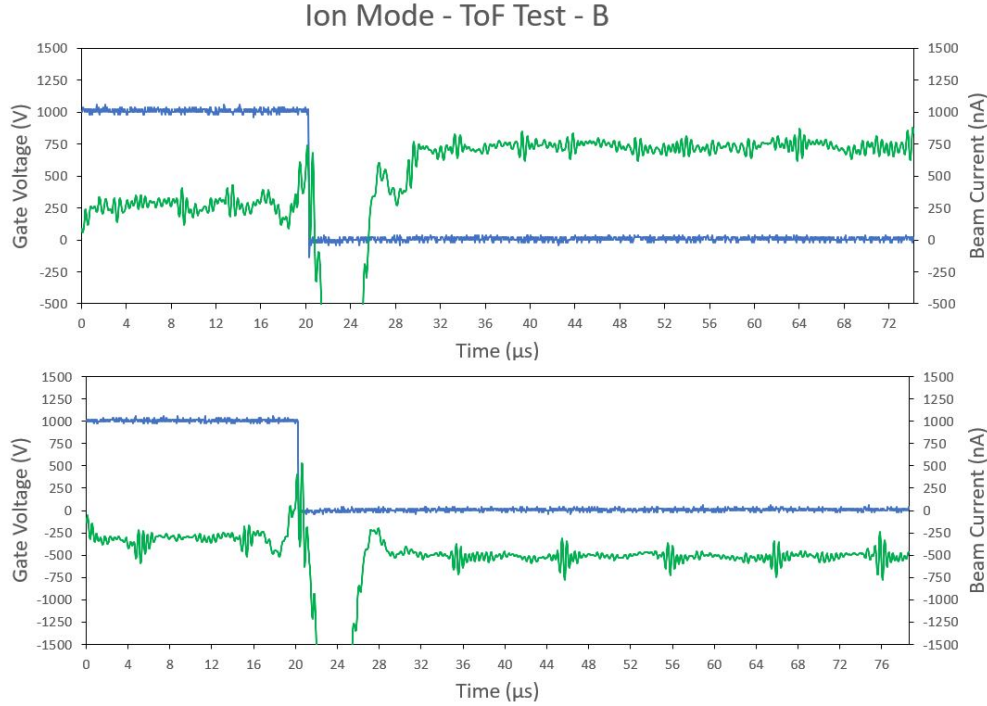Figure 6.19: Filtered droplet mode ToF results from 0 to 450 μs. The top graph shows the positive polarity results and the bottom shows the negative.

To better present the ToF data, the current was normalized in Figure 6.20 starting from the point where the BNG was deactivated (time = 0). In order to show both ion and droplets, the normalized data was presented over 400 μs. Based on the timings of the current step increases, the positive current beam composition consisted of approximately 44% monomer ions, 39% dimer ions, and 17% droplets. As described in Section 6.3.1.2, the ToF data was used to indirectly calculate the emitter's mass flow rate, thrust, and specific impulse. In the positive emission, the thrust was determined to be around 14.5 μN, and specific impulse of 140.6 s. Thrust and specific impulse were not calculated for the negative emission due to inconclusive ToF data. A summary of the measure droplet mode parameters is presented in Table 6.6.
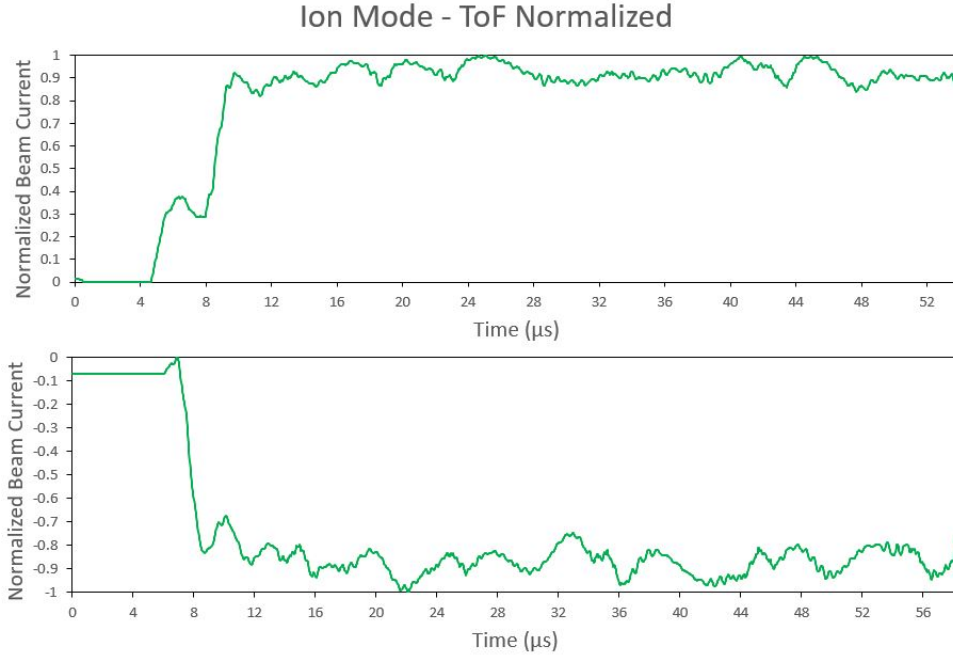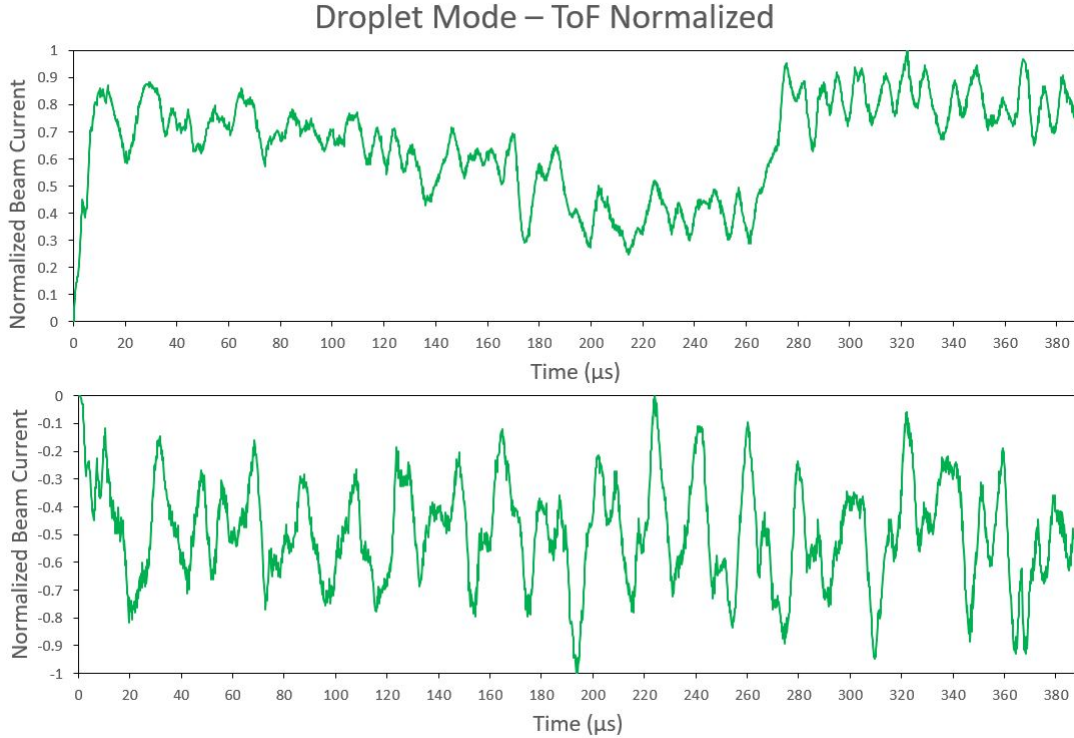
Figure 6.20: Normalized ToF data for the droplet mode emitter. The start of the plot (time = 0) is when the BNG is deactivated. Positive polarity on the top graph shows a current jump around 300 μs indicating the presence of droplets. No significant trend was inferred from the negative polarity results on the bottom graph.

Table 6.6: Summary of calculated performance parameters of droplet mode emitter. Values were calculated using data from ToF testing. *Droplet mass was calculated using ToF measurement. The atomic mass of ions was known.

Droplet Mode Performance Results							
Performance Parameter	Atomic Mass (amu)	Expected Flight Time (μs)	Measured Flight Time (μs)	Beam Composition (%)	Mass Flow Rate ($\mu g/s$)	Thrust (μN)	Specific Impulse (s)
EMI^+	111	5.47	3.4 $\pm$0.6	44 $\pm$6	0.0103		
$(EMI\text{-}BF_4)EMI^+$	309	9.12	9.4 $\pm$1.2	39 $\pm$6	0.025	14.5	140.6
$(EMI\text{-}BF_4)_2\ EMI^+$	507	N/A	N/A	0	N/A		
$Droplets$	281,033*	N/A	275 $\pm$2	17 $\pm$10	10.464		
BF_4^-	87	4.84	4.2 $\pm$0.8	27 $\pm$5	0.004		
$(EMI\text{-}BF_4)BF_4^-$	285	8.67	19.6 $\pm$1	73 $\pm$5	0.041	N/A	N/A
$(EMI\text{-}BF_4)_2BF_4^-$	483	11.40	N/A	0	N/A		
$Droplets$	N/A	N/A	N/A	0	N/A		

6.4 Multimodal Testing Discussion and Recommendations

The multimodal thruster demonstrated how a high thrust droplet mode, and high efficiency ion mode could be combined using porous electrospray emitters. The prototype thruster used two porous wedge emitters as a proof-of-concept design. Uncertainty measurements in the results were derived from the variation in values over multiple tests. The indirectly calculated values of mass flow rate, thrust, and specific impulse for each emitter are estimates of performance not exact values. For space flight, a thruster needs to demonstrate that it can operate for tens of thousands of hours without a significant loss in performance. Some preliminary lifetime testing of both emitters was conducted. The emitters were tested for a maximum of one hour at a time. The ion mode emitter was able to reach one hour of emission on multiple occasions in both the full beam and ToF configurations without a significant drop in performance. In tests where one hour was not reached the reason for failure was short circuiting within the thruster. The droplet mode emitter seemed to operate in two forms of emission. At lower voltages around emission onset, the output current was stable for extended periods of time. When the applied voltage was increased, there was a large jump in the current output. This spike in current is hypothesized to be a transition between predominately ion to predominately droplet emission. When the droplet mode emitter entered this high current output regime, emission only lasted from ten seconds to one minute. This behaviour was repeated during testing and made it difficult to collect large samples of data. Future research should perform additional investigations on the endurance of electrospray emitters.

6.4.1 Ion mode Discussion

Full beam testing of the ion mode emitter had a measured current range of approximately ± 2 μA. This was close to the ESPET predicted value (3.68 μA) from section 4.4. The indirectly calculated thrust (0.14 μN) was very close to the value predicted by ESPET (0.33 μN). Interestingly, the calculated specific impulse (4040 s) was more than double the value predicted by ESPET (1865 s). This can be attributed, in part, to the lower mass flow rate and that ESPET predicted the ion emitter would operate in the mixed ion-droplet regime instead of the experimentally demonstrated PIR. This lower flow rate can be attributed to the inefficiency of the porous wedge emitters. ESPET predicts a consistent number of emission sites based on the length of the emitter. A recent study of porous wedge emitters has shown that emission sites are not necessarily evenly distributed. During operation, the number of sites can be unpredictable and dependant on the applied voltage [242]. Although this was not experimentally verified, it is likely that the ion mode wedge emitter had fewer than expected emission sites, leading to a lower total mass flow rate and thrust.

Results indicated that the ion mode emitter operated in the expected PIR. The beam composition of the ion mode was determined to consist of around 42% monomers and 58% dimers with no droplets identified. The beam composition percentage was derived from the amount of beam current measured at the collector for each species of particle. The results are in line with previous ToF testing using purely ionic electrosprays with EMI-BF$_4$ propellant [243, 42, 128]. While the result indicates the PIR, there is a possibility that the emitter was operating in the mixed ion-droplet regime comprised of predominated ions. As previously mentioned, the BNG was only operationally capable of deflecting around 70% of positive current emission. The remaining 30% not deflected could potentially include larger ion species and liquid droplets. Throughout the analysis and calculation of ion emitter parameters, the assumption was made that the total particle beam was comprised of only monomer and dimer ions.

The carbon xerogel samples produced in-house performed well as the ion mode emitter substrate. The fabrication of the carbon xerogel samples was a time-consuming process. It took four attempts

to achieve the final batch presented in Section 4.2.6. While not requiring many hours of labour in the lab, each batch took approximately two and half weeks to synthesize and cure. The first three attempts ended up producing a substrate which was not noticeably porous. Several minor changes to the xerogel fabrication process were made including letting the initial solution gel for a longer period of time, including an acetone bath prior to pyrolysis and proper use of air-tight containers, contributed to the final xerogel run being successful. The targeted average pore size for the substrate was in the range of 500-700 nm. The final batch used for the ion mode emitters had an average measured pore size of 1.204 μm as seen in Figure 4.11. Even though this result was double the anticipated pore size, this batch was used in emitter fabrication, since the pore size was considered sufficient to achieve purely ionic emission. The laser ablation of the ion mode emitters worked well, forming the desired wedge emitter with an emitter apex radius of curvature of 10 microns. The emitters themselves were quite delicate. Two of the three fabricated emitters were destroyed by minor abrasions during thruster assembly. When the xerogel samples went through the drying process, the edges of the samples became warped as seen in Figure 4.7. The warped surfaces made it challenging to produce surfaces which were perfectly flat and level. Sanding the substrates to produce a flat surface after the emitters had been laser ablated was a challenging process and other options should be explored in the future.

6.4.2 Droplet mode Discussion

The full beam current measurements of the droplet mode emitter (20 - 80 μA) were several magnitudes lower than the values predicted using ESPET (275 μA). From the ToF testing, the measured thrust (14.5 μN) and mass flow rate (10.5 μg/s) were also a magnitude lower than the expected values (543 μN, 448 μg/s). The measured specific impulse of 140.6 s which was close to the expected value, demonstrates the short comings of the droplet mode emitter. Other forms of propulsion such as cold-gas thrusters [244] and resistojets [245] reliably produce thrust in the mN range with a comparable specific impulse to the droplet mode emitter. In its current state the droplet mode emitter could be considered a low thrust, and low efficiency form of propulsion. Even with lower-than-expected performance, the droplet mode emitter is part of an integrated multimodal system, using the same propellant as the ion mode emitter. This makes the droplet mode emitter one part of a more versatile system, instead of a stand alone form of propulsion. If the expected thrust levels were achieved, it would improve the system's viability. Two potential reasons for measured thrust being lower than expected are measurements being taken in the stable emission regime and the lack of uniformity of the droplet substrate emitter tip.

During full beam testing the droplet mode emitter operated in either a stable low current regime or an unstable high current regime. Due to the short duration and unreliability of the high current regime, ToF measurements were taken during the more stable, low current regime. This can be seen in Figures 6.14 and 6.19, where ToF data shows ion mode current measurement being three times larger than the droplet mode emission. The total current measured at the collector during droplet ToF testing was on the order of 250 nA. This value was much lower than expected. It likely indicates that droplet mode ToF readings were taken during the consistent emission regime identified in the full beam measurements, and not during the high current regime. It was expected that the droplet mode emitter would either emit purely droplets or predominately droplets. The ToF results indicated an emission comprised of around 83% ions and 17% droplets. If the ToF measurements had been taken in the high current regime, it is likely that the beam composition would be more heavily weighted with droplets. The dramatic increase of current and prevalence of short circuits occurring indicate that emission with a higher proportion of droplets was occurring. If this was the case, then the actual thrust being produced during the high current regime may

have been closer to the expected range.

Producing uniform porous wedge emitters from the P3 borosilicate glass was more challenging compared to the carbon xerogel. The glass was chosen because its larger pore sizes would allow for an increased propellant flow rate. These larger pores, as seen in Figure 4.10, also made it difficult to produce a uniform emitter apex radius of curvature of 10 μm. This lack of uniformity likely lead to fewer than expected emission sites along the edge of the emitter. This can be somewhat confirmed by post-test imaging, which revealed brown EMI-BF$_4$ residue on small portions of the emitter's surface.

An additional reason for the variance between the theoretical and experimental results could be the limitations of the experimental set up. The full beam and ToF setups were operated independently. This meant that a single test could not collect both the full beam data and ToF measurements. In order to switch between full beam and ToF tests, high vacuum was removed and several components had to changed before re-pressurizing the vacuum chamber. As a result, a general assumption throughout this work was that both the ion and droplet mode emitters operated the same in both the full beam and ToF tests. In reality, there may have been variation in the emission characteristics between tests, which is a point of uncertainty and could have contributed to the variance in results.

6.4.3   Testing and Challenges

In the initial stage of testing both the ion and droplet mode emitters did not produce the expected emission. It was determined that two primary causes were poor alignment between the emitter and extractor electrode, and the high frequency of short circuits ending tests. It took several thruster design, assembly procedure, and experimental setup changes before the emitters produced emission more consistently. The short circuits were in most cases caused by excess propellant creating a bridge between the high voltage emitter and the grounded extractor. Short circuits during emission were more common in the droplet mode emitter.

The multimodal thruster was designed to have the emitter and extractor automatically aligned using a platform on the emitter fitting into a rectangular shaped hole in the PEEK spacer. In reality, the manufacturing of these components was not precise enough to ensure proper alignment. As a response, the two components were aligned by hand using a light microscope. While this ensured that the emitter and extractor were properly aligned it also introduced an additional source of error between tests and was a time-consuming process. Once the alignment was being done manually, the alignment platform on the electrospray emitters became a hindrance and was carefully removed.

Several design changes were revised during testing, in order to reduce failures caused by electrical short circuiting. The first design change was the addition of a PEEK washer situated between porous reservoir and PEEK spacer. The diameter of the reservoir was slightly larger than the electrospray emitters. The gap caused by this difference could have created a path for excess propellant to cause short circuiting. The PEEK washer was used to fill this gap and prevent propellant from migrating away from the reservoir. Another potential reason that emission of the thruster was inconsistent could have been caused by corner effects caused by the extractor electrode. When the edge of the rectangular extractor slit is too close to the edge of the electrospray emitter, the increased electric field can create unpredictable behaviour. The original design only extended the extractor slit 0.5 mm beyond the edge of the electrospray emitter. During testing, it was determined that the extractor slit could be extended with minimal effort and would remove any ambiguity of potential corner effect impacting emission.

Experimental procedures were also adapted, in an attempt to reduce the prevalence of short circuits. To reduce the likelihood that excess propellant would be transported inside the thruster,

special care was taken during assembly that the exterior of emitters and reservoirs were properly dried and also other components were cleaned to remove any excess propellant. After assembly, an additional connection check was performed to ensure that potential short circuits could be detected prior to putting the thruster into the vacuum chamber. Finally, one procedural change which seemingly made a big difference in emission reliability was the inversion of the ToF set up. Initially the ToF setup had the multimodal thruster oriented downward towards the earth. It may intuitively seem that gravity would aid in propellant transport within the thruster, but in reality gravity was likely causing excess propellant to more easily form short circuits between the emitter and extractor. Once the ToF setup was flipped upside-down, with the multimodal thruster oriented upward, emission was more reliably achieved.

6.4.4 Design Considerations

One aspect of the multimodal thruster design which should be revised in future iterations is the physical connection between the emitter and extractor electrode. In the current design these two components were separated by a PEEK spacer. The PEEK was likely promoting the transfer of excess propellant which was causing the short circuits. In several other electrospray thruster designs the extractor electrode is positioned above the emitters with no physical connections between the two. Future designs should take this into consideration.

Emitter alignment was also a challenge with the current design. Any future thruster designs having alignment controlled by well fitting components should take extra care in the tolerance of parts, and accuracy of the manufacturing process used. Future designs could also incorporate an in-situ alignment system, such as the AFET-2 thruster produced by the Air Force Research Laboratory [170].

The multimodal thruster did not include an integrated propellant feed system. While the same propellant was used for both emitters, both had independent reservoirs. To have a true multimodal system, a common reservoir able to distribute propellant to either type of emitter will have to be developed. Research has been done on pressurized propellant feed systems [179], though ideally the propellant would be passively drawn with any pressurized components.

6.5 Concluding Remarks

A novel multimodal thruster using two types of porous electrospray emitters has been designed, manufactured and tested. A custom full beam and ToF experimental setup were developed to test the thruster. A single externally-wetted emitter was used for preliminary testing. The suppression grid performed as expected, eliminating the impact of secondary electrons emission from the results. The Einzel lens was capable of more than doubling the measured negative beam current. To produce a similar focusing effect on the positive beam current would require a more powerful high voltage source. The BNG successfully demonstrated the capability of deflecting a beam of charged particles away from the collector. At higher applied gate voltages, 100% of beam current was deflected away from the collector. These higher gate voltages also led to a high frequency of gate failure, caused by short circuiting between two of the gate's wires. A gate voltage of +1000 V capable of deflecting a majority of the emitted beam without failure was used throughout ToF testing. The externally-wetted emitter was used to test the ToF system. Results from these tests were inconclusive due to the low current emitted from the single emitter.

Results demonstrated the concept of the combination of a high efficiency ion mode emitter combined with a high thrust droplet mode emitter using a common propellant within a unified multimodal system. The ion and droplet mode emitters which comprised the multimodal thruster

were independently tested. The ion mode emitter produced results close to the theoretically predicated values. The ion emitter had a calculated thrust of 0.14 μN and specific impulse of 4040 s. ToF measurements indicated the emitter was operating in the PIR, with a beam composition of around 42% monomer and 58% dimer ions. The droplet mode emitter had a calculated thrust of 14.5 μN and specific impulse of 140.6 s. ToF results indicated the emitter was operating in the mixed ion-droplet regime with a beam composition of around 44% monomer ions, 39% dimer ions, and 17% droplets. The thrust and droplet percentages were lower than expected. This could be attributed to the ToF results being taken during the steadier low current emission of the droplet emitter and the roughness of the emitter's apex.

7 Concluding Remarks and Future Work

This thesis investigated the potential utility of a multimodal electrospray thruster to provide propulsion for small spacecraft. The thruster combined different types of porous electrospray emitters using a single unified room temperature ionic liquid (IL) propellant. One emitter was designed to operate in an efficient ion mode emission and the other was designed to provide high thrust by emitting liquid droplets. Combining high thrust with high efficiency would allow small spacecraft greater mission capability and flexibility. Using a single IL propellant between both modes of operation provides weight and space savings. Electrospray emitters come in three main types: capillary, externally-wetted, and porous. Using porous electrospray emitters removed the need for a pressurized system and removed the need for any kind of ionization or neutralization process.

In order to conduct testing on the experimental thruster, two custom apparatus setups were used. A full beam measurement setup, consisting of a beam collector and suppression grids, was used to measure the entire current emitted by a full electrospray beam. The beam collector was an electrically isolated, metallic plate connected to a high speed current amplifier. The suppression grids were made of 0.025mm diameter tungsten wire interleaved through a PEEK frame. Applying a suppression voltage of -30 V to the grids reliably eliminated experimental measurement offsets caused by secondary electron emission. A separate time-of-flight (ToF) setup consisted of a Bradbury-Nielsen Gate (BNG), Einzel lens, and the same collector and suppression grids from the full beam setup. The asymmetric Einzel lens consisted of three steel electrodes aligned and spaced using a PEEK frame. The lens demonstrated the ability to focus an electrospray beam. The lens was capable of more than double the beam current could be measured at the collector when the lens was activated. The BNG was constructed from two sets of electrically isolated 0.025 mm diameter tungsten wire strung through a PEEK frame. The gate was capable of deflecting approximately 70% of the emitted electrospray beam and allowed for the flight time measurement of various emitted particle species. The ToF setup was successfully used to indirectly determine the thrust and specific impulse of the tested multimodal electrospray thruster.

The multimodal thruster was comprised of two porous wedge electrospray emitters. Each emitter had a height of 0.3 mm, length of 4 mm, and an apex curvature radius of 10 μm. Laser ablation was used to mill the emitters over a series of 25 passes. Both emitters were in contact with a porous stainless steel distal electrode / propellant reservoir. The ion mode emitter was made using in-house produced carbon xerogel which had a mean pore size of 1.2 microns. The carbon xerogel emitter operated in the purely ionic regime producing a beam comprised of approximately 42% monomer ions and 58% dimer ions. The ion mode emitter produced a calculated thrust of 0.14 μN and specific impulse of 4040 s. The droplet mode emitter was made from a porous P3 borosilicate glass which had a mean pore size of 40 microns. The glass emitter operated in the mixed ion/droplet regime producing a beam comprised of approximately 83% ions and 17% liquid droplets. The glass

emitter produced a calculated thrust of 14.5 μN and a specific impulse of 140.59 s. The two emitters have demonstrated that both a high efficiency and high thrust porous electrospray can be formed into a multimodal system. The measured thrust force was lower than expected for both emitters. The droplet mode emitter also produced a lower composition of emitted droplets than expected. This could be attributed to an inconsistent number of emission sites, the roughness of the droplet emitter apex, and the variance between full beam and ToF testing. If this proof-of-concept thruster was refined and scaled up using larger emitter arrays, it could function as an effective multipurpose propulsion system for satellites operating in low earth orbit.

The electrospray thruster was operated using a custom in house bi-polar, voltage switching circuit. Two high voltage sources were fed into a custom PCB circuit board. The circuit used two high voltage optocouplers to alternate the output voltage polarity every three seconds. Polarity switching reduced electrochemical effects within the prototype electrospray thrusters and eliminated the need for a neutralizer. The voltage and current at the electrospray emitter was measured using a voltage divider and shunt resistor on a second circuit board. The BNG was quickly activated and deactivated using a high speed, high voltage Behlke switch. Experimental control and data acquisition was handled using a custom LabView virtual instrument. The operational setup allowed for the control signal measurement of output signals for all key testing apparatus and thruster outputs.

The computational fluid dynamics (CFD) simulation was developed to predict the behaviour of a single electrospray conejet emitter and droplet formation. The simulation was capable of replicating the general behaviour of electrospray droplet emission. Improving the electrospray to incorporate electrospray beam spreading, accurate Taylor Cone shape and formation, and expected ejection velocity would allow for a more realistic simulation.

7.1 Future Work and Recommendations

Future iterations of the multimodal electrospray thruster should incorporate lessons learned from this work including improvements to the design of the emitters, ToF system, and the addition of new diagnostic test equipment. Future designs could also incorporate arrays of many ion and droplet mode emitters to increase the thrust density of each mode. While effective, laser ablation was an involved, time consuming and costly emitter fabrication method. Testing additional methods of fabricating emitters, such as using common CNC machines with small drill bits and tabletop CNC machines, may produce desirable results in a shorter period of time. The multimodal thruster focused on the individual electrospray emitters. To simplify testing both emitters were isolated, each having their own extractor electrode and propellant reservoir. A truly multimodal system will require a unified propellant reservoir, with some kind of feed system, to send propellant to different emitters as required. Ideally this feed system would be passive and not require any pressurized gas components. Developing a power processing unit (PPU) which is capable of operation within a small satellite will be critical to building a complete propulsion system.

A new test electrospray emitter should be developed to replace the externally-wetted emitter. The test emitter should have a more static emitter and include more robust emitter alignment and extractor electrode control. The externally-wetted emitter used for preliminary testing in this work was unreliable, was prone to local arcing, and required manual alignment of the tungsten wire emitter. A new more robust emitter would greatly improve testing efficiency.

One recommendation is to build and design an electrospray specific diagnostic system from the ground up. The new set up should include a large collector using for full electrospray beam analysis, a long flight path used to take ToF measurements, and a retarding potential analyzer

(RPA). Several designs incorporating all three can be found in literature. The current experimental capabilities include a torsional thrust balance, full beam, and ToF measurement. Each of these three systems operate independently from one another and cannot be used at the same time. When testing electrospray thrusters using the current set up, needing to perform multiple different tests leads to potential error from variation in electrospray emission. Having all required measurement apparatus integrated into a single system would reduce error, and greatly improve on the efficiency of experimental testing. The new design could incorporate a stepper motor to allow for *in situ* manipulation, allowing for many types of measurement to occur in a single test. A schematic giving an overview of this new system can be seen in Figure 7.1.
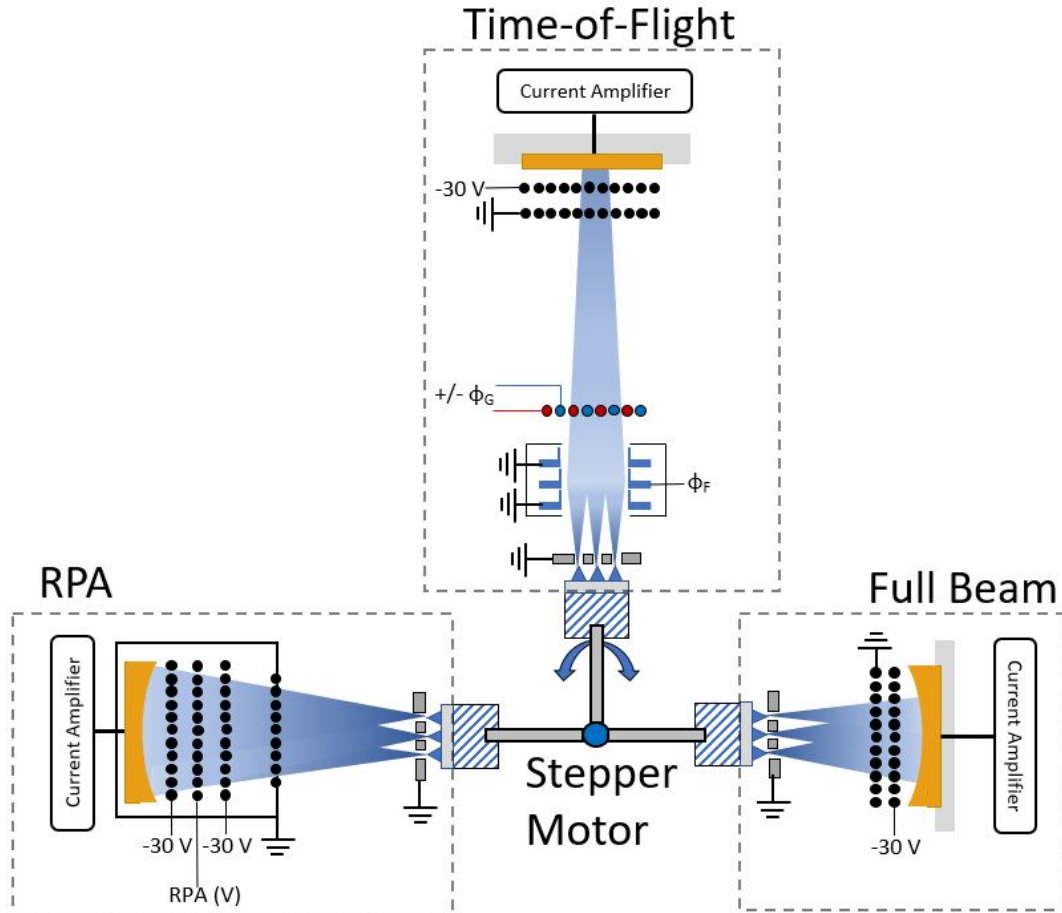
Figure 7.1: Design of future electrospray focused testing apparatus. The setup would allow for full beam, time-of-flight, and RPA measurements to be taken during a single test.

Using more powerful laboratory equipment in the next phase of research could enhance the utility of the current testing apparatus. A more powerful, high voltage source would improve the capability of the designed Einzel lens. The BNG could be improved with the addition of a second high voltage source and Behlke switch. This would allow for bipolar operation of the gate, which would improve the gates deflection capability in both polarities. The current diameter of tungsten wire has led to the testing equipment being very delicate and prone to failure. Using wire with a larger diameter could reduce short circuits during testing and make components more robust.

The trade-off of a higher percentage of the electrospray beam being blocked by the gate would be overshadowed by the capability to consistently deflect 100% of the beam. The EMCO H60 power supplies used to operate the electrospray thrusters are currently limited to a maximum output of +/-3000 V by the custom PCB circuit boards. A new bipolar circuit board should be designed, with high voltage in mind, allowing for applied emitter voltages up to +/-6000 V.

The CFD simulation could be further improved to create more realistic Taylor Cone formation and droplet formation. Future work should also investigate developing models to simulate ion electrospray emission. Since the mechanisms behind ion emission are not fully understood, a new model could be an effective method to improve understanding of the physics involved. Eventually a model combining a CFD simulation for liquid droplets and an ion simulation method such as molecular dynamics could be combined into a holistic electrospray simulator.

In the longer term, a more robust stainless steel chamber vacuum chamber capable of ultra high vacuum pressures should be used in testing. The chamber could use multiple turbo-molecular pumps or cryo-pumps to achieve vacuum. The high vacuum levels reduce the likelihood of local arcing which have been shown to lead to short circuits.

Appendices

A Carbon Xerogel Fabrication

The silicon elastomer mold was produced by adding the Sylgard elastomer kit and PDMS-b-PEO components to a 1L beaker and stirred manually using a stainless steel stirring rod. This mixture was then added to an aluminum mold fabricated at the RMC machine shop.

The resorcinol formaldehyde (RF) solution components was added to a 50ml round bottom flask. Mixing was performed using a magnetic stirring bar controlled by a Corning Pyroceram Hot plate stirrer at max rpm (1,150). A rubber stopper was used to prevent evaporation during mixing.

The RF solution in the silicon molds were placed in an airtight plastic container. The sealed containers were used in the curing process, and part of the drying process. A Thermo Scientific Thermolyne Furnace Model: F6000 was used as the low temperature oven for the carbon xerogel curing / drying process. The oven was non-programmable, so changes in temperature had to be manually set at the correct timings.
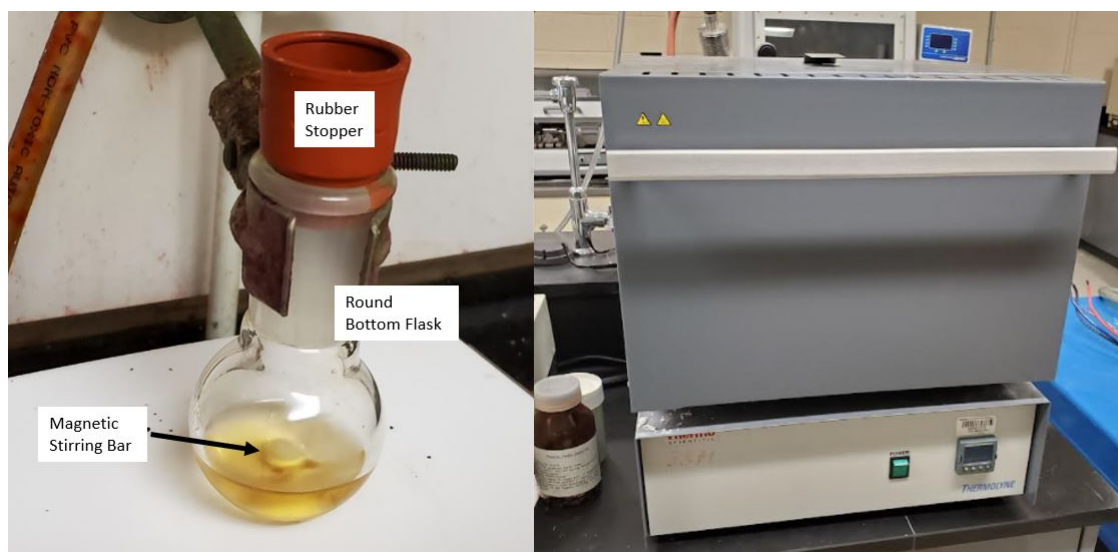
Figure A.1: LHS shows the lab equipment used to create the RF xerogel sol solution. RHS is the furnace used for low temperature curing/drying

In the initial attempts to pyrolize the samples, a Thermo Scientific Series 1269 high temperature tube furnace was used. The furnace was programmed to slowly increase to a maximum temperature of 900°C for 3 hours and then slowly cool down to room temperature. After several failed pyrolysis attempts, cracks in the tube furnace's ceramic tube were discovered. The cracks allowed air into the furnace causing the sample to combust and be destroyed. The second pyrolysis set up used a smaller LECO TF-1 tube furnace seen in Figure A.2. During high temperature operation, the samples were kept in an argon environment which was supplied from a pressurized tank of pure

argon from ALPHAGAZ supplied by Air Liquide. The flow of Argon was initially controlled using a Harris model 52 multistage gas regulator. Since the required Argon flow rate was lower than could be accurately measured by the regulator, a flow meter capable of measuring flow from 0 - 500 standard cubic centimeters per minute (SCCM) was used. 450 SCCM of argon was inserted to the samples in one end of the enclosed tube, and the opposite end was connected to a ventilation hood in the lab.

Figure A.2: Overview of the lab equipment used to pyrolize the carbon xerogel samples.
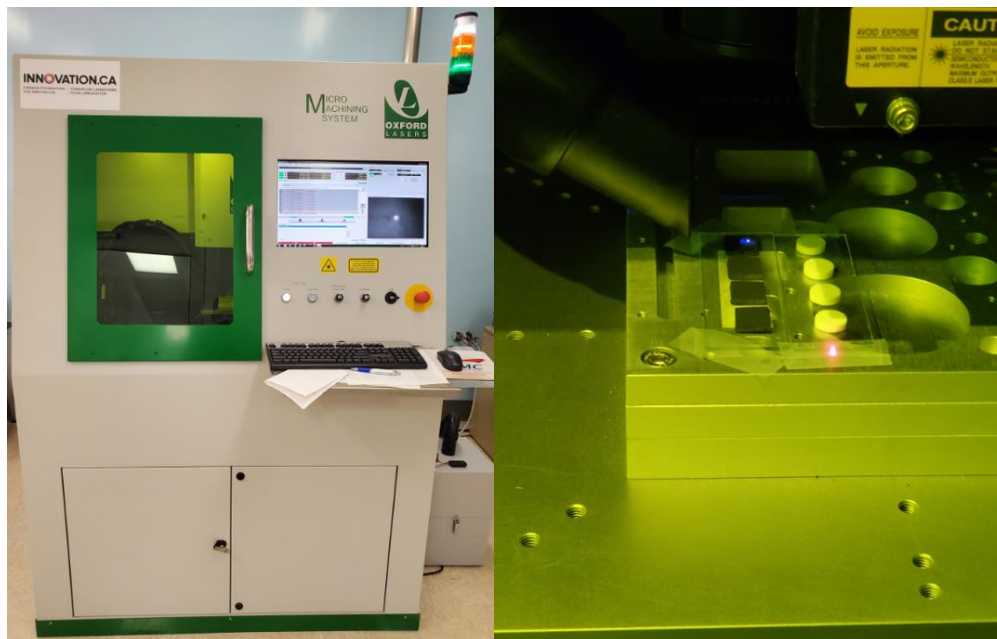
Figure A.3: The Oxford series A picosecond laser in use producing the electrospray emitters.

B Electrospray Operation System

B.1 Overview of Power Circuits

The circuitry, power supply, and data acquisition components used to operate the electrospray thrusters and the associated testing apparatus are detailed in this appendix. A general overview of the components and power supplies used can be seen in Figure B.1 below.
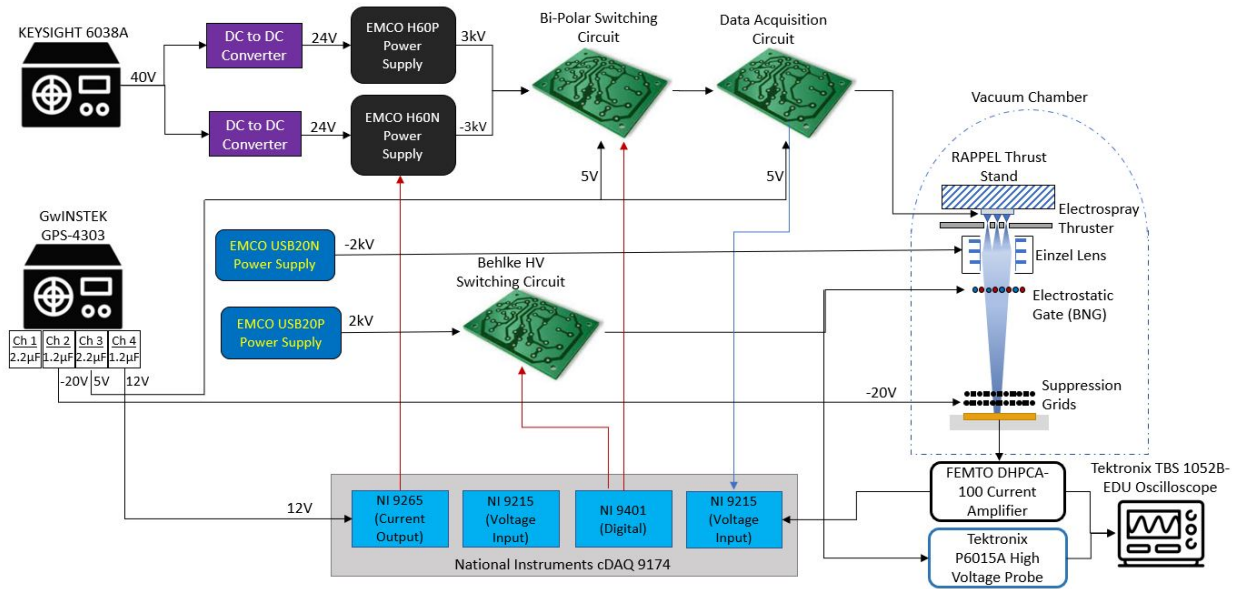
Figure B.1: Overview of the power supplies and circuitry used to test electrospray thrusters.

In addition to the electrospray source, there were also several components in the ToF diagnostic system which required power supplies. Two EMCO H60s, two EMCO USB20, a Keysight 6038A, and multiple channels on the GPS-4303 are used to power components in the system. To reduce noise produced by the GPS-4303 power supply, capacitors (1.2μF-2.2μF) were placed in parallel with each output channel.

B.2 Circuit Boards

RAPPEL utilizes several custom-made printed circuit boards (PCBs) to test and monitor various electrospray source emissions. The original design and fabrication of these PCBs were performed in previous work at RAPPEL [238]. During this work, several of the circuit boards were upgraded with

new components and functionality. This section will elaborate on the various circuitry elements and control systems for each of the PCB circuit boards.

B.2.1 High Voltage Bipolar Switch

One of the main advantages of electrospray thrusters is their ability to produce a quasi-neutral particle beam through bipolar operation. Bipolar refers to rapidly switching between positive and negative voltages so that both polarities of particles are emitted from the electrospray source. Two high voltage power supplies are connected to the push-pull bipolar switch circuit board which can be seen in figure B.3. The voltage polarity output from the board was alternated using two HMV technology OPTO-150 high voltage optocouplers. A square wave signal from the LabVIEW control program insured that both positive and negative polarities were not activated simultaneously. Each optocoupler contained an LED emitter and a high voltage photo detector diode rated to 15kV. When the optocoupler was activated, the photodiode detected the LED which completes a path ground, allowing the high voltage to pass through to the output. 5 VDC input power was supplied by the GwINSTEK 4303 power supply to each optocoupler. The opening and closing of the two optocoupler LED's was controlled by a STS10DN3LH5 chip from STMicroelectronics, which contained two metal-oxide semiconductor field-effect transistors (MOSFETs). A square wave signal from the LabVIEW control program sent a 5V control signal to each MOSFET from the NI 9401 digital module. The MOSFETs were used to turn the optocoupler's LEDs on and off. The voltage output of the EMCO H60 power supplies were also controlled through the LabVIEW control program using the NI 9265 current output module. Each current output was placed in parallel with a 4.7 kΩ resistor producing a 0-to-2.5-volt signal equating to 0-3kV output voltage of the EMCO H60 power supplies. A detailed circuit diagram of the bipolar switch can be seen in figure B.2.

Throughout testing, the bipolar switching board experienced several instances of arcing, while being operated at high voltage. The arcing usually occurred above 2,700 volts, but through dozens of experiments, arcing began to occur as low as 2,200 volts. An example of arcing caught on film can be seen in Figure B.4. Each instance of arcing would cause a component on the circuit board to be overloaded and fail. In most cases, the MOSFET chip was destroyed and needed to be replaced before testing could continue. It was identified that the board did not have proper spacing between high voltage lines and other conductive elements. To eliminate the arcing, a Dremel rotary tool was used to polish away any copper plating near high voltage lines. The high voltage lines were then covered in 419D acrylic conformal coating from MG chemicals, which helped to reduce the likelihood of arcing. After the changes, the voltage was reliably be raised to 3,000 volts without issue.
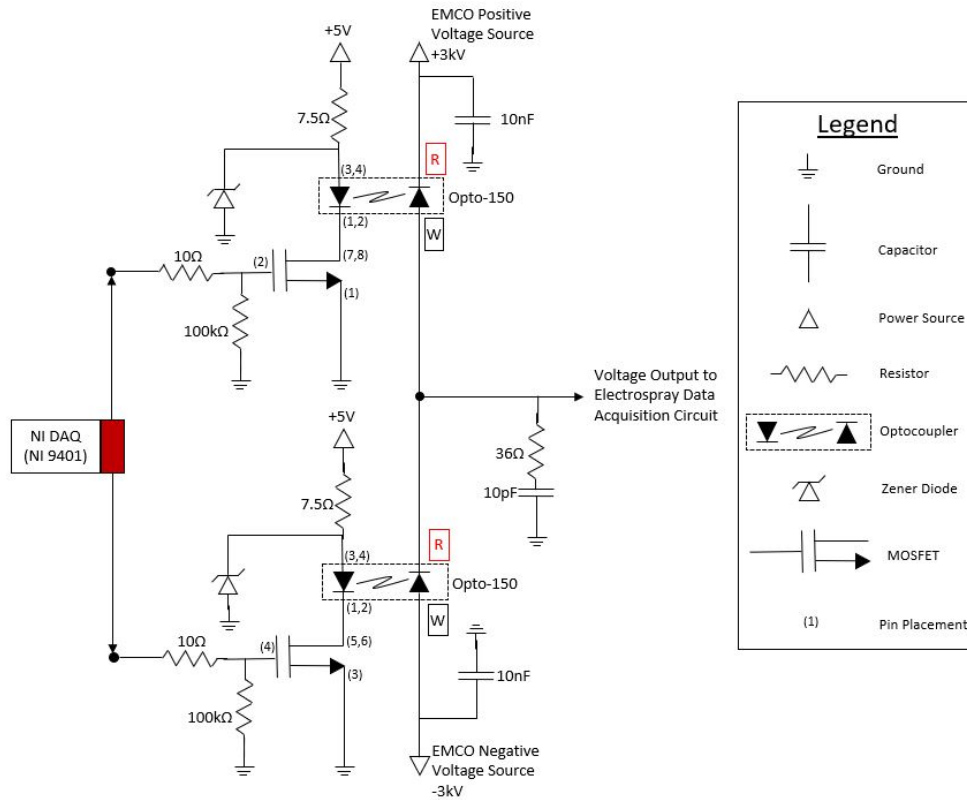
Figure B.2: Circuit diagram of the bipolar switching circuit.
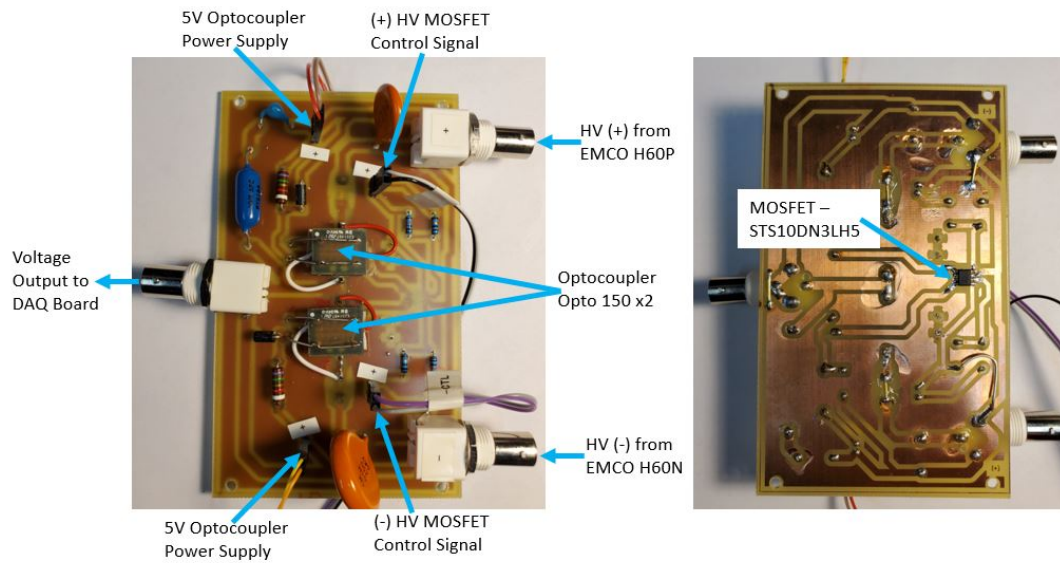
Figure B.3: Circuit board of the bipolar switching PCB. LHS - The top of the board, RHS - The underside of the board.
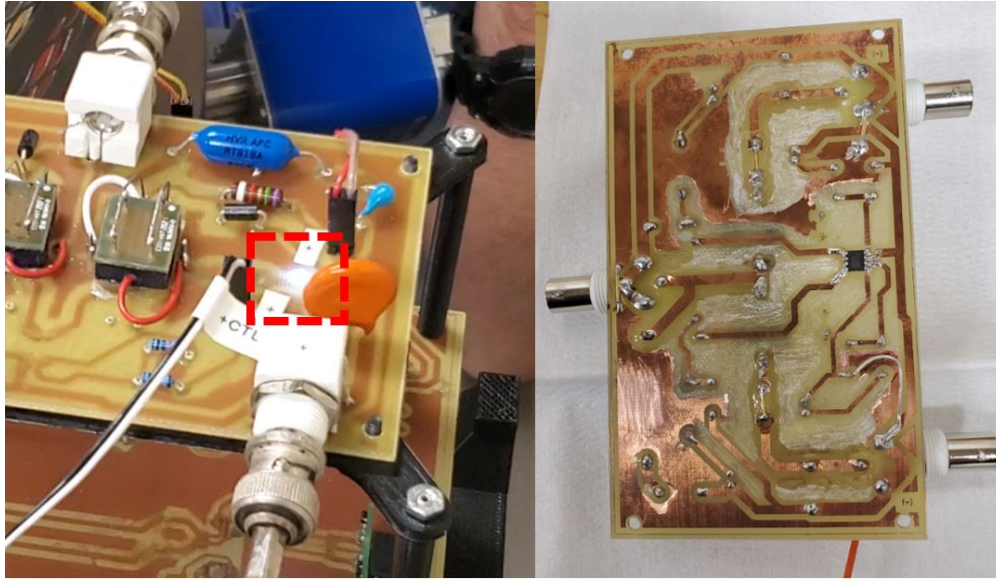
Figure B.4: LHS - Example of arcing between circuit board components during high voltage operation, RHS - Circuit board after excess copper was removed.

B.2.2 Electrospray Data Acquisition Circuit

The data acquisition PCB was used to measure both the voltage and current applied to the electrospray source. The physical PCB board and its various components can be seen in figure B.6. The output of the bipolar switching circuit board connects directly to the data acquisition board. The output voltage was measured using a voltage divider scheme where a 100MΩ and 10kΩ resistor in series would convert a +/-3kV input voltage to a measurable +/-0.3V. An AMC1100 isolation amplifier took the analogue signal and provided a gain of 8 to produce a voltage output of +/-2.4V. The actual voltage output was slightly different, since the 25kΩ isolation amplifier's input impedance acted as an additional in-parallel resistor to the voltage divider. A DCH010505S DC-DC converter was placed before the AMC1100 isolation amplifier to provide an isolated power source. Both the isolation amplifier and the DC/DC converter required a 5 VDC power source which was supplied by the GwINSTEK GPS-4303 power supply.

The output current was measured using a shunt resistor. The voltage difference between the input and output through a 25kΩ resistor was used to measure the current. Another DCH010505S DC/DC converter and AMC1100 isolation amplifier were used to take the analogue signal from the shunt resistor and convert it into a measurable signal. A measured output voltage of +/-0.25V equated to 10μA of current. An image of the data acquisition PCB can be seen in Figure B.6
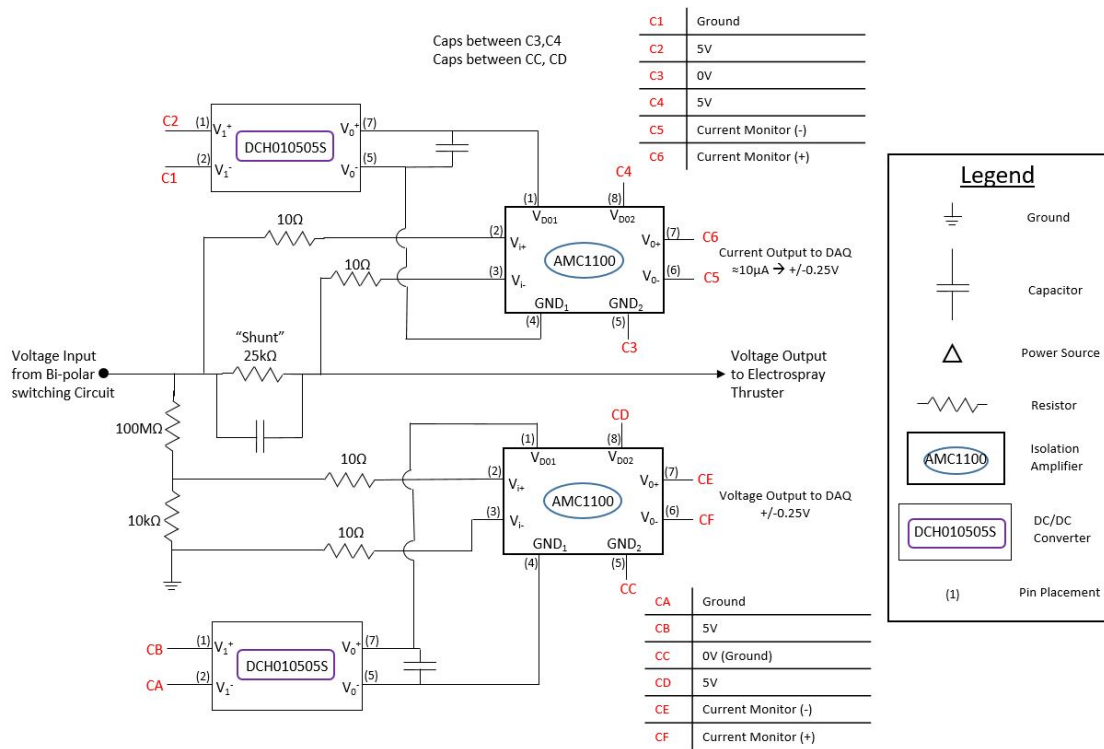
Figure B.5: Data acquisition circuit diagram.
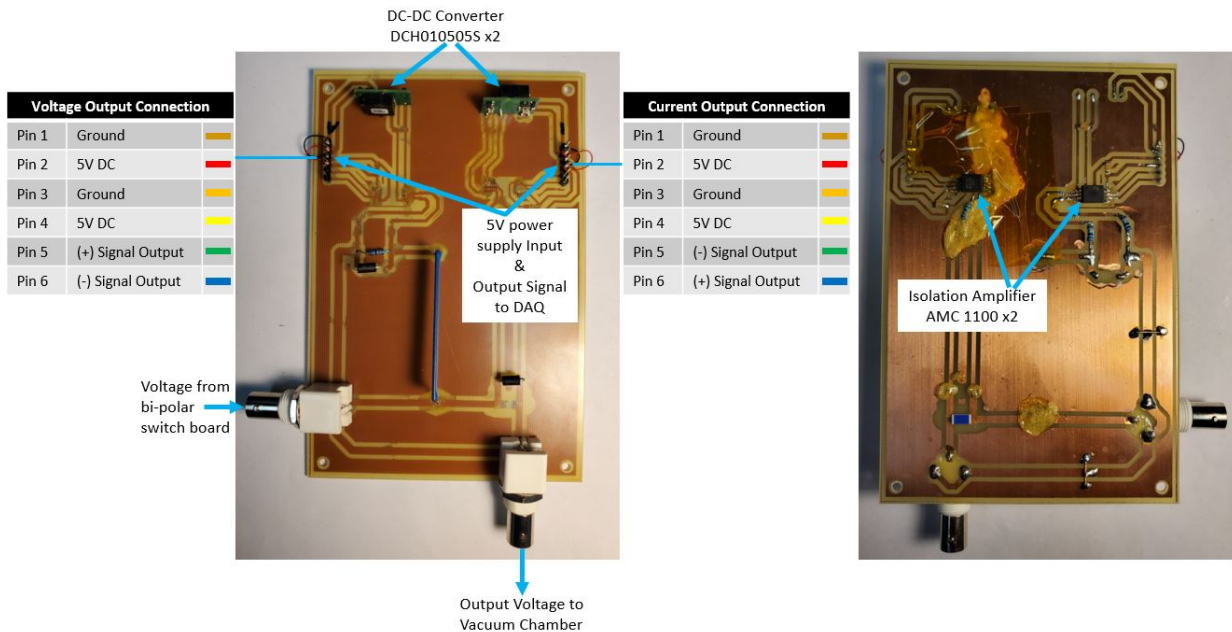
Figure B.6: Circuit board of data acquisition PCB. LHS - The top of the board, RHS - The underside of the board.

B.2.3 Electrostatic Gate Control Circuit

The BNG used in the ToF system required a high-speed, high voltage switch to operate. A Behlke HTS 31-03-HB-C switch capable of unipolar voltages up to 3kV was used to produce the high speed pulses required to operate the gate. The Behlke switch was controlled using an on/off switch actuated through the LabVIEW control program, which sent a current control signal from the NI 9401 digital output module output to the Behlke switch. Each current output was placed in parallel with a 4.7 kΩ resistor, so that a 5 volt signal was sent from LabVEIW to the Behlke switch. The switch itself required 5 VDC, which was supplied by the GwINSTEK GPS-4303 power supply. An EMCO USB20P power supply was used to supply a 0-2 kV voltage to the switch. When activated, the switch allowed high voltage to pass to the BNG, turning it on.
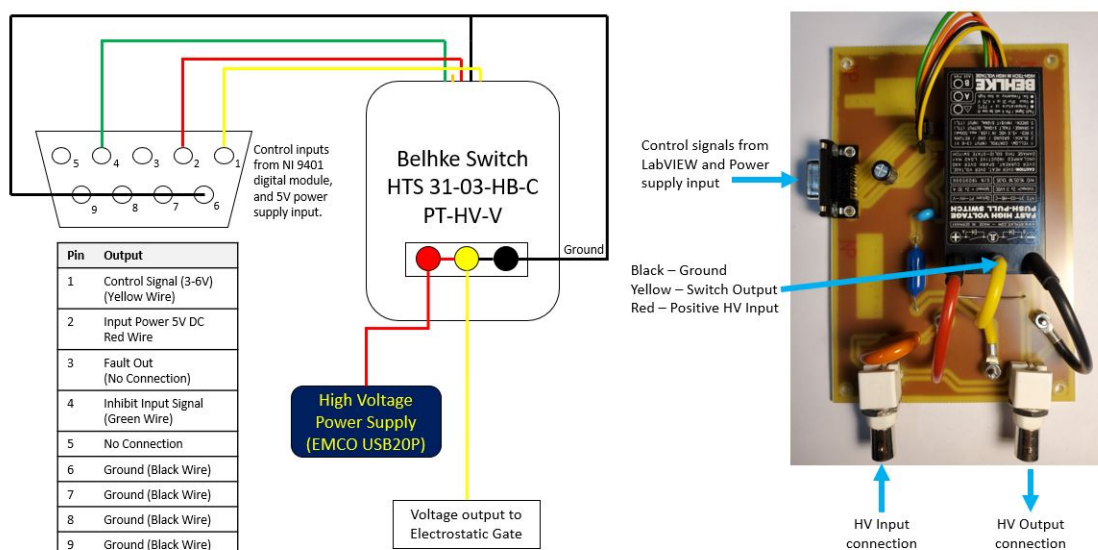
Figure B.7: LHS - The circuitry and connections used to operate the Behlke switch, RHS - The Behlke switch PCB.

In initial tests of the Behlke switch, at high voltages, it was found that turning the switch off caused a resonance pattern to form in the signal. It was determined that the circuitry was not sufficient to ground the high voltage fast enough, which caused reflections of the HV signal. An additional alligator clip was attached to the ground wire on the Behlke switch PCB and was connected to the ground of the EMCO USB20P power supply. This extra connection was able to remove the resonance and allowed the switch to operate as intended. The results described here can be seen in figure B.8.

B.3   Data Acquisition Instruments

A National Instruments data acquisition system was used to output control signals and measure input signals from the electrospray system. A cDAQ 9174 chassis was equipped with four (4) data modules: cDAQ1Mod1 - NI 9401 bi-directional digital module, cDAQ1Mod2 - NI 9215 voltage input module, cDAQ1Mod3 - NI 9215 voltage input module, cDAQ1Mode4 - NI 9265 current output module. The system was connected to the LabVIEW program shown below. The program
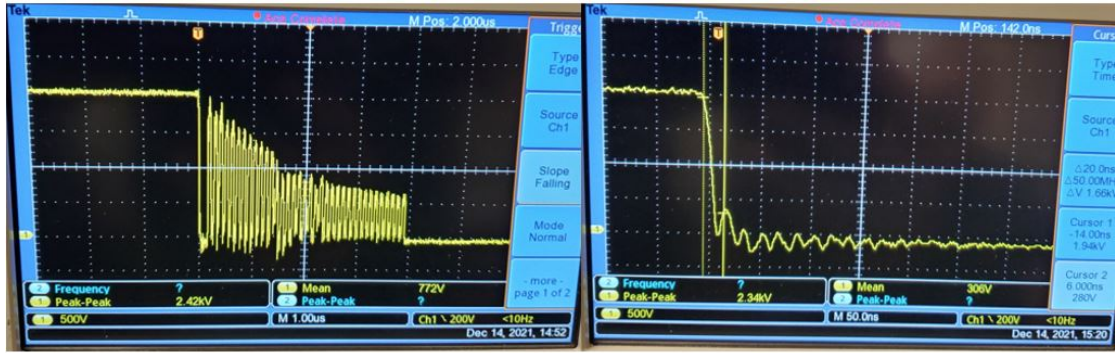
Figure B.8: LHS - Voltage reflection resonance observed at high voltage operation, RHS - Resonance greatly reduced with additional connections to ground.

produced output signals and monitored / recorded input signals. The complete signal configuration and wire detail can be seen in figure B.9.
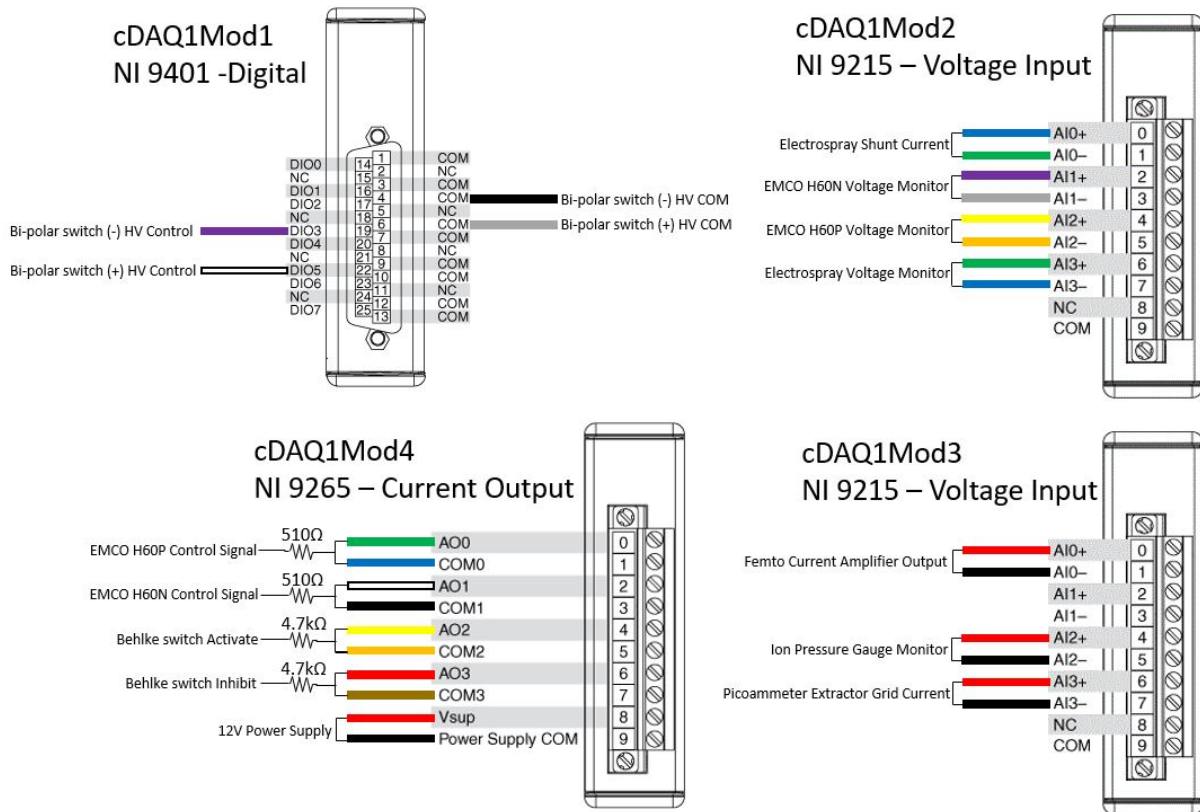
Figure B.9: DAQ configuration.

The custom LabView program virtual instrument (VI) developed to control electrospray operation is an evolution of previous work at RAPPEL [237]. Figure B.10 shows a snapshot of the Labview VI, while Figures B.11 and B.12 show the back end block diagram structure of the program.

B.4 LabVIEW Program
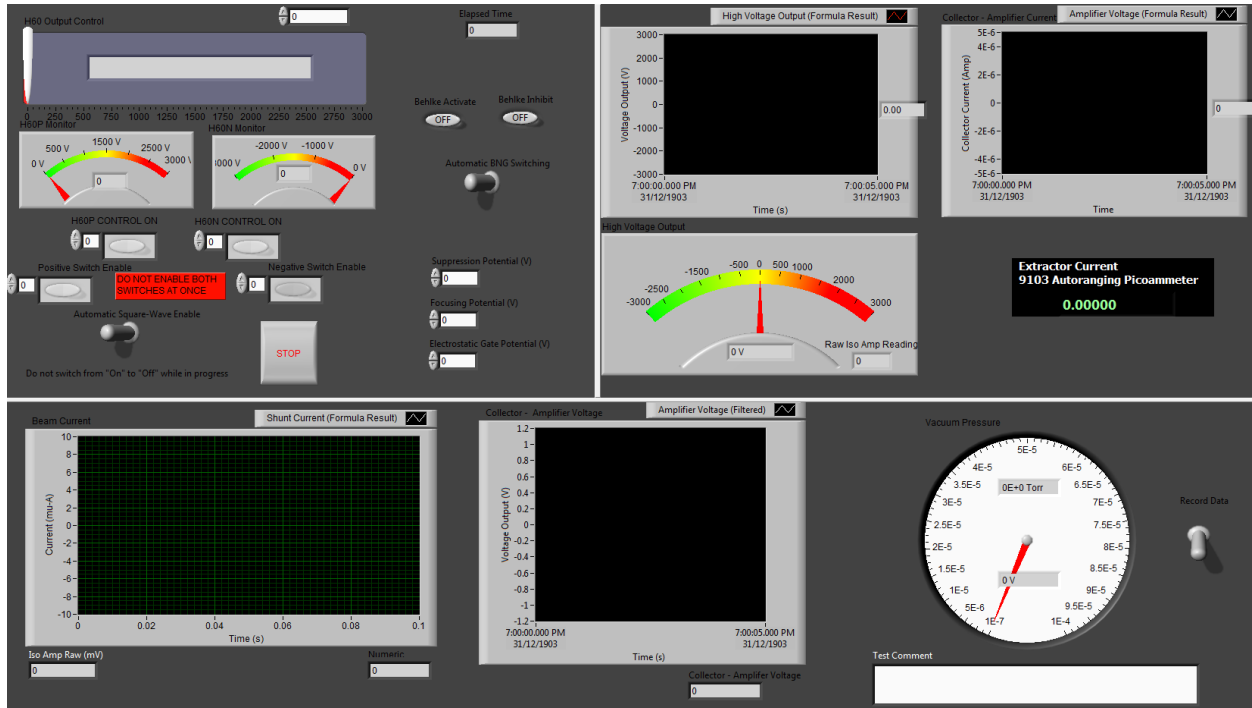
Figure B.10: The custom LabView VI used for control electrospray thruster.
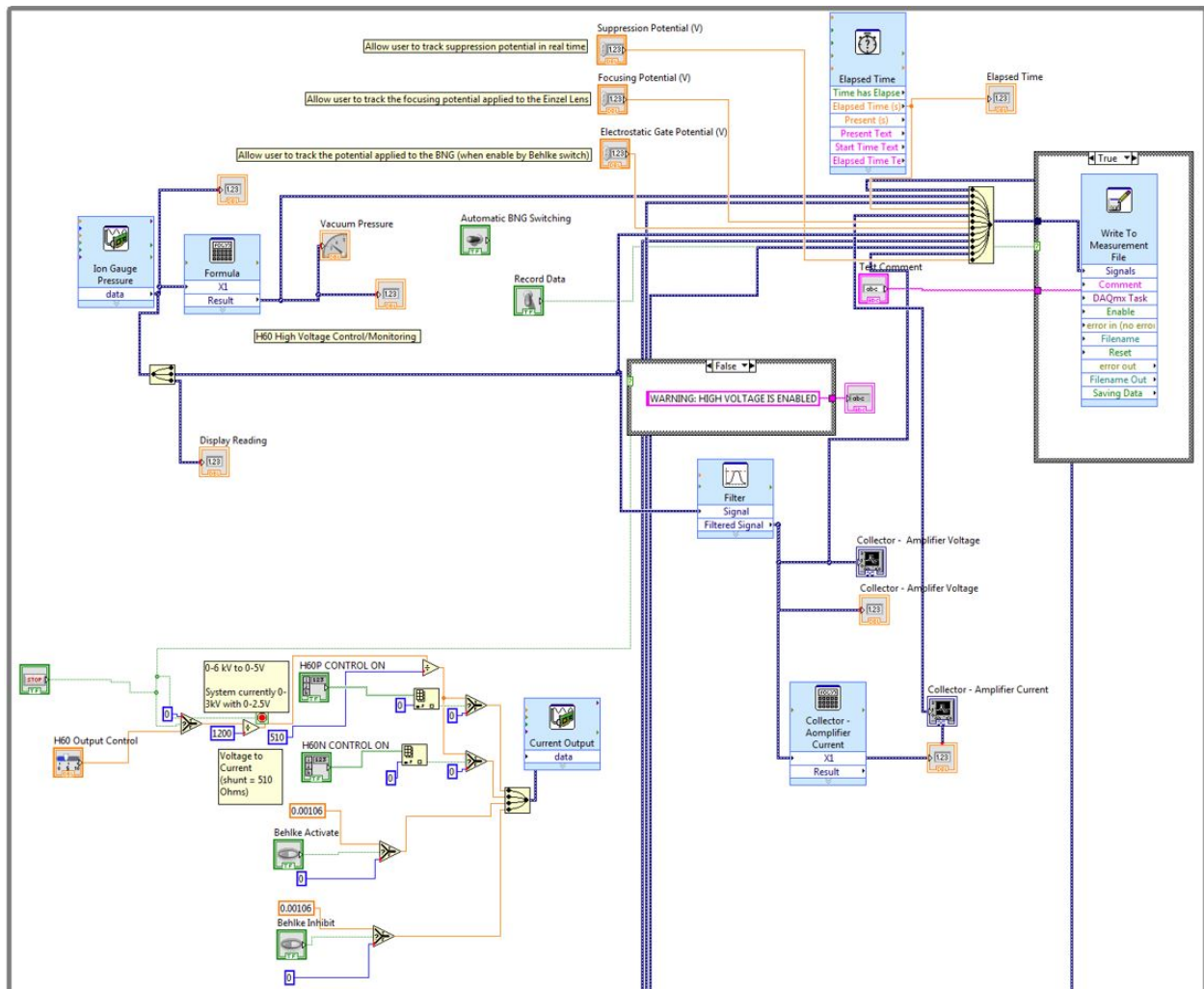
Figure B.11: LabView block diagram - top section.
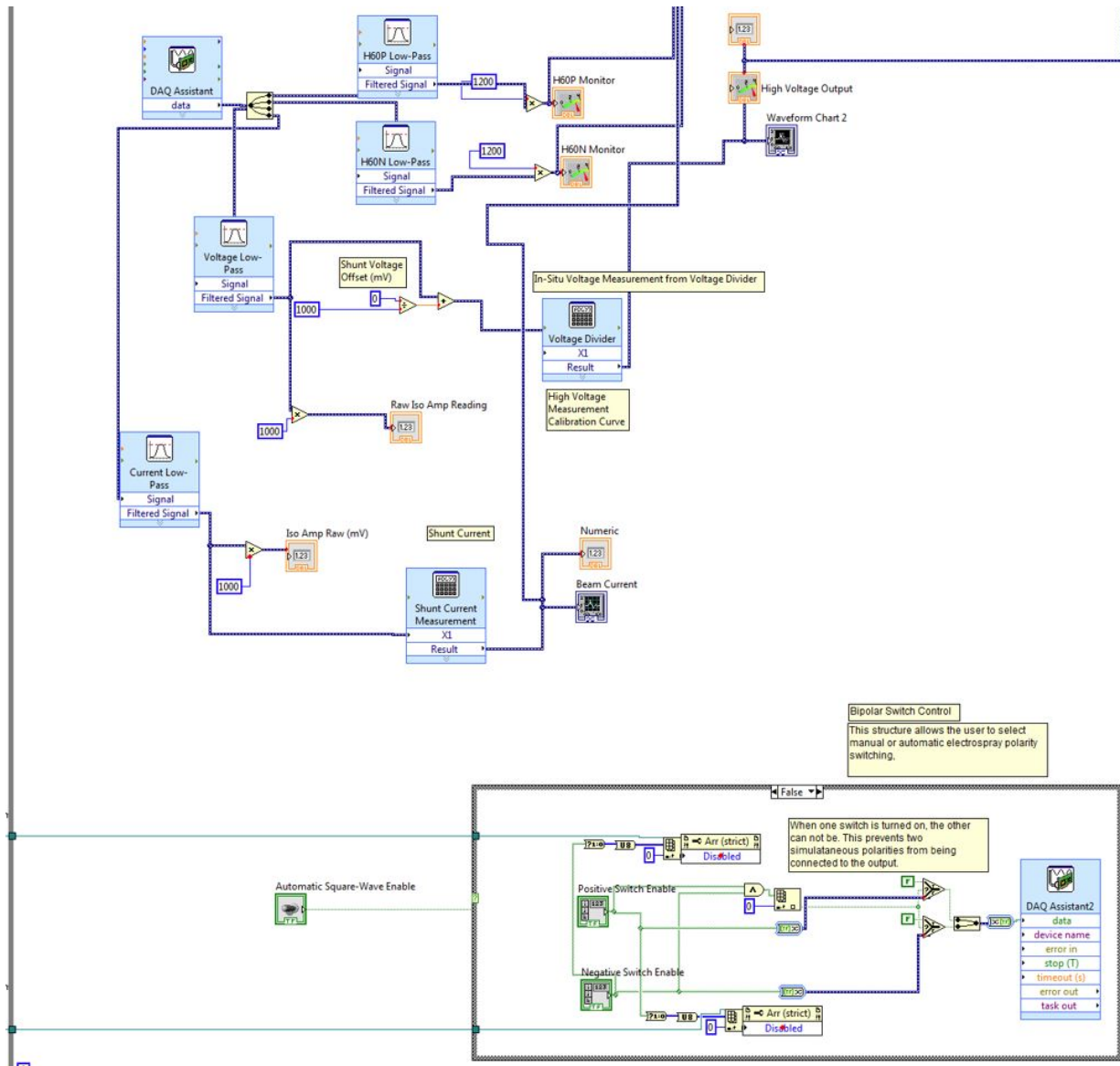
Figure B.12: LabView block diagram - bottom section.

Bibliography

[1] Charles M Dalfen. The Telesat Canada domestic communications satellite system. *Stan. J. Int'l Stud.*, 5:84, 1970.

[2] Stanley Q Kidder, Rushworth M Kidder, and Thomas H Vonder Haar. *Satellite meteorology: an introduction*. Gulf Professional Publishing, 1995.

[3] Oliver Montenbruck and Pere Ramos-Bosch. Precision real-time navigation of LEO satellites using global positioning system measurements. *GPS Solutions*, 12(3):187–198, 2008.

[4] JV King. Cospas-Sarsat: an international satellite system for search and rescue. *Space communications*, 18(3, 4):139–150, 2002.

[5] Jenelle White, Aaron A Berg, Catherine Champagne, Yinsuo Zhang, Aston Chipanshi, and Bahram Daneshfar. Improving crop yield forecasts with satellite-based soil moisture estimates: An example for township level canola yield forecasts over the canadian prairies. *International Journal of Applied Earth Observation and Geoinformation*, 89:102092, 2020.

[6] Jun Yang, Peng Gong, Rong Fu, Minghua Zhang, Jingming Chen, Shunlin Liang, Bing Xu, Jiancheng Shi, and Robert Dickinson. The role of satellite remote sensing in climate change studies. *Nature climate change*, 3(10):875–883, 2013.

[7] R Cargill Hall. Origins and development of the vanguard and explorer satellite programs: Winning Essay of The Robert H. Goddard Historical Essay Competition for 1963 Sponsored by the National Space Club, Washington, DC. *The Air Power Historian*, 11(4):101–112, 1964.

[8] Canadian Space Agency. Alouette 1 and 2. *https://www.asc-csa.gc.ca/eng/satellites/alouette.asp*, 2018.

[9] National Aeronautics and Space Association. International space station facts and figures. *https://www.nasa.gov/feature/facts-and-figures*, 2021.

[10] Martin Sweeting. Modern small satellites-changing the economics of space. *Proceedings of the IEEE*, 106(3):343–361, 2018.

[11] Robyn M Millan, Rudolf von Steiger, Meir Ariel, Sergey Bartalev, Maurice Borgeaud, Stefano Campagnola, Julie C Castillo-Rogez, René Fléron, Volker Gass, Anna Gregorio, et al. Small satellites for space science: A cospar scientific roadmap. *Advances in space research*, 64(8):1466–1517, 2019.

[12] Armen Poghosyan and Alessandro Golkar. Cubesat evolution: Analyzing cubesat capabilities for conducting science missions. *Progress in Aerospace Sciences*, 88:59–83, 2017.

[13] George P Sutton. History of liquid propellant rocket engines in the United States. *Journal of Propulsion and Power*, 19(6):978–1007, 2003.

[14] Edgar Y Choueiri. A critical history of electric propulsion: The first 50 years (1906-1956). *Journal of propulsion and power*, 20(2):193–203, 2004.

[15] Stéphane Mazouffre. Electric propulsion for satellites and spacecraft: established technologies and novel approaches. *Plasma Sources Science and Technology*, 25(3):033002, 2016.

[16] Marc G Millis and Eric W Davis. *Frontiers of propulsion science*. American Institute of Aeronautics and Astronautics, 2009.

[17] George P Sutton and Oscar Biblarz. *Rocket propulsion elements*. John Wiley & Sons, 2016.

[18] J Hunley. The history of solid-propellant rocketry-what we do and do not know. In *35th joint propulsion conference and exhibit*, page 2925, 1999.

[19] Olwen Morgan and Dennis Meinhardt. Monopropellant selection criteria-hydrazine and other options. In *35th Joint Propulsion Conference and Exhibit*, page 2595, 1995.

[20] Alan Lawrie. The Saturn V rocket: A new review of manufacturing, testing and logistics. In *42nd AIAA/ASME/SAE/ASEE Joint Propulsion Conference & Exhibit*, page 5031, 2006.

[21] Assad Anis. Cold gas propulsion system-an ideal choice for remote sensing small satellites. *Remote sensing-advanced techniques and platforms*, pages 447–462, 2012.

[22] Peter E Glaser. An overview of the solar power satellite option. *IEEE Transactions on Microwave Theory and Techniques*, 40(6):1230–1238, 1992.

[23] Leon Alkalai. Advanced microelectronics technologies for future small satellite systems. *Acta Astronautica*, 46(2-6):233–239, 2000.

[24] Christophe Koppel, Frederic Marchandise, Mathieu Prioul, Denis Estublier, and Franck Darnon. The smart-1 electric propulsion subsystem around the moon: In flight experience. In *41st AIAA/ASME/SAE/ASEE Joint Propulsion Conference & Exhibit*, page 3671, 2005.

[25] David Manzella. Low cost electric propulsion thruster for deep space robotic missions. In *2007 NASA Science Technology Conference*, pages 07–0116. Citeseer, 2007.

[26] Martin JL Turner. *Rocket and spacecraft propulsion: principles, practice and new developments*. Springer Science & Business Media, 2008.

[27] Robert G Jahn. *Physics of electric propulsion*. Courier Corporation, 2006.

[28] Ahmed ES Nosseir, Angelo Cervone, and Angelo Pasini. Review of state-of-the-art green monopropellants: For propulsion systems analysts and designers. *Aerospace*, 8(1):20, 2021.

[29] Robert G Jahn. Electric propulsion. *American Scientist*, 52(2):207–217, 1964.

[30] Andrea Kodys and Edgar Choueiri. A critical review of the state-of-the-art in the performance of applied-field magnetoplasmadynamic thrusters. In *41st AIAA/ASME/SAE/ASEE Joint Propulsion Conference & Exhibit*, page 4247, 2005.

[31] Michael LaPointe, Eugene Strzempkowski, and Eric Pencil. High power MPD thruster performance measurements. In *40th AIAA/ASME/SAE/ASEE Joint Propulsion Conference and Exhibit*, page 3467, 2004.

[32] K Toki, Y Shimizu, and K Kuriki. Application of MPD thruster systems to interplanetary missions. *Journal of Propulsion and Power*, 2(6):508–512, 1986.

[33] G Serianni, N Vianello, F Paganucci, P Rossetti, V Antoni, M Bagatin, and M Andrenucci. Plasma diagnostics in an applied field MPD thruster. *IEPC Paper*, pages 01–135, 2001.

[34] Dan Lev. *Investigation of Efficiency in Applied Field MagnetoPlasmaDynamic Thrusters*. PhD thesis, 01 2012.

[35] European Space Agency Website. T6 ion thruster firing. *https://www.esa.int/ESA_Multimedia/Images/2016/04/T6_ion_thruster_firing*, 2016.

[36] Edgar Yazid Choueiri. Fundamental difference between the two hall thruster variants. *Physics of Plasmas*, 8(11):5025–5033, 2001.

[37] Tommaso Misuri, Cosimo Ducci, Stefan Gregucci, Daniela Pedrini, Federico Cannelli, Ugo Cesari, Francesco Nania, Alessandro Vicini, Giovanni Pace, Francesco Magistro, et al. SITAEL HT100 thruster unit, full ground qualification. In *Proceedings of the 36th International Electric Propulsion Conference University of Vienna, Vienna, Austria*, pages 15–20, 2019.

[38] Nathaniel R Demmons, Zack Wood, and Nereo Alvarez. Characterization of a high thrust, pressure-fed electrospray thruster for precision attitude control applications. In *AIAA Propulsion and Energy 2019 Forum*, page 3817, 2019.

[39] Kristina Lemmer. Propulsion for cubesats. *Acta Astronautica*, 134:231–243, 2017.

[40] Geoffrey Ingram Taylor. Disintegration of water drops in an electric field. *Proceedings of the Royal Society of London. Series A. Mathematical and Physical Sciences*, 280(1382):383–397, 1964.

[41] Benjamin D Prince, Bruce A Fritz, and Yu-Hui Chiu. Ionic liquids in electrospray propulsion systems. In *Ionic Liquids: Science and Applications*, pages 27–49. ACS Publications, 2012.

[42] Robert S Legge Jr and Paulo C Lozano. Electrospray propulsion based on emitters microfabricated in porous metals. *Journal of Propulsion and Power*, 27(2):485–495, 2011.

[43] Timothy Fedkiw, Zackary D Wood, and Nathaniel R Demmons. Environmental and lifetime testing of the BET-300-P electrospray thruster. In *AIAA Propulsion and Energy 2020 Forum*, page 3614, 2020.

[44] Peter Musen. The influence of the solar radiation pressure on the motion of an artificial satellite. *Journal of Geophysical Research*, 65(5):1391–1396, 1960.

[45] Osamu Mori, Hirotaka Sawada, Ryu Funase, Mutsuko Morimoto, Tatsuya Endo, Takayuki Yamamoto, Yuichi Tsuda, Yasuhiro Kawakatsu, Junichiro Kawaguchi, Yasuyuki Miyazaki, et al. First solar power sail demonstration by IKAROS. *Transactions of the Japan Society for Aeronautical and Space Sciences, Aerospace Technology Japan*, 8(ists27):To_4_25–To_4_31, 2010.

[46] Vaios Lappas, Nasir Adeli, Lourens Visagie, Juan Fernandez, Theodoros Theodorou, Willem Steyn, and Matthew Perren. Cubesail: A low cost cubesat based solar sail demonstration mission. *Advances in Space Research*, 48(11):1890–1901, 2011.

[47] James B Pezent, Rohan Sood, Andrew Heaton, Kyle Miller, and Les Johnson. Preliminary trajectory design for NASA's solar cruiser: A technology demonstration mission. *Acta Astronautica*, 183:134–140, 2021.

[48] David A Spencer, Bruce Betts, John M Bellardo, Alex Diaz, Barbara Plante, and Justin R Mansell. The LightSail 2 solar sailing technology demonstration. *Advances in Space Research*, 67(9):2878–2889, 2021.

[49] Enrico Lorenzini and Juan Sanmartin. Electrodynamic tethers in space. *Scientific American*, 291(2):50–57, 2004.

[50] M Dobrowolny and NH Stone. A technical overview of TSS-1: the first tethered-satellite system mission. *Il Nuovo Cimento C*, 17(1):1–12, 1994.

[51] E Ahedo and J Sanmartin. Analysis of electrodynamic tethers as deorbiting systems. In *36th AIAA/ASME/SAE/ASEE Joint Propulsion Conference and Exhibit*, page 3763, 2000.

[52] Robert M Zubrin and Dana G Andrews. Magnetic sails and interplanetary travel. *Journal of Spacecraft and Rockets*, 28(2):197–203, 1991.

[53] Daniel R Koeing. Experience gained from the space nuclear rocket programs (Rover/NERVA). Technical report, Los Alamos National Laboratory, Report LA-10062-H, Los Alamos, NM, 1986.

[54] Tony Kim and Michael G Houts. Nasa's nuclear thermal propulsion project. In *AIAA SPACE 2015 Conference and Exposition*, page 4523, 2015.

[55] GR Schmidt, JA Bonometti, and CA Irvine. Project Orion and future prospects for nuclear pulse propulsion. *Journal of Propulsion and Power*, 18(3):497–504, 2002.

[56] George Dyson. Project Orion: The true story of the atomic spaceship, 2002.

[57] Claudio Bruno. *Nuclear Space Power and Propulsion Systems*. American Institute of Aeronautics and Astronautics, 2008.

[58] Andrew V Ilin, Leonard D Cassady, Tim W Glover, and Franklin R Chang Diaz. Vasimr® human mission to mars. In *Space, Propulsion & Energy Sciences International Forum*, pages 1–12, 2011.

[59] Erik Kulu. Nanosats database - www.nanosats.eu. 2022.

[60] David Krejci and Paulo Lozano. Space propulsion technology for small spacecraft. *Proceedings of the IEEE*, 106(3):362–378, 2018.

[61] Gottfried Konecny. Small satellites–a tool for earth observation? In *ISPRS Congress, Commission*, volume 4, pages 12–23. Citeseer, 2004.

[62] University of Toronto Institute for Aerospace Studies Space Flight Lab Website. CANX-4 CANX-5: Mission. *https://www.utias-sfl.net CanX*

[63] *V Hunter Adams and Mason Peck. R-selected spacecraft.* Journal of Spacecraft and Rockets, *57(1):90–98, 2020.*

[64] *Hank Heidt, Jordi Puig-Suari, Augustus Moore, Shinichi Nakasuka, and Robert Twiggs. Cubesat: A new generation of picosatellite for education and industry low-cost space experimentation. 2000.*

[65] *William H Wooden. Navstar global positioning system: 1985. In* Proceedings of the First International Symposium on Precise Positioning with the Global Positioning System, *pages 23–32, 1985.*

[66] *Bassel Al Homssi, Akram Al-Hourani, Ke Wang, Phillip Conder, Sithamparanathan Kandeepan, Jinho Choi, Ben Allen, and Ben Moores. Next generation mega satellite networks: Opportunities, challenges, and performance.* arXiv preprint arXiv:2110.04231, *2021.*

[67] *Jonathan C McDowell. The low earth orbit satellite population and impacts of the SpaceX Starlink constellation.* The Astrophysical Journal Letters, *892(2):L36, 2020.*

[68] *Abid Murtaza, Syed Jahanzeb Hussain Pirzada, Tongge Xu, and Liu Jianwei. Orbital debris threat for space sustainability and way forward.* IEEE Access, *8:61000–61019, 2020.*

[69] *Paul Maskell and Lorne Oram. Sapphire: Canada's answer to space-based surveillance of orbital objects. In* Advanced Maui Optical and Space Surveillance Conference, *2008.*

[70] HR Shea. *Mems for pico-to micro-satellites.* In Moems And Miniaturized Systems VIII, *volume 7208, pages 208–215. SPIE, 2009.*

[71] Dillon O'Reilly, Georg Herdrich, and Darren F Kavanagh. *Electric propulsion methods for small satellites: A review.* Aerospace, *8(1):22, 2021.*

[72] Robert Masse, May Allen, Ronald Spores, and Elizabeth A Driscoll. *Af-m315e propulsion system advances and improvements. page 4577, 2016.*

[73] James J Szabo, Lawrence Byrne, Mike Strain, Surjeet Paintal, Samuel Sawyer, Terry Yu, George Kolencik, Vlad Hruby, Timothy G Gray, Dean P Petters, et al. One million newton-second duration test of a 600 watt hall effect thruster fueled by xenon. page 3651, 2020.*

[74] Norman Chigier and Tevfik Gemci. *A review of micro propulsion technology.* In 41st Aerospace sciences meeting and exhibit, *page 670, 2003.*

[75] A Epstein, S Senturia, O Al-Midani, G Anathasuresh, A Epstein, S Senturia, O Al-Midani, G Anathasuresh, A Ayon, K Breuer, et al. *Micro-heat engines, gas turbines, and rocket engines-the MIT microengine project.* In 28th Fluid dynamics conference, *page 1773, 1997.*

[76] Derek Schmuland, Robert Masse, and Charles Sota. *Hydrazine propulsion module for cubesats.* 2011.*

[77] Richard E Wirz, John R Anderson, and Ira Katz. *Time-dependent erosion of ion optics.* Journal of Propulsion and Power, *27(1):211–217, 2011.*

[78] Craig Clauss, Michael Day, Vladimir Kim, Youri Kondakov, Thomas Randolph, Craig Clauss, Michael Day, Vladimir Kim, Youri Kondakov, and Thomas Randolph. *Preliminary study of possibility to ensure large enough lifetime of SPT operating under increased powers.* In 33rd Joint Propulsion Conference and Exhibit, *page 2789, 1997.*

[79] D Krejci, F Mier-Hicks, C Fucetola, and P Lozano. *High efficiency ionic liquid electrospray propulsion for nanosatellites.* 2016.*

[80] Accion Systems Company Website. *Tile 3 electrospray thruster.* https://accion-systems.com/tile-propulsion/, 2022.*

[81] Enpulsion Company Website. *Enpulsion nano feep thruster.* https://www.enpulsion.com/order/enpulsion-nano/, 2022.*

[82] Scott King, Mitchell Walker, and Craig Kluever. *Small satellite LEO maneuvers with low-power electric propulsion.* In 44th AIAA/ASME/SAE/ASEE Joint Propulsion Conference & Exhibit, *page 4516, 2008.*

[83] Nandasiri Jasentuliyana. *Space debris and international law.* J. Space L., *26:139, 1998.*

[84] *Colloid micro-newton thruster development for the ST7-drs.*

[85] Chris Sabol, Rich Burns, and Craig A McLaughlin. *Satellite formation flying design and evolution.* Journal of spacecraft and rockets, *38(2):270–278, 2001.*

[86] Saptarshi Bandyopadhyay, Giri P Subramanian, Rebecca Foust, Daniel Morgan, Soon-Jo Chung, and Fred Hadaegh. *A review of impending small satellite formation flying missions.* In 53rd AIAA Aerospace Sciences Meeting, *page 1623, 2015.*

[87] Daniel Rankin, Daniel D Kekez, Robert E Zee, Freddy M Pranajaya, Daniel G Foisy, and Alexander M Beattie. *The Canx-2 nanosatellite: expanding the science abilities of nanosatellites.* Acta Astronautica, *57(2-8):167–174, 2005.*

[88] Grant Bonin, Niels Roth, Scott Armitage, Josh Newman, Ben Risi, and Robert E Zee. Canx–4 and CanX–5 precision formation flight: Mission accomplished! 2015.

[89] Eric Hand. Interplanetary small satellites come of age, 2018.

[90] Tomas J Martin-Mur and Brian Young. Navigating marco, the first interplanetary cubesats. 2019.

[91] Benjamin K Malphrus, Anthony Freeman, Robert Staehle, Andrew T Klesh, and Roger Walker. Interplanetary cubesat missions. In Cubesat Handbook, pages 85–121. Elsevier, 2021.

[92] Gianluca Benedetti, Nicoletta Bloise, Davide Boi, Francesco Caruso, Andrea Civita, Sabrina Corpino, Erik Garofalo, Giuseppe Governale, Luigi Mascolo, Gianluca Mazzella, et al. Interplanetary cubesats for asteroid exploration: Mission analysis and design. Acta Astronautica, 154:238–255, 2019.

[93] Christoph Steiger, Elsa Montagnon, Andrea Accomazzo, and Paolo Ferri. Bepicolombo mission to mercury: First year of flight. Acta Astronautica, 170:472–479, 2020.

[94] S Clark, P Randall, R Lewis, D Marangone, D Goebel, V Chaplin, H Gray, K Kempkens, and N Wallace. Bepicolombo—solar electric propulsion system test and qualification approach. In 36th International Electric Propulsion Conference, Electric Rocket Propulsion Soc. Paper IEPC-2019-586, Vienna, Austria, 2019.

[95] Vanni Da Ronco. The challenge of design and develop a dual-mode propulsion system for BepiColombo ESA exploration mission to mercury. In 47th AIAA/ASME/SAE/ASEE Joint Propulsion Conference & Exhibit, page 5833, 2011.

[96] Hiroshi Yamakawa, Hiroyuki Ogawa, Yoshitsugu Sone, Hajime Hayakawa, Yasumasa Kasaba, Takeshi Takashima, Toshifumi Mukai, Takahiko Tanaka, and Masaki Adachi. Bepicolombo mercury magnetospheric orbiter design. Acta Astronautica, 62(12):699–705, 2008.

[97] Johannes Benkhoff, Jan Van Casteren, Hajime Hayakawa, Masaki Fujimoto, Harri Laakso, Mauro Novara, Paolo Ferri, Helen R Middleton, and Ruth Ziethe. Bepicolombo—comprehensive exploration of mercury: Mission overview and science goals. Planetary and Space Science, 58(1-2):2–20, 2010.

[98] Joshua L Rovey, Christopher T Lyne, Alex J Mundahl, Nicolas Rasmont, Matthew S Glascock, Mitchell J Wainwright, and Steven P Berg. Review of multimode space propulsion. Progress in Aerospace Sciences, 118:100627, 2020.

[99] Hiroyuki Koizumi, Tadashi Inagaki, Yusuke Kasagi, Taro Naoi, Tomoyuki Hayashi, Ryu Funase, and Kimiya Komurasaki. Unified propulsion system to explore near-earth asteroids by a 50 kg spacecraft. 2014.

[100] Ryu Funase, Takaya Inamori, Satoshi Ikari, Naoya Ozaki, and Hiroyuki Koizumi. Initial operation results of a 50kg-class deep space exploration micro-spacecraft PROCYON. 2015.

[101] Nicolas Rasmont, Emil J Broemmelsiek, Alex Mundahl, and Joshua Rovey. Linear burn rate of ionic liquid multimode monopropellant. In AIAA Propulsion and Energy 2019 Forum, page 4294, 2019.

[102] Christopher T Lyne, Joshua Rovey, and Steven P Berg. Monopropellant-electrospray multimode thruster testing results: Electrospray mode. In AIAA Propulsion and Energy 2021 Forum, page 3439, 2021.

[103] Bruce Yost, Sasha Weston, Gabriel Benavides, Frederic Krage, John Hines, Stephanie Mauro, Selasi Etchey, Kiara O'Neill, and Barbra Braun. *State-of-the-art small spacecraft technology*. 2021.

[104] Lord Rayleigh. *On the equilibrium of liquid conducting masses charged with electricity*. The London, Edinburgh, and Dublin Philosophical Magazine and Journal of Science, *14(87):184–186, 1882*.

[105] John Zeleny. *The electrical discharge from liquid points, and a hydrostatic method of measuring the electric intensity at their surfaces*. Physical Review, *3(2):69, 1914*.

[106] John Zeleny. *On the condition of instability of electrified drops, with applications to electrical discharge from liquid points. In* Proc. Camb. Phil. Soc., *volume 18, pages 71–83, 1915*.

[107] John Zeleny. *Instability of electrified liquid surfaces*. Physical review, *10(1):1, 1917*.

[108] Paulo C Lozano, Manuel Martínez-Sánchez, and Vlad Hruby. *Electrospray propulsion*. Encyclopedia of Aerospace Engineering, *2010*.

[109] Charles D Hendricks Jr. *Charged droplet experiments*. Journal of Colloid Science, *17(3):249–259, 1962*.

[110] Victor E Krohn Jr. *Glycerol droplets for electrostatic propulsion*. Progress in Astronautics and Aeronautics, *9, 1963*.

[111] MN Huberman, JC Beynon, E Cohen, DS Goldin, PW Kidd, and S Zafran. *Present status of colloid microthruster technology*. Journal of Spacecraft and Rockets, *5(11):1319–1324, 1968*.

[112] MN Huberman and SG Rosen. *Advanced high-thrust colloid sources*. Journal of Spacecraft and Rockets, *11(7):475–480, 1974*.

[113] H Daley, Sr, J Mahoney, and J Perel, Sr. *Colloid annular array thruster development. In* 10th Electric Propulsion Conference, *page 1077, 1973*.

[114] P Kidd and H Shelton. *Life test/4350 hours/of an advanced colloid thruster module. In* 10th Electric Propulsion Conference, *page 1078, 1973*.

[115] Malcolm Dole, Lawrence L Mack, Robert L Hines, Ralph C Mobley, Lowell D Ferguson, and Martin B Alice. *Molecular beams of macroions*. The Journal of chemical physics, *49(5):2240–2249, 1968*.

[116] John B Fenn, Matthias Mann, Chin Kai Meng, Shek Fu Wong, and Craig M Whitehouse. *Electrospray ionization for mass spectrometry of large biomolecules*. Science, *246(4926):64–71, 1989*.

[117] M Cloupeau and B Prunet-Foch. *Electrostatic spraying of liquids: Main functioning modes*. Journal of electrostatics, *25(2):165–184, 1990*.

[118] K Tang and A Gomez. *Generation by electrospray of monodisperse water droplets for targeted drug delivery by inhalation*. Journal of aerosol science, *25(6):1237–1249, 1994*.

[119] Oleg V Salata. *Tools of nanotechnology: Electrospray*. Current nanoscience, *1(1):25–33, 2005*.

[120] Gary Tepper, Royal Kessick, and Dmitry Pestov. *An electrospray-based, ozone-free air purification technology*. Journal of Applied Physics, *102(11):113305, 2007*.

[121] John Ziemer, Thomas Randolph, Garth Franklin, Vlad Hruby, Douglas Spence, Nathaniel Demmons, Thomas Roy, Eric Ehrbar, Jurg Zwahlen, Roy Martin, et al. *Delivery of colloid micro-newton thrusters for the space technology 7 mission. In* 44th AIAA/ASME/SAE/ASEE Joint Propulsion Conference & Exhibit, *page 4826, 2008*.

[122] G Anderson, John Anderson, M Anderson, G Aveni, D Bame, P Barela, K Blackman, A Carmain, L Chen, M Cherng, et al. Experimental results from the st7 mission on lisa pathfinder. Physical Review D, 98(10):102005, 2018.

[123] Tony Schonherr, Bryan Little, David Krejci, Alexander Reissner, and Bernhard Seifert. Development, production, and testing of the IFM nano FEEP thruster. In 36th International Electric Propulsion Conference, pages 1–11, 2019.

[124] Elaine Petro, Amelia Bruno, Paulo Lozano, Louis E Perna, and Dakota Freeman. Characterization of the tile electrospray emitters. In AIAA Propulsion and Energy 2020 Forum, page 3612, 2020.

[125] J Fernandez De La Mora and Ignacio González Loscertales. The current emitted by highly conducting Taylor cones. Journal of Fluid Mechanics, 260:155–184, 1994.

[126] Manuel Martinez-Sanchez and Paulo Lozano. 16.522 space propulsion. Massachusetts Institute of Technology: MIT OpenCourseWare, Lecture 20:155–184, 2015.

[127] Manuel Gamero-Castano. Electric-field-induced ion evaporation from dielectric liquid. Physical review letters, 89(14):147602, 2002.

[128] David Krejci, Fernando Mier-Hicks, Robert Thomas, Thomas Haag, and Paulo Lozano. Emission characteristics of passively fed electrospray microthrusters with propellant reservoirs. Journal of Spacecraft and Rockets, 54(2):447–458, 2017.

[129] Paulo Lozano and Manuel Martinez-Sanchez. Efficiency estimation of EMI-BF$_4$ ionic liquid electrospray thrusters. In 41st AIAA/ASME/SAE/ASEE Joint Propulsion Conference & Exhibit, page 4388, 2005.

[130] Ignacio Romero-Sanz, Rodrigo Bocanegra, J Fernandez De La Mora, and M Gamero-Castano. Source of heavy molecular ions based on Taylor cones of ionic liquids operating in the pure ion evaporation regime. Journal of Applied Physics, 94(5):3599–3605, 2003.

[131] JV Iribarne and BA Thomson. On the evaporation of small ions from charged droplets. The Journal of chemical physics, 64(6):2287–2294, 1976.

[132] FJ Higuera. Model of the meniscus of an ionic-liquid ion source. Physical Review E, 77(2):026308, 2008.

[133] IG Loscertales and J Fernandez De La Mora. Experiments on the kinetics of field evaporation of small ions from droplets. The Journal of chemical physics, 103(12):5041–5060, 1995.

[134] Trevor Morris, Cecile Malardier-Jugroot, and Manish Jugroot. Characterization of electrospray beams for micro-spacecraft electric propulsion applications. Journal of Electrostatics, 71(5):931–938, 2013.

[135] Chase Spenser Coffman. Electrically-assisted evaporation of charged fluids: Fundamental modeling and studies on ionic liquids. PhD thesis, Massachusetts Institute of Technology, 2016.

[136] Paulo Lozano and Manuel Martinez-Sanchez. Ionic liquid ion sources: characterization of externally wetted emitters. Journal of colloid and interface science, 282(2):415–421, 2005.

[137] Sergio Castro, Carlos Larriba, Juan Fernandez de la Mora, Paulo Lozano, and Selim Sümer. Capillary vs. externally wetted ionic liquid ion sources. In 42nd AIAA/ASME/SAE/ASEE Joint Propulsion Conference & Exhibit, page 4645, 2006.

[138] Carla S Perez-Martinez and Paulo C Lozano. *Visualization of beams from ionic liquid ion sources for focused ion beam applications.* Journal of Vacuum Science & Technology B, Nanotechnology and Microelectronics: Materials, Processing, Measurement, and Phenomena, *30(6):06F601, 2012.*

[139] David Krejci, Fernando Mier-Hicks, Corey Fucetola, Paulo Lozano, Andrea Hsu Schouten, and Francois Martel. *Design and characterization of a scalable ion electrospray propulsion system. 2015.*

[140] Renato Krpoun and HR Shea. *Integrated out-of-plane nanoelectrospray thruster arrays for spacecraft propulsion.* Journal of Micromechanics and Microengineering, *19(4):045019, 2009.*

[141] Robert S Legge, Paulo Lozano, and Manuel Martinez-Sanchez. *Fabrication and characterization of porous metal emitters for electrospray thrusters. In* International Electric Propulsion Conference, *page 145. Electric Rocket Propulsion Soc. Fairview Park, OH, 2007.*

[142] Daniel George Courtney. Ionic liquid ion source emitter arrays fabricated on bulk porous substrates for spacecraft propulsion. *PhD thesis, Massachusetts Institute of Technology, 2011.*

[143] Chase S Coffman and Paulo C Lozano. *On the manufacturing and emission characteristics of dielectric electrospray sources. In* 49th AIAA/ASME/SAE/ASEE Joint PropulsionConference, *page 4035. 2013.*

[144] Theodore F Baumann, Marcus A Worsley, T Yong-Jin Han, and Joe H Satcher Jr. *High surface area carbon aerogel monoliths with hierarchical porosity.* Journal of Non-Crystalline Solids, *354(29):3513–3515, 2008.*

[145] Steven Mark Arestie. Porous material and process development for electrospray propulsion applications. *PhD thesis, Massachusetts Institute of Technology, 2014.*

[146] Jimmy Rojas-Herrera, Iulia Jivanescu, Dakota Freeman, David Krejci, Corey Fucetola, and Paulo Lozano. *Porous materials for ion-electrospray spacecraft microengines.* Journal of Nanomechanics and Micromechanics, *7(3):04017006, 2017.*

[147] Natalya Brikner and Paulo C Lozano. *The role of upstream distal electrodes in mitigating electrochemical degradation of ionic liquid ion sources.* Applied Physics Letters, *101(19):193504, 2012.*

[148] Natalya Anna Brikner. On the identification and mitigation of life-limiting mechanisms of ionic liquid ion sources envisaged for propulsion of microspacecraft. *PhD thesis, Massachusetts Institute of Technology, 2015.*

[149] Chengyu Ma, Thomas Gregory Bull, and Charles Ryan. *Time-of-flight characterization of electrospray thrusters using porous emitters with high emission currents.* Journal of Propulsion and Power, *2021.*

[150] Daniel G Courtney, Hanqing Q Li, and Paulo Lozano. *Emission measurements from planar arrays of porous ionic liquid ion sources.* Journal of Physics D: Applied Physics, *45(48):485203, 2012.*

[151] Daniel G Courtney, Simon Dandavino, and Herbert Shea. *Comparing direct and indirect thrust measurements from passively fed ionic electrospray thrusters.* Journal of Propulsion and Power, *32(2):392–407, 2016.*

[152] Daniel G Courtney and Herbert Shea. *Influences of porous reservoir laplace pressure on emissions from passively fed ionic liquid electrospray sources.* Applied Physics Letters, *107(10):103504, 2015.*

[153] Peter L Wright and Richard E Wirz. Multiplexed electrospray emission on a porous wedge. Physics of Fluids, 33(1):012003, 2021.

[154] W David Carrier III. Goodbye, hazen; hello, kozeny-carman. Journal of Geotechnical and Geoenvironmental Engineering, 129(11):1054–1056, 2003.

[155] M Gamero-Castano and V Hruby. Electrospray as a source of nanoparticles for efficient colloid thrusters. Journal of Propulsion and Power, 17(5):977–987, 2001.

[156] Michael Freemantle. An introduction to ionic liquids. Royal Society of chemistry, 2010.

[157] C Larriba, D Garoz, C Bueno, I Romero-Sanz, S Castro, J Fernandez De La Mora, Y Yoshida, G Saito, R Hagiwara, K Matsumoto, et al. Taylor cones of ionic liquids as ion sources: The role of electrical conductivity and surface tension. ACS Publications, 2007.

[158] Joan Fuller, Richard T Carlin, and Robert A Osteryoung. The room temperature ionic liquid 1-ethyl-3-methylimidazolium tetrafluoroborate: electrochemical couples and physical properties. Journal of the Electrochemical Society, 144(11):3881, 1997.

[159] Zhi-Bin Zhou, Hajime Matsumoto, and Kuniaki Tatsumi. Structure and properties of new ionic liquids based on alkyl-and alkenyltrifluoroborates. ChemPhysChem, 6(7):1324–1332, 2005.

[160] Alan B McEwen, Helen L Ngo, Karen LeCompte, and Jay L Goldman. Electrochemical properties of imidazolium salt electrolytes for electrochemical capacitor applications. Journal of the Electrochemical Society, 146(5):1687, 1999.

[161] Y Yoshida, J Fujii, K Muroi, A Otsuka, G Saito, M Takahashi, and T Yoko. Highly conducting ionic liquids based on l-ethyl-3-methylimidazolium cation. Synthetic metals, 153(1-3):421–424, 2005.

[162] Timothy P Fedkiw and Paulo C Lozano. Development and characterization of an iodine field emission ion source for focused ion beam applications. Journal of Vacuum Science & Technology B: Microelectronics and Nanometer Structures Processing, Measurement, and Phenomena, 27(6):2648–2653, 2009.

[163] Jonathan G Huddleston, Ann E Visser, W Matthew Reichert, Heather D Willauer, Grant A Broker, and Robin D Rogers. Characterization and comparison of hydrophilic and hydrophobic room temperature ionic liquids incorporating the imidazolium cation. Green chemistry, 3(4):156–164, 2001.

[164] Adam F Visentin, Stephanie Alimena, and Matthew J Panzer. Influence of ionic liquid selection on the properties of poly (ethylene glycol) diacrylate-supported ionogels as solid electrolytes. ChemElectroChem, 1(4):718–721, 2014.

[165] Monika Součková, Jaroslav Klomfar, and Jaroslav Pátek. Temperature dependence of the surface tension and 0.1 mpa density for 1-cn-3-methylimidazolium tris (pentafluoroethyl) trifluorophosphate with n= 2, 4, and 6. The Journal of Chemical Thermodynamics, 48:267–275, 2012.

[166] D Garoz, C Bueno, C Larriba, S Castro, I Romero-Sanz, J Fernandez de La Mora, Y Yoshida, and G Saito. Taylor cones of ionic liquids from capillary tubes as sources of pure ions: The role of surface tension and electrical conductivity. Journal of Applied Physics, 102(6):064913, 2007.

[167] I Guerrero, R Bocanegra, FJ Higuera, and J Fernandez De La Mora. Ion evaporation from Taylor cones of propylene carbonate mixed with ionic liquids. Journal of Fluid Mechanics, 591:437–459, 2007.

[168] Ignacio Romero-Sanz, I Aguirre de Carcer, and J Fernandez de la Mora. *Ionic propulsion based on heated Taylor cones of ionic liquids.* Journal of Propulsion and Power, *21(2):239–242, 2005.*

[169] Luis Fernando VelAsquez-Garcia. *The design, fabrication and testing of micro-fabricated linear and planar colloid thruster arrays. PhD thesis, 2004.*

[170] MR Natisin, HL Zamora, WA McGehee, NI Arnold, ZA Holley, MR Holmes, and D Eckhardt. *Fabrication and characterization of a fully conventionally machined, high-performance porous-media electrospray thruster.* Journal of Micromechanics and Microengineering, *30(11):115021, 2020.*

[171] Malcolm C Gower. *Laser micromachining for manufacturing mems devices. In* MEMS Components and Applications for Industry, Automobiles, Aerospace, and Communication, *volume 4559, pages 53–59. International Society for Optics and Photonics, 2001.*

[172] Bryan Little and Manish Jugroot. *Bimodal propulsion system for small spacecraft: Design, fabrication, and performance characterization.* Journal of Spacecraft and Rockets, *57(4):707–719, 2020.*

[173] Brian R Donius and Joshua L Rovey. *Ionic liquid dual-mode spacecraft propulsion assessment.* Journal of Spacecraft and Rockets, *48(1):110–123, 2011.*

[174] Ewan Fonda-Marsland and Charlie Ryan. *Preliminary ionic liquid propellant selection for dual-mode micro-propulsion systems. In* 53rd AIAA/SAE/ASEE Joint Propulsion Conference, *page 5019, 2017.*

[175] Steven P Berg and Joshua L Rovey. *Decomposition of monopropellant blends of hydroxylammonium nitrate and imidazole-based ionic liquid fuels.* Journal of Propulsion and Power, *29(1):125–135, 2013.*

[176] Steven P Berg, Joshua Rovey, Benjamin Prince, Shawn Miller, and Raymond Bemish. *Electrospray of an energetic ionic liquid monopropellant for multi-mode micropropulsion applications. In* 51st AIAA/SAE/ASEE Joint Propulsion Conference, *page 4011, 2015.*

[177] Mitchell J Wainwright, Joshua L Rovey, Shawn W Miller, Benjamin D Prince, and Steven P Berg. *Electrospray mass spectroscopy of a HAN-based monopropellant. In* 2018 Joint Propulsion Conference, *pages 9–11, 2018.*

[178] Animesh Sharma, Anthony C Adducci, Joshua Rovey, Chengyu Ma, Charles N Ryan, Steven Berg, Michael Lembeck, and Zachary R Putnam. *Green ionic liquid multimode monopropellant based chemical micro-thruster. In* AIAA SCITECH 2022 Forum, *page 1733, 2022.*

[179] Amelia R Bruno. Design of a Bimodal Chemical-Electrospray Propulsion System using Ionic Liquid Monopropellants. *PhD thesis, Massachusetts Institute of Technology, 2021.*

[180] Amelia Bruno, Madeleine Schroeder, and Paulo C Lozano. *Characterization of electrospray thrusters with HAN-based monopropellants for multimode propulsion applications. In* AIAA SCITECH 2022 Forum, *page 2490, 2022.*

[181] Kento Masuyama and Paulo C Lozano. *Bimodal propulsion system using ionic liquid propellant for pico-and nano-satellite applications. In* 49th AIAA/ASME/SAE/ASEE Joint PropulsionConference, *page 3962. 2013.*

[182] Peter L Wright, Henry Huh, Nolan M Uchizono, Anirudh Thuppul, and Richard E Wirz. *A novel variable mode emitter for electrospray thrusters. In* International Electric Propulsion Conference, *2019.*

[183] Selim Sümer, Paulo Lozano, and Manuel Martínez-Sánchez. *Characterization of a variable isp ionic liquid electrospray thruster beam*. In 42nd AIAA/ASME/SAE/ASEE Joint Propulsion Conference & Exhibit, *page 4641, 2006.*

[184] Chase Spenser Coffman. Considerations for a multi-modal electrospray propulsion system. *PhD thesis, Massachusetts Institute of Technology, 2012.*

[185] John K Ziemer. *Performance measurements using a sub-micronewton resolution thrust stand. 2001.*

[186] Anthony G Cofer, Stephen D Heister, and Alina Alexeenko. *Improved design and characterization of micronewton torsional balance thrust stand*. In 49th AIAA/ASME/SAE/ASEE Joint PropulsionConference, *page 3856. 2013.*

[187] J Soni and S Roy. *Design and characterization of a nano-newton resolution thrust stand.* Review of Scientific Instruments, *84(9):095103, 2013.*

[188] James E Polk, Anthony Pancotti, Thomas Haag, Scott King, Mitchell Walker, Joseph Blakely, and John Ziemer. *Recommended practice for thrust measurement in electric propulsion testing.* Journal of Propulsion and Power, *33(3):539–555, 2017.*

[189] Paulo C Lozano. *Energy properties of an emi-im ionic liquid ion source.* Journal of Physics D: Applied Physics, *39(1):126, 2005.*

[190] Joseph E Campana. *Time-of-flight mass spectrometry: a historical overview.* Instrumentation Science and Technology - Taylor Francis, *Volume 16(1), 1987.*

[191] I Romero-Sanz and J Fernandez de la Mora. *Energy distribution and spatial structure of electrosprays of ionic liquids in vacuo.* Journal of applied physics, *95(4):2123–2129, 2004.*

[192] Manuel Gamero-Castaño. *The structure of electrospray beams in vacuum.* Journal of Fluid Mechanics, *604:339–368, 2008.*

[193] Peter Wright and Richard E Wirz. *Transient flow in porous electrospray emitters*. In AIAA Propulsion and Energy 2021 Forum, *page 3437, 2021.*

[194] Paulo César Lozano-Tovar. Studies on the ion-droplet mixed regime in colloid thrusters. *PhD thesis, Massachusetts Institute of Technology, 2003.*

[195] Nathan C Contino, Elizabeth E Pierson, David Z Keifer, and Martin F Jarrold. *Charge detection mass spectrometry with resolved charge states.* Journal of the American Society for Mass Spectrometry, *24(1):101–108, 2012.*

[196] Kent J Gillig, Brandon T Ruotolo, Earle G Stone, and David H Russell. *An electrostatic focusing ion guide for ion mobility-mass spectrometry.* International Journal of Mass Spectrometry, *239(1):43–49, 2004.*

[197] Omer Sise, Melike Ulu, and Mevlut Dogan. *Multi-element cylindrical electrostatic lens systems for focusing and controlling charged particles.* Nuclear Instruments and Methods in Physics Research Section A: Accelerators, Spectrometers, Detectors and Associated Equipment, *554(1-3):114–131, 2005.*

[198] Ryan C Blase, Joshua A Silveira, Kent J Gillig, Chaminda M Gamage, and David H Russell. *Increased ion transmission in ims: A high resolution, periodic-focusing dc ion guide ion mobility spectrometer.* International Journal of Mass Spectrometry, *301(1-3):166–173, 2011.*

[199] Subha Chakraborty, Caglar Ataman, Daniel G Courtney, Simon Dandavino, and Herbert Shea. *A tof-ms with a highly efficient electrostatic ion guide for characterization of ionic liquid electrospray sources.* Journal of The American Society for Mass Spectrometry, *25(8):1364–1373, 2014.*

[200] Norris E Bradbury and Russell A Nielsen. *Absolute values of the electron mobility in hydrogen.* Physical Review, *49(5):388, 1936.*

[201] R Weinkauf, K Walter, C Weickhardt, U Boesl, and EW Schlag. *Laser tandem mass spectrometry in a time of flight instrument.* Zeitschrift für Naturforschung A, *44(12):1219–1225, 1989.*

[202] Paul R Vlasak, Douglas J Beussman, Michael R Davenport, and Christie G Enke. *An interleaved comb ion deflection gate for m/z selection in time-of-flight mass spectrometry.* Review of scientific instruments, *67(1):68–72, 1996.*

[203] Ansgar Brock, Nestor Rodriguez, and Richard N Zare. *Characterization of a hadamard transform time-of-flight mass spectrometer.* Review of Scientific Instruments, *71(3):1306–1318, 2000.*

[204] Oh Kyu Yoon, Ignacio A Zuleta, Matthew D Robbins, Griffin K Barbula, and Richard N Zare. *Simple template-based method to produce bradbury-nielsen gates.* Journal of the American Society for Mass Spectrometry, *18(11):1901–1908, 2007.*

[205] Sharad Medhe. *Mass spectrometry: detectors review.* Chem Biomol Eng, *3:51–58, 2018.*

[206] Neil A Mehta and Deborah A Levin. *Molecular dynamics electrospray simulations of coarse-grained ethylammonium nitrate (ean) and 1-ethyl-3-methylimidazolium tetrafluoroborate (emim-bf4).* Aerospace, *5(1):1, 2017.*

[207] Orest Lastow and Wamadeva Balachandran. *Numerical simulation of electrohydrodynamic (ehd) atomization.* Journal of electrostatics, *64(12):850–859, 2006.*

[208] Thomas P Forbes, F Levent Degertekin, and Andrei G Fedorov. *Electrohydrodynamics of charge separation in droplet-based ion sources with time-varying electrical and mechanical actuation.* Journal of the American Society for Mass Spectrometry, *21(4):501–510, 2011.*

[209] MA Herrada, JM López-Herrera, Alfonso M Gañán-Calvo, EJ Vega, JM Montanero, and S Popinet. *Numerical simulation of electrospray in the cone-jet mode.* Physical Review E, *86(2):026305, 2012.*

[210] Henry Huh and Richard E Wirz. *Numerical simulation of electrospray thruster extraction.* IEPC-2019-650, 36th International Electric Propulsion Conference, *2019.*

[211] Wei-Cheng Yan, Pooya Davoodi, Yen Wah Tong, and Chi-Hwa Wang. *Computational study of core-shell droplet formation in coaxial electrohydrodynamic atomization process.* AIChE Journal, *62(12):4259–4276, 2016.*

[212] Qingxing Xu, Hao Qin, Zhenyuan Yin, Jinsong Hua, Daniel W Pack, and Chi-Hwa Wang. *Coaxial electrohydrodynamic atomization process for production of polymeric composite microspheres.* Chemical engineering science, *104:330–346, 2013.*

[213] DA1435033 Saville. *Electrohydrodynamics: the Taylor-Melcher leaky dielectric model.* Annual review of fluid mechanics, *29(1):27–64, 1997.*

[214] Geoffrey Ingram Taylor. *Studies in electrohydrodynamics. i. the circulation produced in a drop by an electric field.* Proceedings of the Royal Society of London. Series A. Mathematical and Physical Sciences, *291(1425):159–166, 1966.*

[215] Elaine M Petro, Ximo Gallud, Sebastian K Hampl, Madeleine Schroeder, Carl Geiger, and Paulo C Lozano. *Multiscale modeling of electrospray ion emission.* Journal of Applied Physics, *131(19):193301, 2022.*

[216] Ximo Gallud and Paulo Lozano. *The current emitted by ionic liquid ion sources in the pure-ionic regime - IEPC-2022-218*. 2022.

[217] Sebastian Hampl, Marshall Waggoner, Elaine Petro, Ximo Gallud, and Paulo Lozano. *Comparison of computational methods for modelling an electrospray plume with a n-body simulation - IEPC-2022-222*. 2022.

[218] Rafid Bendimerad and Elaine Petro. *Molecular dynamics studies of ionic liquid-surface interactions for electrospray thrusters - IEPC-2022-229*. 2022.

[219] Cyril W Hirt and Billy D Nichols. *Volume of fluid (vof) method for the dynamics of free boundaries.* Journal of computational physics, *39(1):201–225, 1981.*

[220] JM López-Herrera, Stéphane Popinet, and MA Herrada. *A charge-conservative approach for simulating electrohydrodynamic two-phase flows using volume-of-fluid.* Journal of Computational Physics, *230(5):1939–1955, 2011.*

[221] Ivo Roghair, Michiel Musterd, Dirk van den Ende, Chris Kleijn, Michiel Kreutzer, and Frieder Mugele. *A numerical technique to simulate display pixels based on electrowetting.* Microfluidics and nanofluidics, *19(2):465–482, 2015.*

[222] Henry Huh and Richard Wirz. *Numerical simulation of cone-jet and emission processes for electrospray thrusters - IEPC-2022-211*. 2022.

[223] Peter Mallalieu and Manish Jugroot. *Investigation of droplet mode electrospray emitters for use in multimodal systems for spacecraft.* In AIAA Propulsion and Energy 2021 Forum, *page 3438, 2021.*

[224] Thomas Patrick Forbes. Electrohydrodynamics and ionization in the Array of Micromachined UltraSonic Electrospray (AMUSE) ion source. *PhD thesis, Georgia Institute of Technology, 2010.*

[225] Benjamin St Peter, Rainer A Dressler, Yu-hui Chiu, and Timothy Fedkiw. *Electrospray Propulsion Engineering Toolkit (ESPET).* Aerospace, *7(7):91, 2020.*

[226] AM Ganan-Calvo, J Davila, and A Barrero. *Current and droplet size in the electrospraying of liquids. scaling laws.* Journal of aerosol science, *28(2):249–275, 1997.*

[227] C Larriba, D Garoz, C Bueno, I Romero-Sanz, S Castro, J Fernandez De La Mora, Y Yoshida, G Saito, R Hagiwara, K Matsumoto, et al. *Taylor cones of ionic liquids as ion sources: The role of electrical conductivity and surface tension. ACS Publications, 2008.*

[228] Anirudh Thuppul, Peter Wright, and Richard E Wirz. *Lifetime considerations and estimation for electrospray thrusters.* In 2018 Joint Propulsion Conference, *page 4652, 2018.*

[229] Chengyu Ma. Design and characterisation of electrospray thrusters with high emission density. *PhD thesis, University of Southampton, Department of Aeronautical and Astronautical, 2020.*

[230] Marianna Rinaldi, Federico Cecchini, Lucia Pigliaru, Tommaso Ghidini, Francesco Lumaca, and Francesca Nanni. *Additive manufacturing of polyether ether ketone (peek) for space applications: A nanosat polymeric structure.* Polymers, *13(1):11, 2020.*

[231] Jimmy Rojas-Herrera and Paulo C Lozano. *Mitigation of anomalous expansion of carbon xerogels and controllability of mean-pore-size by changes in mold geometry.* Journal of Non-Crystalline Solids, *458:22–27, 2017.*

[232] RW Pekala. *Organic aerogels from the polycondensation of resorcinol with formaldehyde.* Journal of materials science, *24(9):3221–3227, 1989.*

[233] R Brandt, R Petricevic, H Pröbstle, and J Fricke. *Acetic acid catalyzed carbon aerogels.* Journal of Porous Materials, *10(3):171–178, 2003.*

[234] Carla Sofia Perez Martinez. Engineering ionic liquid ion sources for ion beam applications. *PhD thesis, Massachusetts Institute of Technology, 2016.*

[235] Mingjin Yao and Ji Fang. *Hydrophilic peo-pdms for microfluidic applications.* Journal of Micromechanics and Microengineering, *22(2):025012, 2012.*

[236] Michael D Abràmoff, Paulo J Magalhães, and Sunanda J Ram. Image processing with imagej. Biophotonics international, *11(7):36–42, 2004.*

[237] Byran Little. *Development, design, and testing of a bimodal micro-propulsion system for spacecraft. Master's thesis, Royal Military College of Canada, 2019.*

[238] Bryan Little and Manish Jugroot. *Development of a microthrust balance and ion beam measurement system: Characterizing a dual-mode thruster for spacecraft.* Vacuum, *164:367–380, 2019.*

[239] Austin Chambers. Basic vacuum technology. *CRC Press, 1998.*

[240] Peter Mallalieu and Manish Jugroot. *Development of a time-of-flight diagnostic system for electrospray thrusters - IEPC-2022-197. 2022.*

[241] Trevor Morris, Martin Forget, Cecile Malardier-Jugroot, and Manish Jugroot. *Multi-scale investigation of a colloid micro-propulsion system.* Plasma Processes and Polymers, *8(6):478–489, 2011.*

[242] Peter L Wright, Nolan M Uchizono, Adam L Collins, and Richard E Wirz. *Characterization of a porous tungsten electrospray emitter. 2022.*

[243] S Castro and J Fernandez De La Mora. *Effect of tip curvature on ionic emissions from Taylor cones of ionic liquids from externally wetted tungsten tips.* Journal of Applied Physics, *105(3):034903, 2009.*

[244] Ravi Ranjan, SK Chou, Fahid Riaz, and Kumarasamy Karthikeyan. Cold gas micro propulsion development for satellite application. Energy Procedia, *143:754–761, 2017.*

[245] A Cervone, B Zandbergen, D Cordeiro Guerrieri, M De Athayde Costa e Silva, I Krusharev, and H Van Zeijl. Green micro-resistojet research at delft university of technology: new options for cubesat propulsion. CEAS Space Journal, *9(1):111–125, 2017.*